Probing Light Sterile Neutrinos with the First Five Science Runs of the KATRIN Experiment

Zur Erlangung des akademischen Grades einer
DOKTORIN DER NATURWISSENSCHAFTEN (Dr.rer.nat.)

von der KIT-Fakultät für Physik des
Karlsruher Instituts für Technologie (KIT)
angenommene

DISSERTATION

von

M. Sc. Shailaja Mohanty

Tag der mündlichen Prüfung:	18.07.2025
1. Referentin:	Prof. Dr. Kathrin Valerius Institut für Experimentelle Teilchenphysik, KIT
2. Korreferenten:	Prof. Dr. Guido Drexlin Institut für Experimentelle Teilchenphysik, KIT

Declaration of authorship Herewith I affirm that I wrote the current thesis on my own and without the usage of any other sources or tools than the cited ones and that this thesis has not been handed neither in this nor in equal form at any other official commission.

Erklärung der Selbstständigkeit Hiermit versichere ich, die vorliegende Arbeit selbstständig angefertigt zu haben und keine Hilfsmittel jenseits der kenntlich gemachten verwendet zu haben. Weiterhin habe ich weder diese noch eine äquivalente Version dieser Arbeit bei einer anderen Prüfungskommission vorgelegt.

Stutensee, June 10, 2025

Shailaja Mohanty

Abstract

Neutrino masses remain one of the most compelling open questions in particle physics, being orders of magnitude smaller than those of other known particles and lacking an established generation mechanism in the Standard Model of elementary particles. The Karlsruhe Tritium Neutrino (KATRIN) experiment measures the effective electron (anti-)neutrino mass by performing precision spectroscopy of the tritium β-decay spectrum near its 18.6 keV endpoint. The first science run was conducted in spring 2019. Subsequent measurement campaigns have progressively enhanced statistical precision. Over time, the experimental configuration has been modified to better mitigate systematic effects, background levels have been reduced, and data analysis techniques have been improved. These developments introduce additional complexity to perform a consistent and rigorous combined analysis of the full dataset. Based on its first five measurement campaigns, KATRIN obtains an upper limit of $m_\nu < 0.45\,\mathrm{eV/c^2}$ (90% C.L.), with further data analysis in progress.

In addition to probing the active neutrino mass, KATRIN exploits its ultra-precise β-spectrum measurement to search for light sterile neutrino states at the eV mass scale. A sterile neutrino would introduce a kink in the β-decay spectrum, appearing as a spectral distortion of the β-spectrum at an energy corresponding to its mass. Because this effect depends only on the spectral shape and not its absolute normalization, it provides a complementary and robust probe alongside neutrino-oscillation disappearance searches.

Initial sterile-neutrino searches by KATRIN based on the first two science runs (KNM1 and KNM2) already excluded large regions of parameter space associated with the reactor and gallium anomalies and challenged the Neutrino-4 claim. This thesis extends that work by performing a combined analysis of the first five KATRIN science runs (KNM1–KNM5), comprising 259 days of high-statistics data and approximately 36 million analyzed events in the region of interest. The analysis incorporates improved experimental configurations, enhanced background reduction, refined systematic uncertainties, and optimized statistical analysis techniques. No significant sterile-neutrino signal is observed. The resulting exclusion limits further improve upon previous tritium β-decay constraints and exclude additional regions of the parameter space favored by the Baksan Experiment on Sterile Transitions (BEST) and Gallium anomalies. This thesis contributes to the global effort to resolve outstanding anomalies in the neutrino sector and to test physics beyond the three-flavor neutrino paradigm.

Zusammenfassung

Die Neutrinomassen gehören nach wie vor zu den spannendsten offenen Fragen der Teilchenphysik, da sie um Größenordnungen kleiner sind als die anderer bekannter Teilchen und es im Standardmodell der Elementarteilchen keinen etablierten Entstehungsmechanismus dafür gibt. Das Karlsruhe Tritium Neutrino (KATRIN)-Experiment misst die effektive Elektron-(Anti-)Neutrinomasse durch präzise Spektroskopie des Tritium-β-Zerfalls-Spektrums nahe seinem Endpunkt bei 18,6 keV. Der erste wissenschaftliche Durchlauf wurde im Frühjahr 2019 durchgeführt. Nachfolgende Messkampagnen haben die statistische Präzision schrittweise verbessert. Im Laufe der Zeit wurde die Versuchsanordnung modifiziert, um systematische Effekte besser zu kompensieren, die Hintergrundwerte wurden reduziert und die Datenanalysetechniken verbessert. Diese Entwicklungen führen zu einer zusätzlichen Komplexität bei der Durchführung einer konsistenten und rigorosen kombinierten Analyse des gesamten Datensatzes. Basierend auf den ersten fünf Messkampagnen erhält KATRIN eine Obergrenze von

$$m_\nu < 0{,}45\,\mathrm{eV/c^2} \quad (90\%\ \mathrm{C.L.}),$$

wobei weitere Datenanalysen noch laufen.

Zusätzlich zur Untersuchung der aktiven Neutrinomasse nutzt KATRIN seine ultrapräzise β-Spektrumsmessung, um nach leichten sterilen Neutrinoständen im eV-Massenbereich zu suchen. Ein steriles Neutrino würde eine Knickstelle im β-Zerfalls-Spektrum verursachen, die als spektrale Verzerrung des β-Spektrums bei einer Energie erscheint, die seiner Masse entspricht. Da dieser Effekt nur von der Spektralform und nicht von seiner absoluten Normierung abhängt, stellt er neben der Suche nach dem Verschwinden von Neutrinooszillationen eine ergänzende und robuste Untersuchungsmethode dar.

Erste Suchen nach sterilen Neutrinos durch KATRIN auf der Grundlage der ersten beiden wissenschaftlichen Durchläufe (KNM1 und KNM2) schlossen bereits große Bereiche des Parameterraums aus, die mit den Reaktor- und Galliumanomalien in Verbindung stehen, und stellten die Behauptung von Neutrino-4 in Frage. Diese Arbeit erweitert diese Untersuchung durch eine kombinierte Analyse der ersten fünf wissenschaftlichen Durchläufe von KATRIN (KNM1–KNM5), die 259 Tage mit hochstatistischen Daten und etwa 36 Millionen analysierte Ereignisse im interessierenden Bereich umfassen. Die Analyse umfasst verbesserte experimentelle Konfigurationen, eine verbesserte Hintergrundreduktion, verfeinerte systematische Unsicherheiten und optimierte statistische Analysetechniken. Es wird kein signifikantes steriles Neutrino-Signal beobachtet. Die daraus resultierenden Ausschlussgrenzen verbessern die bisherigen Beschränkungen für den Tritium-β-Zerfall weiter und schließen zusätzliche Bereiche des Parameterraums aus, die vom Baksan Experiment on Sterile Transitions (BEST) und den Gallium-Anomalien favorisiert werden. Diese Arbeit leistet einen Beitrag zu den weltweiten Bemühungen, offene Anomalien im Neutrino-Sektor aufzuklären und die Physik jenseits des Drei-Flavour-Neutrino-Paradigmas zu testen.

Acknowledgements

I would like to express my deepest gratitude to all those who have contributed to the realization of this thesis. Without their guidance, encouragement, and support, this work would not have been possible.

First and foremost, I am profoundly indebted to my primary supervisor, Prof. Kathrin Valerius. From the outset of my DAAD scholarship application to the successful completion of this thesis, her unwavering mentorship has been invaluable. As my host and academic guide, Prof. Valerius provided expert advice on every aspect of my research, from honing my skills to meeting deadlines. Her generosity in sharing both her scientific knowledge and administrative expertise enabled me to navigate the challenges of being an international student. I am especially grateful for her support of my candidature while I was still in India, for coordinating research assistant appointments when required, and for encouraging my participation in summer schools, international conferences, and workshops. Her meticulous revisions of my manuscripts, precise and insightful feedback on my presentations and posters, and readiness to meet with me at short notice ensured that my work remained rigorous and timely. Beyond her scientific mentorship, Prof. Valerius made me feel at home far from my own, bolstered my confidence, and instilled in me the principles of good scientific practice and time management.

I also wish to thank my second supervisor, Prof. Guido Drexlin, for his insightful guidance and encouragement throughout my doctoral studies. His willingness to discuss new ideas and help me think through the puzzles arising in my research was instrumental in shaping my scientific approach. I appreciate his efforts to accommodate my schedule and provide constructive feedback whenever I sought his advice.

A special word of thanks goes to my constant mentor, Dr. Alexey Lokhov. I cannot imagine completing this thesis without his patient support. From impromptu visits to his office and extensive whiteboard discussions to collaborative analysis, Dr. Lokhov has been more than a mentor; he has been a source of reassurance during challenging periods. His encouragement and consistent motivation helped me remain focused and resilient. I am also grateful for his invaluable feedback on my thesis.

I am also grateful to Dr. Ferenc Glück for his generosity with time and expertise, especially in interpreting experimental results and participating in long, thoughtful meetings. In particular, I would like to acknowledge Cláudio Silva for performing simulations crucial to my analysis. I sincerely appreciate all the developers and contributors of the KATRIN software frameworks and cluster managers that supported my computational work. Their prompt and effective troubleshooting support, even during holidays, was instrumental in enabling the timely completion of my results for conference submissions and poster presentations

My thanks extend to Prof. Diana Parno for coordinating and supporting various aspects of my research activities; her collaborative spirit made it possible for tasks to be completed efficiently. I am grateful to Dr. Thierry Laserre for his seamless coordination of the KATRIN sterile neutrino search. I also extend my appreciation to Prof. Ulrich Nierste for serving as an additional mentor during my doctoral studies. Thank you, Prof. Magnus Schlösser, for inviting me to work with the Rear Wall Group, which greatly expanded my knowledge and skills. I also thank Prof. Sanshiro Enomoto for instructing me in data processing and sanitation.

I would like to thank Dr. Florian Frankle and Dr. Ferenc Glück for providing feedback on parts of this thesis.

I have benefited enormously from working with the entire KaFit team: Weiran Xu, Leonard Köllenberger, Stephanie Hickford, Moritz Machatschek, Richard Salomon, and Jaroslav Štorek, for their dedication in developing, performing, and maintaining the software infrastructure.

I take special pride in the KaFit software we developed together. I also acknowledge Sonja Schneidewind, Fabian Block, Max Aker, Dominic Batzler, Joscha Lauer, Neven Kovač, Svenja Heyns and Dominic Hinz for engaging physics discussions. Collaborating with the KATRIN data analysis teams, the data monitoring group, the hardware teams, and the IT managers has been a privilege; our discussions were always constructive and productive. A special gratitude to the entire sterile neutrino analysis team for collaborative problem-solving, which greatly enhanced the robustness of this work. I sincerely thank Armen Beglarian for introducing me to the KATRIN control room infrastructure and making my days as an operator both engaging and educational.

Finally, I owe my deepest appreciation to my family and friends. To my parents, who have consistently motivated me despite the distance, and to my beloved husband, Shrinivas, whom I met during my research and whose tenacious support made this journey possible. Your guidance helped me overcome procrastination and stay focused on my goals. I thank you Shri, for being a constant source of support both as a friend and as a partner. My sincere thanks go to all the research assistants: Lukas Mettler, Lara Bauer, and Vanessa Breitenstein, for their invaluable help in achieving every milestone. To my dear friend Pratik: thank you for brightening my days with hiking, biking, and culinary explorations, as well as for your boundless encouragement. To Sofia, for being my emotional pillar, and to Hans and Hannelore Lackner, who made my apartment feel like home. From secret Santa surprises to celebrating your 80th birthday, you treated me not just as a tenant but as a member of your family. Finally, thank you, God, for everything.

This thesis stands as a testament to the dedication and generosity of the many individuals mentioned above. To all of you, I offer my heartfelt thanks.

Funding and resource acknowledgement

The work was made possible with the support of a scholarship from the **German Academic Exchange Service (Deutscher Akademischer Austauschdienst, DAAD)**. The funding included:

- doctoral stipend
- travel allowance
- coverage for health, accident, and liability insurance

DAAD also supported institutional resources through its Material Resources Programme, providing essential laboratory equipment, scientific databases, and specialized literature. I am deeply grateful for this support, which was instrumental in successfully completing this study.

Contents

Preface

The KATRIN collaboration, established in 2001, is an international team comprising approximately 150 members from more than 20 institutions across seven countries. From the initial design phase through commissioning, nearly two decades of concerted effort were required before the first science run in 2019. Data taking is planned to continue through 2025. Realizing KATRIN's physics goals has demanded coordinated work from hardware engineers, technicians, and R&D specialists to design, install, and maintain every component of the apparatus, from ultra-high-vacuum systems and precision high-voltage supplies to superconducting magnet technology and segmented silicon detectors. Concurrently, dedicated teams are responsible for data acquisition and hardware operations, ensuring stable running conditions and continuous monitoring of data quality. In parallel, independent analysis groups process and interpret the collected data, which at present span over sixteen concluded science runs, cross-validating each other's results to ensure robustness. Two teams employ separate, independently developed analysis frameworks. The primary distinction between the two frameworks lies in their approach to modeling the experimentally recorded β-decay spectrum. Netrium employs a neural network trained on simulated spectra to rapidly predict the theoretical spectrum across parameter space. In contrast, KaFit performs a numerical integration of the analytical β-decay model, convolving it with the experimental response function, while employing caching and multiprocessing to optimize computational efficiency. Experts on various specific systematic effects contribute detailed models and input parameters to both analysis pipelines. These include source-related effects, background rates, detector response functions, and magnetic field systematics. The coordinated team efforts in hardware development, data acquisition operations, and data analysis have made it possible to perform the high-precision kinematic measurements of the tritium β-decay spectrum that form the basis of this thesis.

This work primarily focuses on the search for eV-scale sterile neutrinos using data from the first five KATRIN science runs (KNM1-5), analyzed through a well-established Frequentist framework. As a secondary objective, a Bayesian analysis approach tailored to sterile neutrino searches with KATRIN was developed and demonstrated on simulated data. Both methods were implemented using the KaFit framework, which served as the foundation for all analyses presented in this thesis. The results, obtained in collaboration with the Netrium team, were released by the collaboration in Spring 2025 (arXiv:2503.18667, submitted for peer review) and presented at the Moriond EW 2025 conference. This branch of the KATRIN data analysis, dedicated to the search for light sterile neutrinos, is based on integral contributions of three doctoral theses, including the works of Xaver Stribl and Christoph Köhler at TU Munich, and was coordinated by Dr. Thierry Lasserre (CEA/TU Munich).

All KaFit-based analysis presented in this sterile-neutrino search was led by me, including work I conducted independently as well as components I guided in collaboration with others. The following points summarize the key contributions I made, either directly or by supervising and supporting related efforts.

- Analyzed data collected during the first five science runs to search for an eV-scale sterile neutrino using a Frequentist framework.
- Conducted supporting studies to validate and ensure the robustness of the Frequentist analysis.

- Developed and demonstrated on an Asimov dataset, a Bayesian analysis framework and associated software based on the KaFit platform, tailored for sterile neutrino searches with KATRIN.

- Participated in data taking from 2022 onward through shift work assigned by the run coordination team, contributing to KATRIN's goal of accumulating 1,000 total measurement days by 2025.

- The sterile neutrino search and neutrino mass analyses were performed independently on the same dataset from the first five KATRIN science runs by separate teams. An unexpected sterile neutrino signal upon first unblinding indicated a potential in the combination of data from different measurement periods or unaccounted systematic effect in the shared dataset, which could also bias the neutrino mass measurement. As a member of the eV-sterile neutrino analysis team, I collaborated with the neutrino mass analysis team to investigate potential problems in data combination and systematic treatments and helped resolve the discrepancy. Consequently, the sterile neutrino analysis acted as a critical consistency check prior to the final release of the neutrino mass results.

- Investigated systematics related to tritium accumulation on the gold-coated rear-wall electrode (placed in the rear end of KATRIN beam tube) by performing in-situ measurements of the secondary beta spectrum, monitoring tritium flux, and analyzing these data to generate systematic inputs for data analysis from KNM5-10. This work led to the identification and correction of an issue in the neutrino-mass analysis by reanalyzing the rear-wall signal calculations for KNM1–5.

- Studied electron energy loss from scattering within the KATRIN rear-wall and collaborated with members of the TRISTAN team to quantify this effect through data analysis and detailed simulations, addressing a systematic effect critical to the future measurement program of the TRISTAN detector at KATRIN.

- Presented the sterile neutrino sensitivity findings at international conferences and workshops like EPS-HEP 2023, NuMass 2024, Neutrino 2024, and actively participated in KATRIN analysis workshops and collaboration meetings from 2022 until the completion of this thesis.

- Supervised Master's and Bachelor's students on KATRIN-related analysis tasks, including:
  - Guided a research project focused on the implementation and validation of the analysis chain for sterile-neutrino sensitivity studies across KATRIN's full measurement interval. This included evaluating the applicability of Wilks' theorem, which is commonly used to justify chi-squared approximations for confidence intervals, and exploring alternative approaches for quantifying systematic uncertainties in the sterile-neutrino analysis.
  - Supervised a project analyzing rear-wall β-spectrum data to quantify systematics arising from tritium accumulation. Responsibilities included overseeing data processing, interpretation, and validation, as well as coordinating with members of the CMU group to cross-check results and ensure consistency across independent analyses.
  - Tutoring a Bachelor's student in basic neutrino physics, training her to perform a sterile-neutrino sensitivity analysis for KATRIN's sixth science run.

In addition to the individual contributions listed above, selective use was made of digital tools during the preparation of this thesis. These included Grammarly for grammar refinement, Zotero for reference management, OpenAI's ChatGPT for improving clarity, academic tone, and code debugging, and GitHub for version control and code management.[1] These tools were not used to generate scientific content, perform data analysis, or interpret results. All scientific contributions, conceptual development, and analyses presented herein are solely my own.

---

[1] ChatGPT (OpenAI, 2025), available at https://chat.openai.com; Grammarly, available at https://www.grammarly.com; Zotero, available at https://www.zotero.org; Overleaf, available at https://www.overleaf.com; GitHub repository for KaFIT: https://github.com.

Introduction

Neutrino experiments over the past two decades have unequivocally shown that the three active neutrinos mix and possess nonzero masses, in stark contrast to the minimal Standard Model (SM) framework, which predicts massless, purely left-handed neutrinos [198]. These discoveries raise several fundamental questions: what is the ordering and absolute scale of neutrino masses; how large is CP-violation in the lepton sector; are neutrinos Dirac or Majorana particles; what are the precise values of the mixing angles; is the three-neutrino mixing paradigm complete or are there deviations such as sterile neutrinos, a non-unitary PMNS matrix; what mechanism generates light neutrino masses?. Addressing these questions underpins a broad research program and motivates extensions of the SM that seek to explain the origin of neutrino masses and mixing.

Alongside the fundamental discovery of neutrino oscillations, a collection of experimental anomalies were observed and remain unresolved [6]. Two anomalies involve the appearance of electron (anti) neutrinos in muon (anti) neutrino beams: LSND (pion decay-at-rest) and MiniBooNE (pion decay-in-flight), while two others show an overall deficit of reactor (Reactor Neutrino Anomaly) and ^{71}Ga source (Gallium Anomaly) electron (anti)neutrinos. The later is reaffirmed by the BEST collaboration [38]. A minimal (3+1) mixing framework in which the three active neutrinos are complemented by a sterile state ν_4 with mass $m_4 \gtrsim 1\,\mathrm{eV}$ and a short-baseline mass-squared splitting defined as

$$\Delta m^2_{\mathrm{SBL}} \equiv m_4^2 - m_1^2 \gtrsim 1\,\mathrm{eV}^2,$$

has been proposed to account simultaneously for LSND, MiniBooNE, GA, and RAA, albeit with some tension among datasets [77, 50]. Recent studies suggest that the RAA deficit has diminished and that the Gallium Anomaly requires further scrutiny [6, 255, 84], while the Short-Baseline Neutrino Programme [5, 61] aims to resolve the LSND and MiniBooNE anomalies. The existence of an ∼eV-scale sterile neutrino therefore remains an open question, and its confirmation would represent a major breakthrough.

From a broader theoretical standpoint, sterile neutrinos arise naturally as Standard Model gauge singlet fermions. Once allowed, such singlets can appear at essentially any mass scale and couple to active neutrinos through Yukawa terms in the so-called neutrino portal, the only possible renormalizable coupling between SM particles and new singlet fermions [72]. This coupling permits both Dirac and Majorana mass terms and provides the foundation for a range of seesaw mechanisms that explain the smallness of active neutrino masses [256]. In this framework, sterile neutrinos are not ad hoc additions but minimal and generic extensions of the SM. Their masses span many orders of magnitude, with sub-eV states potentially responsible for short-baseline oscillation anomalies, keV-scale states serving as warm dark matter candidates, and heavier states (GeV–TeV). The eV scale is especially compelling: it lies at the confluence of neutrino oscillation anomalies and direct experimental accessibility, and is one of the few regimes where sterile neutrinos could be discovered or ruled out within the current generation of laboratory experiments. Despite the theoretical motivations, global fits to oscillation data reveal severe tension: the parameter regions favored by appearance anomalies conflict with stringent disappearance limits from reactor, accelerator, and cosmological probes [75]. This tension underscores the need for an independent, model-agnostic test of sterile neutrinos. In this context of conflicting hints and stringent bounds, direct kinematic probes become essential. Precision β-decay spectroscopy offers a model-independent window: in a $3+1$ framework, mixing of a heavy mass state ν_4 with the electron flavor produces a distinct spectral distortion at electron kinetic energy $E = E_0 - m_4$, where E_0 is the β-decay endpoint energy and m_4 is the sterile neutrino mass.

The Karlsruhe Tritium Neutrino (KATRIN) experiment [67], achieves high resolution near the 18.6 keV endpoint, by using a high-luminosity windowless tritium source and magnetic adiabatic collimation with an electrostatic (MAC-E) filter. KATRIN's exclusion limits based on data from first two campaigns had already surpassed Mainz and Troitsk limits and covered a significant portion of the original Reactor and Gallium anomaly parameter spaces [11, 12]. This thesis presents the analysis of 259 days of data (36 million electrons), six times the statistics of previous data releases. The result obtained further challenges the remaining Gallium-favored region and the Neutrino-4 claim [137].

- *Chapter 1:* Introduces the fundamentals of neutrino physics, motivates the search for eV-scale sterile neutrinos, and outlines the sensitivity of the KATRIN experiment to such states.
- *Chapter 2:* Describes the design and operational principles of the KATRIN experimental setup, including its main components.
- *Chapter 3:* Details the modeling framework used to compare the theoretical electron rates with those measured at KATRIN, incorporating relevant systematic effects.
- *Chapter 4:* Presents the Frequentist analysis framework for the sterile neutrino search and summarizes sensitivity projections and exclusion bounds based on data from the first five science runs.
- *Chapter 5:* Introduces a Bayesian analysis approach for the sterile neutrino search and illustrates its application using simulated data.
- *Chapter 6:* Investigates the backscattering of electrons from the rear wall through dedicated measurements and comprehensive Monte Carlo simulations.

Looking ahead, the forthcoming TRISTAN detector upgrade [58] for KATRIN, a multi-pixel silicon drift detector array is designed to extend sensitivity into the keV mass range with order-of-magnitude improvements. Together with the Fermilab Short-Baseline Neutrino (SBN) program (SBND, MicroBooNE, ICARUS) and continued reactor spectral-ratio measurements, KATRIN's kinematic search stands currently as the best laboratory experiment capable of directly testing eV–keV sterile-neutrino hypotheses independently of oscillation and cosmological inputs.

1 Neutrinos in and Beyond the Standard Model

> *"It doesn't matter how beautiful your theory is, it doesn't matter how smart you are. If it doesn't agree with experiment, it's wrong."*
>
> — Richard P. Feynman

This chapter begins with a brief history of neutrinos, from postulation to discovery of neutrino oscillations in Section 1.1. Section 1.2 summarizes neutrinos within the framework of the Standard Model. Section 1.3 presents the theory of neutrino oscillations along with mass-generation mechanisms discussed in Section 1.4, which sets the stage for the introduction of right-handed or sterile neutrinos. In Section 1.5, experimental anomalies suggesting the existence of an eV-scale sterile neutrino are examined, along with a description of its characteristic signature. Finally, Section 1.6 explains how single β-decay offers a direct, model-independent method to search for sterile neutrinos using KATRIN.

1.1 Historical Context and Early Experimental Evidence

The neutrino was first postulated in 1930 by Pauli (1945 Nobel Laureate in Physics) to resolve the apparent non-conservation of energy, spin and angular momentum observed in β-decay [203]. In 1933, Fermi (1938 Nobel Laureate in Physics) and Perrin [205] proposed a measurement of neutrino mass through the investigation of the β-spectrum near the endpoint. Their proposal was a four-fermion interaction theory, where neutron (n) decay is described as a point-like process yielding a proton (p), an electron (e^-), and an electron-antineutrino ($\bar{\nu}_e$) [88]. The initial neutrino mass measurements using the Fermi–Perrin method yielded an upper limit of $m_\nu < 500\,\mathrm{eV/c^2}$ [148], which was further tightened to $m_\nu < 250\,\mathrm{eV/c^2}$ in the 1950s [158], thereby demonstrating that the neutrino mass, if nonzero, was much smaller than the electron mass. The extremely weak coupling of neutrinos to matter explained their elusiveness in detection. Experimental confirmation came in 1956, when antineutrinos were observed by Reines and Cowan, via inverse β-decay ($\bar{\nu}_e + p \to n + e^+$) from a nuclear reactor [69]. The characteristic delayed-coincidence signal, positron annihilation followed by neutron capture, provided the first direct evidence for the neutrino's existence. It was the first experiment, now referred to as a reactor neutrino experiment, where electron antineutrinos ($\bar{\nu}_e$) produced by nuclear reactors were used. In 1956, Lee and Yang proposed that parity (P) and charge conjugation (C) are violated in weak interactions [161], which was confirmed experimentally by Wu et al. in 1957 [253]. In 1957, following the discovery of parity violation in β-decay, Landau [156], Lee and Yang [160], and Salam [226] assumed that the neutrino was massless and described by either a left-handed (ν_L) or a right-handed (ν_R) field. In 1958, Goldhaber et al. [109] measured the neutrino's helicity [1] and confirmed that it is left-handed, in agreement with the two-component theory. However, their measurement could not rule out the possibility of a small, nonzero neutrino mass. This together with evidence of parity violation led to the development of the V–A (vector minus axial) theory in 1958 [89], where the two-component Weyl spinor formalism became a natural description for massless neutrinos, which fundamentally described weak interactions with left-handed neutrinos [202, 160]. After the confirmation of V-A theory, the concept of massive neutrinos became more natural.

In 1957, Pontecorvo [211, 210] proposed that a neutrino produced in a weak interaction is a superposition of two Majorana mass eigenstates, analogous to the K^0–$\bar{K}^0$ system and thus hypothesized neutrino oscillations despite only one neutrino flavor being known at the time. In 1959, Pontecorvo hypothesized that neutrinos from pion decay differ from electron neutrinos (ν_e) [209]. This was confirmed in 1962 at Brookhaven National Laboratory by Lederman, Schwartz, and Steinberger, who showed that a neutrino beam from pion decay produced muons but not electrons, establishing $\nu_\mu \neq \nu_e$ [71]. This result confirmed the existence of at least two lepton families and introduced the muon neutrino (ν_μ) as a new particle in the Standard Model. Moreover, this experiment was the first to use a prepared neutrino beam, now recognized as the first accelerator neutrino experiment. During the 1960s, the electroweak theory was developed [110], describing neutrinos as massless left-handed Weyl fermions interacting solely via weak currents, with lepton flavor numbers (L_e, L_μ, L_τ) conserved in these interactions. Maki, Nakagawa, and Sakata (MNS) proposed neutrino mixing [172] to explain anomalies in hyperon decays and differences in muon and β-decay rates (2 neutrino case). Pontecorvo [212] and later Gribov-Pontecorvo [111] introduced the first phenomenology of neutrino oscillations based on this mixing. In this theory, the two left-handed neutrino fields ν_{eL} and $\nu_{\mu L}$ were linear combinations of the left-handed parts of two Majorana fields with definite masses, and the mass term involved only those left-handed fields. The full theory, including three generations and the 3×3 Maki–Nakagawa–Sakata–Pontecorvo (MNSP or PMNS) mixing matrix, was formulated in the mid-1970s, allowing for possible CP violation in the lepton sector. The subsequent discovery of the tau lepton [204], the tau neutrino by the DONUT experiment at Fermilab[147], and heavier quarks [34] confirmed the three-generation structure of the Standard Model (SM). In 1976, researchers investigated neutrino oscillations using a two-Dirac-neutrino mixing scheme [47, 96], drawing upon an analogy between quarks and leptons, and also considered oscillations within the general Dirac–Majorana framework [45].

Theoretical predictions of the solar neutrino flux were pioneered by Bahcall, who used detailed solar models to estimate the expected neutrino production rate and energy spectrum [36, 37]. "The solar neutrino problem" emerged in the late 1960s when the Homestake experiment [73], led by Davis Jr., detected only about one-third of the electron neutrinos predicted by the Standard Solar Model (SSM) using a chlorine-based detector [63]. This discrepancy raised questions about either the solar model's accuracy or the fundamental properties of neutrinos. To further investigate this anomaly, additional experiments employing different detection methods were conducted. The GALLEX [114, 115] and SAGE [3] experiments used gallium-based detectors sensitive to low-energy neutrinos, particularly those from the initial pp reactions in the Sun. These experiments also observed a deficit in the detected ν_e flux compared to SSM predictions. Water Cherenkov detectors, such as the Kamiokande experiment in Japan [120], detected neutrinos through the observation of Cherenkov radiation emitted by electrons scattered by ν_e.

---

[1] Helicity is defined as the projection of a particle's spin vector $\mathbf{S}$ onto the direction of its momentum $\mathbf{p}$, i.e.,

$$h = \frac{\mathbf{S} \cdot \mathbf{p}}{|\mathbf{p}|},$$

which takes values $+1$ (right-handed antineutrino) or -1 (left-handed neutrino) for a spin-$\frac{1}{2}$ particle.

These detectors confirmed the ν_e deficit and, for the first time, provided real-time detection and directional information, reinforcing the solar origin of the neutrinos.

The resolution of the solar neutrino problem came with two newer experiments: the Super-Kamiokande experiment [239, 240, 241] and the Sudbury Neutrino Observatory (SNO) [236, 237]. The observation of flavor transformation in atmospheric neutrinos by the Super-Kamiokande experiment, along with the finding by the SNO that solar neutrinos change type rather than vanishing on their way to Earth, provided definitive evidence of neutrino oscillations. This groundbreaking discovery proved that that neutrinos possess mass and mix, leading to the 2015 Nobel Prize in Physics [243].

Moreover, the phenomenon of neutrino oscillation also implies that the Standard Model (SM) needs to extended to explain massive neutrinos.

1.2 The Standard Model and Massless Neutrinos

The SM is the established framework in particle physics that describes how matter particles with spin$\frac{1}{2}$) fermions, interact via the electromagnetic, weak, and strong forces, each mediated by spin(1) gauge bosons: the photon for electromagnetism, gluons for the strong interaction, and the massive W and Z bosons for the weak interaction. It required nearly five decades of theoretical and experimental effort, from the early 1960s to 2012, to develop the Standard Model. The SM of particle physics successfully unifies the electromagnetic, weak, and strong interactions under the gauge group $\mathrm{SU}(3)_C \times \mathrm{SU}(2)_L \times \mathrm{U}(1)_Y$ [198]. Following the discovery of the Higgs boson [60, 1], all elementary particles predicted by the SM have been experimentally confirmed. Among these, neutrinos marked the first major success of the Standard Model. As electrically neutral, colorless fermions, neutrinos interact only via the electroweak force mediated by the $W^\pm$ and Z^0 gauge bosons, and are inert to electromagnetic and strong forces. This limited interaction profile renders them elusive and fundamentally distinct from other matter particles.

The weak and electromagnetic forces can be combined in the electroweak theory using the gauge group $\mathrm{SU}(2)_L \times \mathrm{U}(1)_R$. In the SM, the elementary fermions are grouped into left-handed fields to form doublets, while right-handed fields form singlets [256]. Neglecting the quarks, each lepton generation, labeled by $\ell = e, \mu, \tau$, consists of the left-handed $\mathrm{SU}(2)_L$ doublet

$$L_\ell = \begin{pmatrix} \nu_{\ell L} \\ \ell_L \end{pmatrix}, \tag{1.1}$$

and the right-handed charged-lepton singlet ℓ_R. Consequently, neutrinos are represented as three left-handed Weyl fermions, each associated with a lepton generation, forming weak isospin doublets alongside their corresponding charged leptons. Lepton family numbers L_e, L_μ, and L_τ, as well as the total lepton number $L = L_e + L_\mu + L_\tau$ are conserved in the weak interaction. Right-handed neutrino fields $\nu_{\ell R}$ are absent in the minimal SM and thus can not participate in weak interaction [106].

Neutrinos participate in weak interactions through two distinct types of neutrino interaction vertices that couple them to the weak gauge bosons: the neutral-current (NC) vertex and the charged-current(CC) vertex [206]. The neutral-current vertex couples the neutrino current of a given flavor to the neutral gauge boson Z^0 without mixing between lepton generations (see Figure 1.1 a). The charged-current vertex couples each neutrino to its corresponding charged-lepton current via the charged gauge bosons $W^\pm$ (see Figure 1.1 b). Neutral-current interactions were first observed in 1973 through $\nu_\mu + N \to \nu_\mu + X$ events lacking charged leptons, confirming the Z^0 boson's role in weak processes [116, 196].

(a) Neutral Current Interaction (b) Charged Current Interaction

Figure 1.1: Feynman diagrams showing (a) neutral current neutrino interaction and (b) charged current neutrino interaction vertices according to the Standard Model, where $\ell = e, \mu, \tau$ and ν_ℓ respective neutrino states

The chiral structure of the weak interaction, characterized by the $V - A$ form, implies that only left-handed fermions and right-handed anti-fermions participate in charged-current processes [89, 256]. Accordingly, neutrinos appear exclusively as left-handed fields in weak interactions. In the massless limit, chirality coincides with helicity, a fact experimentally confirmed by the Goldhaber experiment [109], which demonstrated that neutrinos are left-helical and parity is violated in weak interactions.

Prior to electroweak symmetry breaking, the Standard Model treats all elementary fermions as massless to maintain gauge invariance. Fermion masses arise only after spontaneous symmetry breaking (SSB) via the Higgs mechanism [119, 141]. In this mechanism, left-handed and right-handed fermion fields couple to the Higgs field through *Yukawa interactions*. After that, Higgs field acquires non-zero vacuum expectation value and then each Yukawa coupling generates a mass term that links the corresponding left- and right-handed fermion fields [256]. Because no right-handed neutrino fields exist in the minimal SM, no Yukawa coupling for neutrinos is possible. As a result, neutrinos remain strictly massless within this description, consistent with the absence (at the time) of experimental evidence for non-zero neutrino masses.

Gauge invariance and the particle content of the early SM impose strict constraints on neutrino mass terms. The three facts imply neutrinos being massless in early SM:

1. **Absence of Right-Handed Neutrinos:** Since the minimal SM does not include gauge-singlet right-handed neutrino fields ν_R, it is impossible to construct a Dirac mass term which require both left- and right-handed components.

2. **Single Higgs Doublet:** With only one Higgs doublet in the SM, generating Majorana mass terms for neutrinos necessitates higher-dimensional operators or additional scalar fields, which are absent in the minimal model.

3. **Requirement of renormalizable theory:** The SM is constructed to be a renormalizable quantum field theory, meaning all its interaction terms have coupling constants with non-negative mass dimensions. A Majorana mass term constructed only from the existing fields would violate $\mathrm{SU}(2)_L \times \mathrm{U}(1)_Y$ gauge symmetry.

These features imply that the SM Lagrangian contains neither Dirac nor Majorana mass terms for neutrinos, enforcing neutrino mass, $m_\nu = 0$ at tree level.

Measurements of the invisible decay width of the Z^0-boson at the LEP collider constrain the number of light neutrino species that couple to the Z^0:

$$N_\nu = 2.984 \pm 0.008, \tag{1.2}$$

indicating the existence of only three light, active neutrino flavors [227]. Any additional neutrinos must either have masses above $m_Z/2$ or must not couple to the the Z^0 boson—i.e. it would have to be "sterile" with respect to Standard Model gauge interactions.

Despite the success of SM, experimental observation of neutrino oscillations provides irrefutable evidence that neutrinos are massive and mix among flavors. This phenomenon violates individual lepton flavor conservation and demonstrates that the minimal SM is incomplete. Explaining nonzero neutrino masses and mixings necessitates the introduction of new degrees of freedom beyond the SM framework. The following section will discuss potential SM extensions that accommodate neutrino mass generation and the neutrino oscillation phenomenology.

1.3 Theory of Neutrino Oscillations: Road Map to Massive Neutrinos

Neutrino oscillation is a quantum mechanical interference phenomenon in which neutrinos change their flavor during propagation [201]. In this phenomenon, the neutrino flavor eigenstates do not coincide with the neutrino mass eigenstates. Rather, the flavor states $|\nu_\alpha\rangle$, with $\alpha \in \{e, \mu, \tau\}$, are linear combinations of the mass eigenstates $|\nu_i\rangle$, $i \in \{1, 2, 3\}$, connected through a unitary 3×3 mixing matrix U:

$$\begin{pmatrix} \nu_e \\ \nu_\mu \\ \nu_\tau \end{pmatrix} = U \begin{pmatrix} \nu_1 \\ \nu_2 \\ \nu_3 \end{pmatrix}. \tag{1.3}$$

This unitary matrix, commonly called the PMNS matrix, can be parameterized by three Euler mixing angles $\theta_{12}, \theta_{13}, \theta_{23}$ and one Dirac CP-violating complex phase δ in the standard parametrisation [201]. A convenient factorization is

$$U = \begin{pmatrix} U_{e1} & U_{e2} & U_{e3} \\ U_{\mu 1} & U_{\mu 2} & U_{\mu 3} \\ U_{\tau 1} & U_{\tau 2} & U_{\tau 3} \end{pmatrix} = \begin{pmatrix} 1 & 0 & 0 \\ 0 & c_{23} & s_{23} \\ 0 & -s_{23} & c_{23} \end{pmatrix} \begin{pmatrix} c_{13} & 0 & s_{13}e^{-i\delta} \\ 0 & 1 & 0 \\ -s_{13}e^{i\delta} & 0 & c_{13} \end{pmatrix} \begin{pmatrix} c_{12} & s_{12} & 0 \\ -s_{12} & c_{12} & 0 \\ 0 & 0 & 1 \end{pmatrix}, \tag{1.4}$$

with $c_{ij} = \cos\theta_{ij}$ and $s_{ij} = \sin\theta_{ij}$. Two additional phases enter the PMNS matrix for the case where neutrino is a Majorana particle and are neglected as they are irrelevant for neutrino oscillations (see [201] for a review).

When neutrinos propagate, each mass eigenstate ν_i of energy E and momentum $p \approx E$ evolves as $\exp(-iE_i t + ip_i x)$. Since

$$E_i \simeq p + \frac{m_i^2}{2E},$$

different mass eigenstates accumulate phase at different rates. Because each mass eigenstate propagates with its own phase velocity, the combined neutrino state gradually deviates from its initial flavor alignment, leading to the phenomenon of neutrino oscillations [201]. The probability $P(\nu_\alpha \to \nu_\beta)$ that a neutrino produced in flavor state ν_α will be observed as flavor state ν_β (with $\alpha, \beta = e, \mu, \tau$) after traveling a distance L with neutrino energy E is given by:

$$P(\nu_\alpha \to \nu_\beta) = |\langle \nu_\beta(L)|\nu_\alpha(0)\rangle|^2 = \left| \sum_{i=1}^{n} U_{\beta i} U_{\alpha i}^* e^{-i\frac{m_i^2 L}{2E}} \right|^2 \tag{1.5}$$

The oscillatory behavior is described by phase term $\exp\left(-i\frac{m_i^2 L}{2E}\right)$, leading to interference between mass eigenstates with squared mass splittings $\Delta m_{ij}^2 = m_i^2 - m_j^2$. The oscillation probability is a function of the neutrino energy E and the propagation distance L and in many cases, the phenomenology of neutrino oscillations a two-flavor approximation suffices [50]: The oscillation probability then simplifies to:

$$P(\nu_\alpha \to \nu_\beta) \simeq \left|\delta_{\alpha\beta}{}^{2} - \sin^2(2\theta_{ij})\sin^2\left(\frac{\Delta m_{ij}^2 L}{4E}\right)\right| \tag{1.6}$$

$$= \left|\delta_{\alpha\beta} - \sin^2(2\theta_{ij})\sin^2\left(1.27\frac{\Delta m_{ij}^2\,[\mathrm{eV}^2]\;L\;[\mathrm{km}]}{E\;[\mathrm{GeV}]}\right)\right| \tag{1.7}$$

Here, the mixing angles θ_{ij} $(i, j = 1, 2, 3)$ are related to the PMNS matrix elements by

$$\sin^2(\theta_{12}) = \frac{|U_{e2}|^2}{1-|U_{e3}|^2}, \quad \sin^2(\theta_{13}) = |U_{e3}|^2, \quad \sin^2(\theta_{23}) = \frac{|U_{\mu 3}|^2}{1-|U_{e3}|^2}.$$

and Δm_{ij}^2. $\sin^2(2\theta)$ sets the oscillation amplitude and Δm_{ij}^2 controls the oscillation wavelength or frequency of oscillation. Oscillation length [6] in vacuum, which is the distance of maximum oscillation, follows

$$L_{\mathrm{osc}} = \frac{4\pi E}{\Delta m^2} \approx 2.48\,\frac{E\,[\mathrm{MeV}]}{\Delta m^2\,[\mathrm{eV}^2]}\ \mathrm{m}. \tag{1.8}$$

Neutrino oscillation phenomena can be categorized into three regimes depending on the relation between the baseline L, neutrino energy E, and the mass-squared difference Δm^2, as illustrated in Figure 1.2:

- **High-energy limit** $(4E \gg \Delta m^2 L)$: Oscillatory terms are suppressed and no oscillation effects are observed.
- **Resonant regime** $(4E \sim \Delta m^2 L)$: Oscillations are observable with frequency determined by Δm^2 and amplitude governed by the mixing angle $\sin^2(2\theta)$.
- **Low-energy or long-baseline limit** $(4E \ll \Delta m^2 L)$: Oscillations become too rapid to resolve, leading to averaged fluxes. The observed transition probability is then approximated by

$$\left|\delta_{\alpha\beta} - \frac{1}{2}\sin^2(2\theta)\right|.$$

The amplitude depends on the absolute values of the mixing matrix elements $|U_{\alpha i}|^2$. Moreover, the oscillation term $\sin^2(\frac{\Delta m^2 L}{4E})$ remains unchanged under $\Delta m^2 \to -\Delta m^2$. Hence, in the two-flavor approximation, assuming no matter effects, the oscillation probability does not reveal whether Δm^2 is positive or negative, and thus is insensitive to the mass ordering.

Matter effects can modify the neutrino oscillation probability in Equation 1.7 via Mikheyev Smirnov Wolfenstein (MSW) effect [198]. Coherent forward scattering of neutrinos on electrons leads to an effective potential that changes the Hamiltonian in flavor space. In the Sun, for example, electron neutrinos experience both charged-current and neutral-current interactions, while muon and tau neutrinos interact only via neutral currents. This “MSW effect” can enhance or suppress flavor conversion, depending on the neutrino energy and the electron density profile. Observations of solar neutrinos confirm that the effective mass-squared difference in matter differs from that in vacuum, establishing that $m_2^2 > m_1^2$. New experiments like Deep Underground Neutrino Experiment (DUNE) [81], are being prepared to employ the MSW effect to determine the sign of the other mass-squared splitting.

---

[2] The quantity $\delta_{\alpha\beta}$ is the Kronecker delta, defined by the orthogonality condition of the flavor eigenstates $\langle\nu_\alpha|\nu_\beta\rangle = \delta_{\alpha\beta}$, which equals 1 when $\alpha = \beta$ and 0 otherwise.

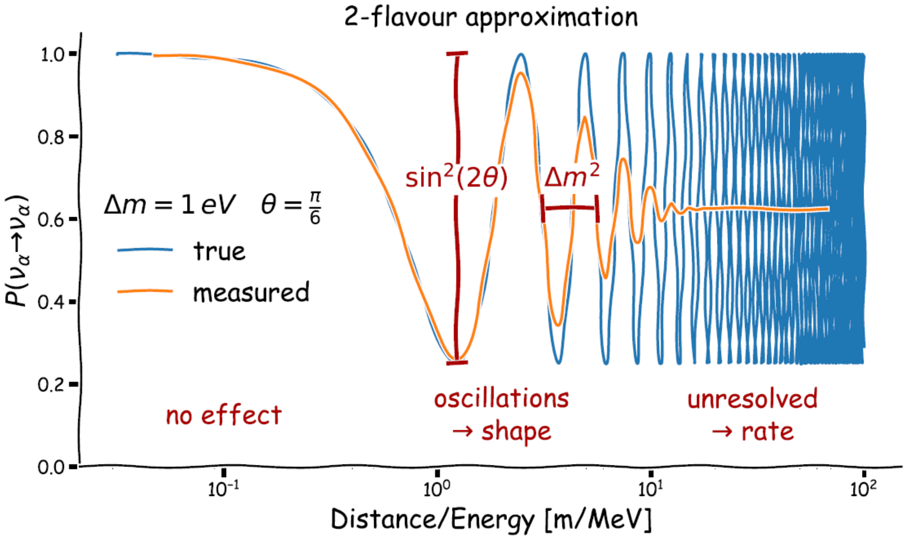

Figure 1.2: Illustration of two-flavor neutrino oscillation survival probability $P(\nu_\alpha \to \nu_\alpha)$ as a function of L/E. The oscillation amplitude is set by $\sin^2(2\theta)$, the periodicity by Δm^2, and at large L/E the rapid oscillations average out and cannot be resolved. Image source [50].

1.4 Neutrino Mass Generation Mechanism

In the Standard Model (SM), all particle masses arise from interactions with the Higgs field [119, 1]. Neutrinos are introduced as massless, left-handed fermions. Observations of neutrino oscillations, however, imply nonzero neutrino masses and mixing between flavor eigenstates ν_α $(\alpha = e, \mu, \tau)$. To explain neutrino mass, the model must be extended in one of two ways.

One possibility is to introduce explicit right-handed neutrino fields and generate Dirac mass terms via the Higgs mechanism preserving lepton number [119]. An alternative is to allow lepton number violation, enabling neutrinos to acquire Majorana masses. In this case, neutrinos are Majorana particles and the right-handed components are related to the charge-conjugates of left-handed fields. The details on phenomenology of massive neutrino can be found in [47, 105, 256].

Once the extended model is in place, a mass term can be written in the Lagrangian, as in [256]. Whether Dirac or Majorana, left(L)- and right(R)-handed flavor neutrino fields couple to the Higgs field. As a result, one obtains a complex, symmetric mass matrix M,

$$U^T M U \;=\; \mathrm{diag}\,(m_1,\, m_2,\, m_3)$$

when mass terms are expressed in the flavor eigenstates $\{\nu_e, \nu_\mu, \nu_\tau\}$. Diagonalizing the matrix M in Equation 1.9 via a unitary transformation yeilds the mass eigenbasis form shown in Equation 1.10, with eigenstates $\{\nu_1, \nu_2, \nu_3\}$ corresponding to respective masses m_1, m_2, and m_3. These mass eigenstates also describe the propagation of the neutrinos in vacuum as given by Equation 1.3. After diagonalization, the Lagrangian's mass term can be expressed using the neutrino masses and their mass eigenstates, see Equation 1.10.

$$\mathcal{L}_{\mathrm{mass}} \sim \begin{pmatrix} \nu_e & \nu_\mu & \nu_\tau \end{pmatrix}_R M \begin{pmatrix} \nu_e \\ \nu_\mu \\ \nu_\tau \end{pmatrix}_L + \text{h.c.} \tag{1.9}$$

$$\mathcal{L}_{\text{mass}} \sim \begin{pmatrix} \nu_1 & \nu_2 & \nu_3 \end{pmatrix}_R \begin{pmatrix} m_1 & 0 & 0 \\ 0 & m_2 & 0 \\ 0 & 0 & m_3 \end{pmatrix} \begin{pmatrix} \nu_1 \\ \nu_2 \\ \nu_3 \end{pmatrix}_L + \text{h.c.} \tag{1.10}$$

By introducing right-handed neutrino fields, which are singlets under the $\mathrm{SU}(2)_L \times \mathrm{U}(1)_Y$ gauge group, the Standard Model Lagrangian can include Majorana mass terms of the form

$$\mathcal{L}_M \; = \; -\tfrac{1}{2}\, M_{ss'}\, \nu_{sR}^T\, C\, \nu_{s'R} \; + \; \text{h.c.},$$

where $M_{ss'}$ is a symmetric mass matrix in the sterile-flavor indices s, s', and C is the charge-conjugation matrix satisfying $C\gamma_\mu C^{-1} = -\gamma_\mu^T$.

The corresponding mass terms cannot be generated by standard Higgs mechanism. These right-handed neutrino fields or so-called sterile neutrinos could be a potential explanation for the small neutrino masses compared to other lepton masses in the SM.

1.5 Sterile Neutrinos

Sterile neutrinos (ν_s) are hypothetical right-handed gauge singlets that, unlike the three active flavors ν_e, ν_μ, ν_τ, do not participate in weak interactions. Although sterile neutrinos do not couple directly to SM forces, they can still mix with active neutrinos through mass terms in the Lagrangian. This mixing provides a natural mechanism for generating non-zero neutrino masses. Several theoretical frameworks aim to explain why neutrino masses are so small [199]. These include

- The Type-I seesaw mechanism, which introduces heavy sterile neutrinos (often predicted by Grand Unified Theories (GUTs)).
- The Type-II seesaw mechanism, which add a Higgs triplet to the SM and
- A more general description via effective dimension-five operators, which parametrize neutrino mass without specifying high energy details of the model.

There is no known limit on the number of right-handed neutrino fields, so instead of three fields $\nu_{\alpha R}$ with $\alpha = e, \mu, \tau$, a general theory considers N_s right-handed fields ν_{sR} with $s = 1, \ldots, N_s$, as in the "Extended Standard Model." In the simplest ("Type-I") seesaw with one active (ν_a) and one sterile field (ν_s), the neutrino mass terms after electroweak symmetry breaking are

$$\mathcal{L}_{\text{mass}} = -\tfrac{1}{2} \begin{pmatrix} \overline{\nu_a^c} & \overline{\nu_s^c} \end{pmatrix} \begin{pmatrix} 0 & m_D \\ m_D & m_M \end{pmatrix} \begin{pmatrix} \nu_a \\ \nu_s \end{pmatrix} + \text{h.c.},$$

where m_D is the Dirac mass and m_M the Majorana mass of the sterile state. Calculating the eigenvalues of M and using their absolute values a light ν_{light} and ν_{heavy} mass eigen states are found with respective masses

$$m_{\text{light}} \; \approx \; \frac{m_D^2}{m_M}, \qquad m_{\text{heavy}} \; \approx \; m_M,$$

and mixing angle $\theta \sim m_D/m_M$. For $m_D \ll m_M$, the mostly-active state acquires a small mass $m_{\text{light}} \sim 200$ GeV, while the mostly sterile state is heavy $m_{\text{heavy}} \sim 10^{15}$ GeV and feebly coupled [106]. In this scenario, the right-handed neutrinos are sterile and decoupled from low-energy physics, with their mixing to light neutrinos strongly suppressed, making them theoretically important but phenomenologically inactive. However, if multiple right-handed neutrino fields exist, some may be light and appear in low-energy physics beyond the Standard Model, potentially connected to Dark Matter; such neutrinos can have masses ranging from the TeV scale down to the sub-eV scale. Additionally, the introduction of sterile neutrinos is allowed because they have little or no effect on the effective number of active neutrinos contributing to the Z-boson decay, which has been precisely measured by LEP experiments to be close to three [20].

The thesis at hand focuses on sterile neutrinos at the eV scale that can produce observable effects in short-baseline neutrino oscillation experiments. The next subsections reviews signatures for the existence of eV-mass sterile neutrino and experimental anomalies that motivated such light states. Shortly, the interpretation of these anomalies is also discussed.

1.5.1 Impact of Sterile Neutrinos

Throughout this thesis, the so-called $(3+1)$ neutrino scheme is considered. This is the simplest extension of the standard three-neutrino (3ν) mixing framework, achieved by introducing a non-standard massive neutrino at the eV scale. This has consequences not only for neutrino oscillations but also for cosmology and direct neutrino mass experiments.

- *Neutrino oscillation searches*: To accommodate this additional sterile state, the unitary PMNS mixing matrix must be extended to a 4×4 form. In this framework, the flavor eigenstates $(\nu_e, \nu_\mu, \nu_\tau, \nu_s)^T$ are expressed as linear combinations of the mass eigenstates $(\nu_1, \nu_2, \nu_3, \nu_4)^T$, via the extended mixing matrix $U_{\alpha i}$:

  $$\begin{pmatrix} \nu_e \\ \nu_\mu \\ \nu_\tau \\ \nu_s \end{pmatrix} = \begin{pmatrix} U_{e1} & U_{e2} & U_{e3} & U_{e4} \\ U_{\mu 1} & U_{\mu 2} & U_{\mu 3} & U_{\mu 4} \\ U_{\tau 1} & U_{\tau 2} & U_{\tau 3} & U_{\tau 4} \\ U_{s1} & U_{s2} & U_{s3} & U_{s4} \end{pmatrix} \begin{pmatrix} \nu_1 \\ \nu_2 \\ \nu_3 \\ \nu_4 \end{pmatrix}. \tag{1.11}$$

  The additional state ν_s corresponds to a sterile neutrino, which does not participate in the weak interaction. If ν_4 were perfectly aligned with ν_s, corresponding to $U_{s4} = 1$ and $U_{\alpha 4} = U_{si} = 0$ for $\alpha = e, \mu, \tau$ and$i = 1, 2, 3$, it would not influence neutrino oscillations but only gravitational effects. However, like for the active states, if this alignment is imperfect, the active flavor states acquire a small admixture of ν_4, thereby altering their oscillation behavior.

  Experimental neutrino oscillation data permit such a scenario provided that the active-sterile mixing satisfies $|U_{\alpha 4}|^2 \ll 1$ for all active flavors. Moreover, the fourth mass state ν_4 is hypothesized to reside at the eV scale, $m_4 \gg m_3, m_2, m_1$, such that the associated mass-squared splittings $\Delta m^2_{4i} \sim 1$ eV^2 dominate over both the solar and atmospheric splittings (see Equations (1.12) and (1.13)). Accordingly, in experimental configurations where the relation $4E \sim \Delta m^2_{4i} L$ holds, oscillations driven by sterile neutrinos become observable, while the solar and atmospheric mass splitting terms are not effective. In the three-flavor framework, two independent mass-squared differences exist: the solar splitting

  $$\Delta m^2_{\mathrm{SOL}} = \Delta m^2_{21} \simeq 7.53\,(\pm 0.18) \times 10^{-5}\,\mathrm{eV}^2, \tag{1.12}$$

  and the atmospheric splitting

  $$\Delta m^2_{\mathrm{ATM}} = |\Delta m^2_{31}| \simeq 2.45\,(\pm 0.33) \times 10^{-3}\,\mathrm{eV}^2, \tag{1.13}$$

with $\Delta m^2_{\mathrm{ATM}} \simeq 34\,\Delta m^2_{21}$ [113, 198]. By convention, $\Delta m^2_{\mathrm{SOL}} \equiv \Delta m^2_{21}$ with $m_2 > m_1$, while the ordering of ν_3 can be normal or inverted. Short-baseline [3] anomalies imply the existence of at least one additional mass-squared splitting beyond these two.

The choice of $\Delta m^2_{41} \sim 1$ eV^2 is motivated empirically by anomalies reported in short-baseline reactor, gallium, and accelerator experiments, which display oscillation patterns consistent with the existence of an additional sterile neutrino at this mass scale.

At distances L and energies E where active neutrino oscillations are negligible but flavor transitions involving the sterile neutrino occur, a two-flavor approximation Equation 1.7 effectively describes the oscillation probability [46]:

$$P(\nu_\alpha \to \nu_\beta) = \left|\delta_{\alpha\beta} - \sin^2(2\theta_{\alpha\beta})\sin^2\left(\frac{\Delta m^2_s L}{4E}\right)\right|,$$

where $\Delta m^2_s \sim 1\,\mathrm{eV}^2$, and

$$\sin^2(2\theta_{\alpha\beta}) = 4|U_{\alpha 4}|^2\left|\delta_{\alpha\beta} - |U_{\beta 4}|^2\right|.$$

Since only the absolute values of the mixing-matrix elements appear, this oscillation pattern does not distinguish between neutrinos and antineutrinos. The dependence on L/E allows experimental investigation using various neutrino sources, including radioactive isotopes, reactors, accelerator beams, and atmospheric neutrinos. Sterile-neutrino oscillations, driven by a large mass–squared difference $\Delta m^2_{41} \gg \Delta m^2_{21}, \Delta m^2_{31}$, exhibit much shorter wavelengths than oscillations among active flavors. The oscillation length in Equation 1.8 gives the neutrino oscillation period:

$$\left(\frac{L}{E}\right)_{\mathrm{osc}} \propto \frac{1}{\Delta m^2}\,.$$

Thus, sterile-neutrino searches are conducted at short baselines, typically tens of meters for reactor neutrinos and hundreds of meters for accelerator neutrinos, where the active–to–sterile oscillation is well approximated by a two-flavor framework.

Active-to-sterile neutrino disappearance in the same-flavor channels $\nu_e \to \nu_e$ and $\nu_\mu \to \nu_\mu$ is described by mixing angles, where the oscillation amplitudes are given by

$$\sin^2(2\theta_{\alpha\alpha}) = 4|U_{\alpha 4}|^2\left(1 - |U_{\alpha 4}|^2\right), \quad \alpha = e, \mu. \tag{1.14}$$

Active-to-active Neutrino appearance channels, such as $\nu_\mu \leftrightarrow \nu_e$, arises from the mixing involving the fourth mass eigenstate, with the transition amplitude given by

$$\sin^2(2\theta_{e\mu}) = 4|U_{e4}|^2|U_{\mu 4}|^2 = \sin^2(2\theta_{14})\sin^2(\theta_{24}),$$

where the resonance condition $4E \sim \Delta m^2_s L$ suppresses standard three-flavor oscillations at eV-scale sterile neutrino energies. Further, given a light sterile neutrino, the PMNS 3×3 sub-matrix would not be unitary. Hence, tests of the unitarity of the PMNS matrix can be performed in the search for sterile neutrinos [122, 200].

- *$0\nu\beta\beta$ searches*: The presence of light sterile neutrinos modifies the effective Majorana mass $|m_{\beta\beta}|$ that governs neutrinoless double-beta-decay ($0\nu\beta\beta$). In the $(3+1)$ neutrino mixing framework, the effective mass is expressed as the coherent sum over four mass eigenstates:

---

[3] Long-baseline neutrino oscillation experiments have source–detector distances and neutrino energies tuned to probe oscillations driven by the atmospheric splitting $\Delta m^2_{\mathrm{ATM}}$ in Equation 1.13. Experiments sensitive to larger mass-squared differences (Δm^2) are referred to as “short-baseline”.

$$|m_{\beta\beta}| = \left|\mu_1 + \mu_2 e^{i\alpha_2} + \mu_3 e^{i\alpha_3} + \mu_4 e^{i\alpha_4}\right|,$$

where $\mu_k = |U_{ek}|^2 m_k$, with m_k representing the mass of the k-th neutrino eigenstate, U_{ek} the corresponding 4×4 mixing matrix elements, and α_k the Majorana phases. Given that the sterile neutrino mass m_4 is generally much larger than the active neutrino masses m_1, m_2, m_3, the possible range of $|m_{\beta\beta}|$ is significantly broadened [103]. This affects the predicted decay rates and allows for both enhancement and cancellation of the effective mass depending on the relative phases, thus impacting the interpretation of experimental results and constraints on sterile neutrinos. To date, there is no confirmed experimental evidence for Majorana neutrinos, but investigations in this field remain active and ongoing. From the current best lower bounds on the $0\nu\beta\beta$-decay half-lives of ^{136}Xe [132], ^{76}Ge [101] and ^{130}Te [64], limits on neutrino masses can be derived, assuming neutrinos are Majorana particles. These limits translate into experimental upper bounds on the effective Majorana mass, defined as

$$m_{\beta\beta} = \left|\sum_i U_{ei}^2 m_i\right|.$$

These limits range from 0.079 - 0.180 eV (90% CL) from GERDA [101], 0.070 - 0.240 eV (90% CL) from CUORE [64], and 0.036 - 0.156 eV (90% CL) from KamLAND-ZEN [132] and depend on large uncertainties from nuclear matrix elements. The nature of neutrino (Dirac or Majorana) is still unknown and explored by $0\nu\beta\beta$ experiments (see recent review from [9])

- *Cosmology*: Sterile neutrinos can contribute additional relativistic degrees of freedom in the early Universe, thereby increasing the effective number of neutrino species N_{eff}. This increase accelerates the expansion rate during the radiation-dominated era, notably affecting Big Bang Nucleosynthesis (BBN) by altering the primordial abundances of light elements such as helium and deuterium. Furthermore, depending on their mass and thermal history, sterile neutrinos can behave as either radiation (if relativistic) or matter (if non-relativistic) in cosmological epochs, influencing the Cosmic Microwave Background (CMB) anisotropies and the formation of Large Scale Structure (LSS). Their mass and phase-space distribution affect the matter power spectrum by suppressing small-scale structure growth through free-streaming effects. This contribution is determined by the sum of neutrino masses, $\sum_i m_i$, individual mass-splittings and momenta of the neutrino species. Cosmological observations thus place stringent constraints on sterile neutrino properties, including their effective mass and thermalization degree. A joint analysis combining BBN) and Cosmic CMB data provides a recent measurement of the effective number of neutrino species as $N_\nu = 2.898 \pm 0.141$ [254].

- *Kinematic β-decay searches*: Direct neutrino mass experiments provide a model-independent approach by probing distortions near the kinematic β-decay endpoint, where the presence of a heavier sterile neutrino induces a distinct kink-like spectral feature. Since this thesis focuses on sterile neutrino searches via β-decay kinematics, the detailed signature of sterile neutrino in β-decay is provided in Section 1.6.

Even though the solar neutrino problem was resolved by the discovery of neutrino oscillations, several short-baseline neutrino experiments have reported persistent anomalies characterized by either an excess or a deficit of detected events compared to theoretical predictions [29]. While the three-flavor neutrino oscillation paradigm has successfully explained data from solar, atmospheric, reactor, and accelerator experiments, these anomalous findings, with significances at the $2-4\,\sigma$ level, challenge the completeness of the standard 3ν framework [6]. These anomalies can be broadly categorized based on oscillation probabilities into two types: appearance anomalies, where unexpected neutrino flavors appear, and disappearance anomalies, where the flux of a given neutrino flavor is lower than expected. The following subsections discuss these anomalies in detail and their implications for sterile neutrino searches.

1.5.2 Experimental anomalies for eV-Scale Sterile Neutrinos

Anomalies occur when measurements conflict with theoretical predictions, leading to careful re-evaluation of experimental methods and models and, if both prove reliable, indicating the presence of new physics. In the (3+1) framework, a sterile neutrino ν_4 with $m_4 \gtrsim 1$ eV and $\Delta m^2_{\mathrm{SBL}} = m_4^2 - m_1^2 \gtrsim 1\,\mathrm{eV}^2$ is introduced. This scheme can accommodate the LSND anomaly, the MiniBooNE low-energy excess, the Gallium and Reactor Antineutrino anomalies, despite with persistent tensions [77, 6].

Appearance Searches

- **LSND and the observation of Anomalous $\bar{\nu}_\mu \to \bar{\nu}_e$ Appearance:** The Liquid Scintillator Neutrino Detector (LSND) experiment [33], conducted at the Los Alamos Meson Physics Facility (LAMPF), was designed to investigate short-baseline $\bar{\nu}_\mu \to \bar{\nu}_e$ oscillations. Utilizing an 800 MeV proton beam incident on a beam-stop target, the experiment produced a neutrino flux predominantly from pion decay-at-rest (DAR) processes. The decay chain $\pi^+ \to \mu^+ + \nu_\mu$, followed by $\mu^+ \to e^+ + \nu_e + \bar{\nu}_\mu$, yielded a well-characterized $\bar{\nu}_\mu$ flux with minimal intrinsic $\bar{\nu}_e$ contamination, estimated at $\sim 7.8 \times 10^{-4}$ of the $\bar{\nu}_\mu$ flux. The LSND detector comprised a cylindrical tank containing 167 tons of mineral oil doped with scintillator, instrumented with 1220 8-inch photomultiplier tubes (PMTs). Located 29.8 m from the neutrino source, the detector was capable of detecting both Cherenkov and scintillation light, facilitating particle identification. The primary detection channel for $\bar{\nu}_e$ appearance was inverse β-decay (IBD): $\bar{\nu}_e + p \to e^+ + n$, characterized by a prompt positron signal followed by a delayed 2.2 MeV gamma ray from neutron capture on a proton. Throughout multiple data-taking campaigns from 1993 to 1998, LSND consistently reported a statistically significant excess of $\bar{\nu}_e$-like events above the predicted backgrounds [168]. The final analysis reported 87.9 ± 22.4 (stat.) $\pm\, 6.0$ (sys.) excess events, corresponding to an oscillation probability of $(0.264 \pm 0.067 \pm 0.045)\%$ for $\bar{\nu}_\mu \to \bar{\nu}_e$ transitions. A two-neutrino oscillation analysis favored a mass-squared difference of $\Delta m^2 \approx 1.2$ eV^2 and a mixing amplitude of $\sin^2 2\theta \approx 0.003$ [168, 6], significantly higher than the solar and atmospheric neutrino oscillation scales, suggesting the existence of at least one additional, sterile neutrino state near the eV mass scale.

  Operating under the same stopped-π^+ DAR principle but with reduced statistics, the KARMEN (KArlsruhe Rutherford Medium Energy Neutrino) experiment [134] did not observe any excess of $\bar{\nu}_e$ events. Located only 17 m from its source (versus 29.8 m for LSND), KARMEN recorded 15 $\bar{\nu}_e$ candidates in agreement with an expected background of 15.8 ± 0.5, and thus set 90% C.L. limits of

  $$\sin^2(2\theta) < 8.5 \times 10^{-3} \quad (\Delta m^2 > 1\ \mathrm{eV}^2), \quad \sin^2(2\theta) < 4.0 \times 10^{-2} \quad (\Delta m^2 \approx 0.2\ \mathrm{eV}^2),$$

  excluding much of the LSND-favored region [134]. However, a combined fit of LSND's 3.8σ excess ($87.9 \pm 22.4 \pm 6.0$ events) and KARMEN's null result still retains "islands" of allowed oscillation parameters around $\Delta m^2 \approx 0.5$–1 eV^2 with $\sin^2(2\theta) \sim 10^{-3}$ [191]. These surviving regions underline the necessity of further short-baseline experiments [5], such as MiniBooNE, MicroBooNE, SBND, and ICARUS, to definitively confirm or refute the eV-scale sterile-neutrino hypothesis.

- **MiniBooNE Low-Energy Excess:** The MiniBooNE experiment, conducted at Fermilab, was designed to test the LSND result at higher energy ($\sim 800\,\mathrm{MeV}$) and longer baseline ($541\,\mathrm{m}$), while preserving a similar $L/E \sim 1\,\mathrm{m/MeV}$ ratio [10]. The MiniBooNE experiment employed a 12.2 m diameter mineral-oil Cherenkov detector located 541 m downstream of the Fermilab Booster Neutrino Beam to test the LSND $\bar{\nu}_\mu \to \bar{\nu}_e$ signal at $\Delta m^2 \sim 1\,\mathrm{eV}^2$ [10, 190]. In its 2009 neutrino-mode data set (6.46×10^{20} POT), MiniBooNE reported an excess of 544 observed electron-like events versus 415.2 ± 43.4 expected in the 200–475 MeV reconstructed energy window, corresponding to a 3.0σ anomaly above background expectations [189]. This low-energy excess (LEE) persisted and when combined with antineutrino data reached a global significance of 4.8σ by 2021 [192]. Interpretations within a minimal 3+1 sterile-neutrino model, $P(\nu_\mu \to \nu_e) = \sin^2 2\theta_{\mu e}\,\sin^2(1.27\,\Delta m^2_{41} L/E)$, could fit the LEE for $\Delta m^2_{41} \sim 1\,\mathrm{eV}^2$ and $\sin^2 2\theta_{\mu e} \sim 10^{-3}$, unifying LSND and MiniBooNE signals [189, 107].

  Dedicated studies of photon-production backgrounds (e.g. NC $\Delta \to N\gamma$, π^0 misidentification) have shown these Standard Model sources are too small by factors of 2–4 to explain the full LEE [249]. Alternative beyond-the-Standard-Model mechanisms—such as heavy neutral leptons with magnetic dipole interactions or dark-sector mediators decaying to e^+e^- pairs—can be tuned to reproduce the spectrum but often conflict with cosmological or laboratory constraints and remain under active theoretical investigation [184, 140] In analyses of 6.8×10^{20} POT, MicroBooNE found no significant excess of electron-like events in the 200–600 MeV range across multiple final states, including the 1e1p CCQE topology [242], the 0π CCQE-like sample [187], the inclusive ν_e CC selection [185], and in single-photon NC $\Delta \to N\gamma$ searches [186]. A combined 3+1 oscillation fit places a $> 95\%$ CL exclusion on most of the MiniBooNE-preferred $\Delta m^2_{41} \sim 0.1$–$10\,\mathrm{eV}^2$, $\sin^2 2\theta_{\mu e} \gtrsim 10^{-2}$ region [66]. These results collectively indicate that the simplest sterile-neutrino and photon-background hypotheses for the MiniBooNE anomaly are strongly disfavored. Global fits including disappearance data from reactor and accelerator experiments reveal significant tension with this simple sterile-neutrino hypothesis [75, 77]. They allow for tighter constraints on active–sterile oscillation parameters but have not yet provided a definitive conclusion on the existence of eV-scale sterile neutrinos [50]

Disappearance searches

- **The Gallium Anomaly (GA)** refers to a persistent deficit in electron neutrino flux observed during calibration runs of the GALLEX [114] and SAGE [2] solar neutrino experiments, which used intense radioactive sources (^{51}Cr and ^{37}Ar) to probe ν_e interactions via inverse β-decay on gallium. Both experiments consistently observed fewer neutrino interactions than expected, with the combined ratio of measured to predicted events being $\bar{R} = 0.84 \pm 0.05$, corresponding to a deficit at the level of approximately 2.9σ [84]. This was interpreted as possible evidence for oscillations involving a light sterile neutrino.

  To further investigate this, the SAGE setup was upgraded into the Baksan Experiment on Sterile Transitions (BEST) experiment in 2014, enabling very-short-baseline measurements ($\mathcal{O}(1\text{ m})$) with controlled source deployment. The latest results from BEST, published in 2022 [38], continue to support the anomaly, showing a 3σ preferred region corresponding to a mass-squared difference $\Delta m^2 \gtrsim 1\text{ eV}^2$. Although BEST conformed a significant 20–24% deficit in electron-neutrino capture, the anomaly still persists at approximately 4σ significance.

  Unlike the Reactor Antineutrino Anomaly, which involves $\bar{\nu}_e$ flux deficits at baselines of 10-100 meters and average energies around 4 MeV, the Gallium Anomaly arises from MeV-scale ν_e sources over meter-scale baselines.

- **The Reactor Antineutrino Anomaly (RAA)** [182] refers to a deficit of the measured antineutrino inverse β-decay rates at very short-baseline reactor experiments compared to the theoretically improved predictions (i.e. the Huber-Mueller model [123, 195]). These measurements show a deficit of about 6% in the integrated antineutrino flux, observed with a significance exceeding the 2σ level [182]. This discrepancy was attributed to possible oscillations involving sterile neutrinos. However, in 2021, revised reactor flux models incorporating updated fission spectra of ^{235}U and ^{239}Pu reduced the predicted antineutrino flux by about 5%, aligning better with observed data. As a result, the statistical significance of the RAA has decreased to around 1.1σ when compared against the updated flux predictions, weakening the anomaly's support for light sterile neutrinos [104]. In an recent article [255] it is discussed that RAA cannot be resolved by the sterile neutrino hypothesis due to large model uncertainties, spectral shape discrepancies, and isotopic effects so, it is recommended to exclude the RAA-allowed region from electron-neutrino disappearance analyses or to increase the Huber–Mueller model uncertainty to at least 5% when producing such limits.

  Recent results from the PROSPECT [26], STEREO [22], DANSS [171], DayaBay [24], Double Chooz [4], MINOS [193] and KARMEN [134] experiments have placed stringent limits on the existence of light sterile neutrinos by measuring reactor antineutrino fluxes and spectra with high precision. None of these experiments observed significant deviations consistent with sterile neutrino oscillations, effectively excluding much of the parameter space previously favored by the Reactor Antineutrino Anomaly (RAA). Consequently, these findings significantly weaken the sterile neutrino interpretation of the RAA, suggesting that the anomaly is nearly resolved. Although the GA and RAA have been interpreted as possible signatures of active-sterile neutrino oscillations, global fits reveal significant tension between the preferred regions of these anomalies and constraints from disappearance and spectral data [50, 106]. In particular, the 3+1 sterile neutrino framework struggles to simultaneously accommodate all datasets without invoking fine-tuned model assumptions or introducing additional sources of systematic uncertainty. These inconsistencies highlight the limitations of relying solely on oscillation-based interpretations and underscore the need for complementary, model-independent approaches. One such method involves direct kinematic searches in nuclear β-decay, which are sensitive to the absolute neutrino mass scale and potential admixtures of heavier mass states without dependence on baseline or neutrino flux modeling.

1.6 Single β-decay Searches for Sterile Neutrinos

Although sterile neutrinos do not interact via the weak force, their mixing with active flavors allows them to leave observable imprints in single β decay, where the electron antineutrino ($\bar{\nu}_e$) contains a small admixture of the fourth mass eigenstate. Hereafter, we denote the active neutrino mass as m_ν and the sterile neutrino mass as m_4. To establish a reference, we first review the standard β-decay spectrum governed by active neutrinos only, which serves as the basis for identifying sterile-induced distortions.

The neutrino mass can be inferred from precise measurements of the β-decay electron spectrum. High-precision single β-decay experiments provide a model-independent determination of the absolute neutrino mass scale by probing electron kinematics via the weak interaction, independent of assumptions about the neutrino's Majorana or Dirac nature. Nuclear β decay is a weak process in which a neutron transforms into a proton, emitting an electron and an electron antineutrino, as described by

$$n \to p + e^- + \bar{\nu}_e. \tag{1.15}$$

The total decay energy Q (about 18.6 keV) is given by the mass difference between the initial and final nuclei, corrected for the electron mass,

$$Q = m(A, Z) - m(A, Z+1) - m_e c^2, \tag{1.16}$$

where $m(A, Z)$ and $m(A, Z+1)$ are the masses of the parent and daughter nuclei, respectively. The energy available to the leptons, termed the endpoint energy E_0, is

$$E_0 = Q - E_{\text{rec}}, \tag{1.17}$$

where E_{rec} is the recoil energy of the daughter nucleus.

Energy conservation dictates the relation

$$E_0 = E + E_\nu, \tag{1.18}$$

where E is the kinetic energy of the emitted electron and E_ν is the total energy of the antineutrino. Even if the neutrino is produced at rest, the electron energy endpoint is reduced by the neutrino rest mass.

The electron-flavor antineutrino is not a state of definite mass, but a superposition of mass eigenstates $|\nu_i\rangle$ with masses m_i, weighted by the elements of the PMNS matrix U_{ei}:

$$|\bar{\nu}_e\rangle = \sum_{i=1}^{3} U_{ei} |\nu_i\rangle. \tag{1.19}$$

Assuming CPT symmetry, neutrinos and antineutrinos are assigned identical masses. Due to the small mass splittings and current experimental resolution limits of neutron β-decay, β-decay experiments are sensitive to an effective electron neutrino mass squared defined as

$$m_\nu^2 = \sum_{i=1}^{3} |U_{ei}|^2 m_i^2. \tag{1.20}$$

This effective mass parameter enters the kinematic description of β-decay and influences the spectral shape of the emitted electron near the endpoint. While the general theory applies to both free and nuclear β-decay, practical sensitivity to the neutrino mass requires a source with favorable nuclear properties. Tritium, with its low endpoint energy of approximately 18.6 keV, short half-life, and superallowed transition, offers an excellent combination of statistical and systematic advantages. It is therefore a prime candidate for direct neutrino mass measurements, as exploited by the KATRIN experiment.

According to Fermi theory, the differential decay rate of the beta electron as a function of kinetic energy E near the endpoint is given by [87]:

$$\begin{aligned} \frac{d\Gamma}{dE}(E, m_\nu^2) = \frac{G_F^2 \cos^2\theta_c}{2\pi^3} |M_{\text{nucl.}}|^2 \cdot F(Z, E) \cdot (E + m_e)\sqrt{(E + m_e)^2 - m_e^2} \\ \cdot (E_0 - E)\sqrt{(E_0 - E)^2 - m_\nu^2} \cdot \Theta(E_0 - E - m_\nu) \end{aligned} \tag{1.21}$$

where

- Γ is the decay probability
- G_F is the Fermi coupling constant with $G_F = 1.166\,378\,8(6) \times 10^{-5}\,\text{GeV}^{-2}(\hbar c)^3$ [113].
- θ_c is the Cabibbo angle with $\cos\theta_c = 0.97373$ [113].

- $|M_{\mathrm{nuc}}|$ is the nuclear part of the transition matrix. For superallowed tritium β-decay, it is independent of the electron energy.
- $F(Z, E)$ is the Fermi function accounting for the Coulomb interaction between the outgoing electron with kinetic energy E and the daughter nucleus of atomic number Z.
- m_{e} is the electron mass
- Θ is the Heaviside step function enforcing energy conservation.
- m_ν is the neutrino mass

The observable m_ν^2 predominantly affects the endpoint region of the β-decay spectrum, where electron kinetic energy approaches E_0 and decay probability is minimal, thus requiring a high-activity source and high energy resolution near E_0 for neutrino mass measurement.

The presence of a sterile neutrino ν_4 with mass m_4 significantly larger than the active neutrino masses modifies this spectral shape. Within the 3ν+1 framework, if the electron flavor neutrino contains a small admixture of this non-zero fourth mass eigenstate (m_4), characterized by a mixing matrix element $|U_{e4}|^2$, the β-decay spectrum in Equation 1.21 is extended by an additional decay branch called sterile branch. The differential β-electron energy spectrum is a superposition of active branch and sterile branch :

$$\frac{d\Gamma}{dE}(E,\, m_\nu^2,\, m_4^2,\, |U_{e4}|^2) = \underbrace{(1 - |U_{e4}|^2)\, \frac{d\Gamma}{dE}(E,\, m_\nu^2)}_{\text{Active branch}} + \underbrace{|U_{e4}|^2\, \frac{d\Gamma}{dE}(E,\, m_4^2)}_{\text{Sterile branch}} \tag{1.22}$$

Accordingly Equation 1.20 can be redefined as

$$m_\nu^2 = \sum_{i=1}^{3} |U_{ei}|^2 m_i^2 \xrightarrow{3+1} \sum_{i=1}^{3} \frac{|U_{ei}|^2}{1 - |U_{e4}|^2} m_i^2 \tag{1.23}$$

As illustrated in Figure 1.3a, the sterile neutrino contribution manifests as a kink-like distortion in the β-spectrum at energies below the endpoint by $E \leq E_0 - m_4$, due to the large mass splitting and energy conservation. The kink's position corresponds to the sterile neutrino mass m_4, while its amplitude depends on the mixing parameter $|U_{e4}|^2$. The distinct discontinuity in the spectral slope is the characteristic experimental signature of a sterile neutrino in single β-decay searches. The observable $m^2(\nu_e)$ primarily affects the β-decay spectrum near the endpoint E_0, where electron kinetic energies are highest but decay probabilities are minimal (see Equation 1.21 and Equation 1.22). Consequently, precise neutrino mass measurements, currently conducted by KATRIN, require both a high-activity source and excellent energy resolution around E_0. Since KATRIN's primary goal is to measure the active neutrino mass as defined in Equation 1.22, its sensitivity also extends to potential sterile neutrino signatures in the corresponding energy range. KATRIN measures the molecular tritium β-decay spectrum in an integrated mode, where the number of electrons with kinetic energy above a variable retarding potential is recorded. The effect of a sterile neutrino admixture on the integrated β-decay spectrum is illustrated in Figure 1.3b. The spectral distortion from a sterile neutrino is clearly visible in the differential spectrum (see Figure 1.3a) but appears significantly smeared in the integrated spectrum due to the cumulative nature of the measurement. The details of the measurement procedure and the experimental apparatus enabling this high-precision technique are discussed in Chapter 2.

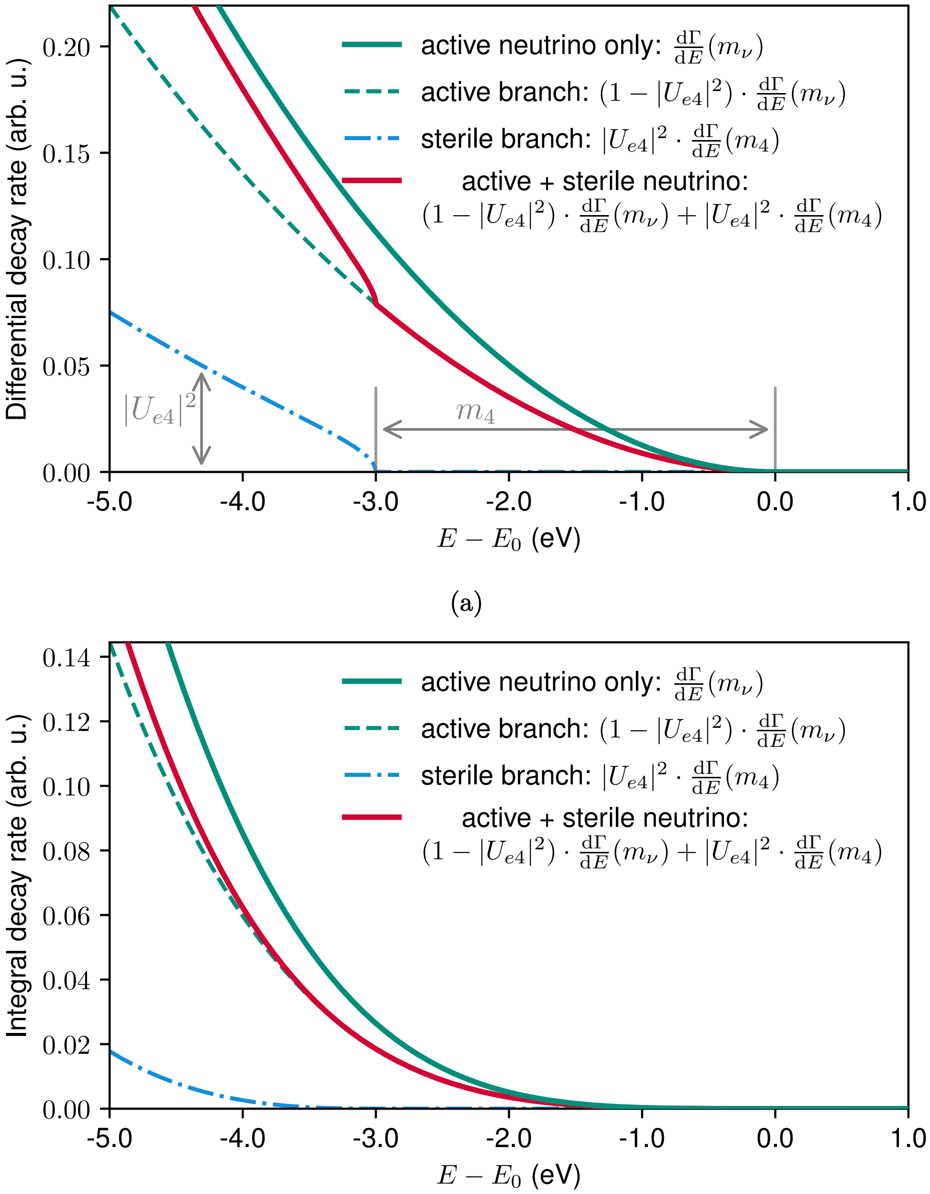

(a)

(b)

Figure 1.3: Differential and Integral spectra of electrons from β-decay of molecular Tritium including contributions from active and sterile neutrino. The sterile neutrino produces a kink-like spectral distortion The sterile neutrino produces a kink-like spectral distortion below the endpoint energy of the spectrum, at an energy offset corresponding to its mass and an amplitude proportional to the mixing matrix element $|U_{e4}|^2$.

2

The KATRIN Experiment

The Karlsruhe Tritium Neutrino (KATRIN) experiment is designed to determine the effective electron antineutrino mass with sub-eV sensitivity through high-precision spectroscopy of the tritium β-decay spectrum near its kinematic endpoint. Following an initial tritium commissioning phase in 2018, KATRIN began routine data-taking in 2019. Within the first two measurement campaigns, the experiment reached sub-eV sensitivity on the neutrino mass [13]. With a planned total data collection period of 1000 days, KATRIN aims to achieve a sensitivity better than 0.3 eV at the 90% confidence level (CL) [135]. Prior to KATRIN, the Mainz and Troitsk experiments provided upper limits for the electron neutrino mass around 2 eV [153, 31]. KATRIN was developed to surpass these limits through several significant advancements [136, 135]:

- **Enhanced Sensitivity:** KATRIN targets a sensitivity below 0.3 eV/c^2 (90% C.L.) for $m(\nu_\mathrm{e})$, improving upon the Mainz [153] and Troitsk [31] upper limits of 2.3 eV/c^2 and 2.1 eV/c^2, respectively, and covering the full range of degenerate neutrino masses.
- **Improved energy resolution:** The experiment employs a large, high-resolution electrostatic spectrometer based on the principle of magnetic adiabatic collimation with electrostatic filtering (MAC-E filter). Based on the design values, the spectrometer can achieve an energy resolution of 0.93 eV at endpoint energy of 18.6 keV [67], far superior to that of Troitsk and Mainz.
- **High-Purity Tritium Source:** KATRIN utilizes a windowless gaseous molecular tritium source (WGTS) with high stability in injection pressure and temperature, ensuring a consistent and well-characterized β-decay environment.

Enhancing and exceeding the precision of its predecessors, KATRIN currently provides the most accurate method for the direct and model-independent determination of the neutrino mass. Section 2.1 outlines the fundamental operating principle of the KATRIN experiment, while Section 2.2 provides an overview of the complete experimental setup. The individual components of the KATRIN beamline are subsequently described in detail in the corresponding subsections of Section 2.2. For a comprehensive account of the KATRIN experiment and its technical design, the reader is referred to [65, 67].

2.1 Measurement Principle of KATRIN

Building upon the legacy of the Mainz and Troitsk experiments, KATRIN extends its physics goals to probe the existence of sterile neutrinos in the eV mass range by performing high-precision spectral analysis of the tritium β-decay spectrum. The measurement principle relies on the precision determination of the kinetic energy of electrons from the β-decay of tritium:

$$\mathrm{T}_2 \rightarrow {}^3\mathrm{HeT}^+ + \mathrm{e}^- + \bar{\nu}_\mathrm{e} + Q(\mathrm{T}_2) \tag{2.1}$$

The available surplus energy $Q \approx 18.6\,\mathrm{keV}$ released in β-decay is shared between the kinetic energy of the emitted $\beta-$particle (electron), the total energy carried away by the antineutrino, the small recoil energy of the much heavier daughter nucleus, and, if applicable, the energy used to excite the daughter nucleus to a higher energy state. Any β-emitting isotope can, in principle, be used. However, Tritium is a suitable candidate for determining neutrino mass, due to follwoing reasons:

- **Short Half-Life**: Tritium has a half-life of approximately 12.3 years, resulting from its transition to helium-3 ($^3\mathrm{H} \rightarrow\ ^3\mathrm{He}$). This short half-life means only a small amount of radioactive material is required to achieve a high decay rate [169] .
- **Low Q Value**: With a Q value of about 18.6 keV, tritium's decay spectrum exhibits a low endpoint energy (E_0). This maximizes the impact of the neutrino mass on the observed events, allowing for more precise measurements [199].
- **Simple nuclear structure for β-spectrum calculations**: Tritium with an atomic number of $Z = 1$, undergoes a relatively simple decay process, with limited Coulomb interactions with the nucleus. The use of a gaseous tritium source (T_2) further simplifies the system, facilitating accurate calculations of the final state distribution, particularly for its decay product, $^3\mathrm{HeT}^+$ [224, 49].

Beta electrons emitted from the Windowless Gaseous Tritium Source (WGTS) are magnetically guided through the transport and pumping sections to the main MAC-E spectrometer, where only those with sufficient kinetic energy to overcome the electrostatic retarding potential are transmitted to the detector. By varying the retarding potential, the spectrometer measures the integrated β-spectrum near the endpoint. The impact of the neutrino mass on the electron's kinetic energy is maximal near this spectral endpoint, where the neutrino becomes non-relativistic, enabling precise neutrino mass determination. The electron spectrum is modified as:

$$\frac{\mathrm{d}N}{\mathrm{d}E} \propto \sum_i |U_{ei}|^2 \cdot F(Z,E) \cdot p \cdot (E + m_e) \cdot (E_0 - E) \cdot \sqrt{(E_0 - E)^2 - m_i^2} \tag{2.2}$$

where U_{ei} are the PMNS matrix elements, E_0 is the endpoint energy, and m_i are the mass eigenstates of the neutrino. Note that the neutrino mass terms enter Equation 2.2 as squared masses m_i^2. Consequently, kinematic methods for neutrino mass measurement aim to determine the effective squared neutrino mass m_ν^2. In the following subsections 2.1.1 and 2.1.2, the mechanisms of adiabaticity and electron transmission through the MAC-E filter are presented.

2.1.1 Magnetic Adiabatic Collimation with Electrostatic (MAC-E) filter

The MAC-E filter combines magnetic adiabatic collimation and an electrostatic energy filter to achieve high energy resolution, and is particularly suited for the KATRIN experiment. MAC-E filter principle further relies on magnetic flux conservation maintaining the flux tube geometry of the experiment. MAC-E filters are capable of achieving exceptional energy resolution in the eV range, even at keV electron energies, with ultra-high luminosity and large acceptance angle nearly 2π [164, 207].

2.1.1.1 Magnetic Adiabatic Collimation:

For an electron moving through a magnetic field, the resulting cyclotron motion is associated with a magnetic moment μ, given by:

$$\mu = \frac{p_\perp^2}{2m_\mathrm{e}B},$$

where $p_\perp$ is the component of the electron's momentum perpendicular to the magnetic field, m_e is the electron mass, and B is the magnetic field strength. The condition for adiabatic motion requires that the relative change in the magnetic field over the distance of one cyclotron orbit is much less than unity:

$$\frac{\nabla B}{B} \ll 1.$$

This ensures that the magnetic moment remains approximately conserved throughout the electron's motion [41].

In the KATRIN experiment, electrons are emitted from the β-decay of tritium in a molecular gaseous source, which is placed in a strong magnetic field of strength B_src. These electrons must travel approximately 23 meters [67, 65] to reach the analyzing plane. Such a long path length is required to ensure that the magnetic field strength decreases gradually to a minimum value $B_\mathrm{ana} \ll B_\mathrm{src}$ at the analyzing plane. Under the assumption of adiabatic motion, conservation of the magnetic moment implies:

$$\frac{p^2_{\perp,\mathrm{src}}}{B_\mathrm{src}} = \frac{p^2_{\perp,\mathrm{ana}}}{B_\mathrm{ana}}. \tag{2.3}$$

Let θ_src and θ_ana denote the pitch angles of the electron at the source and the analyzing plane, respectively. A pitch angle of 0° implies the electron is traveling parallel to the beamline. Assuming conservation of total momentum ($p_\mathrm{src} = p_\mathrm{ana}$) and applying Eq. (2.3), the pitch angles are related by:

$$\sin^2(\theta_\mathrm{ana}) = \frac{B_\mathrm{ana}}{B_\mathrm{src}} \sin^2(\theta_\mathrm{src}),$$

where the perpendicular momentum component is given by $p_\perp = p\sin(\theta)$.

Since $B_\mathrm{ana} \ll B_\mathrm{src}$, it follows that $\sin^2(\theta_\mathrm{ana}) \approx 0$, so $\theta_\mathrm{ana} \approx 0$. In other words, electrons emitted with various pitch angles at the source become effectively collimated by the time they reach the analyzing plane. This collimation process is illustrated in Figure 2.1.

2.1.1.2 Filter Width

At the analyzing plane, a retarding potential of approximately -18.6 kV, corresponding to the tritium endpoint energy, is applied. This potential effectively acts as an electrostatic high-pass energy filter for the collimated electrons. Perfect collimation of all electrons, irrespective of their initial pitch angles, would require $B_\mathrm{ana} = 0$ T. However, for practical, non-zero values of B_ana, the electrons retain a non-negligible perpendicular kinetic energy component, given by

$$E_{\perp,\mathrm{kin}} = E_\mathrm{kin} \cdot \frac{B_\mathrm{ana}}{B_\mathrm{src}} \sin^2(\theta_\mathrm{src}), \tag{2.4}$$

where E_kin is the initial kinetic energy of the electrons. The maximum value of $E_{\perp,\mathrm{kin}}$ at fixed kinetic energy occurs for $\theta_\mathrm{src} = 90°$ and defines the filter width of the filter, denoted as ΔE.

For electrons with kinetic energy $E_\mathrm{kin} = 18.6$ keV, the corresponding Lorentz factor is

$$\gamma = \frac{E_\mathrm{kin}}{m_\mathrm{e}\mathrm{c}^2} + 1 \approx 1.0365, \tag{2.5}$$

where $m_\mathrm{e}\mathrm{c}^2 = 511$ keV is the rest energy of the electron.

Due to the relativistic energy of the electrons, the energy-momentum relation is given by

$$p^2 = E_\mathrm{kin}(E_\mathrm{kin} + 2m_\mathrm{e}\mathrm{c}^2), \tag{2.6}$$

where p is the relativistic momentum and E_kin is the kinetic energy.

Incorporating relativistic corrections, the filter width of the filter becomes

$$\Delta E = \frac{B_{\text{ana}}}{B_{\text{src}}} \cdot E_{\text{kin}} \cdot \left(\frac{\gamma + 1}{2}\right). \tag{2.7}$$

The filter width ΔE directly determines the precision with which the β-spectrum is measured. For the nominal KATRIN settings, $B_{\text{src}} = 2.5$ T and $B_{\text{ana}} = 0.6$ mT, resulting in a filter width of $\Delta E \approx 4.7$ eV at $E_{\text{kin}} = 18.6$ keV.

2.1.2 Transmission Probability

Electrons are transmitted through the MAC-E filter if their longitudinal kinetic energy component exceeds the retarding potential energy, expressed as

$$E_{\|,\text{kin}} - qU > 0,$$

where q is the elementary charge and U is the retarding potential. Consequently, whether an electron crosses the analyzing plane depends on the electron's initial kinetic energy, its pitch angle at the source, and the applied retarding potential. This dependence is captured by the transmission condition:

$$T(E_{\text{kin}}, \theta_{\text{src}}, qU) = \begin{cases} 1 & \text{if} \quad E_{\text{kin}} \left(1 - \sin^2(\theta_{\text{src}}) \cdot \frac{B_{\text{ana}}}{B_{\text{src}}} \cdot \frac{\gamma+1}{2}\right) - qU > 0, \\ 0 & \text{otherwise.} \end{cases} \tag{2.8}$$

To suppress background electrons originating from the walls of the main spectrometer, a pinch magnet is used to reflect electrons arriving at the detector with large pitch angles [13, 144, 12, 135]. This magnetic mirror also reflects signal electrons from the WGTS if their initial pitch angle exceeds a critical value:

$$\theta_{\max} = \arcsin\left(\sqrt{\frac{B_{\text{src}}}{B_{\text{pinch}}}}\right), \tag{2.9}$$

where B_{src} and B_{pinch} are the magnetic field strengths at the source and the pinch magnet, respectively. For the nominal KATRIN settings, $B_{\text{src}} = 2.5$ T and $B_{\text{pinch}} = 4.2$ T, resulting in a maximum pitch angle of $\theta_{\max} = 50.8°$.

Because only electrons with $\theta_{\text{src}} < \theta_{\max}$ can reach the detector, the effective filter width improves accordingly:

$$\Delta E = \frac{B_{\text{ana}}}{B_{\text{src}}} \sin^2(\theta_{\max}) \cdot E_{\text{kin}} \cdot \left(\frac{\gamma+1}{2}\right) = \frac{B_{\text{ana}}}{B_{\text{pinch}}} \cdot E_{\text{kin}} \cdot \left(\frac{\gamma+1}{2}\right) \approx 2.8\,\text{eV}. \tag{2.10}$$

Assuming isotropic emission of electrons from the source, the angular probability distribution is proportional to $\sin(\theta_{\text{src}})$. Therefore, the angle-integrated transmission function for an electron with kinetic energy E_{kin} at retarding potential U is given by:

$$T(E_{\text{kin}}, qU) = \int_0^{\theta_{\max}} T(E_{\text{kin}}, \theta_{\text{src}}, qU) \cdot \sin(\theta_{\text{src}})\, \mathrm{d}\theta_{\text{src}}. \tag{2.11}$$

To compute this integral analytically, the maximum transmissible pitch angle θ^* is defined from the equality in Equation 2.8:

$$\sin^2(\theta^*) = \frac{B_{\text{src}}}{B_{\text{ana}}} \cdot \frac{2}{\gamma+1} \cdot \left(1 - \frac{qU}{E_{\text{kin}}}\right) \tag{2.12}$$

The transmission is nonzero only if $\theta^* \leq \theta_{\max}$, where θ^* is the maximal pitch angle for which an electron with kinetic energy E_{kin} can still be transmitted through the spectrometer. The total transmission probability is obtained by integrating over the angular distribution of emitted electrons:

$$\int_0^{\theta^*} \sin(\theta)\,\mathrm{d}\theta = 1 - \cos(\theta^*). \tag{2.13}$$

Thus, the angle-integrated transmission function takes the form:

$$T(E_{\text{kin}}, qU) = \begin{cases} 0, & \text{if } \sin^2(\theta^*) < 0, \\ 1 - \cos(\theta^*), & \text{if } 0 \leq \theta^* \leq \theta_{\max}, \\ 1 - \cos(\theta_{\max}), & \text{if } \theta^* > \theta_{\max}. \end{cases} \tag{2.14}$$

Using the trigonometric identity $\cos(\arcsin(x)) = \sqrt{1 - x^2}$, the transmission probability function can be expressed as:

$$T(E_{\text{kin}}, qU) = \begin{cases} 0, & E_{\text{kin}} - qU < 0, \\ 1 - \sqrt{1 - \dfrac{B_{\text{src}}}{B_{\text{ana}}} \cdot \dfrac{2}{\gamma + 1} \cdot \left(1 - \dfrac{qU}{E_{\text{kin}}}\right)}, & 0 \leq E_{\text{kin}} - qU \leq \Delta E, \\ 1 - \sqrt{1 - \dfrac{B_{\text{src}}}{B_{\text{pinch}}}}, & E_{\text{kin}} - qU > \Delta E, \end{cases} \tag{2.15}$$

where ΔE is the improved filter width from Equation 2.10.

Equation 2.15 provides the transmission probability function, incorporating the effects of both electrostatic retardation and magnetic reflection due to the pinch magnet configuration.

2.2 KATRIN's Experimental Design

The KATRIN experiment is located in Karlsruhe, Germany, hosted by the Tritium Laboratory Karlsruhe (TLK) at the Karlsruhe Institute of Technology (KIT). Figure 2.2 illustrates the layout of the KATRIN experimental setup, which extends approximately 70 meters in length. The entire experimental setup is divided into three distinct functional sections: the Rear Section, the Source and Transport Section (STS), and the Spectrometer and Detector Section (SDS). Each of these components is optimized to support high-precision measurements through control of systematic effects, stable source operation, and accurate electron energy analysis.

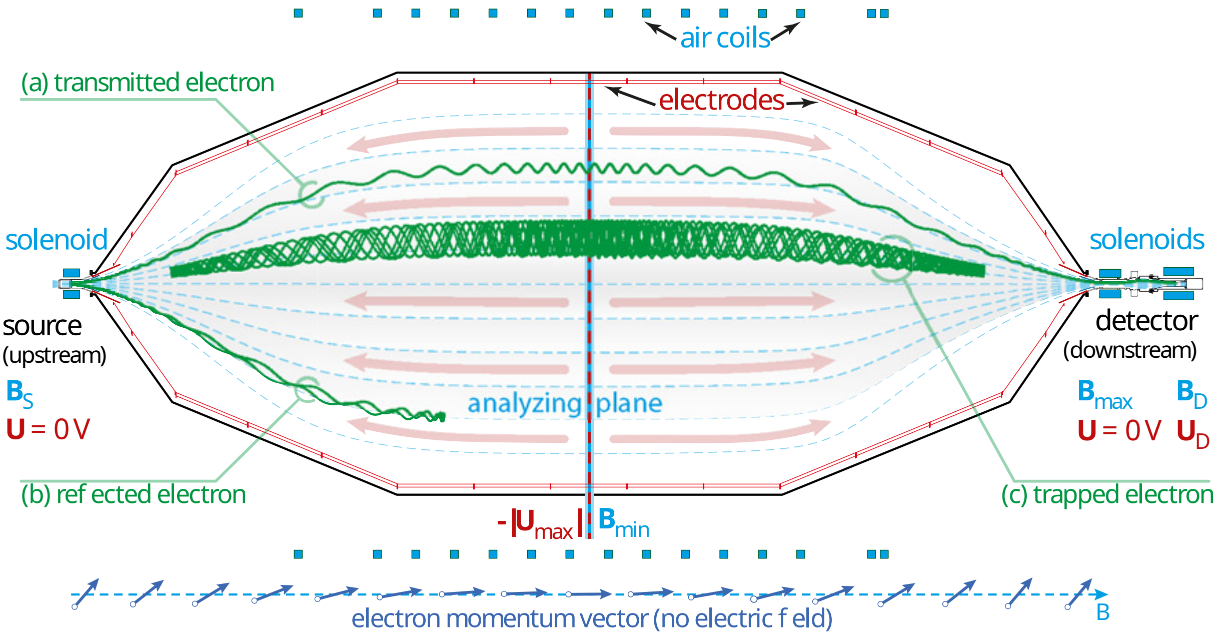

Figure 2.1: Schematic representation of the MAC-E filter principle. Superconducting solenoids at both ends establish a guiding magnetic field, while electrostatic retarding potentials are formed by inner electrodes. Electrons emitted from the source are adiabatically collimated along magnetic field lines. Those with sufficient longitudinal kinetic energy surpass the electrostatic potential and reach the detector (a), whereas lower-energy electrons are reflected (b). Electrons produced within the spectrometer may become confined by the magnetic bottle effect (c). At the bottom, adiabatic collimation is illustrated via electron momentum vectors in the absence of retardation. The entire spectrometer is enclosed by air coils (indicated by the dotted structures at the top and bottom) to fine-tune the magnetic field configuration. Image source [67, Figure 25].

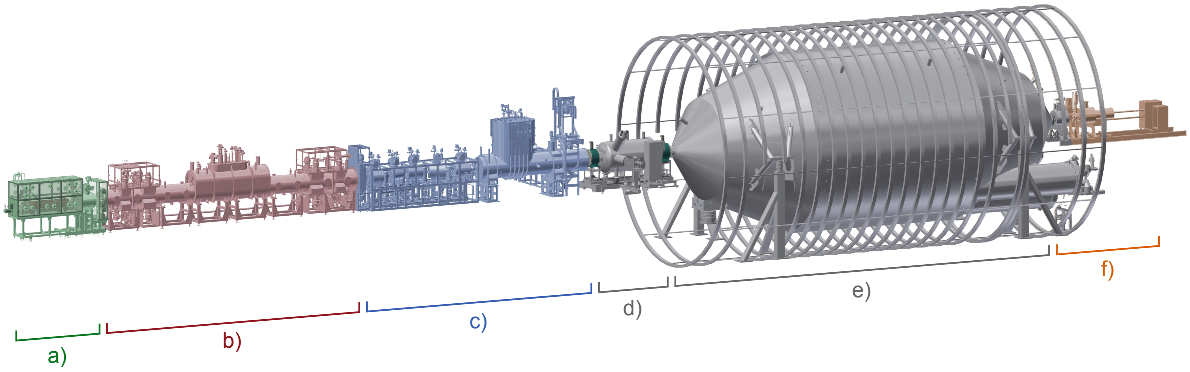

Figure 2.2: Schematic overview of the 70-meter-long KATRIN beamline, divided into three main sections. The rear section (a): includes the rear wall and the electron gun (e-gun), used for source calibration and monitoring. The source and transport section contains: (b) the windowless gaseous tritium source (WGTS), where β-decay electrons are generated, and (c) the transport system consisting of the differential pumping section (DPS) and cryogenic pumping section (CPS), which guide electrons while removing tritium gas. The spectrometer and detector section comprises (d) the pre-spectrometer (PS), which filters out low-energy electrons; (e) the main spectrometer (MS), where electron energy is precisely analyzed; and (f) the detector system including the focal plane detector (FPD), which counts electrons with sufficient surplus energy. Image source [151].

2.3 Rear Section

The Rear Section (RS) is located at the upstream end of the KATRIN beamline, directly adjacent to the Windowless Gaseous Tritium Source (WGTS), as shown in Figure 2.2. An overview of the Rear Section layout is shown in Figure 2.3 It contains the rear wall, BIXS [1] system, electron gun (e-gun) system and a superconducting magnet, which guides the calibration electrons into the beamline. These components play an essential role in monitoring key experimental parameters such as source activity, gas composition, and spectrometer high-voltage stability [90, 18].

2.3.1 Rear Wall

The Rear Wall (RW) is a 145 mm diameter stainless steel disk coated with a 1 µm layer of gold, enabling a uniform work function and stable surface potential. It acts as the termination point for the magnetic flux tube in KATRIN's rear system, where a significant amount of circulated tritium is evacuated, regulated by the Differential Pumping System (DPS1-R) at the rear side. This pumping system, part of a series of differential pumping ports equipped with turbomolecular pumps (TMPs), effectively reduces tritium flow and maintains a pressure of approximately 1×10^{-5} mbar. Additional details on the DPS are given in Section 2.4.2.1.

The RW is positioned at the front of the rear section and, as shown in Figure 2.4, it features a central 5 mm aperture to allow electrons emitted from the electron gun to pass through. The rear magnet operates at 4.0 T, while the magnetic field at the RW during β-decay measurements is 1.23 T. This magnetic configuration guides beta electrons from tritium decay, low-energy ions, and secondary electrons to the RW. Some secondary electrons from tritium ionization may escape through the aperture. The RW defines the ground potential of the cold plasma [2] in

---

[1] Beta-Induced X-ray Spectroscopy

[2] A plasma is a quasi-neutral medium of positive ions and electrons which occur during the tritium ionization in WGTS.

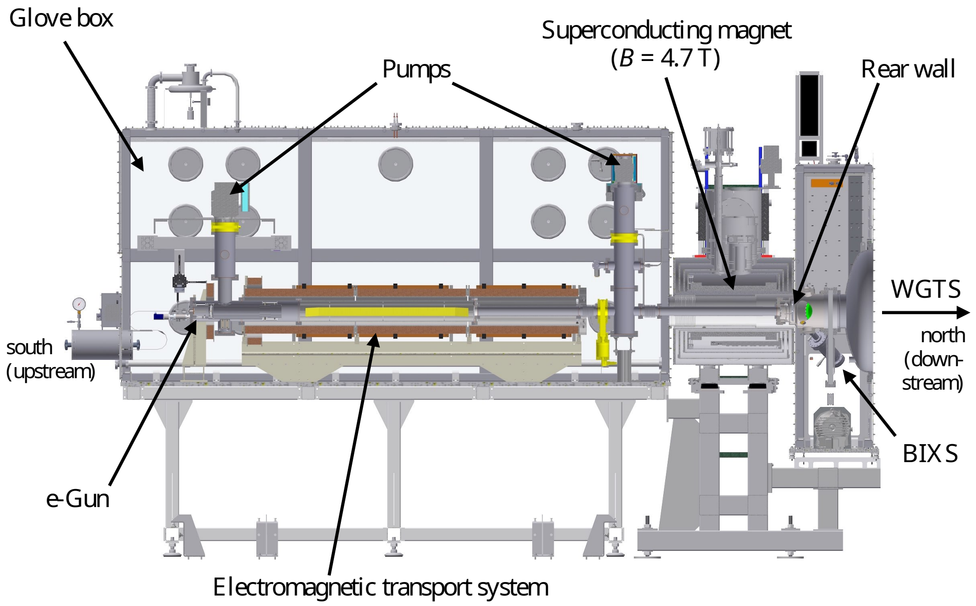

Figure 2.3: Schematic CAD representation of the KATRIN Rear Section (RS), viewed from the southern side. Located at the upstream end, it faces the Windowless Gaseous Tritium Source (WGTS). Key components include a quasi-monoenergetic electron gun (e-gun) system for calibration and monitoring, and a superconducting magnet for electron guidance. The Rear Wall (RW) separates the RS from the WGTS. The BIXS detector measures X-rays from the RW to monitor tritium source activity. Components exposed to tritium are enclosed within a sealed glovebox for safety and containment. Image source [67].

the WGTS [139, 154], which provides the starting potential of the β electrons. The formation of local space charges in the plasma can lead to spatial inhomogeneities and plasma potential distribution can be controlled and modified by rear wall. As plasma exhibit both longitudinal and radial variations, the total energy of the electrons depends on their location of generation. The magnetic flux of 191 Tcm^2 mapping into the rear wall couples the source cold plasma to it and defines the ground potential. The rear wall voltage is optimized to provide the best coupling conditions and reduce longitudinal plasma effects. The RW enhances plasma conductivity and maintains quasi-neutrality through far-UV illumination. The work function of the gold layer ensures temporal stability. To compensate for the work function difference between the gold RW and the stainless steel WGTS beam tube, a bias voltage is applied. Although voltages up to ±500 V are possible, typical β-decay measurements operate with a bias around ±0.1 V. Simulations indicate that a spatially homogeneous RW potential minimizes plasma potential inhomogeneities [154, 170]. Thus, the RW bias is optimized before each campaign by β-rate scans or analyzing the radial variation of the L_3 line of metastable ^{83m}Kr in tritium. Additionally, surface-adsorbed tritium undergoes β-decay, contributing to a secondary β-spectrum that differs from the gaseous source in shape and endpoint [17]. This can introduce distortions in the total spectrum and affect the analysis. The spectrum depends on adsorbed species and molecular structure, currently not well known. Quantifying tritium accumulation on the RW is necessary to account for systematic uncertainties.

The RW lies within the exit cone of DPS1-R, in a 1.4–1.6 T magnetic field, ensuring full flux tube coverage. Most of the flux intersects the gold-coated surface, leaving a 1.3 mm gap to the PEEK ring[3]. This gap can be adjusted ±5 mm to optimize positioning. The RW thus electrically terminates the WGTS plasma and defines the plasma potential.

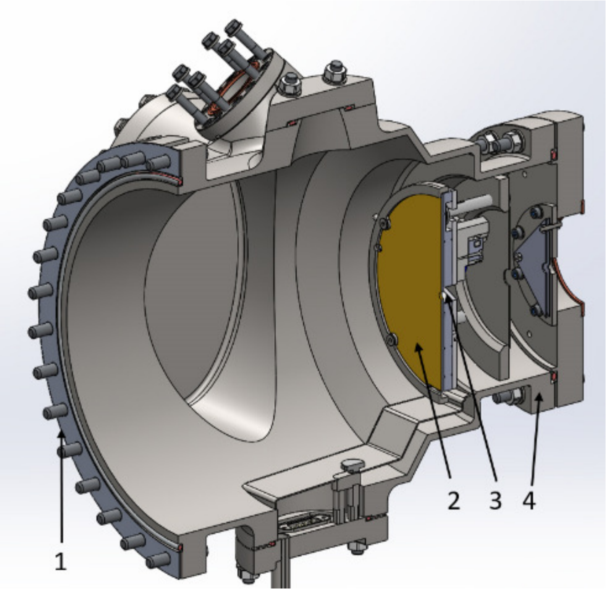

Figure 2.4: Cross-section of the integrated rear wall (RW) unit. (1) Flange connecting the RW chamber to the WGTS magnet cryostat. (2) The RW itself. (3) Central aperture for e-gun beam transmission. (4) Flange connecting the RW chamber to the Rear System. Image source [67, Figure 17]

2.3.2 BIXS

The RW in KATRIN acts as a diagnostic tool where beta electrons interacting with a gold layer generate X-rays via bremsstrahlung, detected by a silicon drift detector. The Beta-Induced X-ray Spectrometry (BIXS) technique, proposed by Matsuyama [177, 180], correlates X-ray intensity with tritium activity, providing crucial data on tritium retention in surface layers and depth profiles [178, 179, 176, 175].

Integrated into the calibration and monitoring system (CMS), BIXS uses two silicon drift detectors to measure X-rays produced by beta-electron interactions with the RW. With approximately 10^{11} tritium β-decays per second in the WGTS, most beta electrons are directed toward the RW, generating X-rays proportional to tritium decay. The system achieves 99.9% electron redirection, enhancing X-ray production. In the energy regime of KATRIN, the energy loss of electrons within materials primarily results from ionization and bremsstrahlung effects.

Two types of X-rays are produced:

- **Characteristic X-rays:** Emitted as discrete spectral lines due to atomic ionization and subsequent electron transitions.
- **Bremsstrahlung:** A continuous spectrum according to Kramers' law [152].

---

[3] PEEK (Polyether Ether Ketone) is a high-performance thermoplastic polymer that provides excellent electrical insulation and mechanical stability. In the KATRIN experiment, PEEK is used to fill the 1 mm gap between the Rear Wall (RW) and the vessel wall, ensuring effective electrical insulation while maintaining the vacuum system's integrity.

BIXS detects these X-rays using KETEK AXAS-M Silicon Drift Detectors (SDDs), each with a 92 mm^2 active area. 250 μm beryllium windows, optionally gold-coated, prevent tritium ingress [221].

Two BIXS systems are installed at CF-40 ports as illustrated in Fig. 2.5 at a 33-degree angle in the RW chamber to ensure optimal detection of emitted X-rays. The attenuation of X-rays as they traverse a material follows an exponential law given by $I = I_0 \exp\left(-\int n\sigma\, dx\right)$, where I_0 is the initial intensity, n is the particle density of the medium, σ is the interaction cross-section, and x denotes the path length. BIXS achieves a signal rate of 10^4 counts per second (cps), offering 0.1% accuracy over 100-second intervals. Despite challenges from the memory effect [220] due to tritium accumulation, BIXS enables continuous tracking of tritium retention. The e-gun measures column density, and BIXS monitors electron rates and tritium accumulation on the RW. As tritium gas is pumped out, BIXS tracks flow, estimating column density. For decreasing flow rates, BIXS can estimate column density based on the flow rate. Background signals from potential back-scattered electrons and surface contamination may affect the accuracy of overall measurement [221].

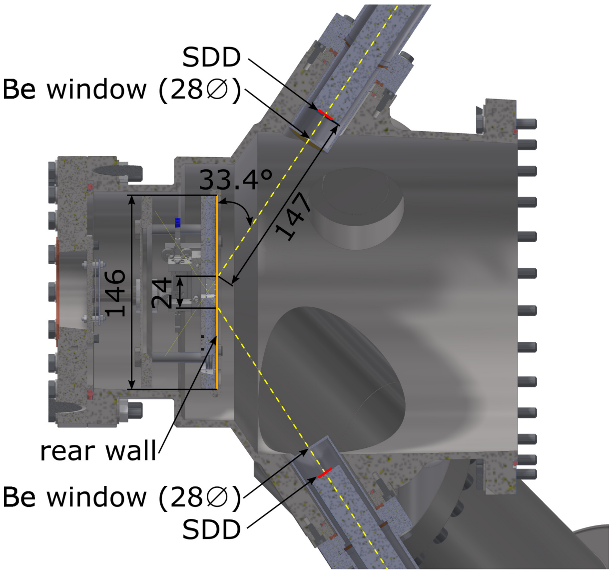

Figure 2.5: Schematic representation of the rear wall chamber featuring the BIXS system and the rear wall. In this setup, the silicon drift detector (SDD) of the BIXS system is situated behind a beryllium window coated with gold. Image source [223].

2.3.3 Photoelectric Electron Gun

The photoelectric electron gun (e-gun) provides a quasi-monoenergetic, angular-selective electron beam used for precision calibration and systematic studies within the KATRIN experiment, particularly in beamline transmission and detector characterization. Its development and commissioning spanned several years [246, 245, 80, 125, 44, 43], including the implementation of a rear-section e-gun for full beamline transmission measurements [35].

Electron emission is driven by the photoelectric effect: ultraviolet light, delivered via optical fiber, back-illuminates a thin (20–40 nm) Ag or Au photocathode. The emitted electrons are accelerated across a potential difference of approximately 4 kV between two parallel plates separated by 10 mm. Tilting these plates by an angle α_p with respect to the magnetic field direction imparts a pitch angle $\theta = \angle(\vec{p}, \vec{B})$ to the electrons [246, 44]. Rapid, non-adiabatic acceleration results in beam collimation, while subsequent cylindrical electrodes further accelerate the electrons to energies of up to 32 keV. The beam is then guided adiabatically by superconducting magnets to the spectrometer entrance, permitting pitch angles from 0° to 90°. A grounded vacuum enclosure ensures stable operation at count rates of up to 10^4 cps. The final energy distribution is governed by the UV wavelength and the effective work function of the photocathode.

Understanding inelastic scattering in the Windowless Gaseous Tritium Source (WGTS) is essential for β-spectrum analysis. At nominal column density, approximately 60% of β-electrons scatter inelastically, losing between 11 eV and 9.3 keV [214]. This scattering probability depends on the product of the column density and the inelastic scattering cross-section. The e-gun facilitates determination of this product [14, 149], as well as the mean energy loss per scattering event [214, 219, 223, 232, 229].

Furthermore, the e-gun's adjustable energy and pitch angle allow for detailed characterization of the MAC-E filter's transmission function under varying electromagnetic configurations [48].

2.4 Source and Transport Section

The Source and Transport Section (STS), housed within the Tritium Laboratory Karlsruhe (TLK), ensures tritium containment and operational safety via a two-stage glove-box system enclosing all tritium-supplied components. It includes the Windowless Gaseous Tritium Source (WGTS) (see Section 2.4.2) and transport and pumping sections (see Section 2.4.2)

2.4.1 Windowless Gaseous Tritium Source: WGTS

The WGTS is a key component of the KATRIN experiment, consisting of a 10-meter-long stainless steel tube with an inner diameter of 90 mm, specifically engineered to serve as the beta electron source ensuring ultra-high luminosity up to 10^{11} Bq for KATRIN. Within this tube, molecular tritium gas is injected, with an injection pressure of $3.4\ \times 10^{-3}$ mbar, through capillaries at its center and extracted through differential pumping sections (DPS1-R/F) at both ends, as illustrated in Figure 2.6. The open-ended geometry minimizes β-electron scattering losses and supports a stable column density profile. The source activity depends on the tritium atom number, represented by the column-density parameter ρd, where ρ is the gas density and $d = 10$ m. The total number of tritium atoms, N_T, is calculated as:

$$N_\mathrm{T} = 2 \cdot \rho d \cdot A_\mathrm{WGTS} \cdot \varepsilon_\mathrm{T}, \tag{2.16}$$

where A_WGTS is the cross-sectional area, and

$$\varepsilon_T = \frac{N_{\mathrm{T}_2} + \frac{1}{2}(N_\mathrm{HT} + N_\mathrm{DT})}{\sum_i N_i} \tag{2.17}$$

represents the tritium purity. Laser Raman (LARA)[18] spectroscopy system monitors the gas composition, determining the purity and the ratio of impurities like HT and DT in the gas. The tritium purity typically varies between 97% and 99%.

The gas mixture primarily contains tritium isotopologues (T_2, DT, and HT), with minimal concentrations of stable isotopologues (D_2, HD, H_2). The tritium activity depends on its purity and column density, achieving an activity of 10^{11} Bq. The tritium undergoes isotropic decay, generating helium, an electron, and an electron antineutrino, represented by the equation:

$$\mathrm{T}_2 \rightarrow \mathrm{HeT}^+ + \mathrm{e}^- + \bar{\nu}_\mathrm{e}$$

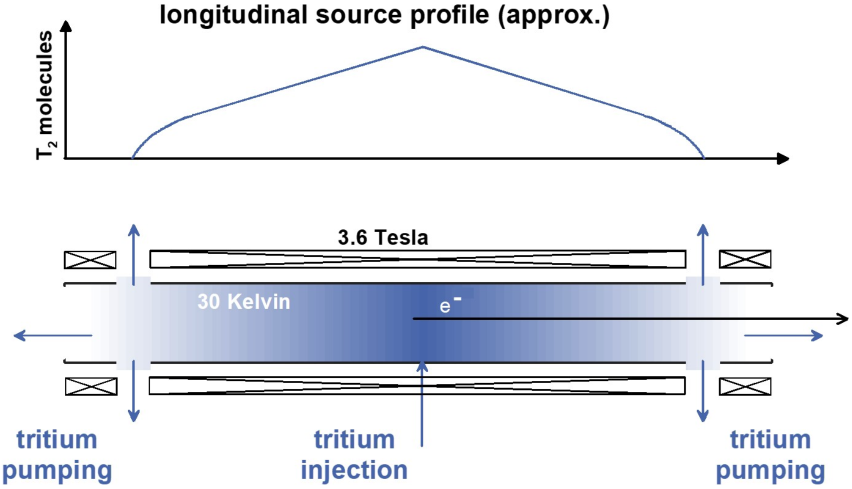

Figure 2.6: Illustration of the 10-meter long, 9 cm diameter WGTS beam tube at KATRIN. Tritium gas is continuously injected at the center of the beam tube, maintaining a constant density profile, while gas is evacuated from both the rear and front ends via the differential pumping sections (DPS1-R and DPS1-F). Image source [67]

The WGTS is operated under specific conditions that maximize the throughput, purity, and stability of the tritium source, keeping systematic effects to a minimum. The WGTS must operate at temperatures below 100 K to maintain low conductance in the beam tube, which allows a greater quantity of tritium to be contained in the source. To ensure a sufficient decay rate, the system requires a daily throughput of 40 g of molecular tritium [238]. Additionally, maintaining temperatures below 100 K reduces Doppler broadening of the tritium spectrum, enhancing the accuracy of neutrino mass measurements. Typically, the source operates at 30 K or 80 K, achieving stability at a sub-per mille level. The WGTS and the tritium gas are housed within a cryostat that cools the system to very low temperatures, reaching down to 30 K. This cooling is crucial to achieving the high column density. The system also allows for the addition of $^{83\mathrm{m}}$Kr to tritium for calibration measurements, enabling the quantification of parameters like plasma density and electron energy-loss, while maintaining beam tube temperatures between 80 K and 100 K to prevent krypton freeze-out [219, 7]

In the WGTS, the ultra-cold tritium gas forms a weak, cold, magnetized plasma composed of low-energy electrons and positive ions, resulting from the high activity of the tritium gas. Most β-electrons escape along magnetic field lines, while the resulting ions are rapidly thermalized and transversely confined by the magnetic field, restricting their diffusion to the vessel walls. Consequently, ion removal is dominated by longitudinal transport toward the differential pumping section (DPS), see Section 2.4.2.1.

This confinement may induce a positive space charge, but it is effectively neutralized by secondary electrons from approximately 15 ionizations per β-electron [65]. These electrons undergo elastic and inelastic scattering with tritium molecules, leading to thermalization. The cryogenic operating temperature plays a critical role in stabilizing the plasma by minimizing spatial plasma potential variations and suppressing unwanted plasma effects. Details on the inhomogeneities of the electric potential in plasma are provided in [7]. The WGTS uses seven superconducting solenoid magnets to generate a 2.5 T magnetic field, directing emitted beta electrons with pitch angles less than 90° toward the spectrometer, while those with greater angles are guided to the rear wall.

2.4.2 Transport and Pumping Section

The transport and pumping system serves a dual purpose: adiabatically guiding β-decay electrons from the WGTS to the spectrometer and reducing tritium gas flow by over 12 orders of magnitude. This reduction is crucial for maintaining an ultra-high vacuum in the spectrometer, minimizing tritium contamination and background interference. The system uses a two-stage approach: **Differential Pumping System (DPS)** followed by **Cryogenic Pumping System (CPS)**.

2.4.2.1 Differential Pumping Section (DPS)

The DPS serves as the first stage in tritium removal, reducing tritium flow by seven orders of magnitude through a combination of geometric and magnetic design. The beam tube is divided into five segments, each connected by turbomolecular pumps (TMPs), which selectively evacuate neutral gas molecules. To enhance pumping efficiency, the beam tube sections are arranged in a chicane-like configuration with 20° tilts, increasing gas-wall collisions and improving molecular removal.

Superconducting solenoids surrounding each segment generate a magnetic flux that guides beta electrons along field lines while impeding ion transport. To mitigate ion contamination, four dipole electrodes create an electric field that, in combination with the magnetic field, induces a $\mathbf{E} \times \mathbf{B}$ drift, directing ions toward metallic surfaces for neutralization and removal. Additionally, a 100 V ring electrode at the DPS exit prevents the passage of residual positive ions, ensuring only neutralized gas molecules and guided electrons proceed downstream [95, 146].

2.4.2.2 Cryogenic Pumping Section (CPS)

The CPS further reduces tritium flow by another seven orders of magnitude via cryosorption. Following the reduction of tritium flow by seven orders of magnitudethrough the DPS, further decrease by an additional factor of 10^7 is not achievable using additional TMPs, due to the back-diffusion effect in the pumps. The 7-meter-long CPS consists of seven beam tube segments, each enclosed by superconducting solenoids that ensure adiabatic electron transport. The second and fifth segments are tilted by 15° to increase gas-wall interactions, enhancing cryosorption efficiency. This results in a maximum allowed tritium flow of $1 \times 10^{-14}\,\mathrm{mbar \cdot L\,s^{-1}}$ downstream from the DPS.

The sorption pump integrated into the beam tube was selected as the primary pump for the next stage, as it meets the key requirements of high pumping speed, long-term tritium retention, and efficient tritium removal during the regeneration phase. A cryo-sorption pump with a condensed argon layer on the gold-plated inner beam tube wall was chosen, as it allows for easy removal of both the layer and the adsorbed tritium, reducing residual contamination. The interior tube surfaces are coated with an argon frost layer, which serves as an adsorbent for tritium molecules. The second to fourth beam tube segments incorporate 90 longitudinal gold-coated fins, each 2 mm long, effectively tripling the adsorption surface area. The cryogenic environment is maintained at 3 K, significantly increasing the retention time of adsorbed tritium molecules.

To sustain long-term performance, the argon frost layer is periodically regenerated. Once tritium accumulation reaches Bq (1 Curie), the CPS is heated to 80 K, allowing desorbed gas to be pumped out. A subsequent helium purge cycle ensures the complete removal of residual tritium, after which a fresh argon frost layer is deposited, restoring full pumping capacity. The CPS regeneration interval has been extended to 445(46) days, surpassing the initial requirement of 60 days [222].

In summary, the transport and pumping section reduces the tritium flow rate to less than 1×10^{-14} mbar L/s, while guiding up to 1×10^{11} tritium β-decay electrons per second within the magnetic flux to the spectrometer section. The magnetic flux, $\Phi = \int \mathbf{B} \cdot dA$, is set to $134\,\mathrm{T\,cm^2}$ during standard operation [135], with a design value of $191\,\mathrm{T\,cm^2}$ [67], where A is the cross-sectional area through which the magnetic field passes.

2.4.3 Forward Beam Monitor

The Forward Beam Monitor (FBM) is a subsystem in the KATRIN experiment, designed to monitor the activity of the tritium source with high precision [42, 83]. Positioned downstream between the Cryogenic Pumping Section (CPS) and the pre-spectrometer, the FBM measures the β-electron flux emitted from the source while avoiding interference with the focal plane detector (FPD). The FBM is placed at the outer 7 mm wide rim of the magnetic flux tube (active radius ~71 mm) to prevent shadowing of FPD pixels. This positioning allows it to sample an electron flux of approximately $10^6\,\mathrm{e^-/s \cdot mm^2}$ representative of the entire beam cross-section The FBM hardware setup is illustrated in Figure 2.7.

The system operates in two modes:

- Monitoring Mode: Stationary measurement in the flux tube's outer rim during neutrino data acquisition.
- Scanning Mode: Calibration scans across the beam cross-section to validate spatial homogeneity.

The FBM tracks fluctuations in source activity and column density (N), which is critical for minimizing uncertainties. Column density stability relies on precise control of WGTS parameters such as temperature ($\sim 80\,\mathrm{K}$), pressure, and tritium purity ($\varepsilon_{\mathrm{T}} > 95\%$) measured by laser Raman spectroscopy (LARA). Combining FBM flux data with LARA measurements reduces systematic uncertainties, and during the 2018 tritium campaign, the FBM demonstrated stability at the per-mille level, with only minor long-term drifts due to electronic noise [67].

2.5 Calibration and Monitoring

The precise measurement of the tritium β-decay spectrum requires continuous calibration and monitoring of both the activity and composition of the source, as well as the energy scale of the electron spectrometer. Several independent and redundant systems are employed across KATRIN to ensure source stability at the 0.1% level and to maintain the tritium purity ϵ_T at 95%. These include the Beta-Induced X-ray Spectroscopy system (BIXS, see Sec. 2.3.2), the Forward Beam Monitor (FBM, see Sec. 2.4.3), and periodic measurements using a photoelectric e-gun (see Sec. 2.3.3). In addition, the tritium gas composition is monitored in real time with the Laser Raman spectroscopy system (LARA). Calibration of the electron energy scale is critical for understanding systematic effects in the integral spectrum and is performed using the e-gun and radioactive sources like the Condensed Krypton Source (CKrS), and the Gaseous Krypton Source (GKrS). The MoS (see Section 2.6.3) in KATRIN serves to monitor the stability of the high voltage system by measuring the K-32 line of $^{83\mathrm{m}}$Kr, ensuring that the high voltage of the monitor spectrometer remains synchronized with the KATRIN main spectrometer for accurate calibration during β-scans.

2.5.1 Condensed Krypton Source (CKrS)

The CKrS [82] provides quasi-monoenergetic electron lines for precise calibration of the spectrometer transmission function and for monitoring the energy scale stability over time. It exploits the isomeric transition of $^{83\mathrm{m}}$Kr, which decays via internal conversion, emitting electrons with well-known energies. The source is produced by condensing $^{83\mathrm{m}}$Kr onto a highly oriented pyrolytic graphite (HOPG) substrate located at the rear end of the beamline, close to the detector. This geometry allows high-statistics measurements with negligible time-of-flight dispersion. Its primary advantage lies in its operational stability and spatially localized emission, which enable detailed response function studies under well-controlled conditions. The prominent K-32 conversion electron line at 17.8 keV is used to determine the spectrometer's energy resolution and monitor potential drifts of the MAC-E filter. CKrS campaigns were periodically conducted between tritium runs, in early measurement phases, serving to define the absolute energy scale and validate spectrometer modeling. The system also includes a high-voltage setup capable of biasing the substrate up to 10 kV to match the energy of the K-32 line to the tritium endpoint, although this feature has not yet been utilized in practice.

2.5.2 Gaseous Krypton Source (GKrS)

The GKrS enables distributed calibration by injecting $^{83\mathrm{m}}$Kr gas into the front of the windowless gaseous tritium source (WGTS), where it is circulated within the closed inner loop. Unlike the CKrS, the GKrS allows mapping of the entire source and transport section under conditions closely resembling tritium operation. The $^{83\mathrm{m}}$Kr atoms decay via internal conversion, emitting electrons from multiple shell transitions, including prominent lines such as L3-32. This spatially extended emission provides sensitivity to variations in the column density, plasma conditions, and electric potential along the beam axis [170]. The GKrS is particularly valuable for investigating potential inhomogeneities, which can lead to spectrum broadening and shifts in the energy loss function (see Section 3.5.2). Because it mimics tritium-like conditions, the GKrS is instrumental in constraining systematic uncertainties related to inelastic scattering and energy losses. It is used during dedicated calibration phases and complements the CKrS by enabling large-volume, distributed electron calibration.

Recent Developments in Calibration Techniques: Double injection mode The Condensed Krypton Source (CKrS) was initially used during KATRIN commissioning and periodically between tritium runs for high-resolution calibration. It was not used during tritium operation but remains crucial for spectrometer calibration.

The Gaseous Krypton Source (GKrS) was first deployed in July 2017, operating at 100 K to prevent krypton freeze-out, based on lessons from the Troitsk experiment [31]. However, pumping constraints limited the achievable tritium column density to 30%.

During the third science run, a new tritium and krypton co-circulation was tested. A detailed description of this new co-circulation mode of krypton with tritium, the so called double injection mode, can be found in [173]. Co-circulation required the WGTS temperature to be raised to 80 K. Starting with the fourth science run, both tritium and krypton measurements were performed using the co-circulation mode at 80 K and 75% nominal column density [7]. This allowed for high-statistics characterization of both source- and spectrometer-related systematics, with precise determination of transmission properties using well-known conversion electron lines such as K-32 and $N_{2,3}$-32. This approach minimized plasma-related systematics and improved the comparability between calibration and physics data. These scans provided crucial information for refining the electromagnetic field configuration and improving the modeling of the response function (see Section 3.5).

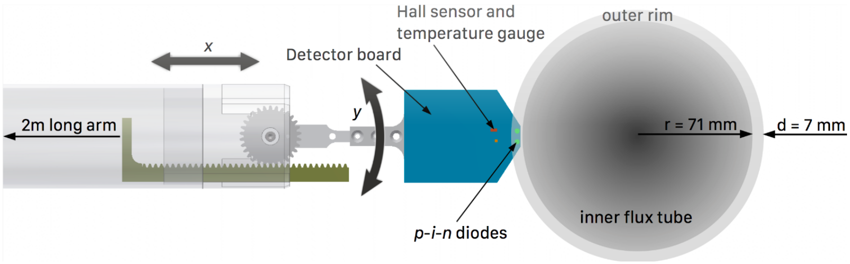

(a)

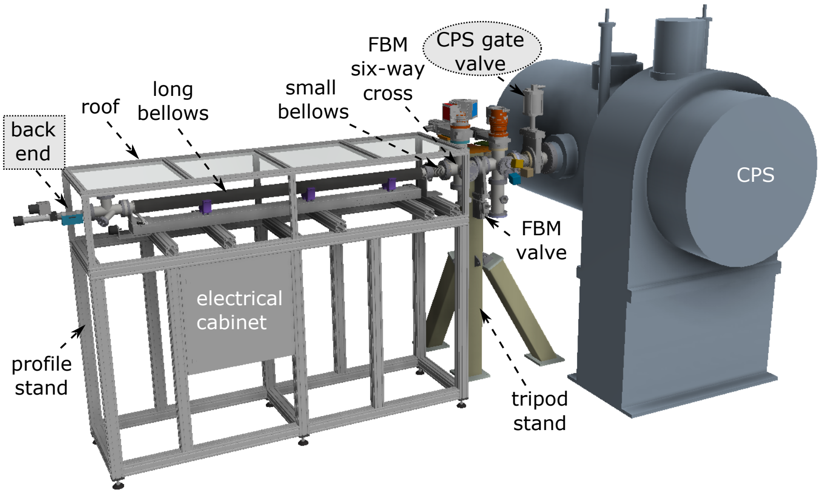

(b)

Figure 2.7: a) The FBM front-end mechanics and monitoring position, where it remains in the outer rim of the flux tube during neutrino mass measurements, enabling continuous source activity monitoring without obstructing the FPD. b) The FBM is positioned perpendicular to the beamline at the CPS, with gate valves isolating it when in the parking position within the six-way cross. A 2 m long bellow allows the detector arm to extend into the flux tube inside the CPS. Image source [42].

2.6 Spectrometer and Detector section

The spectrometer and detector sections of the KATRIN experiment play a central role in analyzing the energy of beta electrons and detecting transmitted events with high precision. The spectrometer system employs MAC-E filter for precise measurement of the β-decay spectrum. KATRIN utilizes three spectrometers: the Pre-Spectrometer (PS) and the Main Spectrometer (MS) in the primary beamline, and the Monitor Spectrometer (MoS) in a parallel setup electrically connected to the MS. The PS serves as a pre-filter for low-energy electrons, the MS provides the high-resolution energy analysis, and the MoS continuously monitors and calibrates the retarding potential applied to the MS.

At the end of the beamline, the detector section consists of the focal-plane detector (FPD) and its associated data acquisition (DAQ) system. The FPD is a segmented monolithic silicon PIN diode array with 148 pixels arranged in a "dartboard" layout, designed to detect electrons that have passed the MS filter. Its pixelated structure allows for spatial resolution and background suppression.

This section provides descriptions of each spectrometer: the PS in Section 2.6.1, the MS in Section 2.6.2, and the MoS in Section 2.6.3. The detector and DAQ systems are described in Section 2.6.4.

2.6.1 Pre-Spectrometer

Located downstream of the CPS, the Pre-Spectrometer (PS) has a length of 3.4 m and a diameter of 1.7 m. It was originally constructed as a prototype for the Main Spectrometer (MS).

Only a small fraction of the β-decay spectrum, specifically electrons within the final 40 eV below the endpoint, contribute to the determination of the neutrino mass and the search for sterile neutrinos. The PS can therefore be employed as an energy pre-filter to remove low-energy electrons [213]. This prevents their transmission into the MS and reduces background originating from scattering on residual gas [183]. When operated at a retarding potential of $-10\,\mathrm{kV}$, the PS suppresses the electron flux by approximately 85%.

However, applying high voltages to both the PS and MS creates an inter-spectrometer Penning trap in which electrons can accumulate and produce positive ions. These ions may propagate into the MS and generate low-energy secondary electrons, thereby increasing the background rate [16].

To mitigate this effect, a Penning wiper is employed between measurements to remove trapped charges. Until the fourth measurement campaign (KNM4), the PS operated at $-10\,\mathrm{kV}$. During the KNM4-e sub-campaign, the retarding potential was set to 0 V in order to eliminate the Penning trap and the associated background. An internal electrode was maintained at $-100\,\mathrm{V}$ to monitor ion flow. Beginning with the fifth measurement campaign (KNM5), the PS was completely deactivated [135].

2.6.2 Main Spectrometer

The Main Spectrometer (MS) is the central component of KATRIN's energy analysis system, designed for high-precision measurements of the tritium β-decay spectrum near the endpoint. With a length of 23.8 meters and a diameter of 9.8 meters, it is substantially larger than the Pre-Spectrometer. The cylindrical vacuum vessel is made of low-magnetic stainless steel and maintained at ultra-high vacuum (10^{-11} mbar) through a combination of turbomolecular and cryogenic pumping systems. This environment minimizes scattering events and background contributions from residual gases.

A gradual magnetic field reduction, from $B_{\mathrm{src}} = 2.5\,\mathrm{T}$ at the source to $B_{\mathrm{ana}} = 0.6\,\mathrm{mT}$ at the analyzing plane, is necessary to preserve the adiabatic motion of electrons. This field ratio of approximately 4000:1, enabled by the spectrometer's large dimensions, is essential for achieving the required energy resolution and field uniformity across the analyzing plane.

The retarding potential, applied via a negative high voltage on the vessel, reaches approximately 18.6 kV during standard operation [247]. High-voltage stability is ensured by a precision supply system that includes calibrated voltage dividers and digital voltmeters, maintaining relative accuracy at the ppm (10^{-6}) level [216, 218]. Shaping of the electrostatic potential is achieved with the inner electrode (IE) system, which lines the inner surface of the vessel. This segmented structure not only fine-tunes the field but also acts as a barrier to secondary electrons emitted from the vessel walls. Individual segments can be biased independently to eliminate trapped charges and preserve field homogeneity.

Magnetic guidance of electrons is provided by a combination of superconducting solenoids and an external air coil system [28]. The air coil system comprises the Low-Field Correction System (LFCS) and the Earth Magnetic field Compensation System (EMCS), both of which allow fine control over the magnetic field topology. LFCS ensures a uniform low-field environment, while EMCS compensates for distortions from the Earth's magnetic field [86, 108], enabling stable and symmetric conditions in the analyzing region.

2.6.3 Monitor Spectrometer

The Monitor Spectrometer (MoS) provides continuous monitoring of the high-voltage stability applied to the Main Spectrometer (MS), operating as a third MAC-E filter in the KATRIN setup. Utilizing conversion electrons from $^{83\mathrm{m}}\mathrm{Kr}$ decay, whose energies are well known and stable, the MoS functions as a precise voltmeter referenced to a nuclear standard. Accurate knowledge of the retarding potential is essential for interpreting the integral β-spectrum, as even minute voltage fluctuations can introduce systematic shifts in the inferred neutrino mass. To mitigate this, the MoS is linked in parallel to the MS high-voltage system, enabling real-time tracking of potential instabilities by comparing the measured electron energies from the reference source.

The spectrometer reuses components from the former Mainz neutrino mass experiment [153] and consists of a stainless steel vessel maintained under ultra-high vacuum. A system of cylindrical and conical electrodes shapes the retarding electric field, with all components held at the same potential except for a grounded electrode defining the zero point. The magnetic field is guided by a pair of superconducting solenoids located at the entrance and exit, and further shaped by external air coils, ensuring a magnetic configuration comparable to that of the MS.

To match the tritium endpoint energy, the $^{83\mathrm{m}}\mathrm{Kr}$ source is biased accordingly, allowing precise comparison between the reference electrons and the MS retarding potential. A cooled silicon p-i-n diode serves as the electron detector, with both the sensor and preamplifier thermally stabilized via conduction to a liquid-nitrogen reservoir. This setup ensures high stability and energy resolution. In addition to voltage monitoring, the MoS is employed for commissioning of the electron gun [245, 43] and for characterization of TRISTAN detector prototypes [68].

2.6.4 Focal Plane Detector

The Focal Plane Detector (FPD) records β-electrons in the 10–100 keV range with high efficiency (> 0.9), low intrinsic background ($< 1\,\mathrm{mHz}$), and stable operation under ultra-high vacuum

($< 10^{-9}$ mbar) [67, 174]. It consists of a 503 μm thick monolithic silicon p-i-n diode wafer segmented into 148 pixels over a 90 mm diameter [67]. Each pixel (approximately 44 mm^2) is reverse-biased at 120 V in a 2.5 T magnetic field, yielding about 95% detection efficiency. Pixel segmentation enhances spatial resolution, facilitates monitoring of systematics, and allows exclusion of faulty channels.

Electrons from the main spectrometer are guided by superconducting pinch and detector magnets to the FPD. A post-acceleration electrode (PAE) raises their energy by 10 keV, which suppresses backscattering and shifts the signal into a lower-noise spectral region, enhancing detection fidelity [23]. Figure 2.8 shows a schematic of the full detector assembly.

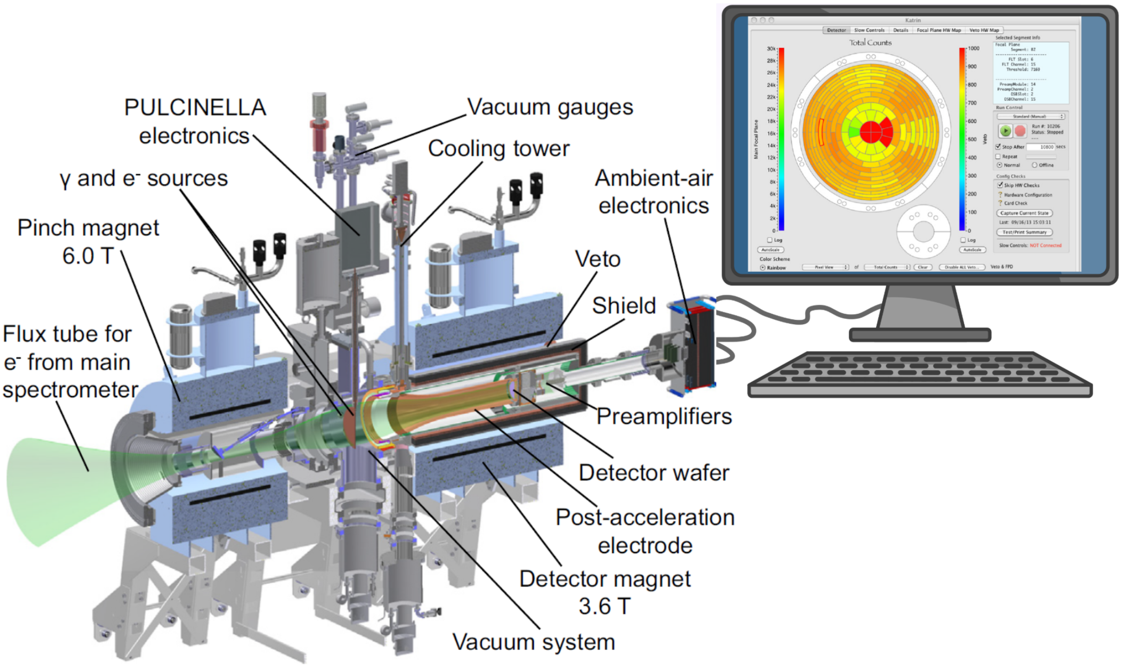

Figure 2.8: Main components of the FPD system. Electrons are guided from the main spectrometer (bottom left) through the pinch and detector magnets, post-accelerated by 10 kV, and finally detected by the segmented p-i-n diode wafer. Image source [23].

Calibration relies on two sources: a fixed 18 MBq γ-source for absolute energy reference, and a UV-illuminated titanium disk producing photoelectrons tunable up to 25 keV. The titanium source operates under vacuum and is monitored by the precision ultra-low current integrating normalization electrometer for low-level analysis (PULCINELLA) electrometer, which measures photocurrents with 3% precision [23].

While the FPD's energy resolution is about 3 keV (FWHM) at 28 keV [135], the main spectrometer defines the experiment's overall energy precision [67]. Nevertheless, the detector's resolution aids background discrimination. Post-acceleration up to 12 kV positions the Region of Interest (ROI) above the noise floor, suppressing low-energy backgrounds.

The FPD is shielded with 3 cm lead and 1.27 cm copper to attenuate external radiation. An active muon veto, comprising 20 mm plastic scintillators, tags cosmic-ray muons for coincidence rejection [23], ensuring ROI purity.

Data acquisition supports rates up to 1 Mcps via a modular system incorporating analog filtering, digitization, and PCIe-based data transfer [65]. Object-oriented Real-time Control and Acquisition (ORCA) software manages configuration and real-time monitoring with a flexible graphical interface [121, 57] .

2.7 From Measurement to Modeling

The KATRIN experiment represents one of the most precise and sensitive instruments ever developed for the measurement of the electron energy spectrum from tritium β-decay. This chapter has outlined the key components of the setup, including the windowless gaseous tritium source (WGTS), the differential and cryogenic pumping sections, the high-resolution MAC-E filter spectrometer, and the segmented focal-plane detector. Each subsystem contributes critically to minimizing systematic uncertainties and enabling a high-fidelity measurement of the β-decay spectrum near its endpoint.

However, the raw data collected by KATRIN cannot directly yield a measurement of the neutrino mass or a result on the sterile neutrino search without a detailed theoretical model of the expected β-spectrum. The interpretation of the observed electron energy distribution requires a comprehensive description of the β-decay process, including the relevant nuclear, atomic, and molecular effects, as well as the instrumental response function. In addition, various background processes, such as those originating from residual radioactivity, cosmic rays, and intrinsic detector noise, must be carefully modeled and accounted for to ensure the integrity of the analysis.

These considerations form the basis of the next chapter, which introduces the theoretical framework and numerical modeling required to extract physical parameters from the KATRIN data.

3

Model of the KATRIN Experiment

Chapter 2 described the KATRIN experiment's hardware setup, including the MAC-E filter spectrometer and the data acquisition procedure. This chapter develops the theoretical model that predicts the electron count rate for each retarding potential setting and the corresponding measurement time.

A central element in this modeling framework is the Measurement Time Distribution (MTD), which defines how measurement time is allocated across the retarding energies. The MTD is particularly important near the spectral endpoint energy E_0, where the sensitivity to neutrino mass is greatest. Section 3.1 provides the definition and details of the MTD. In Section 3.2, the time-independent count rate $\dot{N}_{\text{model}}(qU, \boldsymbol{\theta})$ equation is introduced. It is formed by incorporating the tritium β-decay spectrum, the experimental response function, and background contributions. Detailed discussions of the response function and background modeling appear in Section 3.5 and Section 3.7, respectively.

Using the MTD, the total expected number of electrons at a given retarding energy qU is obtained by multiplying the time-independent count rate $\dot{N}_{\text{model}}(qU, \boldsymbol{\theta})$ by the measurement time $t(qU)$:

$$N_{\text{model}}(qU, \boldsymbol{\theta}) = \dot{N}_{\text{model}}(qU, \boldsymbol{\theta}) \cdot t(qU).$$

This formulation enables the prediction of expected counts under any measurement configuration and provides the foundation for extracting physical parameters, such as the effective electron neutrino mass and, where applicable, sterile neutrino properties (mass and mixing).

3.1 Measurement Configuration and Time Distribution

Each KATRIN measurement campaign comprises several hundred scans of the tritium β-decay spectrum, with each scan lasting approximately three hours. A single scan consists of up to forty discrete retarding energies, denoted $\{qU_i\}_{i=1}^{r}$, where r represents the total number of scan-steps. At each step i, the spectrometer is held at a fixed retarding potential $-U_i$ while electron counts are accumulated over a time interval t_i.

The measurement time distribution (MTD) is optimized to maximize sensitivity to the neutrino mass. This optimization accounts for statistical uncertainties, detector background rates, and practical constraints, leading to longer acquisition times near $qU \approx E_0 - \Delta$, where Δ is on the order of several electronvolts, and shorter times at lower retarding energies with higher electron flux. The retarding energy typically spans the interval $E_0 - 300\,\text{eV} \leq qU \leq E_0 + 135\,\text{eV}$. For sterile neutrino searches, only data collected above $E_0 - 40\,\text{eV}$ are used in the spectral analysis. Scan-steps below this threshold serve calibration and monitoring functions, while those above E_0 are employed to assess and characterize residual backgrounds.

3.2 Expected Electron Rate

To extract key physical parameters such as the active neutrino mass or quantities relevant to sterile neutrino scenarios, the experimentally measured electron counts $N_{\text{exp}}(qU)$ are compared to a theoretical prediction $N_{\text{model}}(qU, \boldsymbol{\theta})$. The parameter vector $\boldsymbol{\theta}$ includes both the physics parameters of interest (such as the squared neutrino mass m_ν^2, the mass of a hypothetical sterile state m_4^2, and its mixing amplitude $|U_{e4}|^2$) as well as nuisance parameters related to experimental systematics.

The model rate prediction $\dot{N}_{\text{model}}(qU, \boldsymbol{\theta})$ is constructed from four main components: the differential β-decay spectrum $\frac{\mathrm{d}\Gamma}{\mathrm{d}E}(E, \boldsymbol{\theta})$, the experimental response function $R(E, qU)$, signal normalization factor A, and the background rate $\dot{N}_{\text{bg}}(qU)$.

The expected integral electron rate is given by

$$\dot{N}_{\text{model}}(qU, \boldsymbol{\theta}) = A \cdot \int_{qU}^{E_0} \frac{\mathrm{d}\Gamma}{\mathrm{d}E}(E, \boldsymbol{\theta}) \cdot R(E, qU)\,\mathrm{d}E + \dot{N}_{\text{bg}}(qU) \tag{3.1}$$

The background contribution is modeled as

$$\dot{N}_{\text{bg}}(qU) = \dot{N}_{\text{bg}} + \dot{N}_{\text{spec, det}}(qU) + \dot{N}_{\text{RW}}(qU), \tag{3.2}$$

where $\dot{N}_{\text{spec, det}}(qU)$ represents the background originating from the spectrometer and detector, and $\dot{N}_{\text{RW}}(qU)$ accounts for contributions from decay of tritium adsorbed on the rear wall [19]. The constant term $\dot{N}_{\text{bg}}$ captures energy-independent background from residual instrumental and environmental sources. Further detail on the background model is provided in Section 3.7.

Each term in Equation 3.1 must be evaluated with care to enable precise extraction of neutrino mass parameters and sensitivity to sterile neutrino admixtures. The differential spectrum $\frac{\mathrm{d}\Gamma}{\mathrm{d}E}(E, \boldsymbol{\theta})$ accounts for molecular effects in tritium decay, including final-state distributions and Doppler broadening due to the motion of the parent molecule. These corrections are described in detail in Section 3.4.

The experimental response function $R(E, qU)$ incorporates the probability that an electron with energy E is transmitted through the MAC-E filter and reaches the detector. It includes inelastic scattering, magnetic collimation, and geometric acceptance effects. The transmission function $T(E, U)$, which defines the core of this response, is introduced in Section 3.5.1.

3.3 Signal Normalization Factor

The measured electron rate depends on several experimental parameters that determine the effective source activity and detection probability. These include the tritium decay rate, the accepted solid angle, and the detector efficiency.

- **Tritium Decay Rate** ($\dot{N}_{\text{T}}$): This is derived from the tritium decay constant $\lambda_{\text{T}} = 1.78 \times 10^{-9}\,\text{s}^{-1}$, the tritium purity ε_{T}, the column density ρd, and the effective magnetic cross-sectional area of the WGTS πr_{WGTS}^2. The factor of 2 accounts for the two tritium atoms in each T_2 molecule. The decay rate within the magnetic flux tube is given by:

$$\dot{N}_{\text{T}} = \lambda_{\text{T}} \cdot \varepsilon_{\text{T}} \cdot 2\rho d \cdot \pi r_{\text{WGTS}}^2. \tag{3.3}$$

- **Accepted Solid Angle** (Ω): Only electrons emitted downstream with initial pitch angles $\theta_{\text{src}} \leq \theta_{\text{max}}$ are transmitted to the focal-plane detector (FPD). The geometrical acceptance is given by:
$$\Omega = \frac{1 - \cos(\theta_{\text{max}})}{2}. \tag{3.4}$$
- **Detector Efficiency and Coverage** (ϵ): The FPD efficiency ϵ_{FPD} [67, 174], along with the number of active detector pixels N_{pixels}, determines the effective detection probability. The efficiency is reduced by factors such as inactive pixels or data selection criteria. The total effective detection efficiency is given by:
$$\epsilon = \epsilon_{\text{FPD}} \cdot \frac{N_{\text{pixels}}}{148}. \tag{3.5}$$

Combining these factors, the effective activity of the WGTS as seen by the detector is:

$$A_{\text{WGTS}} = \dot{N}_{\text{T}} \cdot \Omega \cdot \epsilon. \tag{3.6}$$

Systematic uncertainties in quantities such as the FPD efficiency (e.g., due to readout cuts) and the exact flux tube size can lead to deviations between A_{WGTS} and the true normalization. To account for such effects, a multiplicative signal correction factor Sig is introduced as a nuisance parameter in the spectral fit. The actual normalization is then written as $A = Sig \cdot A_{\text{WGTS}}$, as used in Equation 3.1. When all inputs are accurately determined, $Sig = 1$.

3.4 Differential β-decay spectrum

In Chapter 1, the differential β-decay spectrum was introduced within the simplified theoretical framework of atomic tritium. However, the KATRIN experiment utilizes molecular tritium (T_2) as the β-emitter, necessitating a more comprehensive treatment of the decay spectrum that accounts for molecular effects.

This section presents a detailed analytical description of the β-decay spectrum of gaseous molecular tritium, governed by the reaction

$$\text{T}_2 \rightarrow {}^3\text{HeT}^+ + \text{e}^- + \bar{\nu}_\text{e} + Q(\text{T}_2). \tag{3.7}$$

In contrast to atomic tritium, the decay of molecular tritium introduces corrections associated with differences in electronic binding energies and the excitation of the daughter molecular ion [199, 197]. The total decay energy $Q(\text{T}_2)$, defined as the binding energy difference between the initial and final molecular states, must be corrected accordingly. The spectral endpoint energy is then expressed as

$$E_0(\text{T}_2) = Q(\text{T}_2) - E_{\text{recoil}}, \tag{3.8}$$

where $Q(\text{T}_2) = (18592.071 \pm 0.022)$ eV, and the recoil energy of the daughter nucleus is approximately $E_{\text{recoil}} \approx 1.72$ eV [181].

Following the decay, the daughter ions are produced in a range of excited quantum states. These include rotational and vibrational excitations within the electronic ground state, as well as transitions to electronically excited and continuum states above the dissociation threshold. Theoretical studies have demonstrated that approximately 57% of all T_2 decays populate the electronically unexcited ground state of the daughter ion, broadened by rotational and vibrational excitations. The average excitation energy in this case is approximately 1.7 eV [131].

Each final state f, with probability P_f, shifts the effective spectral endpoint by an energy V_f. This leads to a superposition of spectra, each corresponding to a distinct final state, resulting in a smearing and a systematic downward shift of the observed spectrum near the endpoint. The differential decay rate that incorporates all accessible final states is given by:

$$\frac{\mathrm{d}\Gamma}{\mathrm{d}E} = \frac{G_F^2|V_{ud}|^2}{2\pi^3}|M_{\mathrm{nuc}}|^2 F(Z,E)\cdot p(E+m_{\mathrm{e}})\cdot\sum_f P_f(X)\cdot\epsilon_f\cdot\sqrt{\epsilon_f^2-m_\nu^2}\cdot\Theta(\epsilon_f-m_\nu), \tag{3.9}$$

where $\epsilon_f = E_0 - V_f - E$. Accurate modeling of the final-state distribution (FSD) is therefore critical for achieving sub-eV sensitivity in neutrino mass determination.

In addition to molecular tritium, the source gas in the KATRIN experiment contains trace amounts of other hydrogen isotopologues, such as DT and HT. Each isotopologue exhibits a unique molecular structure, which results in slightly different FSDs. Accordingly, separate calculations of the differential β-decay spectrum must be performed for each species. Close to the endpoint, these FSDs have been computed from first principles [224, 225, 79, 78], incorporating both bound and continuum excitations, as well as recoil kinematics.

The total theoretical spectrum is then obtained as a weighted sum of the isotopologue-specific spectra:

$$\frac{\mathrm{d}\Gamma}{\mathrm{d}E}(E,\boldsymbol{\theta}) = c_{\mathrm{T}_2}\cdot\left(\frac{\mathrm{d}\Gamma}{\mathrm{d}E}\right)_{\mathrm{T}_2} + \frac{1}{2}c_{\mathrm{DT}}\cdot\left(\frac{\mathrm{d}\Gamma}{\mathrm{d}E}\right)_{\mathrm{DT}} + \frac{1}{2}c_{\mathrm{HT}}\cdot\left(\frac{\mathrm{d}\Gamma}{\mathrm{d}E}\right)_{\mathrm{HT}}, \tag{3.10}$$

where $c_{\mathrm{T}_2}, c_{\mathrm{DT}}$, and c_{HT} denote the fractional abundances of the respective isotopologues. In the KATRIN experiment, this combined FSD is predominantly influenced by the T_2 component, which constitutes more than 98% of the source gas. The source composition is quantitatively characterized by the tritium purity, defined as

$$T = c_{\mathrm{T}_2} + \frac{1}{2}c_{\mathrm{DT}} + \frac{1}{2}c_{\mathrm{HT}}. \tag{3.11}$$

For the first two KATRIN data-taking campaigns (KNM1 and KNM2) [14, 13], the FSD was computed under the sudden approximation, which neglects the Coulomb interaction with the emitted β-electron [225, 79]. The dominant variation in the FSD during these campaigns was driven by changes in the source temperature. At thermal equilibrium, the population of rotational states in T_2 follows a Boltzmann distribution that depends explicitly on the source temperature. Since the probability P_f reflects the initial population of these rotational-vibrational states, it is inherently temperature-dependent.

The source temperature was increased from 30.05 K in KNM2 (the “30 K" mode) to 78.85 K by KNM5 (the “80 K" mode), thereby modifying the initial state distribution. An updated FSD model, used in the latest neutrino mass analysis [135], incorporates improvements in numerical convergence, refined external input parameters, and corrections to previous theoretical approximations [231]. This improved model, along with its associated uncertainties, was employed in the search for sterile neutrinos.

3.4.0.1 Additional Correction Factors

The calculation of the β-decay spectrum for neutrino mass analysis employs an approximate treatment of the relativistic three-body decay kinematics. In particular, it neglects the dependence of the daughter molecule’s recoil energy on the neutrino mass and the excitation energy spectrum of the final molecular states. This approximation results in a minor shift of the maximum electron energy by approximately 0.1 meV. However, this shift is effectively absorbed by constraining the spectral endpoint E_0 during the neutrino mass fit. As a result, the simplified two-body model remains valid within the narrow energy region relevant for both active and sterile neutrino mass analyses.

Beyond the final-state distribution, several additional correction factors must be considered. These arise from atomic, particle, and nuclear physics effects and are incorporated multiplicatively into the differential decay rate in Equation 3.10. These corrections are common to both active and sterile neutrino searches.

The dominant correction stems from radiative effects associated with the emission and exchange of virtual and real photons. These contributions are encapsulated in the radiative correction factor $G(E, E_0)$, which accounts for higher-order quantum electrodynamics (QED) effects. The correction exhibits a significant energy dependence, particularly near the spectral endpoint.

Other corrections, such as those related to weak magnetism, recoil-order terms, or finite nuclear size, have been evaluated and found to have negligible impact within the current experimental sensitivity. Consequently, they are omitted from the analysis. A comprehensive treatment of these subdominant correction terms can be found in [144, 251].

3.4.0.2 Doppler Broadening from Thermal Motion

The finite thermal motion of T_2 molecules in the gaseous source introduces an energy broadening in the emitted electron spectrum due to the Doppler effect. This motion follows a Maxwell-Boltzmann velocity distribution that depends on the source temperature [144]. As a result, the kinetic energy of the emitted electron is shifted depending on the direction of the molecular velocity at the moment of decay.

The resulting Doppler broadening is statistically described by a Gaussian distribution centered at the unshifted energy value. The Gaussian function $g(E - E_f)$, which models the energy spread due to this broadening, is given by

$$g(E - E_f) = \frac{1}{\sqrt{2\pi}\,\sigma_E} \exp\left(-\frac{(E - E_f - E_s)^2}{2\sigma_E^2}\right), \tag{3.12}$$

where E is the electron kinetic energy in the laboratory frame, E_f is the energy in the rest frame of the decaying molecule, and $E_s \approx v\sqrt{2E/m_\mathrm{e}}$ represents an energy shift due to the bulk motion of the tritium gas with velocity v. Here, m_e denotes the electron mass. The standard deviation σ_E, representing the width of the Doppler-broadened spectrum, is given by

$$\sigma_E = \sqrt{\frac{2Ek_BTm_\mathrm{e}}{m_{\mathrm{T}_2}}}, \tag{3.13}$$

where k_B is the Boltzmann constant, T is the absolute temperature of the tritium source, and m_{T_2} is the mass of the T_2 molecule.

To incorporate Doppler broadening, the Gaussian function $g(E - E_f)$ is convolved with the differential spectrum in Equation 3.10:

$$\left(g \otimes \frac{\mathrm{d}\Gamma}{\mathrm{d}E}\right)(E) = \int_{-\infty}^{\infty} g(E - E') \cdot \frac{\mathrm{d}\Gamma}{\mathrm{d}E}(E')\,\mathrm{d}E'. \tag{3.14}$$

However, due to the associativity of convolution, it is computationally advantageous to apply the Doppler broadening to the final-state distribution in advance.

3.5 Experimental Response function

The response function $R(E, qU)$ quantifies the probability that an electron emitted with kinetic energy E is transmitted through the spectrometer, which applies an electrostatic retarding potential U. This function encapsulates several key physical effects, including the transmission characteristics of the MAC-E filter (see Section 2.1.1), energy losses due to scattering processes in the source, and modifications arising from the magnetic field configuration and radiative losses.

A comprehensive analytical and numerical model of $R(E, qU)$ is essential for accurately describing the measured electron spectrum. Incorporating all relevant effects, the response function is expressed as an angular integration over the electron emission distribution and a convolution of the transmission function with the energy loss function:

$$R(E, qU) = \int_0^{E-qU} \frac{1}{1-\cos(\theta_{\max})} \int_0^{\theta_{\max}} \varepsilon_{\text{eff}}(\theta) \cdot \underbrace{T(E-\epsilon, \theta, qU)}_{\text{Transmission}} \cdot \sin(\theta) \times \sum_{s=0}^{\infty} \underbrace{P_s(\theta)}_{\text{Scattering Probability}} \cdot \underbrace{f_s(\epsilon)}_{\text{Energy Loss Function}} \, \mathrm{d}\theta \, \mathrm{d}\epsilon, \tag{3.15}$$

where ϵ denotes the total kinetic energy lost by an electron due to inelastic interactions in the source. The transmission function $T(E-\epsilon, \theta, qU)$ represents the probability that an electron with remaining energy $E-\epsilon$ and pitch angle θ is transmitted through the spectrometer. The function $\varepsilon_{\text{eff}}(\theta)$ accounts for the angular dependence of the detector efficiency.

The term $P_s(\theta)$ gives the probability that an electron undergoes exactly s scattering events while traversing the source, and $f_s(\epsilon)$ is the corresponding energy loss distribution for s-fold scattering. The maximum accepted pitch angle $\theta_{\max}$ is set by the magnetic mirror condition and is given by

$$\theta_{\max} = \arcsin\left(\sqrt{\frac{B_{\text{src}}}{B_{\text{pinch}}}}\right), \tag{3.16}$$

where B_{src} and B_{pinch} are the magnetic field strengths at the source and pinch magnet, respectively. Each component of the response function is described in further detail in the subsequent subsections.

3.5.1 Transmission Function and Magnetic Field Effects

The transmission function $T(E, \theta, qU)$ quantifies the probability that an electron with kinetic energy E and pitch angle θ overcomes the retarding potential qU of the MAC-E filter to reach the detector. This function is central to modeling the spectrometer's response and is derived considering the conservation of the magnetic moment and energy of the electrons as they traverse varying magnetic fields.

The transmission condition is given by:

$$T(E, \theta, qU) = \begin{cases} \frac{1}{1-\sqrt{1-\frac{B_{\text{src}}}{B_{\text{pinch}}}}} & \text{if } \theta \leq \theta_{\max} \text{ and } E\left(1-\sin^2(\theta) \cdot \frac{B_{\text{ana}}}{B_{\text{src}}} \cdot \frac{\gamma+1}{2}\right) - qU > 0, \\ 0 & \text{otherwise,} \end{cases} \tag{3.17}$$

where B_{src}, B_{ana}, and B_{pinch} denote the magnetic field strengths at the source, analyzing plane, and pinch magnet, respectively, and γ is the Lorentz factor of the electron. The maximum accepted pitch angle θ_{max} is determined by:

$$\theta_{\mathrm{max}} = \arcsin\left(\sqrt{\frac{B_{\mathrm{src}}}{B_{\mathrm{pinch}}}}\right). \tag{3.18}$$

3.5.1.1 Source Magnetic Field B_{src}

In earlier analyses, the source magnetic field B_{src} was determined through measurements and compared to magnetic field simulations, leading to a relative uncertainty of 1.7% [117]. A more accurate determination of the source magnetic field has been implemented using the magnetic mirror effect, employing electrons emitted from the rear wall as a probe. In this method, the magnetic field at the rear wall is set to 3.0 T and the central field in the WGTS is set to 2.5 T, while the magnetic field in all other regions of the beamline is kept below 2.5 T. The pinch magnet field is then gradually ramped from 2.3 T to 2.7 T. As long as $B_{\mathrm{pinch}} < B_{\mathrm{src}}$, electrons from the rear wall are magnetically reflected before reaching the detector. The onset of a decrease in the detected electron rate corresponds to the condition $B_{\mathrm{pinch}} = B_{\mathrm{src}}$, beyond which the pinch magnet becomes the limiting acceptance. Since the pinch field can be set with a precision better than 0.1%, this method enables a direct and accurate determination of the source magnetic field. This technique yields $B_{\mathrm{src}} = (2.513 \pm 0.003)\,\mathrm{T}$, with a conservative uncertainty of 0.25%. Additionally, detailed field simulations incorporating the axial variation over the 10 m-long WGTS provide an effective average value of $B_{\mathrm{src}} = 2.507\,\mathrm{T}$, which is used in the response function modeling [117, 48].

3.5.1.2 Analyzing Plane Magnetic Field B_{ana}

The magnetic field at the analyzing plane, B_{ana}, is critical as it defines the filter width of the spectrometer. However, B_{ana} cannot be directly measured within the active flux tube and is instead estimated from detailed simulations using the Kassiopeia software [97], supported by external reference measurements. High-precision magnetometers mounted near the main spectrometer provide additional data to constrain these simulations. Since no in-situ measurement of B_{ana} within the active flux tube was performed during early campaigns, the systematic uncertainty was estimated from deviations between simulated and external measurements.

3.5.1.3 Shifted Analyzing Plane (SAP) Configuration

To reduce the background rate in the main spectrometer, the Shifted Analyzing Plane (SAP) configuration was developed. In this setup, the analyzing plane is shifted closer to the detector, resulting in modified electric and magnetic field configurations that suppress the spectrometer background by approximately a factor of two [165].

To accurately characterize the electromagnetic field configuration in SAP, dedicated calibration measurements were performed using monoenergetic conversion electrons from gaseous $^{83\mathrm{m}}\mathrm{Kr}$. Scans of the narrow K-32 and $\mathrm{N}_{2,3}$-32 lines with the MAC-E filter enabled precise determination of the electric potential depression qU_{ana} and the magnetic field B_{ana}. These studies revealed an inhomogeneous field environment within the analyzing plane, with electric potential variations on the order of 3 V and magnetic field variations of approximately 0.2 mT [15].

3.5.2 Energy Loss in the Source

As β-electrons traverse the WGTS, they undergo energy loss primarily due to scattering with tritium molecules. These energy-loss processes significantly distort the observed β-spectrum and must be modeled with high accuracy. Beyond the WGTS, scattering effects become negligible due to the steep pressure gradient along the transport section, which rapidly reduces the gas density.

Accurate modeling of scattering involves two principal components:

3.5.2.1 Scattering Probability Function

The probability $P_s(\theta, E, z)$ that a β-electron scatters exactly s times before leaving the source depends on its initial kinetic energy E, starting position z along the beam axis, and pitch angle θ. As the electron propagates through the tritium gas, its likelihood of scattering is determined by the scattering cross section and the effective column density $\rho d(\theta, z)$ it experiences along its helical path.

The scattering cross section, with units of m^2, quantifies the probability of a scattering event between an electron and a T_2 molecule. Two types of scattering cross sections are distinguished for electrons with energies near the endpoint ($\sim 18.6\,\mathrm{keV}$):

- **Elastic scattering**, which involves a change in the electron's direction without significant energy loss. Elastic events conserve the internal molecular state and have cross sections roughly an order of magnitude smaller than inelastic ones [98, 162]. The typical energy loss is on the order of $2.3\,\mathrm{meV}$ [150], which is negligible for the experiment. Consequently, elastic scattering is not included in the response function.
- **Inelastic scattering**, which excites or ionizes the tritium molecule, leading to measurable energy losses. The corresponding cross section is approximately $\sigma_{\mathrm{inel}}(18.6\,\mathrm{keV}) = 3.64 \times 10^{-22}\,\mathrm{m}^2$ [127, 163, 162].

The effective column density $\rho d(\theta, z)$, defined as the integrated tritium density along the electron's path from position z to the end of the source, increases with pitch angle due to the longer helical path. It is given by:

$$\rho d(\theta, z) = \frac{1}{\cos(\theta)} \int_z^{L/2} \rho(z')\,\mathrm{d}z', \tag{3.19}$$

where $\rho(z')$ is the local gas density and L is the total length of the WGTS.

The local gas density is obtained from dedicated calibration measurements using an electron gun (e-gun) [44, 125]. In these calibrations, monoenergetic electrons with a fixed energy and a known pitch angle traverse the source and lose energy through inelastic scattering. By comparing the measured energy spectrum to theoretical predictions of the inelastic cross section $\sigma_{\mathrm{inel}}(E)$, the absolute value of ρd can be inferred [149, 14].

Because electrons scatter discretely and infrequently, the number of inelastic scattering events follows a Poisson distribution. The probability for exactly s inelastic scatterings is:

$$P_s(\theta, E, z) = \frac{\left(\rho d(\theta, z) \cdot \sigma_{\mathrm{inel}}(E)\right)^s}{s!} \cdot e^{-\rho d(\theta, z) \cdot \sigma_{\mathrm{inel}}(E)}. \tag{3.20}$$

The corresponding mean number of scatterings is:

$$\mu(\theta, E, z) = \rho d(\theta, z) \cdot \sigma_{\text{inel}}(E). \tag{3.21}$$

Thus, the Poisson expression may be written compactly as:

$$P_s(\theta, E, z) = \frac{\mu^s}{s!} \cdot e^{-\mu}. \tag{3.22}$$

For an isotropic source, the scattering probability averaged over all pitch angles up to the spectrometer acceptance angle θ_{max} is:

$$\langle P_s(E, z)\rangle = \frac{1}{1 - \cos(\theta_{\text{max}})} \int_0^{\theta_{\text{max}}} P_s(\theta, E, z) \cdot \sin\theta \, \mathrm{d}\theta. \tag{3.23}$$

This angular averaging accounts for the increased scattering probability of electrons at larger pitch angles due to their longer effective path lengths.

Alternatively, the position-averaged scattering probability $P_s(\theta, E)$ can be obtained by averaging $P_s(\theta, E, z)$ over the starting positions z along the beam axis:

$$P_s(\theta, E) = \frac{1}{L} \int_{-L/2}^{L/2} P_s(\theta, E, z) \, \mathrm{d}z. \tag{3.24}$$

This position averaging reflects the uniform longitudinal distribution of emission points within the source which is justified by the combination of symmetric gas injection, precise temperature control, continuous monitoring, and detailed simulations [214].

3.5.2.2 Energy Loss Function

The energy loss function $f(\epsilon)$ describes the probability density for an electron to lose energy ϵ in a single inelastic scattering event. The KATRIN energy-loss model is a semi-empirical construction combining two distinct components:

- A sum of three Gaussian functions models the excitation region between 11 eV and 15 eV, centered around characteristic excitation energies near 12.6 eV [98].
- A relativistic binary-encounter-dipole (BED) function, which models the ionization continuum for energy losses above the ionization threshold $E_i = 15.5\,\text{eV}$ [143].

To ensure a continuous transition between excitation and ionization regions, the BED function is normalized at the ionization threshold $\epsilon = E_i$ to match the Gaussian model. The resulting energy-loss function is given by:

$$f(\epsilon) = \begin{cases} \sum\limits_{j=1}^{3} a_j \exp\left(-\dfrac{(\epsilon - m_j)^2}{2\sigma_j^2}\right), & \epsilon \leq E_i, \\ \dfrac{f(E_i)}{f_{\text{BED}}(E_i)} \cdot f_{\text{BED}}(\epsilon), & \epsilon > E_i, \end{cases}$$

where m_j, a_j, and σ_j are the mean, amplitude, and width of the three Gaussian components. The parameters are calibrated using dedicated in-situ measurements with monoenergetic, angular-selective electrons from a photoelectron source [214, 223, 229, 232, 219].

For multiple scattering events, the total energy-loss distribution $f_s(\epsilon)$ is obtained via convolution of the single-scattering loss function $f(\epsilon)$ with itself s times:

$$f_0(\epsilon) = \delta(0), \tag{3.25}$$

$$f_1(\epsilon) = f(\epsilon), \tag{3.26}$$

$$f_s(\epsilon) = \underbrace{f * f * \cdots * f}_{s \text{ times}}(\epsilon), \tag{3.27}$$

where $\delta(0)$ is the Dirac delta function representing zero energy loss.

Because the energy range of interest is confined to a narrow window, typically a few tens of eV below the endpoint, and because scattering angles are small due to the high kinetic energy and forward-directed motion of electrons, it is a valid approximation to treat both $f(\epsilon)$ and $P_s(\theta)$ as independent of the initial electron energy E. The approximation holds for both the neutrino mass measurement and eV-scale sterile neutrino searches. The full response function, introduced in Equation 3.15, incorporates the energy loss distributions $f_s(\epsilon)$, each weighted by the respective scattering probabilities $P_s(\theta)$.

3.5.3 Non-isotropic Transmission

Non-isotropic transmission arises when the angular distribution of electrons emitted from the source is modified by scattering events. While the initial emission from the source is assumed to be isotropic, each scattering alters the electron's pitch angle, resulting in a redistribution of emission directions. After scattering, the angular distribution becomes non-isotropic, meaning the likelihood of observing an electron at a given angle deviates from the uniform case. This deviation directly affects the transmission function, which governs the probability that an electron will pass through the spectrometer and reach the detector.

Although scattering angles are generally small due to the high kinetic energy of electrons and the forward-peaked nature of inelastic scattering with low momentum transfer, scattering events still impart measurable angular deviations that accumulate over multiple interactions [214, 98]. In particular, even single scatterings can lead to significant modifications of the angular distribution when integrated over the electron ensemble. Therefore, the transmission function must be adjusted to reflect this angular redistribution, especially for electrons that scatter once and still contribute non-negligibly to the spectral region of interest.

For electrons undergoing exactly s scatterings, the angular distribution becomes

$$\Omega_s(\theta) = \frac{P_s(\theta, E, z) \cdot \sin\theta}{\int_0^{\theta_{\max}} P_s(\theta', E, z) \cdot \sin\theta' \, \mathrm{d}\theta'}, \tag{3.28}$$

where $P_s(\theta, E, z)$ is the pitch-angle-dependent scattering probability as defined in Equation 3.20, and $\theta_{\max}$ is the acceptance angle of the spectrometer.

Because the spectral impact of higher-order scatterings ($s \geq 2$) diminishes due to their broader and smoother energy distributions, the correction in is typically restricted to the $s = 1$ case [214]. This approximation balances physical accuracy with computational efficiency in the modeling of the full response function as the updated equation:

$$\begin{aligned}
R(E, qU) = \int_0^{E-qU} & \frac{1}{1-\cos(\theta_{\max})} \int_0^{\theta_{\max}} \varepsilon_{\text{eff}}(\theta) \cdot T(E-\epsilon, \theta, qU) \cdot \sin(\theta) \cdot P_0(\theta) \, \mathrm{d}\theta \\
& + \int_0^{\theta_{\max}} \varepsilon_{\text{eff}}(\theta) \cdot T(E-\epsilon, \theta, qU) \cdot \Omega_1(\theta) \, \mathrm{d}\theta \\
& + \sum_{s=2}^{\infty} \frac{1}{1-\cos(\theta_{\max})} \int_0^{\theta_{\max}} \varepsilon_{\text{eff}}(\theta) \cdot T(E-\epsilon, \theta, qU) \cdot \sin(\theta) \cdot P_s(\theta) \, \mathrm{d}\theta f_s(\epsilon) \, \mathrm{d}\epsilon.
\end{aligned} \tag{3.29}$$

A comparison of the response and transmission functions under different scattering assumptions is presented in Figure 3.1. Electrons emitted with pitch angles $0 < \theta \leq \theta_{\max}$ require surplus energy $E - qU$ to overcome the electrostatic retarding potential of the MAC-E filter. As the surplus energy increases, electrons that have undergone energy loss due to scattering in the source may still retain sufficient energy to be transmitted, thereby increasing the overall transmission probability.

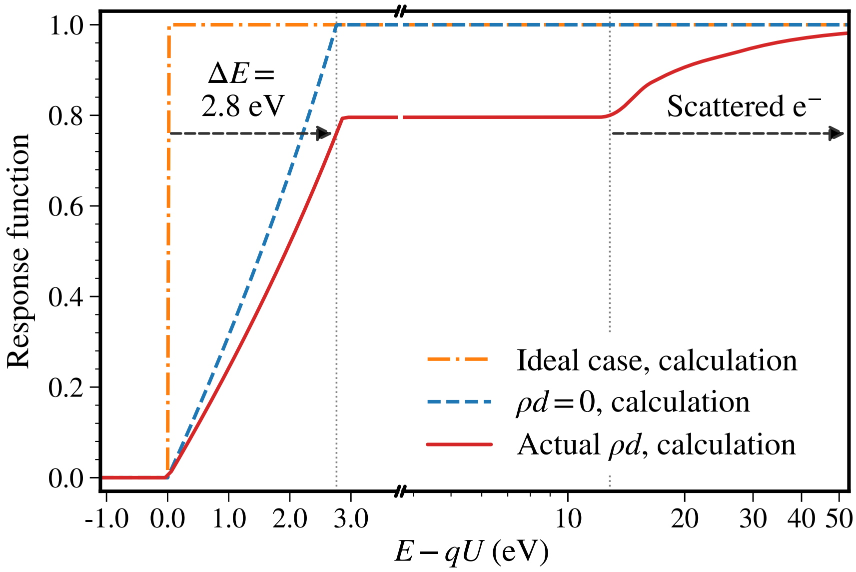

Figure 3.1: Comparison of response and transmission functions under varying scattering assumptions. The dash-dotted orange line represents the idealized response function assuming infinitesimal filter width and no scattering. The dashed blue line shows the actual transmission function of the MAC-E filter without source scattering. The solid red line includes the effects of source scattering. Electrons emitted with pitch angles $0 < \theta \leq \theta_{\max}$ require surplus energy $E - qU$ to overcome the retarding potential. At higher surplus energies, electrons that have lost energy due to scattering in the source can still be transmitted, resulting in an increased overall transmission probability. Image source [14].

3.5.4 Energy Loss Due to Synchrotron Radiation

For accurate modeling of the response function, energy losses due to synchrotron radiation [208], incurred by electrons traversing helical trajectories in the strong magnetic fields of the WGTS and transport sections, are treated as analytical corrections to the electron energy and incorporated into the effective transmission probability. While the pitch-angle dependence of the path length can subtly affect the scattering probabilities and, consequently, the shape of the response function, this effect is subdominant relative to the systematic uncertainties in the source potential and is therefore neglected in this analysis [14].

The energy loss due to synchrotron radiation, denoted E_{sync}, depends on the magnetic field strength B, the electron kinetic energy E (specifically its transverse component $E_{\perp} = E \cdot \sin^2(\theta)$), and the propagation time:

$$t = \frac{l}{v_{\text{e}} \cos(\theta)}, \tag{3.30}$$

where l is the path length and v_e is the electron velocity [112]. The synchrotron energy loss is approximated by:

$$E_{\text{sync}}(E, B, \theta) = \frac{\mu_0}{3\pi m_{\text{e}}^3} \cdot B^2 \cdot E \cdot \sin^2(\theta) \cdot \frac{\gamma + 1}{2} \cdot \frac{l}{v_e \cos(\theta)}, \tag{3.31}$$

where μ_0 is the vacuum permeability, m_e is the electron mass, and γ is the Lorentz factor.

Electrons emitted at larger pitch angles θ_src have higher transverse energies $E_\perp$, leading to greater synchrotron losses. Moreover, these electrons experience longer effective path lengths within the magnetic field, further enhancing radiation losses.

The total synchrotron loss is composed of contributions from both the source and transport sections, characterized by magnetic field strengths B_src and B_t, respectively:

$$E_\mathrm{sync}(E, \theta_\mathrm{src}) = E_\mathrm{sync}(E, B_\mathrm{src}, \theta_\mathrm{src}) + E_\mathrm{sync}(E, B_t, \theta_t), \tag{3.32}$$

where the pitch angle in the transport section, θ_t, is related to the initial angle θ_src via adiabatic invariance:

$$\theta_t = \theta_\mathrm{src} \cdot \sqrt{\frac{B_t}{B_\mathrm{src}}}. \tag{3.33}$$

Synchrotron losses of β-electrons in these strong magnetic fields typically reach magnitudes on the order of $\mathcal{O}(100\,\mathrm{meV})$, reducing the effective surplus energy of electrons and introducing a pitch-angle dependence. These losses are incorporated into the response model either by numerically modifying the effective maximum acceptance angle θ_max or by applying an analytical correction to the transmission function [144, 14].

3.5.5 Angular Detection Efficiency

The angular-dependent detection efficiency of the focal-plane detector (FPD) influences the response function Equation 3.15. In the detector region, the magnetic field strength $B_\mathrm{FPD} \approx B_\mathrm{src} = 2.5\,\mathrm{T}$ is significantly higher than in the analyzing plane. As a result, electrons become de-collimated when exiting the spectrometer, particularly those with large pitch angles, which have a reduced probability of reaching the detector's active region.

This angular dependence of the detection efficiency is modeled by a second-order polynomial:

$$\varepsilon_\mathrm{eff}(\theta) = c_0 + c_1 \cdot \theta + c_2 \cdot \theta^2, \tag{3.34}$$

where θ is the pitch angle and the coefficients c_0, c_1, and c_2 are determined from detailed simulations. This efficiency correction is included in the response function formulation (see Equation 3.15) to improve the fidelity of the spectral model [135, 144].

3.6 Plasma Effects and Source Inhomogeneities

Continuous tritium injection and magnetic confinement in the WGTS result in a low-density plasma of electrons and tritium ions, primarily formed via β-decay and secondary interactions. The radial confinement by the magnetic field and longitudinal electrostatic boundary conditions, particularly the rear wall potential U_RW, govern the plasma potential. Differences in work function between the gold-coated rear wall and the stainless steel beam tube, coupled with incomplete charge equilibration, generate spatial potential inhomogeneities [7].

Three main classes of such inhomogeneities affect the measured β-spectrum:

- **Longitudinal potential broadening:** Axial variations in the plasma potential cause energy smearing, modeled by a Gaussian width parameter σ_0. This broadening adds in quadrature to Doppler effects Section 3.4.0.2:

  $$\sigma^2_\mathrm{total} = \sigma^2_0 + \sigma^2_\mathrm{add}, \tag{3.35}$$

  where σ_add captures unresolved temporal variations.

- **Longitudinal asymmetry:** Longitudinal asymmetries in the plasma potential along the z-axis of the WGTS can induce systematic offsets in the average potential energy between regions that predominantly contribute unscattered electrons (typically downstream) and those contributing scattered electrons (typically upstream). This spatial variation is characterized by the parameter Δ_{10}, defined as the mean potential difference between singly scattered ($i = 1$) and unscattered ($i = 0$) electrons. Although higher-order scattering channels are also affected by such asymmetries, their contributions are subdominant and treated accordingly [170].

  A direct determination of Δ_{10} is not employed in the present analysis due to uncertainties in the energy loss function, which has been experimentally validated for 18.6 keV electrons but not for higher-energy calibration lines. Instead, a conservative theoretical bound is imposed by relating Δ_{10} to the longitudinal broadening parameter σ_0, which quantifies the standard deviation of the plasma potential distribution. This yields the inequality:

  $$|\Delta_{10}| \leq \kappa_1 \sigma_0, \tag{3.36}$$

  where κ_1 is a geometry- and density-dependent coefficient that encapsulates the spatial overlap between the emission regions of unscattered and singly scattered electrons. This bound ensures that any potential-induced energy shifts remain within physically motivated limits [170].

  Experimental constraints on σ_0 and, indirectly, on Δ_{10} are obtained using monoenergetic electrons from $^{83\mathrm{m}}$Kr, particularly the narrow $N_{2,3}$-32 lines. Their centroids and line shapes serve as sensitive probes of the plasma potential profile, assuming minimal perturbation from the krypton admixture.

- **Radial inhomogeneities:** Differences in work function between the rear wall and beam tube result in radial potential variations $\langle U_{\mathrm{src}} \rangle_z(r)$. These are minimized by tuning U_{RW} to an optimal value $U_{\mathrm{RW,opt}}$, and any residual inhomogeneity is absorbed in a radially dependent endpoint $E_0(r)$ [154, 7].

- **Monitoring of the Plasma Potential:** The plasma potential is actively monitored using the IU scan procedure, which modulates U_{RW} and identifies the condition of zero net current to infer the optimal bias. Temporal drifts are tracked via variations in the fitted endpoint energy E_0, with any deviations treated as additional broadening [146, 95, 135].

3.7 Comprehensive Background Model

The full KATRIN background model, as defined in Equation 3.2, consists of four principal contributions:

- A constant, energy-independent background rate $\dot{N}_{\mathrm{bg}}$, originating from ambient radioactivity, cosmic rays, and residual detector noise.

- A retarding-energy-dependent component $\dot{N}_{\mathrm{bg}}^{\mathrm{slope}}(qU)$, capturing weak voltage-dependent variations in the background rate, potentially due to slow detector drifts or energy-dependent electron trapping efficiencies.

- A Penning trap-induced background rate $\langle \dot{N}_{\mathrm{bg}}^{\mathrm{Penning}}(qU) \rangle$, which does not explicitly depend on qU, but varies indirectly with scan step durations at different retarding potentials.

- A spatially and energy-dependent contribution from the rear wall $\dot{N}_{\mathrm{RW}}(qU)$, associated with electrons scattered or emitted from the rear-side of the source section.

These components collectively describe the expected total background rate entering the integral β-spectrum model:

$$\dot{N}_{\mathrm{bg}}(qU) = \dot{N}_{\mathrm{bg}} + \dot{N}_{\mathrm{bg}}^{\mathrm{slope}}(qU) + \langle \dot{N}_{\mathrm{bg}}^{\mathrm{Penning}}(qU) \rangle + \dot{N}_{\mathrm{RW}}(qU). \tag{3.37}$$

The Penning-induced background does not depend explicitly on the retarding potential, but its influence varies indirectly due to the scan-step-duration-dependent exposure at each qU setting. Together, these background components are incorporated into the spectral analysis as either fixed constraints or fit parameters with associated systematic uncertainties.

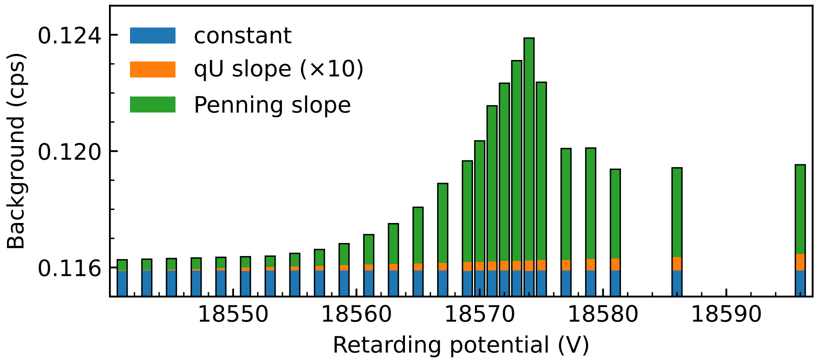

Figure 3.2: Decomposition of the total background rate into its dominant physical components. The energy-independent baseline (blue) is constant across all retarding energies and reflects contributions from ambient sources and detector noise. The retarding-energy-dependent term (orange), scaled by a factor of 10 for visibility, captures slow, nearly linear drifts with the applied potential. The localized Penning trap background (green) appears predominantly between 18.565 keV and 18.575 keV, arising from ionization processes within electromagnetic traps. All components are constrained through dedicated calibration and background studies. Image adapted from [135].

3.7.1 Energy Independent Background

The steady-state background rate $\dot{N}_{\mathrm{bg}}$ is dominated by neutral Rydberg atoms produced via radioactive α-decays of ^{210}Po in the spectrometer walls [27, 16]. These highly excited but electrically neutral atoms (e.g., hydrogen or oxygen species) can traverse the inner electrode system and enter the active flux-tube region. Once inside, black-body radiation ionizes the Rydberg atoms, yielding low-energy electrons. If such electrons are emitted downstream of the analyzing plane, they are accelerated toward the focal-plane detector (FPD); owing to their low initial energy, they can mimic signal electrons and thus contribute to the background [16].

The second-largest contribution to $\dot{N}_{\mathrm{bg}}$ arises from α-decays of radon isotopes (e.g., ^{220}Rn, ^{219}Rn) emerging from spectrometer surfaces or the NEG system, escaping the cooled baffles, and decaying within the spectrometer volume [92, 94]. Each α-decay produces high-energy electrons via atomic relaxation, shake-off, and internal conversion. These electrons often become magnetically trapped due to their large transverse energies. Through collisions with residual gas molecules, trapped electrons generate on the order of 10^2 secondary electrons per primary decay. Like the Rydberg-origin electrons, these secondaries drift toward the FPD and further elevate $\dot{N}_{\mathrm{bg}}$ [92]. Moreover, these trapped-electron cascades induce non-Poissonian fluctuations, which can be quantified by fitting the measured background distribution with both Gaussian and Poisson models. The resulting over-dispersion,

$$g_{\mathrm{NP}} = \frac{\sigma^2_{\mathrm{Gaussian}}}{\sigma^2_{\mathrm{Poisson}}} - 1,$$

can reach values up to 0.1 in Nominal Analyzing Plane (NAP) campaigns. This additional variance is incorporated as a systematic uncertainty or, equivalently, as an inflated statistical uncertainty on $\dot{N}_{\mathrm{bg}}$ for NAP data. In the Shifted Analyzing Plane (SAP) configuration, the altered magnetic trapping conditions mitigate this over-dispersion, and the effect is negligible [165].

In addition to spectrometer-induced backgrounds, the FPD contributes an intrinsic background that depends on the chosen region of interest (ROI) in the detector spectrum [23]. Typical values range from approximately 13 mcps (for a narrow ROI) up to 21 mcps (for a wider ROI). In the spectral analysis, $\dot{N}_{\mathrm{bg}}$ is constrained by measurements above the endpoint and treated as a free nuisance parameter in the fit.

3.7.2 Retarding Energy Dependent Background

A potential dependence of the background rate $\dot{N}^{\mathrm{slope}}_{\mathrm{bg}}(qU)$ on the retarding energy qU is included in the background model. Such a dependence may arise from energy-dependent transmission and detection probabilities of background electrons. At lower retarding potentials ($qU < 10\,\mathrm{keV}$), a gradual variation of the background rate with high voltage has been observed [92], which tends to flatten at higher qU. Nonetheless, because the overall background level is of order 10^2 mcps, a small voltage-dependent component cannot be excluded with high confidence. Physically, this dependence may be driven by the energy-dependent trapping probability of electrons originating from radon decays, whose surplus-energy distribution affects their storage efficiency in the magnetic field.

To accommodate this possibility, a linear term with slope s_{qU} is added to the background rate:

$$\dot{N}^{\mathrm{slope}}_{\mathrm{bg}}(qU) = s_{qU}\,(qU - qU_{\mathrm{ref}}), \tag{3.38}$$

where the reference potential $qU_{\mathrm{ref}} = 18\,588.7\,\mathrm{eV}$ is chosen fifteen electronvolts above the tritium endpoint to avoid bias in the signal region. Centering the linear model at this pivot simplifies interpretation of the background normalization, while the slope s_{qU} is determined from dedicated calibration scans.

In both NAP and SAP configurations, calibration scans over $17.6\,\mathrm{keV} < qU < 18.6\,\mathrm{keV}$ [135] yield

$$s_{qU} = \begin{cases} (0.9 \pm 3.2)\,\mathrm{mcps\,keV^{-1}}, & \mathrm{NAP}, \\ (1.1 \pm 0.7)\,\mathrm{mcps\,keV^{-1}}, & \mathrm{SAP}. \end{cases}$$

These uncertainties are reduced relative to earlier data releases [13, 14] owing to additional calibration scans. The slope component is treated as a systematic uncertainty in the sterile neutrino analysis.

3.7.3 Penning Trap-Induced Background

The Penning trap-induced background originates from the accumulation of low-energy electrons in the region between the pre-spectrometer and main spectrometer, where strong magnetic fields and opposing retarding potentials create an effective electromagnetic trap [16]. Electrons that traverse this region and lose energy via scattering with residual gas molecules or through cyclotron radiation can become magnetically and electrostatically trapped. These trapped electrons initiate ionization cascades, generating both secondary electrons and positive ions. While the positive ions are accelerated toward the spectrometer surfaces and largely removed, the secondary electrons remain confined within the trap, gradually enhancing the background rate observed in the main spectrometer.

This background increases progressively over the duration of each scan-step, eventually reaching an equilibrium state. The time scale for achieving equilibrium is governed by the internal pressure and residual gas composition within the spectrometer volume [135].

To mitigate the buildup of trapped particles, a so-called Penning wiper is activated between scan-steps. This procedure resets the trap by applying a short perturbation to the electromagnetic field configuration, thereby removing accumulated charges and restoring the background rate to baseline. The result is a scan-step-duration-dependent background rate that increases with measurement time during each scan step.

Initially, this time-dependent behavior was modeled with a simple linear form [13]:

$$\dot{N}_{\mathrm{bg}}^{\mathrm{Penning}}(qU_i, t) = p_1 \cdot t, \tag{3.39}$$

where p_1 is the linear background increase rate, and t is the elapsed time within the i^{th} scan-step.

The corresponding time-averaged rate over the full scan duration t_i is given by:

$$\langle \dot{N}_{\mathrm{bg}}^{\mathrm{Penning}} \rangle (qU_i) = \frac{1}{t_i} \int_0^{t_i} \dot{N}_{\mathrm{bg}}^{\mathrm{Penning}}(qU_i, t)\, \mathrm{d}t = \frac{p_1 t_i}{2}. \tag{3.40}$$

Subsequent calibration studies revealed deviations from the linear model and motivated the introduction of a more accurate quadratic form [135]:

$$\dot{N}_{\mathrm{bg}}^{\mathrm{Penning}}(qU_i, t) = p_0(qU_i) + p_1 \cdot t + p_2 \cdot t^2, \tag{3.41}$$

where p_0 is a constant offset specific to each retarding potential, and p_1, p_2 are fit parameters describing the temporal growth of the background rate.

Dedicated measurements have shown that p_1 and p_2 are strongly anti-correlated [93][1], allowing the model to be simplified:

$$\dot{N}_{\mathrm{bg}}^{\mathrm{Penning}}(qU_i, t) = p_0(qU_i) + p_2 \cdot t^2. \tag{3.42}$$

The corresponding mean Penning background rate over a scan duration t_i becomes:

$$\begin{aligned} \langle \dot{N}_{\mathrm{bg}}^{\mathrm{Penning}} \rangle (qU_i) &= \frac{1}{t_i} \int_0^{t_i} \left[p_0(qU_i) + p_2 t^2 \right] \mathrm{d}t \\ &= p_0(qU_i) + \frac{p_2 t_i^2}{3}. \end{aligned} \tag{3.43}$$

The coefficient p_2 is determined from dedicated calibration scans and applied to estimate the time-dependent background contribution for each scan-step.

Failure to properly model this Penning trap-induced background, particularly its nonlinear time dependence, can introduce significant systematic errors, especially in scan configurations with long step durations. Therefore, careful characterization and correction of this effect are essential to the precision and reliability of the spectral analysis.

---

[1] Access to KATRIN internal reports provided on request.

3.7.4 Rear Wall-Induced Background

The rear wall (RW) of the KATRIN beamline is a 145 mm diameter, gold-coated stainless steel disc with a 5 mm central aperture. It defines the upstream electrostatic boundary of the Windowless Gaseous Tritium Source (WGTS). As discussed in Section 2.3.1, it lies along the beam axis and intersects the magnetic flux tube. It is exposed to both neutral tritium molecules and positively charged cluster ions (e.g., T^+, T_3^+) [17], which impinge on the gold surface, leading to adsorption and implantation of tritium atoms. These surface-bound tritium atoms subsequently undergo β decay, generating electrons that follow magnetic field lines toward the Focal Plane Detector (FPD), contributing a distinct background component.

The presence of this RW-induced β activity was confirmed during tritium-free maintenance campaigns in which the WGTS pressure was reduced to less than 10^{-5} of its nominal value. Measurements at a fixed retarding potential ($U_{\mathrm{ret}} = 14$ kV) revealed a residual count rate that scaled with the integrated T_2 throughput. The time evolution of this background—initially exponential, then transitioning to linear growth—is consistent with a saturation of available adsorption sites followed by gradual layer accumulation. These observations confirmed a persistent RW-originated background independent of the gaseous tritium source.

Rear wall activity arises from several processes [19]:

- Adsorption of tritiated water (HTO), which exhibits strong surface binding on metals, including gold.
- Formation of tritiated amorphous carbon (aC:T) through decomposition of hydrocarbons under β irradiation in tritium-rich environments.
- Isotope exchange with pre-existing hydrogenated carbon layers (aC:H).

These mechanisms produce a secondary β-electron spectrum with notable differences from gaseous T_2 decay, including altered final-state distributions, modified electron scattering behavior, and surface-related energy losses. To mitigate RW activity, several in-situ cleaning techniques have been evaluated [19, 17]:

- Extended vacuum pumping,
- Heating up to 165 °C,
- Flushing with N_2, D_2, or humidified air,
- Ultraviolet/ozone (UV/O_3) treatment.

Among these, UV/O_3 exposure proved most effective, achieving a decontamination factor of about 1300 over one week. However, RW activity reaccumulates during normal operation, necessitating ongoing monitoring.

Real-time monitoring of RW activity is achieved through Beta-Induced X-ray Spectrometry (BIXS), which detects X-rays produced when β-electrons strike the RW surface, and via direct electron detection at high retarding voltages ($U_{\mathrm{ret}} \approx 14$ kV), isolating high-energy RW-originating electrons. Since these electrons originate from the far upstream end of the source, they must traverse the full 10-meter WGTS column, increasing their likelihood of scattering. This enhanced scattering is explicitly modeled in the response function (see Equation 3.29) to account for energy losses along the propagation path.

The rear wall β-spectrum is modeled analogously to the gaseous tritium decay spectrum, with key modifications:

- The final-state distribution (FSD) is altered due to unknown molecular configurations of surface-bound tritium.
- The electron energy loss and backscattering models are adapted for surface-origin emission.
- Work function variations can shift the effective endpoint energy, denoted $E_{0,\mathrm{rw}}$.
- A normalization scaling factor $\mathrm{RW}_{\mathrm{Sig}}$ is introduced for the RW spectral amplitude.

The resulting spectrum may exhibit a shifted endpoint, broadened spectral features, and pronounced low-energy tails, all of which can influence the shape of the observed integrated spectrum. A detailed analysis of rear-wall electron backscattering is presented in Chapter 6.

3.8 Focal Plane Detector Efficiency

To accurately model the measured electron count rates in KATRIN, the theoretical prediction given must be corrected for detector effects. This is done by applying the detector efficiency function $\epsilon_{\mathrm{FPD}}(qU)$ in the model rate Equation 3.1. The detector efficiency term is decomposed into the following components:

$$\epsilon_{\mathrm{FPD}}(qU) = \epsilon_c \cdot \epsilon_{\mathrm{ROI}}(qU) \cdot \epsilon_{\mathrm{pu}}(\dot{N}) \cdot \epsilon_{\mathrm{bs}}(qU), \tag{3.44}$$

where:

- ϵ_c is the constant, energy-independent baseline detection efficiency of the focal plane detector (FPD), taken to be 95% based on calibration studies [23].
- $\epsilon_{\mathrm{ROI}}(qU)$ accounts for the energy-dependent efficiency arising from the Region of Interest (ROI) cut.
- $\epsilon_{\mathrm{pu}}(\dot{N})$ is the rate-dependent correction for pile-up effects.
- $\epsilon_{\mathrm{bs}}(qU)$ models losses due to electron backscattering from the detector surface.

In addition, an angular-dependent detection efficiency correction, $\varepsilon_{\mathrm{eff}}(\boldsymbol{\theta})$, is included directly in the response function, as detailed in Section 3.5.5. Each efficiency component is described in the following subsections.

3.8.1 Region of Interest (ROI) Cut

To optimize signal-to-background discrimination, a Region of Interest (ROI) cut is applied to the energy deposited in the FPD. Electrons are post-accelerated by 10 keV, resulting in a typical kinetic energy of 28 keV at the detector. The FPD has an energy resolution of approximately 3 keV (FWHM), which permits precise selection of electron energies within the ROI [135].

The ROI is designed to exclude low-energy noise and pile-up distortions. Two ROI schemes are employed: a wide range from 14–32 keV, and a narrower range from 22–34 keV, depending on the specific analysis goal [67]. The ROI is held fixed across all scan steps; however, since the electron spectrum shifts with the retarding potential qU_i, the fraction of detected electrons within the ROI varies with energy.

To model this variation, the ROI efficiency is defined as:

$$\epsilon_{\text{ROI}}(qU_i) = \frac{N_{qU_i}[\text{ROI}]}{N_{E_0}[\text{ROI}]},$$

where $N_{qU_i}[\text{ROI}]$ and $N_{E_0}[\text{ROI}]$ are the number of counts within the ROI at retarding energy qU_i and at the endpoint E_0, respectively. Since measurements at the endpoint are statistically limited, a fixed reference point 300 eV below E_0 is used to determine the normalization.

To further account for the spectral shift, a shifted ROI is used:

$$\epsilon_{\text{ROI}}(qU_i) = \frac{N[\text{ROI} + \Delta E]}{N[\text{ROI}]}, \quad \text{where} \quad \Delta E = E_0 - qU_i.$$

The resulting ROI efficiency correction exhibits a linear energy dependence with a slope of $(0.700 \pm 0.035)\,\%\,\text{keV}^{-1}$, which is applied across all scan-steps [214].

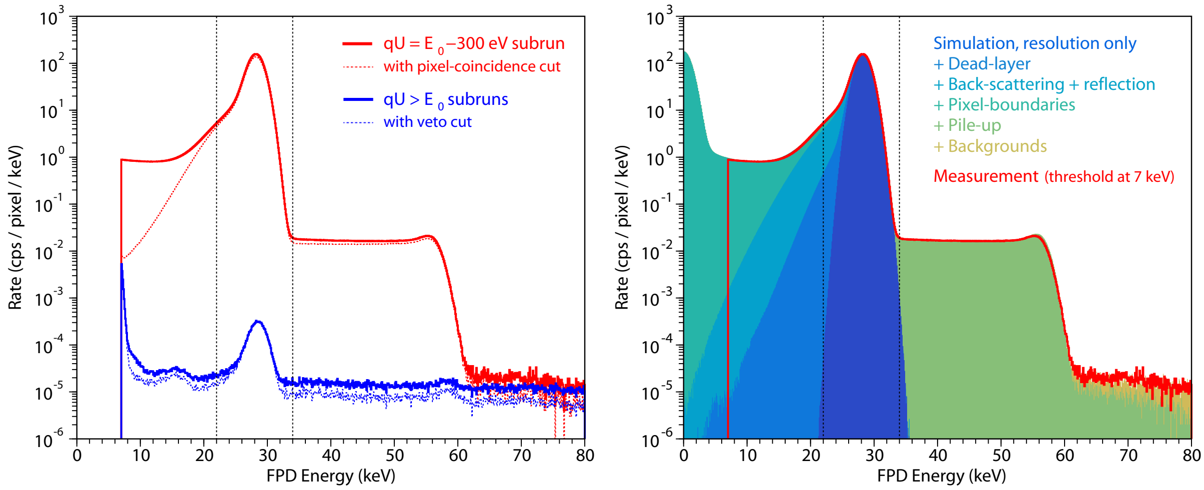

Figure 3.3: Differential energy spectrum measured at the FPD (solid red line) compared to simulation (shaded bands), including effects from energy resolution, dead layer losses, backscattering, pile-up, and background. The ROI cut (dashed lines) spans the [22, 34] keV window. Image source [135].

3.8.2 Pile-up Correction

Pile-up refers to the misidentification of multiple closely spaced electron events as a single higher-energy signal. This becomes relevant at high event rates and leads to a suppression of detected events.

The pile-up correction is modeled as:

$$\epsilon_{\text{pu}}(\dot{N}) = (1 - \beta) \cdot \exp(-2\dot{N} \cdot W) + \beta,$$

where $\dot{N}$ is the observed event rate, $W = 1.26\ \mu\text{s}$ is the event processing window, and β is a rate-independent baseline correction parameter [214]. At 300 eV below the endpoint, this correction results in a reduction of approximately $(0.200 \pm 0.004)\%$, which is applied consistently across all rates.

3.8.3 Backscattering Loss

Some incident electrons scatter off the detector surface and may either be lost or return after a delay. These backscattered electrons can:

- Strike another pixel after reflection,
- Re-enter the same pixel outside the acquisition window,
- Be reflected by the magnetic mirror and retarding potential, depending on their surplus energy.

This effect leads to a spectral distortion characterized by a low-energy tail. The backscattering correction is derived from detailed Monte Carlo simulations [85], yielding an energy-dependent loss rate:

$$\epsilon_{\mathrm{bs}}(E) \approx (0.10 \pm 0.02)\%\,\mathrm{keV}^{-1}.$$

The angular distribution of backscattered electrons and their interactions with the detector's dead layer introduce further complications. These effects are incorporated in the angular efficiency term and discussed in Section 3.5.5.

3.9 Model Summary and Significant Systematic Parameters

This chapter presented the theoretical model used to predict the integral electron count rate measured by the KATRIN experiment as a function of the applied retarding potential. The model incorporates contributions from the tritium β-decay spectrum, the response of the spectrometer, energy loss processes in the source, and detector and background effects. These components form the foundation for interpreting the observed spectrum and enable the search for new physics beyond the Standard Model.

Although the full model includes a large number of parameters, only a subset significantly affects the spectral shape near the endpoint. These dominant parameters are treated as fit parameters in the analysis. Less influential quantities are fixed to their nominal values.

For clarity, the relevant systematic effects are grouped into three categories: source-related, transmission-related, and background-related. The table below lists those parameters identified as significant in the context of the KATRIN search for eV-scale sterile neutrinos. Each is included as a fit parameter to properly account for its impact on the spectral shape.

By incorporating these parameters directly into the spectral fit, the analysis remains sensitive to subtle distortions that could signal the presence of sterile neutrino mass eigenstates at the eV scale. Their inclusion ensures that the model accurately captures the experimental response across the full range of retarding potentials.

Table 3.1: Summary of systematic input parameters considered significant in the search for eV-scale sterile neutrinos.

Parameter	**Unit**	**Description**
σ_0^2	eV^2	Plasma-induced broadening of the electron energy spectrum
$\Delta_{10,\mathrm{eff}}$	V	Effective plasma potential inhomogeneity
$\sigma^2_{\mathrm{shift,drift}}$	eV^2	Variance from unmodeled shifts and drifts in the spectrum
$\mathrm{Bg}_{\mathrm{Penning}}$	$\mathrm{cps/s}^2$	Quadratic coefficient for background rate from Penning trap processes
$\rho d\sigma$	dimensionless	Effective product of column density and inelastic scattering cross section
$\mathrm{Bg}_{\mathrm{slope}}$	cps/eV	Energy-dependent background slope parameter
B_{ana}	T	Magnetic field strength at the analyzing plane
σ^2_{ana}	eV^2	Broadening of the transmission function at the analyzing plane
B_{src}	T	Magnetic field strength at the center of WGTS
E-loss	—	Parameters of the Gaussian mixture model
B_{pch}	T	Magnetic field strength at the pinch magnet
$\mathrm{Sig}_{\mathrm{rw}}$	dimensionless	Amplitude of the rear wall signal contribution
$E_{0,\mathrm{rw}} - 18575$	eV	Endpoint energy of the rear wall contribution relative to 18575 eV
$w_{\mathrm{GS,rw}}$	dimensionless	Final-state distribution weight of the rear wall ground state
$\mathrm{Bg}_{\mathrm{non-Poi}}$	dimensionless	Non-Poissonian overdispersion parameter in background fluctuations

4

Constraints on Sterile Neutrinos from the First Five KATRIN Science Runs

As of April 2025, KATRIN has completed its sixteenth measurement campaign and is set to continue data taking through the end of 2025. The campaigns follow the naming scheme KATRIN neutrino-mass measurement (KNM)x, where x denotes the campaign number. A timeline of the campaigns can be seen in Figure 4.1. Current best limits on the neutrino mass have been recently set using data from the first five neutrino-mass measurement campaigns [135]. The goal of this thesis and the current chapter in particular is to present the analysis methods and results of sterile neutrino search using data from the first five neutrino-mass measurement campaigns. No significant sterile neutrino signal was found from the first five neutrino-mass measurement campaigns. Improved exclusion bounds in the sterile parameter space were obtained and reported in [137].

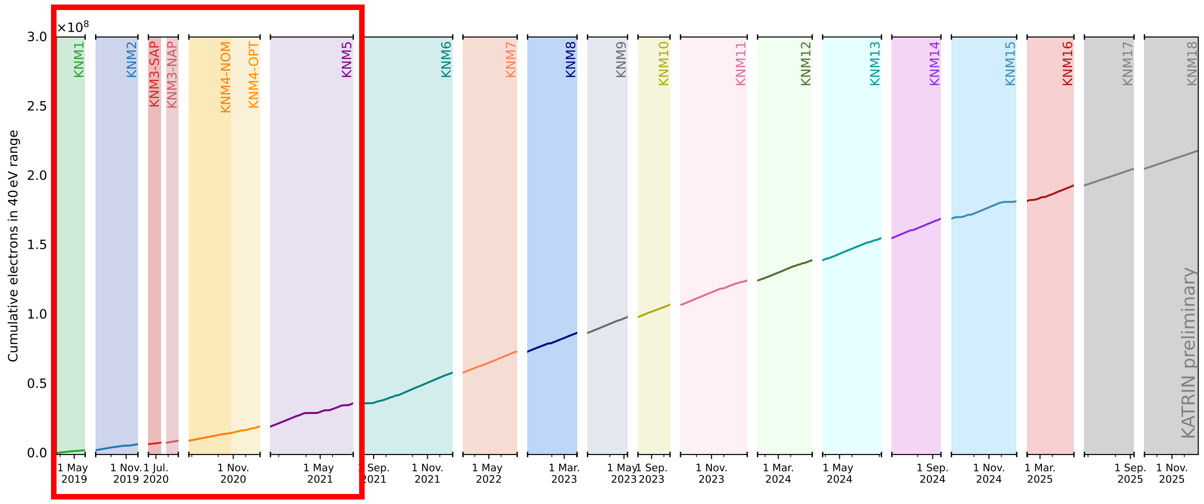

Figure 4.1: Timeline of the KATRIN neutrino-mass measurement campaigns. Highlighted in a red box are the first five campaigns which were analyzed in this thesis.

4.1 Overview of First Five Measurement Campaigns

Over the course of each measurement campaign, several hundred β-spectrum scans are performed, each lasting approximately three hours. During the KNM1–5 period, a total of 1895 such scans were conducted.

Stable operation throughout these scans is crucial for precise measurement of the β-spectrum. To this end, KATRIN employs a comprehensive monitoring and control system that continuously records a wide range of parameters, offering a detailed, real-time overview of experimental conditions for each scan.

Over successive campaigns, the experimental configuration evolved to improve data quality and sensitivity. For an initial "burn-in" period in KNM1, the column density was set to $\rho d = 1.08 \times 10^{21}\,\mathrm{m}^{-2}$. For KNM2 the column density was raised to $4.20 \times 10^{21}\,\mathrm{m}^{-2}$ (84% of design) at a source temperature of $T_{\mathrm{WGTS}} = 30.05\,\mathrm{K}$. In KNM3 a new configuration known as the shifted analyzing plane configuration [165] was tested to improve the signal-to-noise ratio. The mechanism through which the background reduction is obtained in the SAP configuration was discussed in Section 3.5.1. Hence the KNM3 campaign is split as KNM3-NAP, where data was collected in the normal analyzing plane configuration and KNM3-SAP. From KNM4, all β-spectrum measurements have been performed with the SAP configuration. In KNM3-SAP, the T_{WGTS} was raised to 78.85 K, which allowed co-circulation of $^{83\mathrm{m}}$Kr with tritium at a maximum column density of $\rho d = 3.8 \times 10^{21}\,\mathrm{m}^{-2}$. Specifically, KNM3-SAP ran at $\rho d = 2.05 \times 10^{21}\,\mathrm{m}^{-2}$ and $T_{\mathrm{WGTS}} = 78.85\,\mathrm{K}$, while KNM3-NAP used $\rho d = 3.70 \times 10^{21}\,\mathrm{m}^{-2}$. In KNM4, time-dependent Penning-trap backgrounds were mitigated by more frequent wipes and reduced pre-spectrometer potential [16]. The retarding voltages and the measurement time at each retarding voltage was optimized (KNM4-OPT vs. KNM4-NOM) to enhance neutrino-mass sensitivity [145, 232]. From KNM4, the new co-circulation mode of $^{83\mathrm{m}}$Kr was used to characterize electric-potential variations under the same conditions as neutrino-mass measurements [173].

The the Measurement Time Distributions (MTDs) of the first five campaigns are shown in Figure 4.2. Figure 4.2 also lists the number of scan-steps per campaign that were used for the analysis. To compensate for possible drifts in experimental parameters, within each campaign, scans are performed with retarding potentials in increasing (up direction), decreasing (down direction) and random orders. An overview of the number of scans in each direction per campaign is given in Table 4.1.

Table 4.1: Summary of first five KATRIN neutrino-mass measurement campaigns (KNM1-5): duration of each campaign and the count of recorded scans categorized by direction (up, down, random). Additionally, it provides a summary of the relative time dedicated to measuring the background region for each campaign.

Campaign	**Campaign Duration**	**Total**	**Up**	**Down**	**Random**	t_{bg}
KNM1	2019, April to May	274	140	134	–	26%
KNM2	2019, Sept. to Oct.	361	187	174	–	26%
KNM3-SAP	2020, June to July	114	48	47	19	21%
KNM3-NAP	2020, July	116	38	38	40	20%
KNM4	2020, Sept. to Nov.	470	156	156	158	21%
KNM5	2021, March to July	422	144	137	141	21%
KNM1-5	2019 - 2021	1757	713	686	358	22%

Several measurements for the estimation of systematic parameters are performed interleaved with the β-spectrum measurements. The estimates of the systematic parameters and their uncertainties are used as inputs for the neutrino mass analysis and the sterile neutrino search.

4.1.1 Data Processing, Selection and Combination

The experimental conditions during each scan are monitored closely and only those scans with stable conditions meeting strict requirements were selected. For KNM1-5 this meant 1757 out of 1895 scans were selected for analysis. At each retarding voltage set point, measurement starts when the reading of the main spectrometer voltage is within 20 mV of the set point value [218]. After passing the analyzing plane and before hitting the detector, the electron energy is boosted by a post-acceleration of 10 keV. The count rate at each retarding voltage set point is obtained

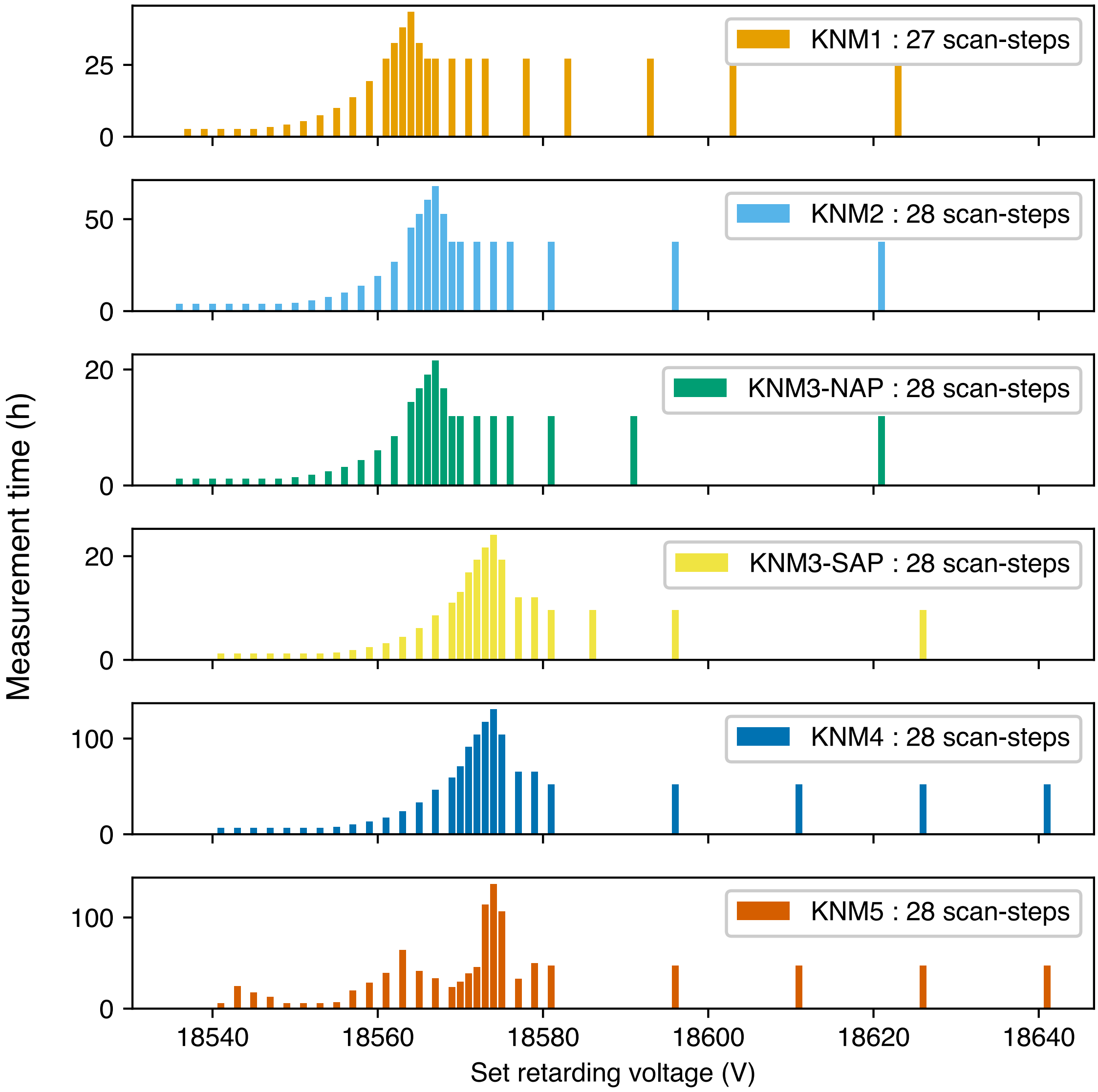

Figure 4.2: KNMx measurement time distributions used in the first five science runs of KATRIN. Most of the measurement time is spent in the endpoint region for optimized sensitivity to facilitate precise neutrino mass measurement. The distributions are shown until 40 eV below the endpoint. Note that the plots are zoomed in for better illustration. KNM2, KNM3-NAP, and KNM3-SAP contain one additional retarding voltage set-point at around 135 eV above the endpoint. The KNM4 distribution shown here is a representative one as four different MTDs were used during the KNM4 period.

by selecting a specific energy range known as region of interest (ROI) [248]. For KNM1 and KNM2 campaigns, ROI was chosen to be between 14 keV and 32 keV. To reduce the detector background contribution, a narrower ROI between 22 keV and 34 keV was used for KNM3 to KNM5 campaigns.

Another dimension of data selection is pixel selection. Out of the 148 pixels of the focal plane detector (FPD), only a subset was selected based on consistency in detected electron rates across the scans in a campaign. For KNM1 and KNM2 117 pixels were selected. From KNM3 on wards, 126 pixels were selected, highlighted as colored pixels in Figure 4.3. Most pixels in the two outermost rings are excluded due to obstruction of the electron flux by structural components of the beamline at these locations, and pixels exhibiting elevated intrinsic noise are also excluded.

For each measurement dataset, the electron counts per pixel per retarding voltage set point can be summed together due to the high precision (<10 mV) and reproducibility of the set points with the advanced post-regulation system [218]. Such a data combination reduces the number of data points significantly, from 60000 to 195 for the first five campaigns. An overview of the data comprising of 36 million electrons that will be used in the analysis is shown in Table 4.2. One noteworthy column in Table 4.2 is the Signal-to-background ratio (Sig./Bg.). A considerably higher signal-to-background ratio was achieved by switching to the SAP configuration.

The counts recorded by each detector pixel can be considered statistically independent of the other pixels. For the datasets recorded with Normal analyzing plane (NAP) configuration, the electron counts from all the selected pixels are summed together effectively reducing the dataset to the size of the retarding voltage set points. Unfortunately, such a combination cannot be performed for measurements with SAP configuration as the shift in the analyzing plane leads to electric-potential and magnetic-field inhomogeneities, leading to significantly different experimental response (see Section 3.5.1) for each pixel. After careful consideration of the response function, a grouping of pixels into 14 ring-like detector “patches” with nine pixels each was proposed [165]. The 14 patches used for the KNM1-5 analysis are shown in Figure 4.3. The patches do not coincide perfectly with the detector rings due to a slight misalignment between the detector wafer and the beamline axis. Grouping of pixels into patches offers a trade-off between the computational cost and background reduction achieved from the SAP configuration.

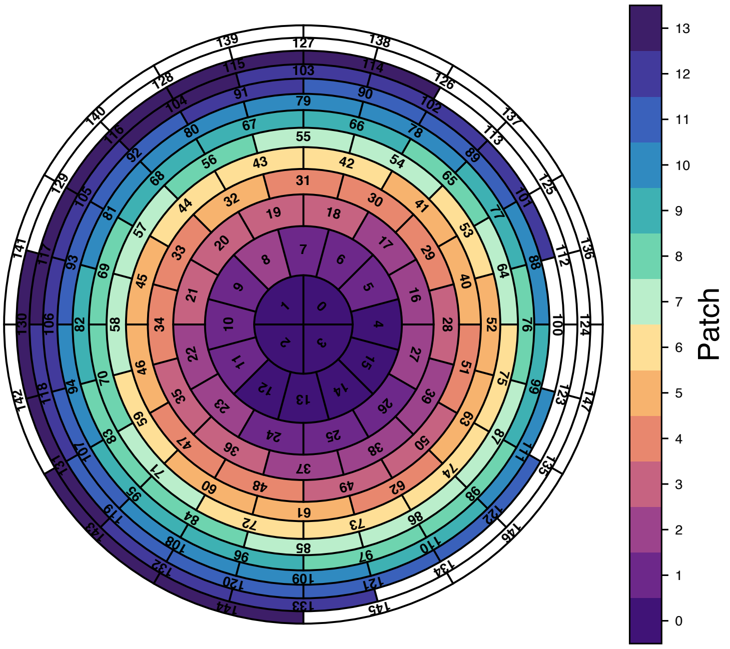

Figure 4.3: Segmented pixel map of the focal-plane detector with the patch layout of the SAP campaigns. The KNM3-NAP campaign combines that data from the colored pixels. White pixels are excluded from the analysis.

Table 4.2: KNM1-5 statistics summary: All values refer to the analysis range down to 40 eV below the endpoint. The number of background electrons is approximated based on the five background scan-steps.

Dataset	Scans	Scan-steps	Active Pixels	Net Meas. Time (h)	Signal Electrons	Background Electrons	Sig./Bg.
KNM1	274	27	117	522	1.49×10^6	5.45×10^5	2.72
KNM2	361	28	117	694	3.76×10^6	5.50×10^5	6.84
KNM3-SAP†	114	28	126	220	9.75×10^5	0.95×10^5	10.26
KNM3-NAP	116	28	126	224	1.25×10^6	1.77×10^5	7.06
KNM4†	470	28	126	1267	9.63×10^6	5.93×10^5	16.24
KNM5†	422	28	126	1226	1.60×10^7	6.18×10^5	25.95

Normal analyzing plane (NAP)
† *Shifted analyzing plane (SAP)*

4.2 Frequentist Approach to the Sterile Neutrino Search with KATRIN

In the Frequentist approach, it is assumed that the form of the distribution underlying the collected data is known and the parameters of the distribution have fixed but unknown values. The collected data is assumed to be a random sample representative of the underlying distribution. The model for the integrated rate $\dot{N}_{\text{model}}(qU, \boldsymbol{\theta})$ described in Chapter 3 was used as the mean of the underlying distribution with all the parameters $\boldsymbol{\theta}$ assumed to have some fixed but unknown values.

For the NAP campaigns as the number of counts at each retarding voltage set-point is $\gtrsim 10000$, the underlying distribution was approximated by a Gaussian distribution, i.e.

$$\dot{N}_{\text{exp}}(qU_i) \sim \mathcal{N}(\dot{N}_{\text{model}}(qU_i, \boldsymbol{\theta}), \sigma^2_{\dot{N},i}), \tag{4.1}$$

where $\dot{N}_{\text{exp}}(qU_i)$ and $\sigma^2_{\dot{N},i}$ are the measured rate and rate uncertainty at the retarding voltage set-point U_i. For the SAP campaigns, as the counts per patch may be less than 10000, the approximation of the Poisson distribution with a Gaussian is no longer valid. Thus the underlying distribution was modeled as the Poisson distribution, i.e.

$$N_{\text{exp}}(qU_i) \sim \text{Pois}(\dot{N}_{\text{model}}(qU_i, \boldsymbol{\theta}) \cdot t_i), \tag{4.2}$$

where $N_{\text{exp}}(qU_i)$ are the electron counts per patch collected during a time interval t_i at the retarding voltage set-point U_i.

Statistical inference of sterile neutrino from data can be divided into four tasks:

1. Maximum likelihood estimation (MLE): Optimization/fitting of the likelihood function to obtain the best-fit sterile neutrino parameters m_4^2 and $|U_{e4}|^2$.
2. Goodness of fit: Measure of how well the data is described by the best-fit sterile neutrino parameters.
3. Hypothesis testing: Given the null hypothesis $m_4^2 = 0\,\text{eV}^2$ and $|U_{e4}|^2$, decide whether to accept or reject it in favor of the alternative hypothesis with the best-fit m_4^2 and $|U_{e4}|^2$.
4. Interval estimation: Construct a contour as a set of m_4^2 and $|U_{e4}|^2$ values which includes the true parameter values at some predefined confidence level.

4.2.1 Likelihood Function and Maximum Likelihood Estimation

The likelihood function for individual datasets is based on the assumed model of the data distribution. For datasets from the NAP campaigns, a Gaussian likelihood was used for each retarding voltage set-point. Assuming independence of rate at each retarding voltage set-point, the maximum likelihood estimation (MLE) of parameters $\boldsymbol{\theta}$ was performed by minimizing the quantity

$$\chi^2_G(\boldsymbol{\theta}) = -2\ln\mathcal{L}_{\text{Gaussian}}(\boldsymbol{\theta}) = \sum_i \frac{(\dot{N}_{\text{exp}}(qU_i) - \dot{N}_{\text{model}}(qU_i,\boldsymbol{\theta}))^2}{\sigma^2_{\dot{N},i}}, \tag{4.3}$$

with respect to all or a subset of the parameters $\boldsymbol{\theta}$. For datasets from the SAP campaigns, assuming independence of counts at each retarding voltage set-point and patch, the MLE of parameters $\boldsymbol{\theta}$ was performed by minimizing the quantity

$$\begin{aligned}\chi^2_P(\boldsymbol{\theta}) &= -2\ln\mathcal{L}_{\text{Poisson}}(\boldsymbol{\theta}) \\ &= \sum_{k=1}^{14}\sum_i 2\left(\dot{N}_{\text{model},k}(qU_i,\boldsymbol{\theta})\cdot t_i - N_{\text{exp},k}(qU_i) + N_{\text{exp},k}(qU_i)\cdot\ln\frac{N_{\text{exp},k}(qU_i)}{\dot{N}_{\text{model},k}(qU_i,\boldsymbol{\theta})\cdot t_i}\right).\end{aligned} \tag{4.4}$$

The function $\chi^2_P(\boldsymbol{\theta})$ is built assuming a Poisson likelihood for each patch k.

For the combined analysis of the first five science runs, the optimization function is given by

$$\begin{aligned}&\chi^2_{\text{combined}}(\boldsymbol{\theta}) = \\ &\sum_{\text{KNM1,2,3-NAP}}\sum_i \frac{(\dot{N}_{\text{exp}}(qU_i) - \dot{N}_{\text{model}}(qU_i,\boldsymbol{\theta}))^2}{\sigma^2_{\dot{N},i}} \\ &+ \sum_{\text{KNM3-SAP,4,5}}\sum_{k=1}^{14}\sum_i 2\left(\dot{N}_{\text{model},k}(qU_i,\boldsymbol{\theta})\cdot t_i - N_{\text{exp},k}(qU_i) + N_{\text{exp},k}(qU_i)\cdot\ln\frac{N_{\text{exp},k}(qU_i)}{\dot{N}_{\text{model},k}(qU_i,\boldsymbol{\theta})\cdot t_i}\right).\end{aligned} \tag{4.5}$$

4.2.2 Systematic-Uncertainty Propagation Using Pull-Terms

The parameter vector $\boldsymbol{\theta}$ includes the parameters of interest $\boldsymbol{\theta}_{\text{physics}} = \{m^2_\nu,\ m^2_4,\ |U_{e4}|^2\}$ and other nuisance parameters such as endpoint E_0, signal factor Sig, constant background rate Bg and column density ρd. These and many other parameters enter the differential spectrum or experimental response function calculation as detailed in Chapter 3. During optimization, the nuisance parameters $\boldsymbol{\theta}_{\text{stat.}} = \{E_0, Sig, Bg\}$ are always considered to be fit parameters along with the parameters of interest while other systematics related nuisance parameters $\boldsymbol{\theta}_{\text{syst.}}$ may be held fixed. The central values and uncertainties on $\boldsymbol{\theta}_{\text{syst.}}$, which are external information for the optimization problem, are estimated from simulations or dedicated measurements as was discussed in Chapter 3. An optimization which considers only statistical uncertainties is termed in short as a "stat.-only fit". For a systematic parameter $\theta_{\text{syst.},i}$ which is assumed to follow the Gaussian distribution, the external information is given in the form of the central value and one sigma uncertainty $\theta_{\text{syst.},i} = \theta_{\text{ext},i} \pm \sigma_{\theta_{\text{ext},i}}$. The correlation between various parameters are described by a combined covariance matrix $\boldsymbol{\Sigma}$. This external information is used in the MLE problem through the pull-term method where an additional penalty term is added to the $\chi^2(\boldsymbol{\theta})$ terms Equation 4.3, Equation 4.4 or Equation 4.5 as

$$\chi^2_{\text{total}}(\boldsymbol{\theta}) = \chi^2(\boldsymbol{\theta}) + (\boldsymbol{\theta}_{\text{syst.}} - \boldsymbol{\theta}_{\text{ext}})^T\cdot\boldsymbol{\Sigma}^{-1}\cdot(\boldsymbol{\theta}_{\text{syst.}} - \boldsymbol{\theta}_{\text{ext}})\,. \tag{4.6}$$

The fit parameters in $\boldsymbol{\theta}$ are optimized to minimize $\chi^2_{\text{total}}(\boldsymbol{\theta})$. The subscript "total" indicates that the χ^2 optimization considers both statistical and systematic uncertainties. The impact of individual systematic uncertainties can be studied by performing the optimization considering only the corresponding subset of $\boldsymbol{\theta}_{\text{syst.}}$ as fit parameters.

4.2.2.1 Covariance Matrix Approach

Sterile neutrino search with KNM1-2 datasets [12] utilized the covariance matrix approach for systematic uncertainty propagation. In the covariance matrix approach, the χ^2 function is given by

$$\chi^2_{\text{total}}(\boldsymbol{\theta}) = (\dot{\boldsymbol{N}}_{\mathbf{exp}} - \dot{\boldsymbol{N}}_{\mathbf{model}}(\boldsymbol{\theta}))^T \cdot \boldsymbol{\Sigma}^{-1}_{\dot{\boldsymbol{N}}} \cdot (\dot{\boldsymbol{N}}_{\mathbf{exp}} - \dot{\boldsymbol{N}}_{\mathbf{model}}(\boldsymbol{\theta})), \tag{4.7}$$

where $\dot{\boldsymbol{N}}_{\mathbf{exp}}$ is the vector of experimental rates, $\dot{\boldsymbol{N}}_{\mathbf{model}}$ is the vector of model rates and $\boldsymbol{\Sigma}_{\dot{\boldsymbol{N}}}$ is the covariance matrix which accounts for both the statistical and systematic uncertainties. Statistical uncertainties are represented by the diagonal elements of $\boldsymbol{\Sigma}_{\dot{\boldsymbol{N}}}$. Monte Carlo propagation is used to obtain the covariances introduced between the set-points due to the systematic uncertainties. Many random samples are drawn from the joint distribution of the systematic parameters. Model rates are then calculated for each set of systematic parameters. Pairwise covariances between the retarding potential set points are calculated from the model rates. Precise computation of the covariance matrix requires large number of samples which grows quickly with the number of systematic parameters considered. In addition, inversion of a high-dimensional covariance matrix can become ill-conditioned leading to difficulty in the optimization. The advantage of the pull-term approach is that it incorporates the information about the systematic uncertainties and correlations derived from dedicated measurements directly into the minimization problem. No intermediate step such as the estimation of the $\boldsymbol{\Sigma}_{\dot{\boldsymbol{N}}}$ matrix is required.

4.2.3 Optimization Software and Hardware

Optimization of Equation 4.3 requires $\mathcal{O}(10^3)$ evaluations of the model rate $\dot{N}_{\text{model}}(qU_i, \boldsymbol{\theta})$ while Equation 4.5 can require $\mathcal{O}(10^5)$ evaluations. Efficient computation of $\dot{N}_{\text{model}}(qU_i, \boldsymbol{\theta})$ is therefore critical to maintain a feasible analysis timeline for the sterile neutrino analysis. The KATRIN-specific fitting framework KaFit, housed within the broader KASPER software suite [44, Section 3.2], has been developed for this purpose. KaFit utilizes MIGRAD from the ROOT (version 6.24/00) package [52] for numerical minimization and MINOS for asymmetric error estimation. The theoretical $\beta-$spectrum model rate $\dot{N}_{\text{model}}$ is calculated by the Source and Spectrum Calculation (SSC) package, which constructs the integrated response model from a modular combination of physical components: source and final state models, differential spectrum, energy loss, transmission, detector response, and others. These are configured through .xml files and support extensive caching and parallelization to reduce redundant computations [144]. A more detailed description of the SSC and KaFit frameworks is provided in Appendix A.9. Several parallel computing and function caching methods have been implemented in KaFit to speed up model rate calculation. Further details of the software framework can be found in Appendix A.9. The results reported in this thesis were computed on the cluster at the Institute of Astroparticle Physics, Karlsruhe Institute of Technology, which uses Intel(R) Xeon(R) Gold 6230 CPUs with 85 cores, running Ubuntu 20.04.5 LTS.

4.2.4 Goodness of Fit Analysis

Optimization of multi-dimensional nonlinear functions like Equation 4.6, is inherently challenging due to the complex nature of the optimization landscape. Incorrect identification of the maximum likelihood parameters can lead to erroneous results. For an optimization problem with $N_{\text{data}-\text{points}}$ data points and $N_{\text{fit}-\text{parameters}}$, the degree of freedom (dof) is defined as

$$\text{dof} = N_{\text{data}-\text{points}} - N_{\text{fit}-\text{parameters}} + N_{\text{constrained}-\text{parameters}}. \tag{4.8}$$

In Equation 4.6, $N_{\text{constrained-parameters}}$ is the length of the vector $\boldsymbol{\theta}_{\text{syst.}}$. A measure known as reduced-χ^2 which is χ^2/dof can be used as an indicator of the fit quality [25]. Value of reduced-χ^2 close to 1 indicates that the model predictions are consistent with the observed data within the expected variance, suggesting a good fit. Table 4.3 summarizes the number of parameters and dofs for the individual datasets and the combined KNM1-5 dataset. While there are significantly more fit parameters in case of "total" fits, the dof remains the same as the "stat.-only" fits, as all the systematic parameters are constrained.

Table 4.3: Summary of the MLE: number of data points, the number of fit parameters and number of constrained parameters per data set. This is for the case where the active neutrino mass is fixed to 0. Numbers are provided for analysis considering only statistical uncertainties and both statistical and systematic uncertainties.

Data set	No. of data points	stat.-only			total		
		Fit param.	Constr. param.	dof	Fit param.	Constr. param.	dof
KNM1	27	5	0	22	24	19	22
KNM2	28	5	0	23	24	19	23
KNM3-SAP	392	44	0	348	106	62	348
KNM3-NAP	28	5	0	23	27	22	23
KNM4	392	44	0	348	106	62	348
KNM5	392	44	0	348	105	61	348
KNM1-5	1259	137	0	1122	282	145	1122

Compatibility of the data with the model corresponding to the most likely value of the parameters can be quantified through the p-value defined as

$$p = 1 - \text{CDF}_{F(\chi^2)}(\chi^2_{\text{bf}}), \tag{4.9}$$

where $\text{CDF}_{F(\chi^2)}$ is the cumulative distribution function of the best-fit χ^2 values (χ^2_{bf}) of the function Equation 4.5. If regularity conditions required by Wilks' theorem are met [252], the best-fit χ^2 statistic asymptotically follows the chi-squared distribution with *dof* degrees of freedom (χ^2_{dof}). In other cases, Monte Carlo studies need to be performed (see Section 4.3) to obtain the empirical distribution on the basis of which the goodness-of-fit statistic Equation 4.9 can be computed. Generally low p-values below 0.05 indicate a poor fit of the model to the data.

4.2.5 Hypothesis Testing and Interval Estimation

In case of the neutrino mass estimation, it is already know that the neutrino has a non-zero mass and its value is to be estimated from the collected data. In case of the sterile neutrino, the primary goal is to test the presence of a sterile neutrino which is formally a hypothesis testing. Two hypotheses were considered. First hypothesis H_0 is the null hypothesis which corresponds to $m_4^2 = 0$ and $|U_{e4}|^2 = 0$. Second hypothesis H_1 corresponds to non-zero values of both m_4^2 and $|U_{e4}|^2$. The maximum likelihood estimation of $\boldsymbol{\theta}$ can be performed for the individual campaigns by minimizing the corresponding χ^2 functions Equations (4.3) and (4.4) or for the combined dataset using Equation 4.5. For H_0, the minimum value of χ^2 function denoted by χ^2_{null} was obtained by fixing $m_4^2 = 0$ and $|U_{e4}|^2 = 0$ and minimizing χ^2 with respect to other parameters in $\boldsymbol{\theta}$. For H_1, the minimum value of χ^2 function denoted by χ^2_{bf} was obtained by minimizing χ^2 with respect to all parameters in $\boldsymbol{\theta}$ including m_4^2 and $|U_{e4}|^2$. The subscript "bf" is short for best-fit. From the two χ^2 values, $\Delta\chi^2 = \chi^2_{\text{null}} - \chi^2_{\text{bf}}$ was calculated. Significance of the non-zero best-fit values of m_4^2 and $|U_{e4}|^2$ can be determined from the $\Delta\chi^2$

value, using its cumulative distribution function $\mathrm{CDF}_{F(\Delta\chi^2)}$. Significance can be reported in terms of percentage as $\mathrm{CDF}_{F(\Delta\chi^2)}(\Delta\chi^2) \times 100\%$ or in terms of p-value $1 - \mathrm{CDF}_{F(\Delta\chi^2)}(\Delta\chi^2)$ which signifies the probability of observing the data given hypothesis H_0 is actually true. A sterile neutrino signal would be considered significant if the significance level was higher than 95%. As in the goodness-of-fit, Wilks' theorem [252] under certain regularity conditions states that, if hypothesis H_0 is true, $\Delta\chi^2$ will follow the chi-squared distribution with two degrees of freedom. In the absence of a significant signal, regions of the sterile neutrino parameter space can be excluded with a certain confidence level. Exclusion regions are typically reported as exclusion contours, defined by pairs of (m_4^2, $|U_{e4}|^2$) values for which

$$\chi^2(m_4^2, |U_{e4}|^2) - \chi^2_{\mathrm{bf}} = \mathrm{CDF}^{-1}_{F(\Delta\chi^2)}\left(\frac{\text{confidence level (\%)}}{100}\right). \tag{4.10}$$

4.2.6 Analysis Algorithms

A so-called “Grid Scan” approach was developed [12] to identify the best-fit set of sterile neutrino parameters (m_4^2, $|U_{e4}|^2$) and to draw contours at desired confidence levels, as a direct minimization treating (m_4^2, $|U_{e4}|^2$) as fit parameters was found to be numerically unreliable (see Appendix A.2).

4.2.6.1 Best-fit search: Grid Scan

1. A two-dimensional logarithmic grid of size 50 × 50 was chosen for the analysis based on a convergence study (see Appendix A.3). The grid parameter space was defined by $m_4^2 \in [0.1, 1600]\ \mathrm{eV}^2$ and $|U_{e4}|^2 \in [0.001, 0.5]$. The upper-limit of $1600\,\mathrm{eV}^2$ on m_4^2 was determined by the fact that the analysis considered electron energies only up to $E_0 - 40\,\mathrm{eV}$.

2. The sterile neutrino parameters were fixed to the respective grid points and minimization of the $\chi^2(\boldsymbol{\theta})$ function Equation 4.6 with respect to the parameters $\boldsymbol{\theta}$ was performed. The optimization was also performed for the null hypothesis ($m_4^2 = 0, |U_{e4}|^2 = 0$) to obtain χ^2_{null}.

3. Best-fit point among all the points including the ($m_4^2 = 0$, $|U_{e4}|^2 = 0$) was identified as the set ($m^2_{4,\mathrm{bf}}$, $|U_{e4}|^2_{\mathrm{bf}}$) corresponding to the lowest value χ^2_{bf}.

4. Significance of of the best-fit parameters was calculated based on $\Delta\chi^2 = \chi^2_{\mathrm{null}} - \chi^2_{\mathrm{bf}}$. The null hypothesis would be considered in tension with the data if the obtained significance exceeded the 95% confidence level.

5. $\Delta\chi^2 = \chi^2 - \chi^2_{\mathrm{bf}}$ values were computed for all pairs of ($m_4^2, |U_{e4}|^2$) on the grid.

6. Contour finding method of `matplotlib` Python library [126] was used to calculate pairs of (m_4^2, $|U_{e4}|^2$) satisfying Equation 4.10. A confidence level (C.L.) of 95% was chosen for this work to draw the contour.

An illustration of the Grid Scan method is shown in Figure 4.4. To ensure that the analysis procedure and software was robust and unbiased, the analysis was performed first on Asimov datasets generated using estimates of the various nuisance parameters from external measurements and for a chosen set of active and sterile neutrino values. For the results presented in this Chapter, the Asimov datasets were generated for $m_\nu^2 = 0\,\mathrm{eV}^2, m_4^2 = 0\,\mathrm{eV}^2, |U_{e4}|^2 = 0$. Applying the Grid Scan procedure to an Asimov dataset results in a sensitivity contour which is an indicator how the sensitivity of the experiment varies over the sterile neutrino parameter space.

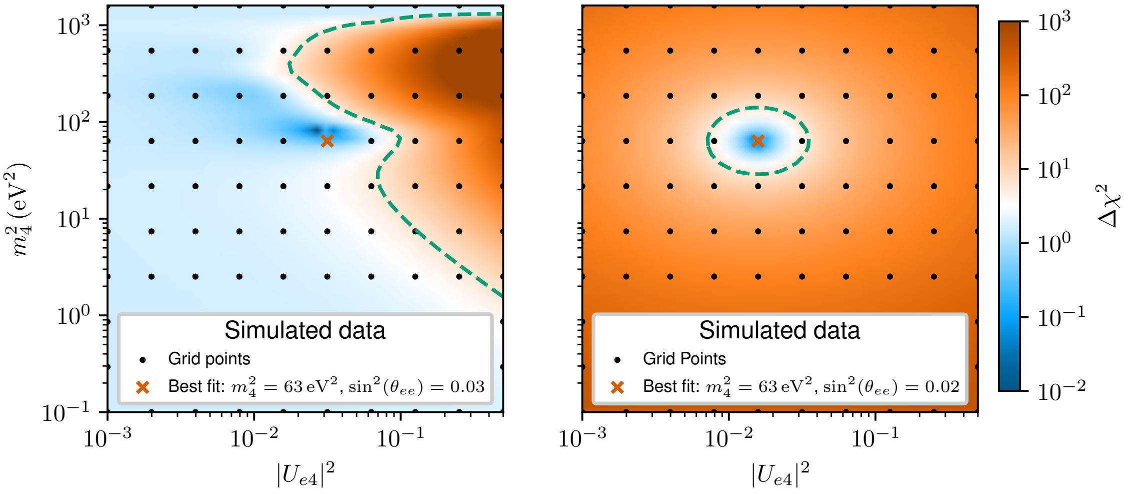

Figure 4.4: Illustration of the grid-search analysis method based on Asimov datasets: (left) In the absence of a sterile-neutrino signal, showing an open contour as the dashed green line; (right) In the presence of a sterile-neutrino signal, showing a closed contour as the dashed green line.

The Asimov datasets can also be used to study the impact of the uncertainty of the systematic parameters on the experiment sensitivity by computing the sensitivity contour while considering specific systematic parameters as fit parameters in Equation 4.6. The impact of each systematic uncertainty was quantified for the different sterile neutrino masses considered on the grid as

$$\sigma_{|U_{e4}|^2,\text{syst.}} = \sqrt{\sigma_{|U_{e4}|^2,\text{stat.+syst.}} - \sigma_{|U_{e4}|^2,\text{stat.}}}. \tag{4.11}$$

The values of $\sigma_{|U_{e4}|^2,\text{stat.}}$ and $\sigma_{|U_{e4}|^2,\text{stat+sys}}$ were calculated using a procedure similar to the Grid Scan henceforth known as "Raster Scan". To obtain $\sigma_{|U_{e4}|^2,\text{stat.}}$, the $\chi^2(\boldsymbol{\theta})$ function with all systematic parameters fixed to the central values was used. Similarly $\sigma_{|U_{e4}|^2,\text{stat.+syst.}}$ was obtained using Equation 4.6 with specific systematic parameters as fit parameters. The Raster Scan results in a so-called "raster contour", defined by pairs of (m_4^2, $\sigma_{|U_{e4}|^2,\text{syst.}}$) values.

4.2.6.2 Systematic Uncertainty Breakdown: Raster Scan

1. A set of minimized $\chi^2_{\text{stat.}}$ values was obtained by optimization for combinations of m_4^2 and $|U_{e4}|^2$ values defined on a grid as in the case of Grid Scan.

2. Similarly a set of minimized $\chi^2_{\text{stat.+syst.}}$ values was obtained by optimization considering certain systematic parameters as additional fit parameters.

3. For each value of m_4^2, the minimum value χ^2_{min} among the χ^2 values corresponding to the various $|U_{e4}|^2$ values was identified. Then $\Delta\chi^2 = \chi^2 - \chi^2_{\text{min}}$ values were computed.

4. Local quadratic spline interpolation was used to interpolate $\Delta\chi^2$ values over $|U_{e4}|^2$ values. The choice of the quadratic spline interpolation is justified through a study of interpolation methods Appendix A.4.

5. The Newton–Raphson method [74] was used to find the value of $|U_{e4}|^2$ for which $\Delta\chi^2 = \Delta\chi^2_{\text{crit}}$, where $\Delta\chi^2 = 1$. The obtained $|U_{e4}|^2$ value was considered a measure of the impact of the uncertainties on $|U_{e4}|^2$. Applying the procedure to $\chi^2_{\text{stat.}}$ values of $\sigma_{|U_{e4}|^2,\text{stat.}}$ were obtained and from $\chi^2_{\text{stat.+syst.}}$ values $\sigma_{|U_{e4}|^2,\text{stat.+syst.}}$ were obtained.

6. Impact of particular systematic uncertainties was then quantified by computing $\sigma_{|U_{e4}|^2,\mathrm{syst.}}$ using Equation 4.11 for each value of m_4^2.

The choice of $\Delta\chi^2 = 1$ for the Raster scan was arbitrary, as the focus was on the relative impact of various uncertainties rather than on absolute values.

4.3 Studying Empirical Distributions of χ^2 and $\Delta\chi^2$

Assessing the goodness-of-fit of a model with its best-fit parameters requires knowledge of the distribution of the χ^2 test statistic (see Section 4.2.4). Likewise, evaluating the significance of a best-fit sterile neutrino hypothesis and constructing exclusion contours relies on the distribution of $\Delta\chi^2$ (see Section 4.2.5). If the regularity conditions required by Wilks' theorem [252] are satisfied, the asymptotic chi-squared distribution of the test statistic may be applied, thereby eliminating the need for computationally intensive Monte Carlo simulations. One such condition requires that the true parameter values lie within the interior of the parameter space, which must be continuous and differentiable. This condition was not fulfilled when the Grid scan method was applied to the Asimov dataset, as the search space was discontinuous and the true parameter values, $m_4^2 = 0, \mathrm{eV}^2$ and $|U_{e4}|^2 = 0$, effectively lay at the boundary of the parameter space.

Monte Carlo simulations performed for the KNM1 and KNM2 datasets [230, Sec. 11.10] demonstrate that, although all conditions required for applicability of Wilks' theorem are not met, the $\Delta\chi^2$ test statistic empirically follows a chi-squared distribution with two degrees of freedom. In the following, results from Monte Carlo studies based on the KNM5 dataset are presented to verify whether this behavior persists under the increased segmentation of the data in the SAP campaigns.

4.3.1 Monte Carlo Simulation Framework

Starting from the Asimov datasets generated with $m_\nu^2 = 0\,\mathrm{eV}^2$, $m_4^2 = 0\,\mathrm{eV}^2$ and $|U_{e4}|^2 = 0$, $\mathcal{O}(10^3)$ randomized pseudo-experiments were generated to account for statistical fluctuations. Each randomized dataset was constructed by treating the count rate in each detector pixel at each retarding potential set-point as a Poisson-distributed random variable, with the mean given by the corresponding Asimov data.

Grid scans were performed with each of the randomized datasets using 25×25 logarithmic grid in the sterile neutrino parameter space $m_4^2 \in [0.1, 1600]\,\mathrm{eV}^2$ and $|U_{e4}|^2 \in [0.001, 0.5]$ considering only statistical uncertainties. The best-fit parameters were determined for each pseudo-experiment, and the corresponding χ^2_{bf} values were recorded, along with the test statistic and $\Delta\chi^2 = \chi^2_{\mathrm{null}} - \chi^2_{\mathrm{bf}}$. The active neutrino mass was fixed to $m_\nu^2 = 0\,\mathrm{eV}^2$.

4.3.2 Quantifying Distribution Similarity

The similarity between the empirical distributions of χ^2_{bf} and $\Delta\chi^2$ and reference distributions, such as chi-squared distributions, can be quantified using the following statistical metrics.

Kolmogorov-Smirnov (KS) Statistic

It is the maximum vertical distance between the empirical CDF (ECDF) and the theoretical CDF [59]. With n samples of a variable x and reference CDF $F(\cdot)$, the statistic can be calculated using the following steps.

1. Sort the samples: $x_{(1)} \leq x_{(2)} \leq \cdots \leq x_{(n)}$
2. Compute $D^+ = \max_i \left(\frac{i}{n} - F(x_{(i)})\right)$ and $D^- = \max_i \left(F(x_{(i)}) - \frac{i-1}{n}\right)$.
3. KS statistic: $D = \max(D^+, D^-)$.

Smaller D indicates higher similarity.

Cramér-von Mises Criterion

It is the integrated squared difference between ECDF and CDF [59], given formally as

$$\omega^2 = \frac{1}{12n} + \sum_{i=1}^{n} \left(F(x_{(i)}) - \frac{2i-1}{2n}\right)^2 \tag{4.12}$$

Smaller ω^2 implies closer match.

The Kolmogorov-Smirnov statistic indicates the maximum discrepancy while Cramér-von Mises criterion compares the overall shape of the CDF. Before applying the metrics to the results of the pseudo-experiments, expected values of the two similarity metrics were estimated using 10000 samples drawn from the χ^2_{348} and χ^2_2 distributions. The empirical cumulative distribution function (ECDF) and the two metrics, along with their associated uncertainties, were calculated using bootstrapping. Bootstrapping involves generating new sample sets by resampling with replacement from the original dataset. From the ECDF of the χ^2_2 samples, the 95th percentile value, $\mathrm{ECDF}^{-1}(0.95)$, was also estimated. This corresponds to the 95% confidence level chosen for the sterile neutrino analysis. The reference and empirical probability density functions (PDFs) and cumulative distribution functions (CDFs) for the χ^2_{348} distribution, along with the values of the two similarity metrics, are presented in Figure 4.5; the corresponding results for the χ^2_2 distribution are shown in Figure 4.6. For both distributions, the empirical PDFs and CDFs exhibit good visual agreement with the corresponding reference distribution functions.

Results for the KNM5 Asimov dataset are shown in Figure 4.7 for χ^2_{bf} and in Figure 4.8 for $\Delta\chi^2$. The empirical PDFs and CDFs exhibit good visual agreement with the corresponding reference chi-squared distributions, indicating low overall discrepancy. This observation is quantitatively supported by the Kolmogorov–Smirnov (KS) and Cramér–von Mises (CVM) similarity metrics. These results are consistent with the findings reported in [230, Sec. 11.10] for the KNM1 and KNM2 datasets, which demonstrate that despite the regularity conditions required for the strict applicability of Wilks' theorem not being fully satisfied, the $\Delta\chi^2$ test statistic empirically follows a chi-squared distribution with two degrees of freedom.

Although direct minimization treating $(m_4^2, |U_{e4}|^2)$ as fit parameters was determined to be unreliable for identifying the best-fit parameters, the resulting empirical distributions of χ^2 and $\Delta\chi^2$ were nonetheless examined (see Appendix A.2). Furthermore, Monte Carlo studies employing the Grid Scan method were conducted on the KNM1–5 Asimov dataset. The outcomes obtained from the Grid Scan analyses of the KNM5 and KNM1–5 pseudo-experiments demonstrated that, despite the regularity conditions required for the strict applicability of Wilks' theorem not being fully satisfied, the empirical distributions exhibited good agreement with the expected chi-squared distributions.

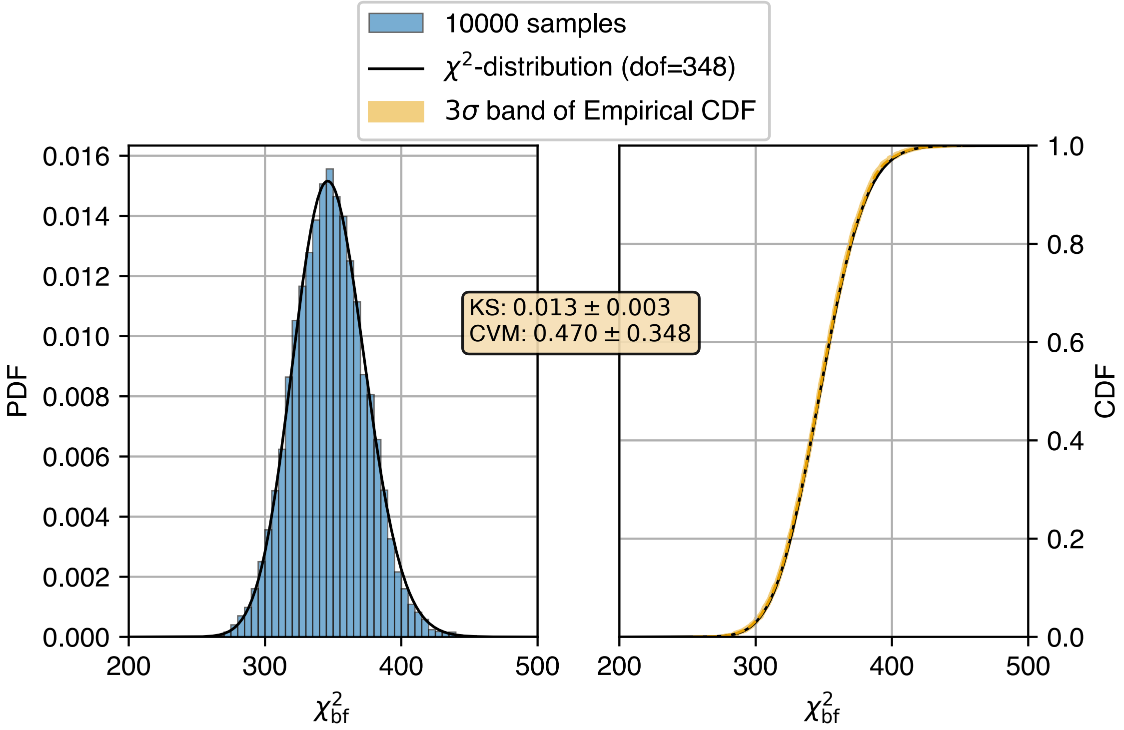

Figure 4.5: Illustration of the Kolmogorov–Smirnov (KS) and Cramér–von Mises (CVM) metrics. Empirical probability density function (PDF, left) and cumulative distribution function (CDF, right) of 10000 samples drawn from the chi-squared distribution with 348 degrees of freedom. The black line represents the reference distribution. The empirical CDF's 3σ confidence band is shown in orange. The Kolmogorov–Smirnov (KS) and Cramér–von Mises (CVM) metrics indicate a low overall discrepancy.

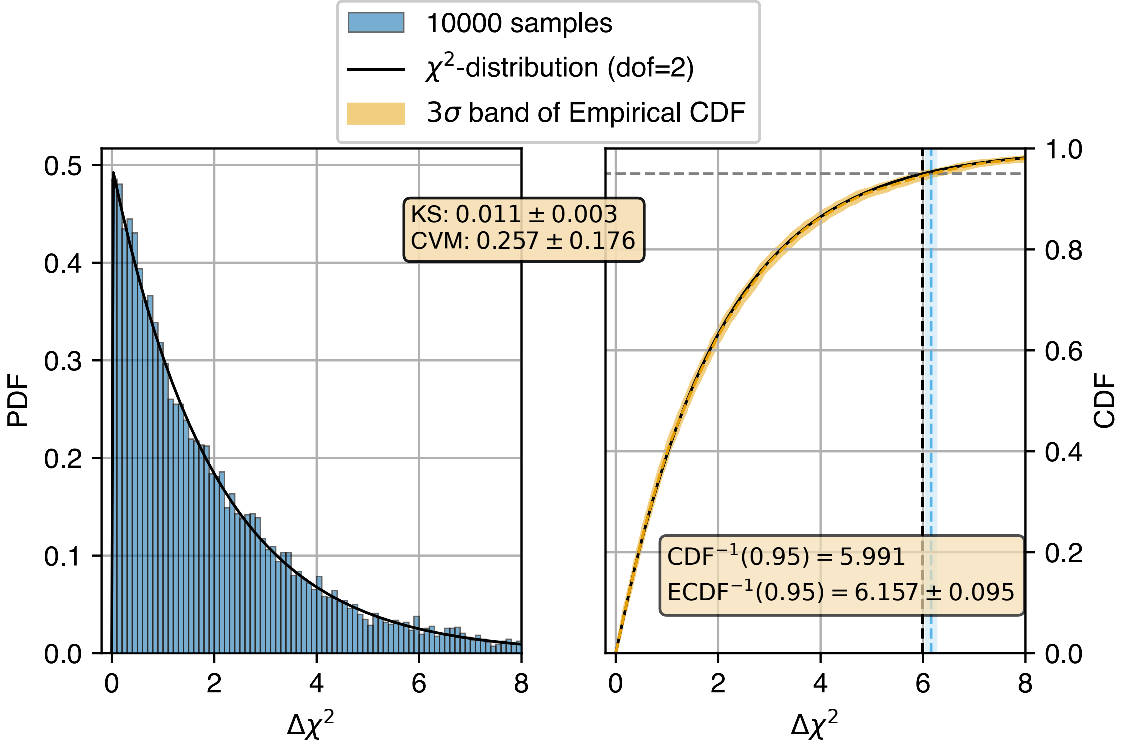

Figure 4.6: Illustration of the Kolmogorov–Smirnov (KS) and Cramér–von Mises (CVM) metrics. Empirical probability density function (PDF, left) and cumulative distribution function (CDF, right) of 10000 samples drawn from the chi-squared distribution with 2 degrees of freedom. The black line represents the reference distribution. The empirical CDF's 3σ confidence band is shown in orange. The Kolmogorov–Smirnov (KS) and Cramér–von Mises (CVM) metrics indicate a low overall discrepancy. The 95th percentile value for the reference distribution is shown with the black dashed line alongside the estimated 95th percentile value with 1σ confidence band in light blue.

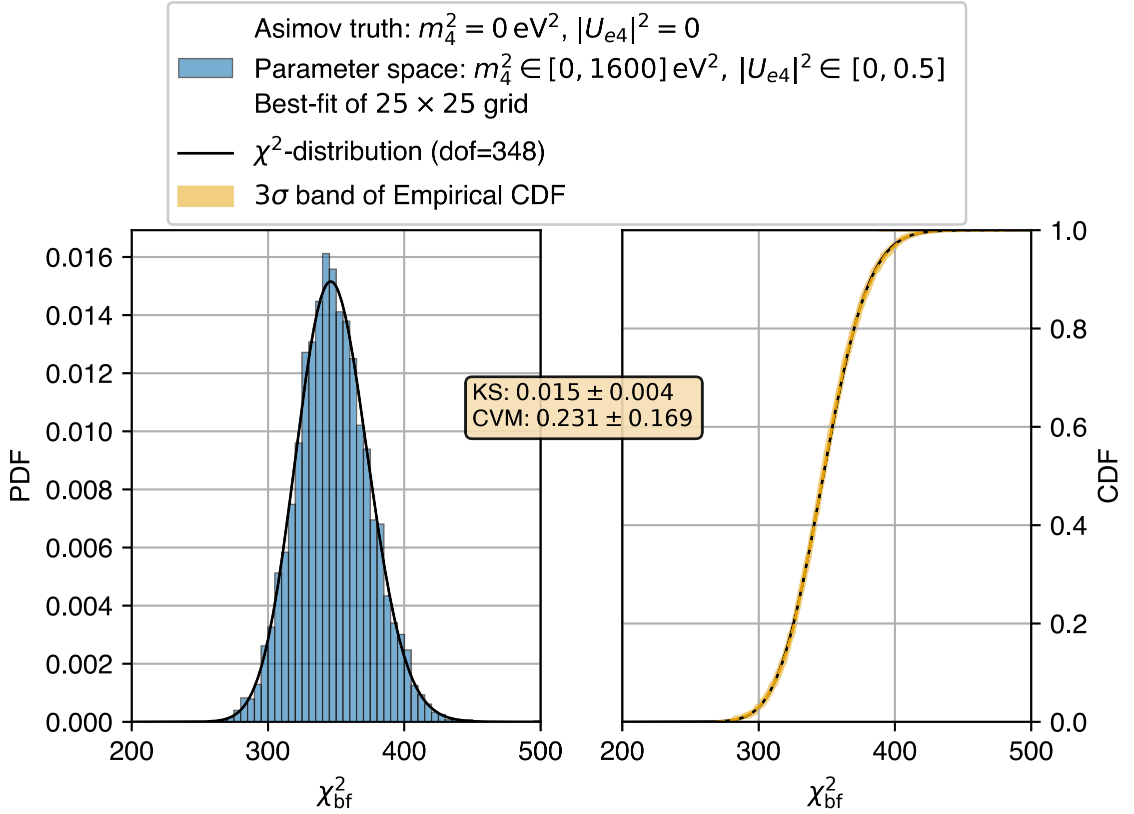

Figure 4.7: Application of the Kolmogorov–Smirnov (KS) and Cramér–von Mises (CVM) metrics. Empirical probability density function (PDF, left) and cumulative distribution function (CDF, right) of the best-fit χ^2_{bf} values obtained from 10000 KNM5 pseudo-experiments using the Grid Scan method, where the sterile neutrino parameters were restricted to the physical domain. The Asimov dataset corresponds to the null hypothesis. The black line represents the reference distribution. The empirical CDF's 3σ confidence band is shown in orange. The Kolmogorov–Smirnov (KS) and Cramér–von Mises (CVM) metrics indicate a low overall discrepancy.

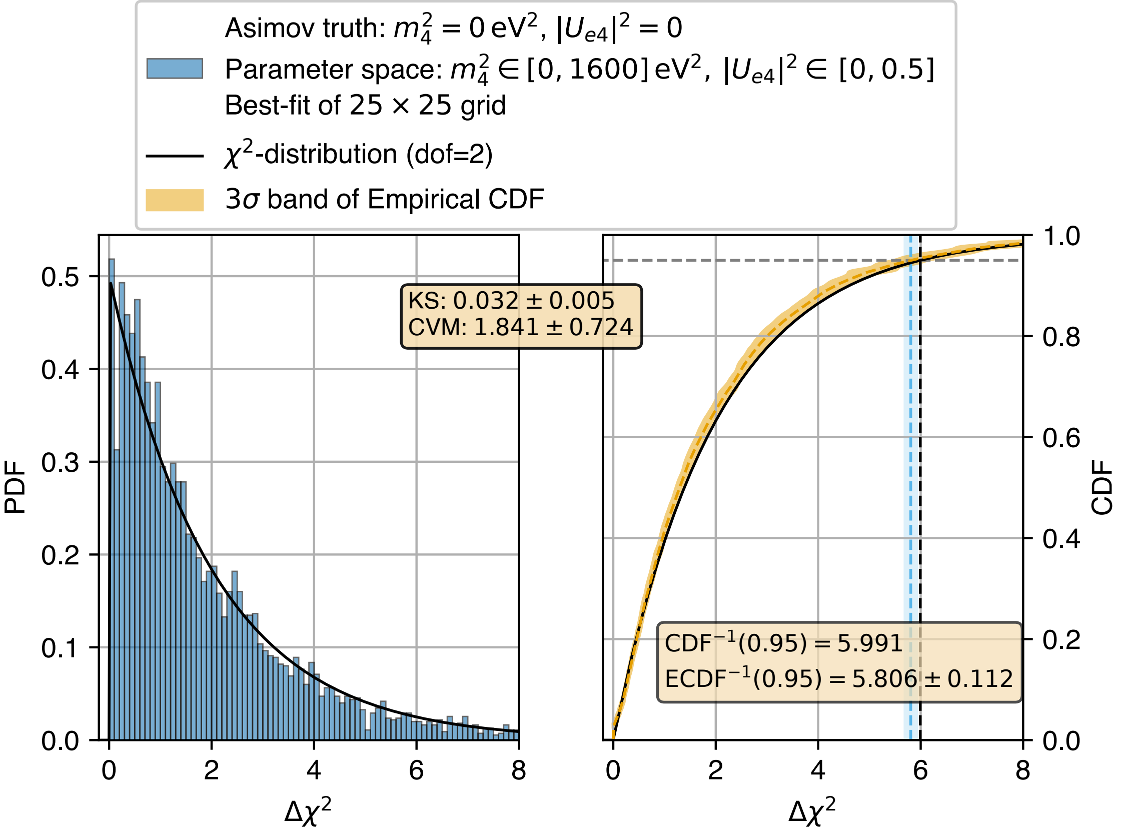

Figure 4.8: Application of the Kolmogorov–Smirnov (KS) and Cramér–von Mises (CVM) metrics. Empirical probability density function (PDF, left) and cumulative distribution function (CDF, right) of the $\Delta\chi^2$ test statistic obtained from 10000 KNM5 pseudo-experiments using the Grid Scan method, where the sterile neutrino parameters were restricted to the physical domain. The Asimov dataset corresponds to the null hypothesis. The black line represents the reference distribution. The Kolmogorov–Smirnov (KS) and Cramér–von Mises (CVM) metrics indicate a low overall discrepancy. The empirical CDF's 3σ confidence band is shown in orange. The 95th percentile value for the reference distribution is shown with the black dashed line alongside the estimated 95th percentile value with 1σ confidence band in light blue.

4.4 Results from First Unblinding

The primary sterile neutrino analysis was performed by fixing the squared active neutrino mass $m_\nu^2 = 0$. Results of different treatment of m_ν^2 can be found in Section 4.9. Following the protocol outlined in Appendix A.1, the sensitivity contours were first evaluated individually for each campaign. The analysis was conducted in parallel by two independent analysis teams, KaFit [145, 112] (see also Appendix A.9) and Netrium [133]. Consistency between the results of both analysis teams was confirmed prior to proceeding with the evaluation of the experimental data. The sensitivity contours considering both the statistical and systematic uncertainties are shown in Figure 4.9. Across all contours, the maximum sensitivity is observed at $m_4^2 \simeq 400\mathrm{eV}^2$. For smaller values of m_4^2, sensitivity diminishes due to a reduced signal amplitude and a lower signal-to-background ratio. Conversely, for $m_4^2 > 400\,\mathrm{eV}^2$ sensitivity declines sharply as the sterile neutrino's influence on the β-decay spectrum shifts beyond the experimental analysis window. The sensitivity contours do not change significantly when the systematic uncertainties are considered. The small difference suggests that the uncertainties are statistically dominated. The impact of the systematic uncertainties on sterile neutrino mixing $|U_{e4}|^2$ for the KNM1-5 dataset is presented in the form of raster contours in Figure 4.10. An equivalent representation for only three values of squared sterile neutrino mass is shown in Figure 4.11. The analysis reveals that the largest systematic effects come from time-dependent Penning background followed by source potential and confirms that the overall sensitivity dominated by statistical uncertainties. For many of the contours in Figure 4.10, a kink is visible for $30\,\mathrm{eV}^2 \lesssim m_4^2 \lesssim 80\,\mathrm{eV}^2$ indicating a very low impact of the systematic for those particular values of m_4^2. From a physical perspective this observation does not have an immediate explanation. The kinks were hypothesized to be an artifact of the measurement time distribution. To test this, a study was conducted using KNM2-like Asimov datasets generated with random retarding voltage set-points with uniform time distribution Appendix A.6. The presence of kinks in numerous datasets from this study indicates that the measurement time distribution is unlikely the sole cause of these anomalies, thereby challenging the hypothesis. A comprehensive explanation remains to be developed.

Based on analysis of the experimental data, the best-fit sterile neutrino parameters along with their significances as confidence levels and p-values are summarized in Table 4.4. For the KNM4 dataset, a significant sterile signal was observed with a p-value of 2×10^{-4}. However, no such significant signal was observed in other datasets. While significance was not at the level defined for declaring discovery, the discrepancy among datasets led to a comprehensive investigation of the issue from the ground up. The signal is significant enough to lead to a closed exclusion contours at 95% C.L. when considering both the statistical and systematic uncertainties in Figure 4.12.

Table 4.4: Summary of the best-fit sterile neutrino parameters: Results presented for each campaign from first unblinding with active neutrino mass $m_\nu^2 = 0\,\mathrm{eV}^2$ and considering statistical and systematic uncertainties. In KNM4, a sterile signal was observed at a significance of 99.94%.

Data set	m_4^2	$\lvert U_{e4}\rvert^2$	$\chi^2_{\mathrm{bf}}/\mathrm{dof}$	p	$\Delta\chi^2_{\mathrm{null}}$	Significance
KNM1	82.63	0.027	21.9/22	0.47	1.37	49.70%
KNM2	0.49	0.500	27.7/23	0.23	0.67	28.58%
KNM3-SAP	30.77	0.058	309.3/348	0.93	2.18	66.46%
KNM3-NAP	55.66	0.016	31.7/23	0.11	0.35	16.02%
KNM4	37.49	0.045	373.5/348	0.17	14.87	99.94%
KNM5	67.82	0.007	309.1/348	0.93	0.76	31.56%

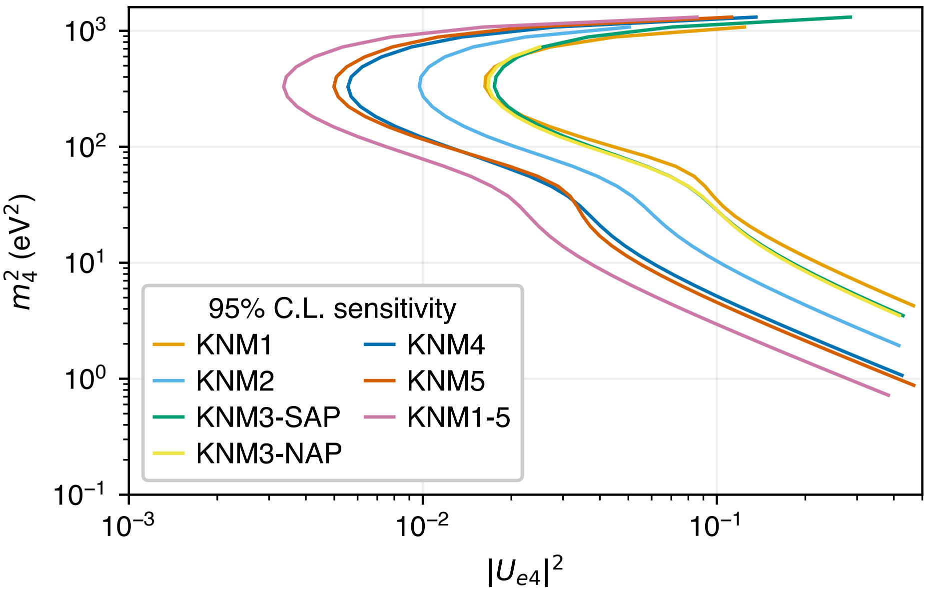

Figure 4.9: Sensitivity contours at 95% C.L. in the sterile neutrino parameters space from first unblinding considering both statistical and systematic uncertainties. There are only minor differences compared to the contours considering only statistical uncertainties. This is an indicator that the analysis is dominated by statistical uncertainties.

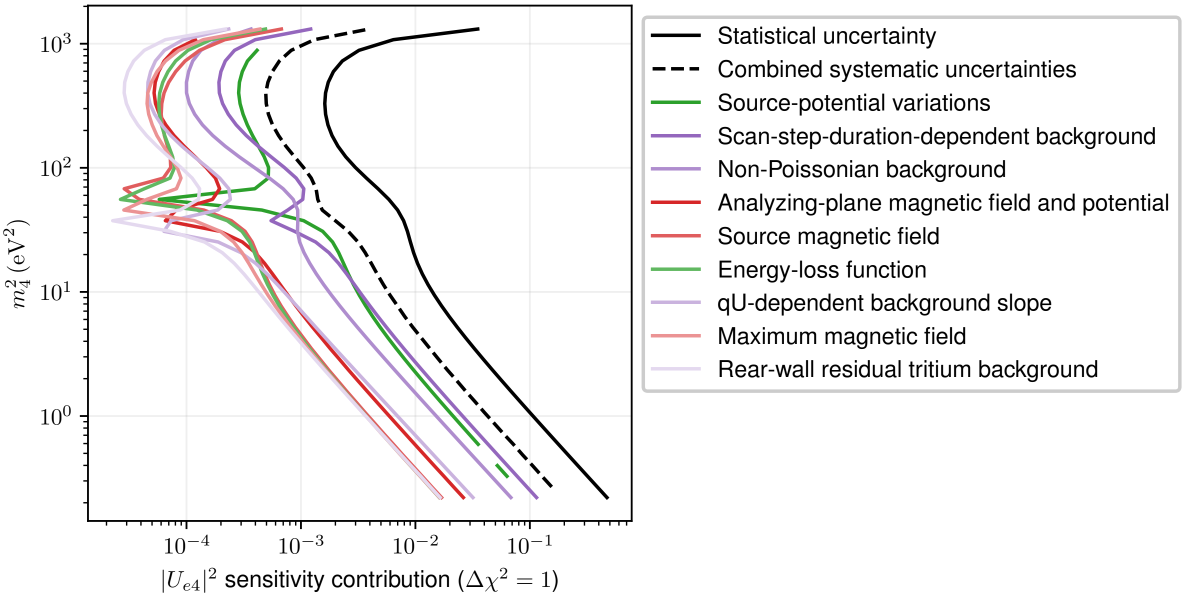

Figure 4.10: Contributions of statistical and systematic uncertainties on sterile neutrino mixing $|U_{e4}|^2$ sensitivity for the KNM1-5 dataset. The presented raster contours are based on the systematic parameters of the first unblinding. Source related systematics are shown in green, background related in purple and transmission related in red. Lightness of the line color indicates the level of impact with higher impact denoted by a darker color. The statistical uncertainty dominates over the combined uncertainty from all systematics.

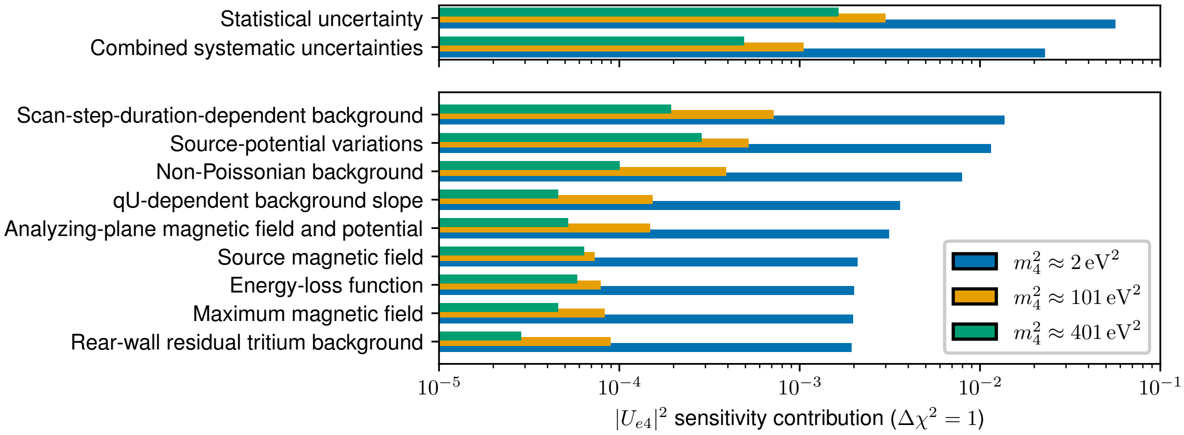

Figure 4.11: Contributions of statistical and systematic uncertainties on sterile neutrino mixing $|U_{e4}|^2$ sensitivity for the KNM1-5 dataset. The presented results are based on the systematic parameters of the first unblinding. It is easier to see how the relative impact of the systematic uncertainties changes with increasing sterile neutrino mass compared to Figure 4.10.

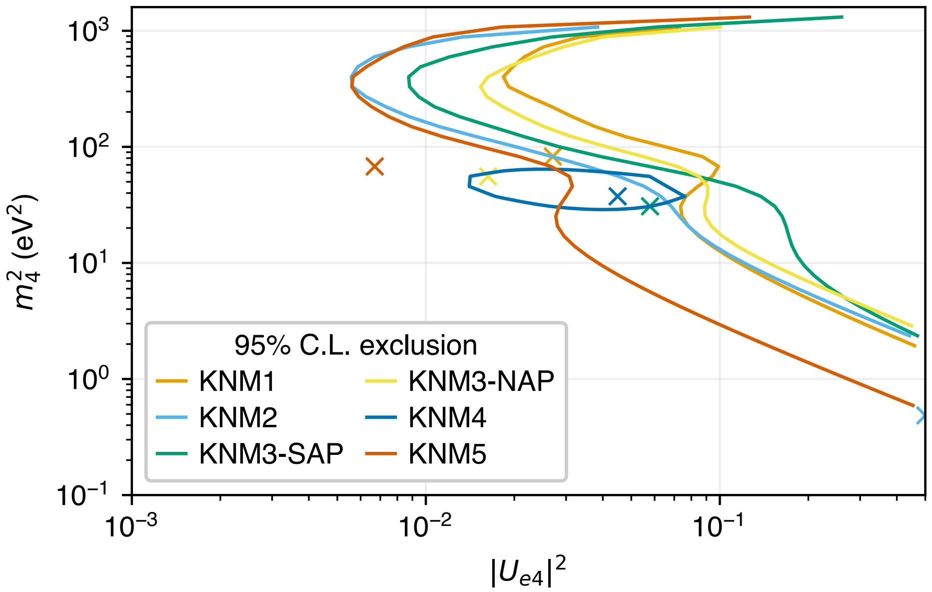

Figure 4.12: Exclusion contours at 95% C.L. in the sterile neutrino parameters space from first unblinding considering both statistical and systematic uncertainties. For KNM4 a closed contour is seen as a sterile neutrino signal was observed at $m_4^2 = 37.49\text{eV}^2$, $|U_{e4}|^2 = 0.045$ at 99.94% C.L.

4.5 Post-unblinding Investigation

Multiple investigative approaches were employed to identify the source of the closed contour in KNM4. A summary of the findings is provided below, with further details available in Appendix A.7.

- **Dataset subdivision and combination**
  - The KNM4 data were divided into "up", "down", and "random" subsets based on scan-set direction, and Grid scans were performed to extract best-fit sterile neutrino parameters.
  - Significant signals were observed in the KNM4-down and KNM4-random subsets.
  - Pairs of KNM4 subsets (up+down, down+random, random+up) were combined and re-analysed, yielding significant signals in all combinations.
  - A similar subdivision of KNM5 data (up, down, random) was performed, but no significant signal was found in any KNM5 subset.
  - These results suggested that scan-direction alone could not fully account for the KNM4 anomaly, motivating further investigation of other experimental factors.
- **Measurement-configuration studies**
  - KNM4 was further divided into five datasets KNM4-(a–e) based on measurement time distributions and Penning-trap operation.
  - Initial analyses using a common scan-step-duration-dependent background parameter found significant signals in datasets KNM4-b and KNM4-e.
  - Dataset-specific background parameters and variances for shift/drift in the source-potential were re-estimated, yet signals persisted in KNM4-b and KNM4-e.
  - For the KNM4-b dataset, scan durations were trimmed from three hours to two hours, reducing but not eliminating the signal.
  - These findings indicated that variations in measurement timing and Penning-trap operation influenced the anomaly but were not sufficient to explain the observed sterile neutrino like signal.
- **Scan-step-duration-dependent background investigations**
  - As a test, the uncertainty on the scan-step-duration-dependent background rate for KNM4-b was increased ten-fold, producing open contours and suppressing the signal.
  - A quadratic time-dependent model for scan-step-duration-dependent background was implemented based on new simulations and dedicated measurements, replacing the linear model.
  - Cross-fitting the Asimov data using both linear and quadratic models demonstrated that model mismatch could lead to a significant change in the resulting contour.
  - Re-analysis of the experimental KNM4-b dataset with the quadratic model yielded open contours but high-significance best-fits near the detection threshold.
  - These studies confirmed that an inaccurate background-rate model could be a contributor to the apparent sterile-neutrino signal in KNM4-b, though additional systematic effects may also play a role.
- **Systematics and energy-loss model studies**

- As a test, source-potential systematics were varied for KNM4-e by increasing uncertainties, but closed contours remained.
- Energy-loss parameters were refitted separately for integral and differential measurements, revealing significant discrepancies.
- Uncertainties on all energy-loss parameters were increased ten-fold, but closed contours remained for KNM4-e.
- Sensitivity-like contours for the combined KNM1–5 Asimov dataset showed degraded sensitivity at high mass due to increased energy-loss uncertainties.
- Dedicated teams focusing on systematic parameter estimation further refined estimates of both the column density and rear-wall background parameters.
- The column density assessment was updated to incorporate the energy-dependent emission angle of the monoenergetic photoelectron source. Details can be found in [135, Section 3.1].
- A minor software bug affecting rear-wall background estimation was identified and corrected. Details can be found in [194].

4.5.1 Re-combination of KNM4 Data

Although the post-unblinding technical investigations led to several methodological and systematic updates, the closed contour observed in the KNM4 dataset remained. A detailed examination of the mean best-fit endpoint (E_0) values, as illustrated in Figure 4.13, revealed a distinct pattern [250]. Specifically, the E_0 values derived from the KNM4-a and KNM4-b datasets were found to be approximately 60 meV lower than those obtained from KNM4-d and KNM4-e, with the KNM4-c subset and the combined KNM4 dataset exhibiting intermediate values.

The drift in the endpoint, combined with difference in the measurement time distributions (MTDs), introduces a distinct structure in the integrated β-decay spectrum of the combined KNM4 dataset. This spectral feature was mistakenly interpreted as a sterile neutrino signature during the analysis [135, Section 5.3]. The observed $\approx 60\,\mathrm{mV}$ shift is effectively captured by the $\sigma^2_{\mathrm{shift,drift}}$ parameter (see Table A.6). Consequently, the KNM4 dataset was divided into two subsets, KNM4-NOM and KNM4-OPT, based on the MTDs (see Figure 4.14).

A comprehensive summary of the statistics in these newly defined datasets is presented in Table 4.5. Furthermore, the updated mean E_0 values across patches for KNM4-NOM and KNM4-OPT are provided in Figure 4.15. The complete set of systematic parameters employed in the final KNM1–5 analysis, including those related to energy loss and potential drifts, is detailed in Table A.9 and Table A.8.

Table 4.5: KNM4 statistics summary after splitting of the dataset: All values refer to the energy range down to 40 eV below the endpoint. The number of background electrons is approximated based on the five background scan-steps.

Dataset	Scans	Scan-steps	Active Pixels	Net Meas. Time (h)	Signal Electrons	Background Electrons	Sig./Bg.
KNM4-NOM†	320	28	126	835	5.25×10^6	3.91×10^5	13.43
KNM4-OPT†	150	28	126	432	4.38×10^6	2.02×10^5	21.65

† *Shifted analyzing plane (SAP)*

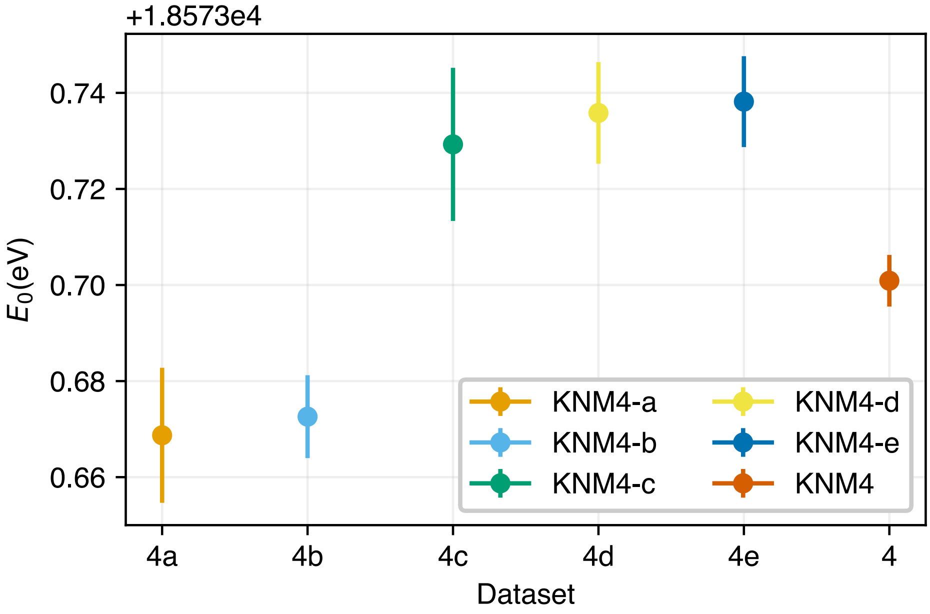

Figure 4.13: Best-fit values and uncertainties of endpoint E_0 for the KNM4-x datasets with $m_\nu^2 = 0\,\mathrm{eV}^2$, $m_4^2 = 0\,\mathrm{eV}^2$ considering only statistical uncertainties.

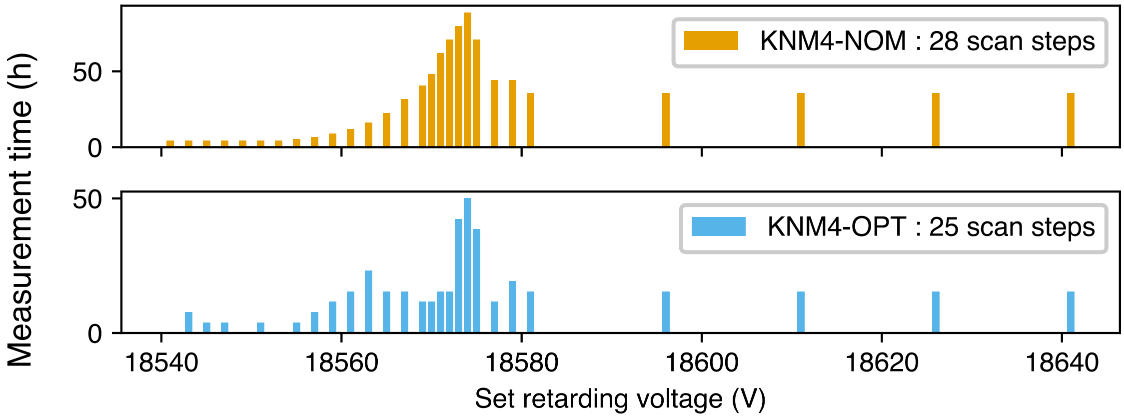

Figure 4.14: Measurement time distributions used during KNM4-NOM and KNM4-OPT periods.

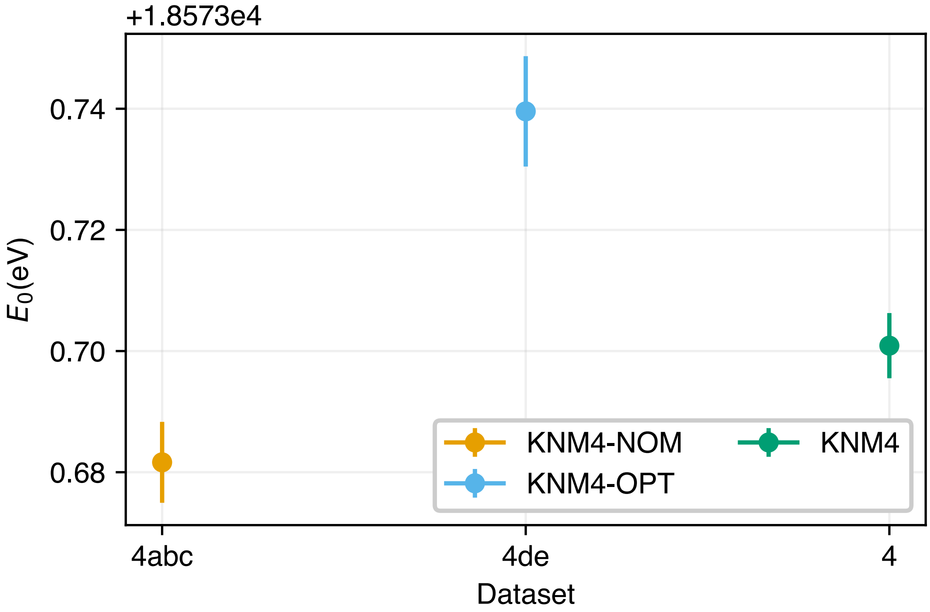

Figure 4.15: Best-fit values and uncertainties of endpoint E_0 for the KNM4-NOM and KNM4-OPT datasets with $m_\nu^2 = 0\,\mathrm{eV}^2$, $m_4^2 = 0\,\mathrm{eV}^2$ considering only statistical uncertainties.

Table 4.6: Summary of the number of data points, the number of fit parameters and number of constrained parameters per data set. This is for the case where the active neutrino mass is fixed to 0. Numbers are provided for analysis considering only statistical uncertainties and both statistical and systematic uncertainties.

Data set	No. of data points	stat.-only			total		
		Fit param.	Constr.	dof	Fit param.	Constr.	dof
KNM1	27	5	0	22	24	19	22
KNM2	28	5	0	23	24	19	23
KNM3-SAP	392	44	0	348	106	62	348
KNM3-NAP	28	5	0	23	27	22	23
KNM4-NOM	392	44	0	348	106	62	348
KNM4-OPT	350	44	0	306	105	61	306
KNM5	392	44	0	348	105	61	348
KNM1-5	1609	180	0	1429	340	160	1429

4.6 Modified Unblinding Protocol

After the first unblinding and addressing the technical issues with data combination in KNM4 and re-evaluation of several systematics, a new protocol was developed for the final unblinding. The analysis was organized into two phases: IND for individual datasets and COMB for the combined dataset.

Phase IND

In the IND phase, Grid scans were performed for each dataset and $\Delta\chi^2 = \chi^2_{\mathrm{bf}} - \chi^2_{\mathrm{null}}$ were computed without looking individually at the values of χ^2_{bf} and χ^2_{null}. The decision criteria included issuing a warning if any $\Delta\chi^2$ exceeded 5.99 (95% C.L.) and pausing the process if $\Delta\chi^2$ exceeded 9.21 (99% C.L.) to review inputs and notify the neutrino mass analysis team.

Phase COMB

In the COMB phase, the $\Delta\chi^2$ for the combined dataset was calculated without revealing the best-fit sterile neutrino parameters. A threshold of 5.99 (95% C.L.) was set to pause the unblinding of the neutrino mass results.

Fast Feedback: Stat.-Only and Total Analysis

Based on the updated grouping of data and systematic uncertainties listed in Table A.9, the analysis was performed with emphasis on only statistical uncertainties for quick feedback before transitioning to detailed analysis including all systematic uncertainties.

No warnings were triggered during the re-analysis with good agreement between the two analysis teams.

4.7 Final Results

The sensitivity contours for the individual datasets considering both the statistical and systematic uncertainties are shown in Figure 4.16. The KNM5 dataset has the best sensitivity for an individual measurement campaign. The KNM2 dataset has the best sensitivity among NAP campaigns and almost matches that of KNM4-OPT dataset. While both datasets have $\approx 4 \times 10^6$ signal electrons, the KNM4-OPT dataset required only 432 hours of measurement compared to the 694 hours for KNM2 dataset due to the significantly reduced background rate in the SAP configuration.

The contributions of systematic uncertainties to the sterile neutrino mixing sensitivity for the combined dataset are shown in Figure 4.17. Although the relative importance of these uncertainties varies between lower and higher sterile neutrino masses, the dominant contributions consistently arise from uncertainties in the product of column density and inelastic cross section, as well as from parameters of the energy-loss function. In NAP campaigns, the non-Poissonian background has the highest contribution. For SAP campaigns KNM3-SAP and KNM4-NOM, the scan-step-duration-dependent background induced by the Penning trap is the dominant systematic contributor. For the other SAP campaigns KNM4-OPT and KNM5, the dominant systematic contributor is the product of column density and inelastic cross section.

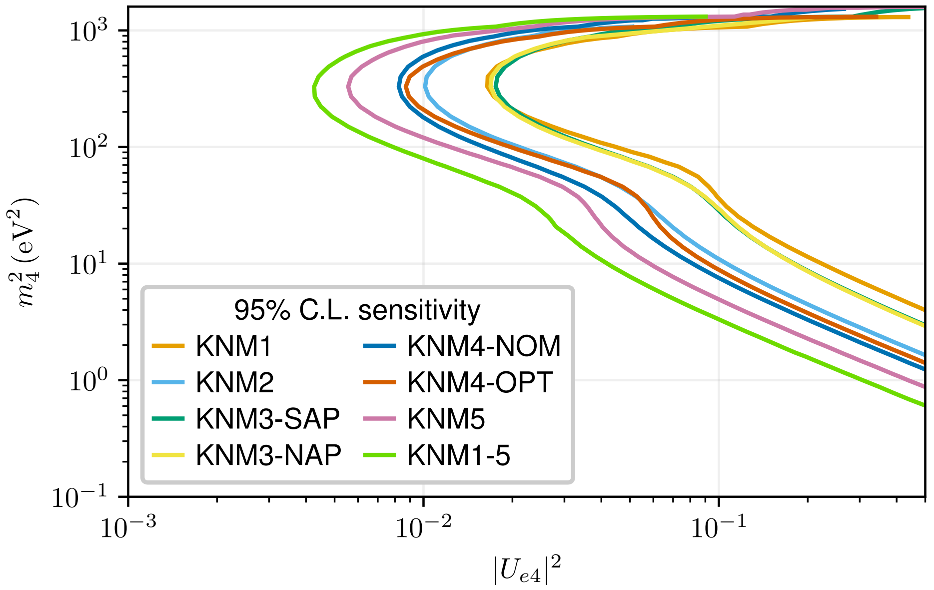

Figure 4.16: Sensitivity contours at 95% C.L. in the sterile neutrino parameters space considering both statistical and systematic uncertainties. There are only minor differences compared to the contours considering only statistical uncertainties.

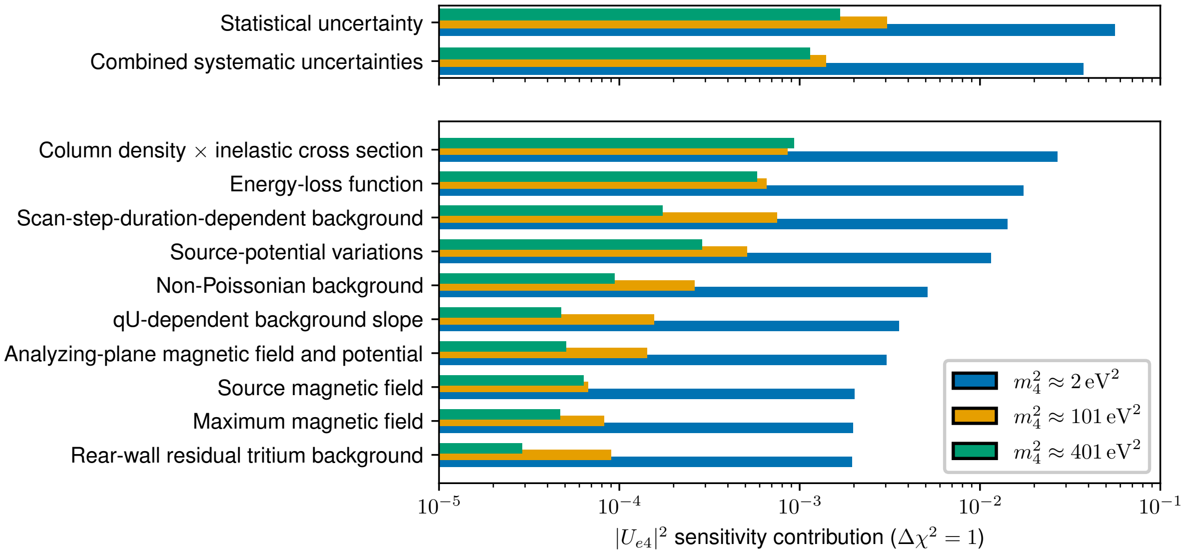

Figure 4.17: Contributions of statistical and systematic uncertainties on sterile neutrino mixing $|U_{e4}|^2$ sensitivity for the KNM1-5 dataset. The presented results are based on the systematic parameters of the final unblinding. Due to the increased uncertainties of column density × inelastic cross section and energy-loss function during the post-unblinding investigation, their impact on the $|U_{e4}|^2$ sensitivity increases significantly compared to their impact in Figure 4.11.

Table 4.7: Summary of the best-fit sterile neutrino parameters for KNM1-5: Results presented for individual and combined dataset. No significant sterile signal observed in any campaign.

Data set	m_4^2	$\lvert U_{e4}\rvert^2$	$\chi^2_{\mathrm{bf}}/\mathrm{dof}$	p	$\Delta\chi^2_{\mathrm{null}}$	Significance
KNM1	82.63	0.027	22.1/22	0.46	1.40	50.36 %
KNM2	0.33	0.500	27.7/23	0.23	0.34	15.77 %
KNM3-SAP	25.26	0.058	309.5/348	0.93	1.75	58.30 %
KNM3-NAP	725.98	0.005	31.1/23	0.12	0.18	8.56 %
KNM4-NOM	45.68	0.024	360.2/348	0.31	2.58	72.48 %
KNM4-OPT	884.56	0.013	309.5/306	0.43	1.69	57.12 %
KNM5	82.63	0.006	309.3/348	0.93	0.88	35.75 %
KNM1-5	55.66	0.011	1374.7/1430	0.85	4.00	86.50 %
KNM1-5 ($m^2_{\nu,\mathrm{bf}} = 0.02\,\mathrm{eV}^2$)	55.66	0.013	1373.3/1429	0.85	2.98	77.47 %

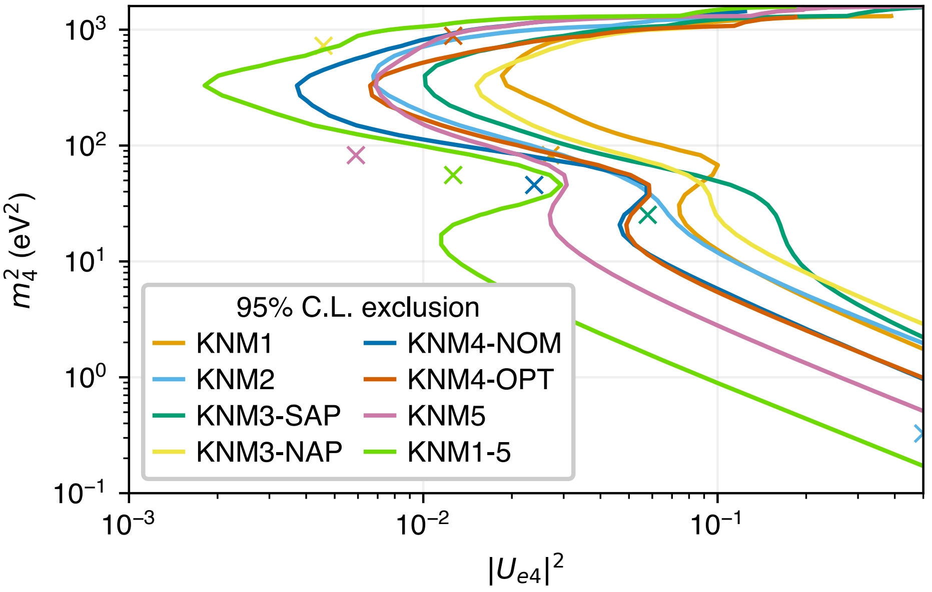

Figure 4.18: Exclusion contours at 95% C.L. in the sterile neutrino parameters space from final unblinding considering both statistical and systematic uncertainties.

Another source of uncertainty not accounted for in the presented analysis was the uncertainty in the final state distribution (FSD) of the daughter nuclei resulting from the β-decay.. As shown in [137, Section 9], using improved estimates of these uncertainties [231], their effect on the $|U_{e4}|^2$ sensitivity is at least an order of magnitude smaller than that of the systematic uncertainties considered in Figure 4.11. Consequently, the uncertainty in FSD is not expected to have a significant impact on the results presented in this thesis.

The best-fit sterile neutrino parameters along with their significances as confidence levels and p-values obtained from the re-analysis of the experimental data are summarized in Table 4.7. No significant sterile neutrino signal was detected in any of the individual datasets or the combined dataset. Exclusion contours at 95% C.L. are reported in Figure 4.18.

The sensitivity and exclusion contours along with the best-fit sterile neutrino parameters considering both the statistical uncertainties and systematic uncertainties are shown in Figure 4.19. In Figure 4.20, the exclusion contours for the KNM1-2 dataset from the re-analysis and the KNM1-5 contour from the final unblinding are compared with the published KNM1-2 exclusion

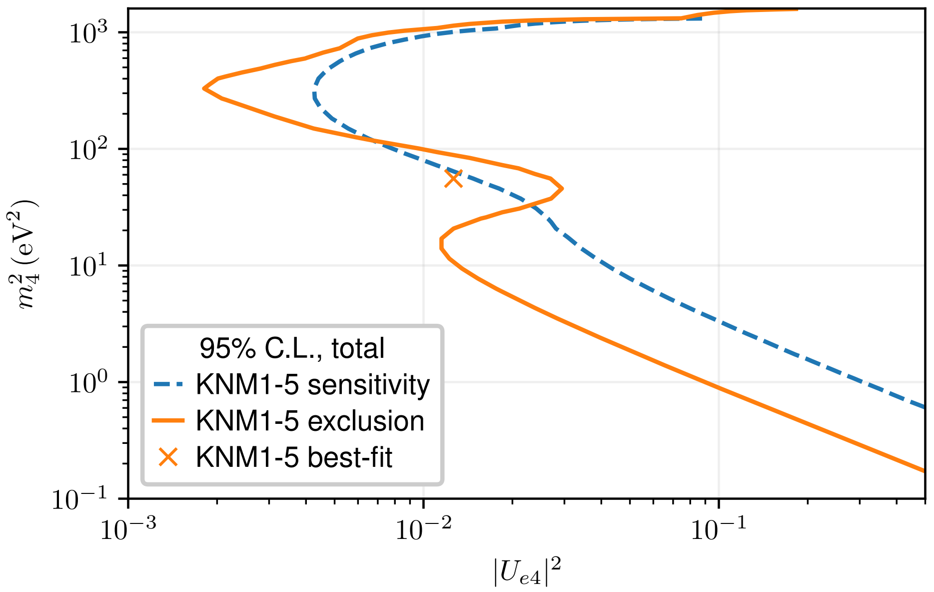

Figure 4.19: Sensitivity and exclusion contours at 95% C.L. in the sterile neutrino parameters space from final unblinding considering both statistical and systematic uncertainties for the KNM1-5 dataset. The best-fit sterile neutrino parameters $m_4^2 = 55.66\,\mathrm{eV}^2$, $|U_{e4}|^2 = 0.013$ correspond to a p-value of 0.1.

contour [12]. The exclusion contour obtained from the re-analysis of the KNM1-2 dataset using the pull-term approach Section 4.2.2 matches well with the published KNM1-2 exclusion contour obtained using the covariance matrix approach Section 4.2.2.1. Significant improvement over the KNM1–2 contour was achieved by the six-fold increase in statistics and tighter control of systematics. Compared to the KNM1-2 exclusion contour, the KNM1-5 exclusion contour has a pronounced feature for $20\,\mathrm{eV}^2 \lesssim m_4^2 \lesssim 100\,\mathrm{eV}^2$ which can be attributed to the value of the best-fit sterile neutrino parameters.

4.8 Crossing of Sensitivity and Exclusion Contours

In Figure 4.19, the sensitivity and exclusion contours are observed to intersect. This intersection was hypothesized to result from statistical fluctuations in the data. To investigate this hypothesis, the Grid scans performed on the KNM5 and KNM1-5 pseudo-experiments, which were described in Section 4.3 and Appendix A.2 for the purpose of studying the empirical distributions of χ^2 and $\Delta\chi^2$, were employed. For each pseudo-experiment, assuming the $\Delta\chi^2$ test statistic follows a 2 degree of freedom chi-squared distribution, contours were computed at the 95% confidence level (C.L.) which corresponds to $\Delta\chi^2 \approx 5.99$. The computed contours were grouped based on the value of $\Delta\chi^2$, specifically whether it was less than or greater than 5.99. The group with $\Delta\chi^2 < 5.99$ contained open contours, while the group while $\Delta\chi^2 > 5.99$ contained closed contours.

The sensitivity contour, exclusion contour, and box plots for the open contours from the KNM5 pseudo-experiments are shown in Figure 4.21. These box plots are constructed based on the median, a robust measure of central tendency less sensitive to outliers than the mean [124]. The boxes represent the interquartile range, encompassing the middle 50% of the data between the first and third quartiles. The whiskers extend to the 2.5th and 97.5th percentiles, illustrating the range within which 95% of the data points lie, thereby providing insight into the data's

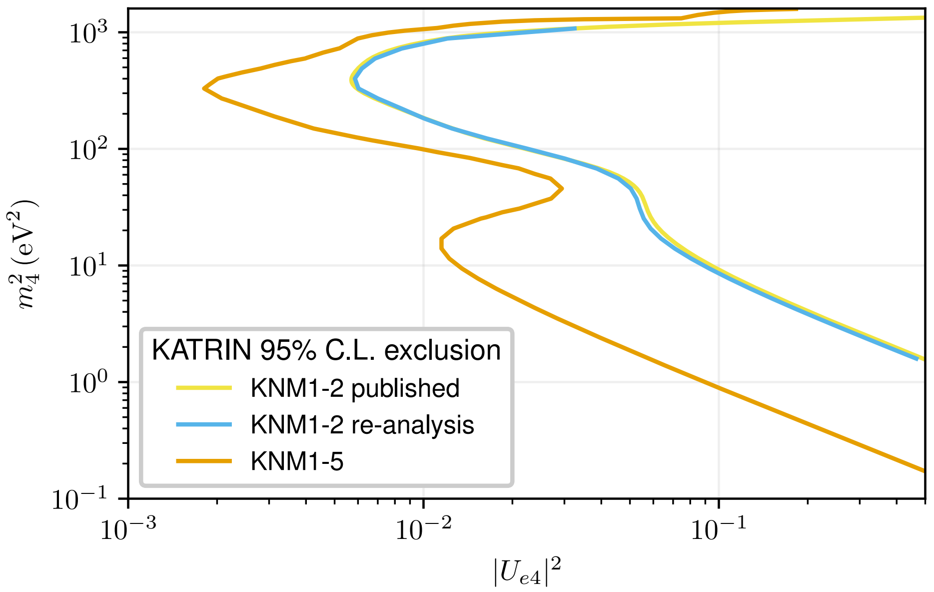

Figure 4.20: Comparison of KATRIN sterile neutrino exclusion contours. The published KNM1-2 contour [12] which was obtained using the covariance matrix approach match well with the KNM1-2 contours obtained using the pull-term approach. Minor differences can be attributed to improved estimation of systematic uncertainties. The contour from the KNM1-5 dataset excludes a significantly larger part of the sterile neutrino parameter space.

variability and potential outliers. The results for the KNM1–5 pseudo-experiments are presented in Figure 4.22.

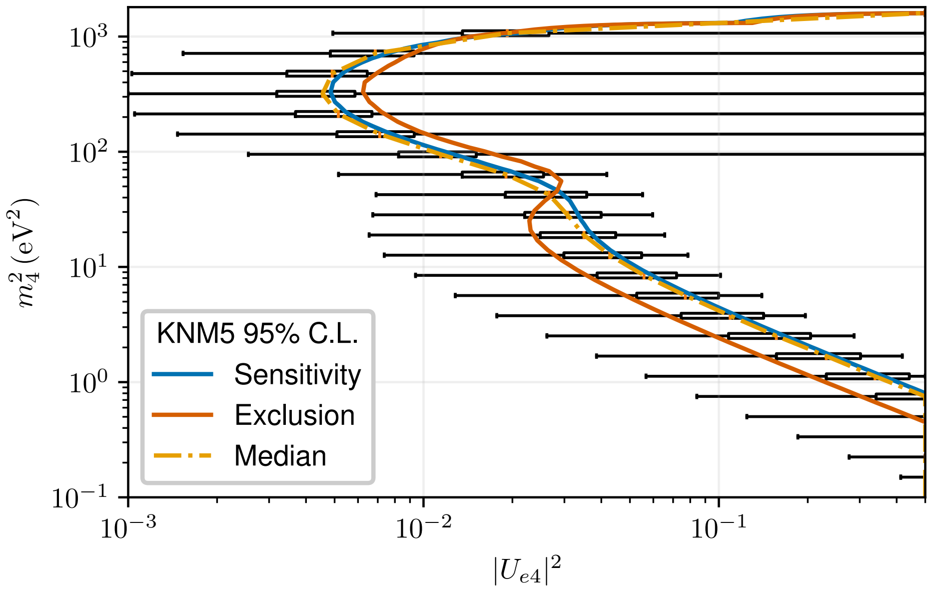

Figure 4.21: Box plots for the open contours from the KNM5 pseudo-experiments, showing the sensitivity contour, exclusion contour, and the median of the open contours. The median of the open contours aligns well with the sensitivity contour.

For KNM5 and KNM1-5, the exclusion contours lie within the 95% intervals, supporting the hypothesis that the observed intersection was likely due to statistical fluctuations in the data.

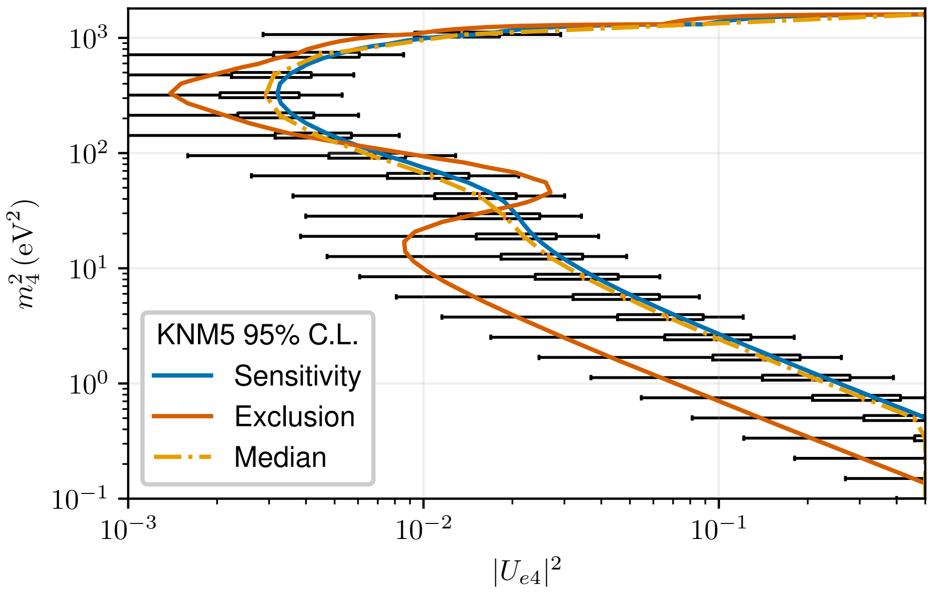

Figure 4.22: Box plots for the open contours from the KNM1-5 pseudo-experiments, showing the sensitivity contour, exclusion contour, and the median of the open contours. The median of the open contours aligns well with the sensitivity contour.

4.9 Active Neutrino Mass as a Fit Parameter

The analyses in the previous sections were performed with $m_\nu^2 = 0$ which is justified if the sterile neutrino mass is considered to be significantly greater than the active neutrino mass. However, for low $m_4^2 \lesssim 1\,\mathrm{eV}^2$ and $|U_{e4}|^2 \approx 0.5$, the active and sterile neutrino branches become degenerate. This section reports exclusion contours when the active neutrino mass is considered a fit parameter. Four scenarios for the active neutrino mass were studied.

1. The squared active neutrino mass is fixed to $0\,\mathrm{eV}^2$.
2. The squared active neutrino mass is an unconstrained fit parameter and is allowed to have non-physical values.
3. The squared active neutrino mass is only allowed to have a physically meaningful value which is always less than the sterile neutrino mass. This is referred to as the “technical constraint”.
4. The active neutrino mass is a fit parameter but is penalized by a pull-term centered around $0\,\mathrm{eV}^2$ with $\sigma = 1\,\mathrm{eV}^2$.

Figure 4.23 shows the exclusion contours considering only statistical uncertainties obtained with different constraints on the active neutrino mass. The technical constraint case is interesting as the contour follows the contour of active neutrino mass fixed to $0\,\mathrm{eV}^2$ for $m_4^2 \lesssim 40\,\mathrm{eV}^2$ and the contour of the unconstrained case for higher masses. This behavior can be better understood by visualizing the best-fit values of the active neutrino mass in Figure 4.24. For $m_4^2 \lesssim 40\,\mathrm{eV}^2$, the best-fit active neutrino mass is negative. Hence with the technical constraint, this leads to the same exclusion as fixing the active neutrino mass to $0\,\mathrm{eV}^2$.

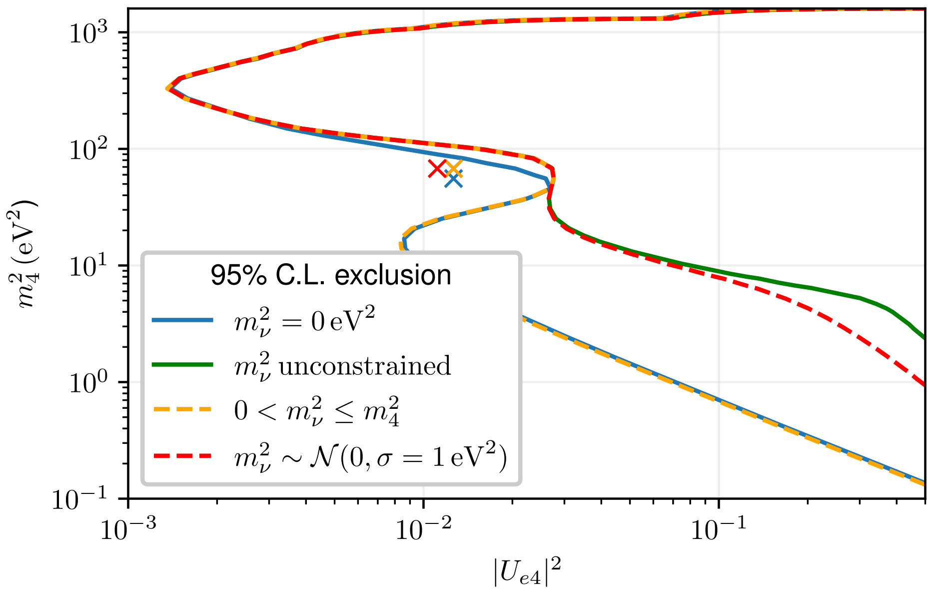

Figure 4.23: Exclusion contours of the KNM1-5 dataset with only statistical uncertainties obtained for different restrictions on the active neutrino mass.

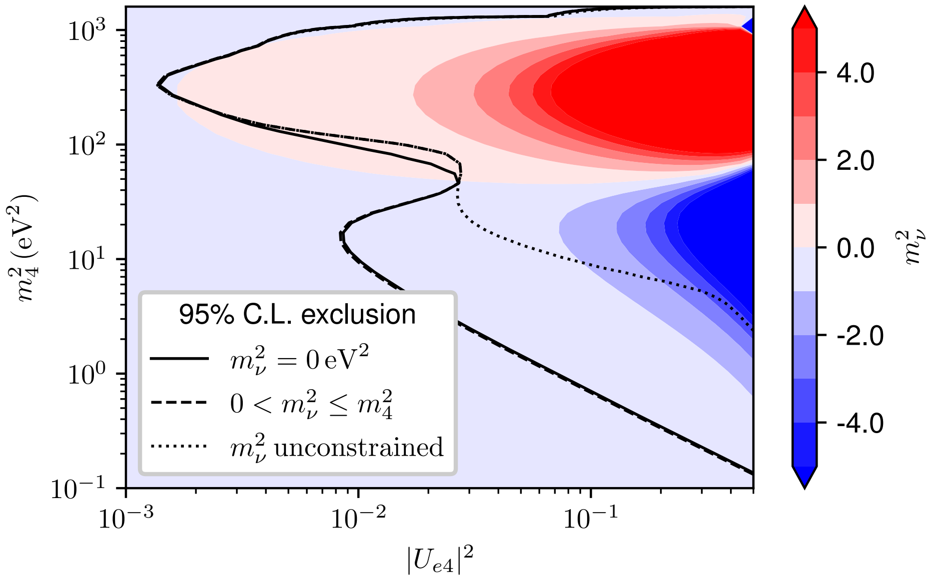

Figure 4.24: Contour map of the best-fit active neutrino mass when it is considered a fit parameter without any restriction shown as background for the sensitivity contours from Figure 4.23. In the lower sterile neutrino mass region the contour with technical constraint follows the contour with neutrino mass fixed to $0\,\mathrm{eV}^2$ as the best-fit active mass is negative.

4.10 Correlation Between Active and Sterile Neutrino Masses

To quantify the correlation between the active and sterile neutrino masses, many Asimov datasets were generated for several different values of m_4^2, $|U_{e4}|^2$ and $m_\nu^2 = 0\,\mathrm{eV}^2$. The generated datasets were based on datasets used in the KNM1-5 final results Section 4.7. For each Asimov dataset, the χ^2 Equation 4.5 was minimized five times by varying m_4^2 stepwise by $\pm 1\,\mathrm{eV}^2$ around the respective true m_4^2 values used to generate the Asimov dataset. The $|U_{e4}|^2$ was fixed to the respective true values. Each minimization was performed with respect to E_0, Sig and Bg parameters and a common m_ν^2 parameter. The approximately linear relationship $m_\nu^2 = \alpha_{\text{slope}} \cdot m_4^2 + \text{const.}$ is determined in the neighborhood each $(m_4^2, |U_{e4}|^2)$ set of values. The value α_{slope} is a quantification of the linear correlation between the squared active and sterile neutrino masses.

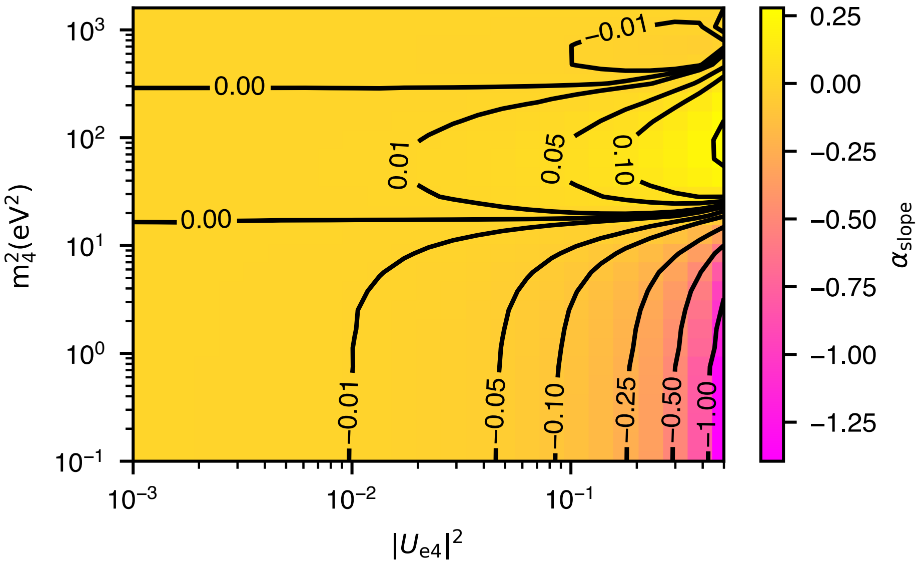

Figure 4.25: Contour map of the best-fit active neutrino mass displayed as a background, overlaid with contour lines representing the correlation between squared active and sterile neutrino masses.

A contour plot of α_{slope} values is shown in Figure 4.25. For small $|U_{e4}|^2 \lesssim 0.01$ values of sterile neutrino mixing, the correlation is small ($|\alpha_{\text{slope}}| < 0.01$). For $m_4^2 \lesssim 20\,\text{eV}^2$ a negative correlation which increases in magnitude with $|U_{e4}|^2$ is observed. As expected, the correlation is maximally negative for $|U_{e4}|^2 \approx 0.5$ and low m_4^2 as the active and sterile branches are degenerate. For $20\,\text{eV}^2 \lesssim m_4^2 \lesssim 300\,\text{eV}^2$, a small positive correlation is observed. In the correlation study for KNM1-2 reported in [12, Fig. 4], the small positive correlation region extends till $m_4^2 \approx 1000\,\text{eV}^2$. However in Figure 4.25 it can be seen that there is a region of extremely weak negative correlation for high $m_4^2 \gtrsim 300\,\text{eV}^2$ and high $|U_{e4}| \gtrsim 0.1$. This minor deviation likely arises from the interplay of the χ^2 optimization process, curve fitting to obtain $|\alpha_{\text{slope}}|$ and contour finding based a 25×25 grid of $|\alpha_{\text{slope}}|$ values. Given the extremely weak correlation observed, this departure from the KNM1-2 results did not warrant further investigation.

4.11 Comparison of KATRIN Bounds with Complementary Experiments

The new 95% C.L. exclusion contour is compared with those from other electron-(anti)neutrino disappearance experiments in Figure 4.26. To align β-decay results (expressed in $|U_{e4}|^2$) with oscillation data (reported as $\sin^2(2\theta_{ee}) = 4|U_{e4}|^2(1 - |U_{e4}|^2)$), the appropriate transformation was applied, and the approximation $\Delta m_{41}^2 \approx m_4^2 - m_\nu^2$ (valid to $2 \times 10^{-4}\,\text{eV}^2$) was used under the assumption $0 \leq m_\nu^2 < m_4^2$ [102]. A large portion of the Reactor Antineutrino Anomaly parameter space was excluded [182], and most of the gallium-anomaly region, including the combined BEST+GALLEX+SAGE best-fit ($\Delta m_{41}^2 \approx 1.25\,\text{eV}^2$, $\sin^2(2\theta_{ee}) \approx 0.34$), was excluded at 96.56% C.L. [38, 39], thereby challenging the light sterile-neutrino hypothesis. Complementarity with reactor-oscillation searches was demonstrated by probing larger Δm_{41}^2 values (up to a few eV^2), with sensitivities intersecting those of reactor experiments at $\Delta m^2_{41} \sim 3\,\mathrm{eV}^2$ for $\sin^2(2\theta_{ee}) \simeq 0.1$. Among reactor studies, the strongest exclusion limits are currently set by PROSPECT [26] and STEREO [22], while DANSS achieved high sensitivity through the collection of $\sim$ 4 million events [171]. Finally, the Neutrino-4 claim at $\Delta m^2_{41} = 7.3\,\mathrm{eV}^2$ ($m_4 \simeq 2.70 \pm 0.22\,\mathrm{eV}$) was fully excluded by the KNM1–5 dataset, and its best-fit was rejected at 99.99% C.L. [234].

The projected final sensitivity of the KATRIN experiment at the 95% confidence level is estimated assuming a net measurement time of 1000 days, following the methodology outlined in [12]. The background rate is anticipated to be 130 mcps, based on 117 active detector pixels, and the systematic uncertainties correspond to those defined in the design configuration [65].

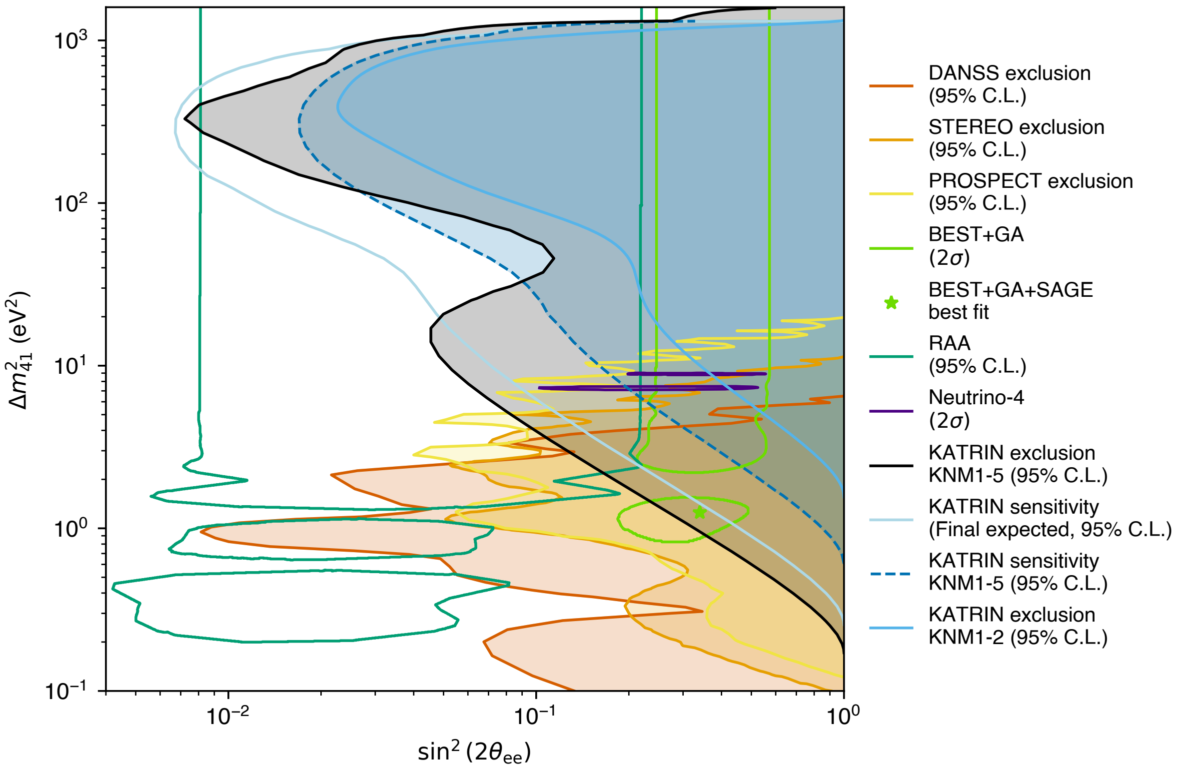

Figure 4.26: 95% C.L. exclusion curve in the $(\Delta m^2_{41}, \sin^2(2\theta_{ee}))$ parameter space obtained from the analysis of the KNM1-5 dataset compared with the 95% C.L. contour of 3+1 neutrino oscillations allowed by the reactor and gallium anomalies [182, 39]. The green star symbol represents the best-fit point from the BEST, GALLEX, and SAGE experiments.

5

A Bayesian Approach to the Sterile Neutrino Search with KATRIN

The analysis framework and results presented in Chapter 4 for the sterile neutrino search with KATRIN were based on the Frequentist paradigm of statistical inference. This paradigm assumes that a true set of parameters exists, and efforts were made to estimate them from a single representative dataset. The goodness-of-fit quantified how well the model with the best-fit sterile neutrino parameters described the observed data, while hypothesis testing, evaluated at a predefined significance level, was employed to assess the presence of a sterile neutrino signal. All model arguments were treated solely as parameters and not as random variables.

An alternative approach is based on the Bayesian paradigm of statistical inference. In this framework, the model parameters are treated as random variables, and the goal is to determine their probability distributions given the observed data. This approach naturally incorporates external information, such as estimates of systematic uncertainties, which are often modeled using Gaussian distributions. The active and sterile neutrino parameters are also treated as random variables with distributions that reflect existing knowledge. The Bayesian analysis then uses the observed data to refine this knowledge, resulting in distributions that reflect both existing knowledge and experimental measurements. One key advantage of the Bayesian approach is that it does not rely on knowledge of the asymptotic distribution of the test statistics under the null hypothesis, verification of which can be computationally intensive in the Frequentist framework.

Bayesian analysis specifically adapted to the KATRIN experiment has garnered significant attention in the context of neutrino mass measurements, as evidenced by numerous publications [233, 188, 118] and several dedicated theses. This chapter focuses on developing a Bayesian analysis framework specifically for the sterile neutrino search with KATRIN. It begins in Section 5.1 with an introduction to Bayesian inference, followed by the development of the mathematical formulation for inferring the squared sterile neutrino mass m_4^2 and mixing parameter $|U_{e4}|^2$, in the context of KATRIN. An approach analogous to hypothesis testing, based on Bayes factor, is introduced in Section 5.2, followed by methods for evaluating the impact of uncertainties in systematic variables in Section 5.3. The numerical integration algorithms employed in the analysis are detailed in Section 5.4. Finally, results obtained from applying the framework to the KNM2 Asimov dataset are presented in Section 5.5, followed by an outlook in Section 5.6.

5.1 Bayesian Framework for Inference

Bayesian inference provides a methodology for updating knowledge about model parameters in light of observed data. Let $\boldsymbol{\theta}$ denote the vector of all model parameters and let $\mathcal{D}$ denote the observed data. Bayes' theorem [40] states that the posterior distribution of $\boldsymbol{\theta}$ given $\mathcal{D}$ is proportional to the product of the likelihood and the prior:

$$p(\boldsymbol{\theta} \mid \mathcal{D}) = \frac{p(\mathcal{D} \mid \boldsymbol{\theta})\, p(\boldsymbol{\theta})}{p(\mathcal{D})}, \tag{5.1}$$

where $p(\boldsymbol{\theta})$ is the prior distribution, expressing prior knowledge or beliefs about $\boldsymbol{\theta}$ before observing data and $p(\mathcal{D} \mid \boldsymbol{\theta})$ is the likelihood function, representing the probability (or probability density) of obtaining the data $\mathcal{D}$ under the assumption that the true parameters are $\boldsymbol{\theta}$ [100, 128]. The term $p(\mathcal{D})$ is the evidence, obtained by integrating the product of likelihood and prior over the entire parameter space:

$$p(\mathcal{D}) \;=\; \int p(\mathcal{D} \mid \boldsymbol{\theta})\, p(\boldsymbol{\theta})\, \mathrm{d}\boldsymbol{\theta}\,. \tag{5.2}$$

The evidence serves as a normalizing constant in Bayes' theorem and allows for model comparison.

The quantity of primary interest is often the posterior distribution $p(\boldsymbol{\theta} \mid \mathcal{D})$, which combines prior information and observed data to yield updated inferences about $\boldsymbol{\theta}$. In many applications, one is interested in a subset of parameters, say $\boldsymbol{\theta}_1$, while treating the remaining parameters $\boldsymbol{\theta}_2$ as nuisance parameters. In such cases, one obtains the marginal posterior for $\boldsymbol{\theta}_1$ by integrating (or marginalizing) over $\boldsymbol{\theta}_2$:

$$p(\boldsymbol{\theta}_1 \mid \mathcal{D}) \;=\; \int p(\boldsymbol{\theta}_1, \boldsymbol{\theta}_2 \mid \mathcal{D})\, \mathrm{d}\boldsymbol{\theta}_2 \;=\; \int p(\boldsymbol{\theta} \mid \mathcal{D})\, \mathrm{d}\boldsymbol{\theta}_2\,. \tag{5.3}$$

Computing these high-dimensional integrals often requires numerical techniques such as quadrature, importance sampling, or Markov chain Monte Carlo (MCMC) [235].

In the context of the KATRIN experiment, the general Bayesian framework is applied to analyze electron count data collected at specific retarding voltage set-points. The following describes how the general expressions in Equation 5.1–Equation 5.3 are expressed for the KATRIN datasets and likelihood models.

The datasets employed in the Bayesian analysis were chosen to match those used in the Frequentist analysis to ensure a consistent basis for comparison. Details on the construction of these datasets from raw measurement data are provided in Section 4.1.1. As in the Frequentist framework, the model for the integrated rate at a given retarding voltage set-point U_i, denoted by $\dot{N}_{\mathrm{model}}(qU_i, \boldsymbol{\theta})$ and described in Chapter 3, was used to compute the expected values of the distributions underlying the observed data.

For NAP campaigns, the measured rate $\dot{N}_{\mathrm{exp}}(qU_i)$ at the set-point U_i was assumed to follow a Gaussian distribution, that is,

$$\dot{N}_{\mathrm{exp}}(qU_i) \sim \mathcal{N}\left(\dot{N}_{\mathrm{model}}(qU_i, \boldsymbol{\theta}), \sigma^2_{\dot{N},i}\right), \tag{5.4}$$

where $\sigma^2_{\dot{N},i}$ represents the uncertainty in the measured rate. Assuming that measurements at different set-points were statistically independent, the joint likelihood $p(\mathcal{D} \mid \boldsymbol{\theta})$ of the observed rates $\dot{N}_{\mathrm{exp}}(qU_i)$ conditioned on the parameter vector $\boldsymbol{\theta}$, denoted by $p_{\mathrm{NAP}}(\dot{\boldsymbol{N}}_{\mathbf{exp}}|\boldsymbol{\theta})$, is given by

$$p_{\mathrm{NAP}}(\dot{\boldsymbol{N}}_{\mathbf{exp}}|\boldsymbol{\theta}) \propto \prod_i \exp\left(-\frac{1}{2}\frac{\left(\dot{N}_{\mathrm{exp}}(qU_i) - \dot{N}_{\mathrm{model}}(qU_i, \boldsymbol{\theta})\right)^2}{\sigma^2_{\dot{N},i}}\right). \tag{5.5}$$

For the SAP campaigns, the measured counts $N_{\mathrm{exp},k}(qU_i)$ at the retarding voltage set-point U_i in patch k were modeled using a Poisson distribution, such that

$$N_{\mathrm{exp},k}(qU_i) \sim \mathrm{Pois}\left(\dot{N}_{\mathrm{model},k}(qU_i, \boldsymbol{\theta}) \cdot t_i\right) \tag{5.6}$$

Assuming statistical independence of the counts across retarding voltage set-points and patches, the joint likelihood $p(\mathcal{D} \mid \boldsymbol{\theta})$ of the observed counts $N_{\mathrm{exp},k}(qU_i)$ conditioned on the parameters $\boldsymbol{\theta}$, denoted by $P_{\mathrm{SAP}}(\boldsymbol{N}_{\mathbf{exp}}|\boldsymbol{\theta})$, is given by

$$P_{\mathrm{SAP}}(\boldsymbol{N}_{\mathbf{exp}}|\boldsymbol{\theta}) \propto \prod_{k=1}^{14}\prod_i \frac{\left(\dot{N}_{\mathrm{model},k}(qU_i, \boldsymbol{\theta}) \cdot t_i\right)^{N_{\mathrm{exp},k}(qU_i)} \cdot \exp\left(-\dot{N}_{\mathrm{model},k}(qU_i, \boldsymbol{\theta}) \cdot t_i\right)}{N_{\mathrm{exp},k}(qU_i)!}, \tag{5.7}$$

where $\boldsymbol{N}_{\mathbf{exp}}$ is the vector of all $N_{\mathrm{exp},k}(qU_i)$ values.

Here, the lowercase letter p is used in Equation 5.5 to denote the probability density function for the continuous-valued measured rates $\dot{\boldsymbol{N}}_{\mathbf{exp}}$, whereas the uppercase letter P is used in Equation 5.7 to denote the probability mass function for the discrete-valued measured counts $\boldsymbol{N}_{\mathbf{exp}}$.

The model parameters $\boldsymbol{\theta}$ were categorized into three groups. The first group, $\boldsymbol{\theta}_{\mathbf{physics}} = \{m_\nu^2, m_4^2, |U_{e4}|^2\}$, included the physics parameters of interest. The second group, $\boldsymbol{\theta}_{\mathbf{syst.}}$, contained parameters associated with experimental systematics. The remaining parameters, $\boldsymbol{\theta}_{\mathbf{stat.}}$, included the nuisance parameters endpoint E_0, the signal normalization factor Sig, and the constant background rate $\dot{N}_{\mathrm{bg}}$.

While the Frequentist approach does not incorporate prior information, a fundamental principle of Bayesian analysis is specifying prior distributions $p(\boldsymbol{\theta})$ over these parameters. The nuisance parameters E_0, Sig, and $\dot{N}_{\mathrm{bg}}$ were assumed to follow a uniform distribution, resulting in the prior

$$p(\boldsymbol{\theta}_{\mathbf{stat.}}) = \frac{1}{E_0^{\mathrm{ul}} - E_0^{\mathrm{ll}}} \frac{1}{Sig^{\mathrm{ul}} - Sig^{\mathrm{ll}}} \frac{1}{Bg^{\mathrm{ul}} - Bg^{\mathrm{ll}}} \tag{5.8}$$

where the superscript $^{\mathrm{ul}}$ denotes upper limit and $^{\mathrm{ll}}$ denotes lower limit. Values $E_0^{\mathrm{ll}} = 18573\,\mathrm{eV}$ and $E_0^{\mathrm{ul}} = 18575\,\mathrm{eV}$ were selected based on the estimated endpoint of 18574 eV, derived from the Q-value and the recoil energy of a T_2 molecule [223, 13]. The limits $Sig^{\mathrm{ll}} = 0.9$ and $Sig^{\mathrm{ul}} = 1.1$ were determined from the tritium source stability [42] and its impact on the signal normalization factor [42] and its implications on the signal normalization factor Sig [144]. For NAP campaigns, $\dot{N}_{\mathrm{bg}}^{\mathrm{ll}} = 0.2$ and $\dot{N}_{\mathrm{bg}}^{\mathrm{ul}} = 0.5$ were based on dedicated background measurements reported in [14, 228]. For SAP campaigns, $\dot{N}_{\mathrm{bg}}^{\mathrm{ll}} = 0.0$ and $\dot{N}_{\mathrm{bg}}^{\mathrm{ul}} = 0.3$ were adopted based on [165]. Although Gaussian priors could have been defined based on reported uncertainties, uniform priors were deliberately chosen here to serve as an initial test of the analysis procedure.

The systematic parameters $\boldsymbol{\theta}_{\mathbf{syst.}}$ were assumed to follow a multivariate Gaussian distribution $p(\boldsymbol{\theta}_{\mathbf{syst.}})$ with mean vector $\boldsymbol{\theta}_{\mathbf{ext}}$ and covariance matrix $\boldsymbol{\Sigma}$, both estimated from simulations or dedicated measurements, as discussed in Chapter 3.

The physics parameters $\boldsymbol{\theta}_{\mathbf{physics}}$ were further divided into two subsets: $\boldsymbol{\theta}_{\mathbf{active}} = \{m_\nu^2\}$ and $\boldsymbol{\theta}_{\mathbf{sterile}} = \{m_4^2, |U_{e4}|^2\}$. A distribution $p(m_\nu^2)$ for the active neutrino mass can be derived from other experiments such as those detailed in [56, 32]. The sterile neutrino mixing parameter $|U_{e4}|^2$ can reasonably be assigned a uniform distribution within the interval $[0, 0.5]$. In contrast, assigning a uniform distribution to the squared sterile neutrino mass m_4^2 is challenging, as a uniform distribution necessitates a finite support, whereas theoretical considerations allow for the existence of sterile neutrinos at any mass scale. For this initial study using an Asimov dataset, two prior choices were investigated. The first employed uniform priors over the ranges $m_4^2 \in [0, 1600], \mathrm{eV}^2$ and $|U_{e4}|^2 \in [0, 0.5]$. The second applied log-uniform priors over the same parameter ranges. The log-uniform prior, also referred to as the Jeffreys prior [129], is considered noninformative and is particularly relevant in this context.

The joint prior distribution over the parameters $\boldsymbol{\theta}$ is expressed as

$$p(\boldsymbol{\theta}) = p(m_\nu^2) p(m_4^2, |U_{e4}|^2) p(\boldsymbol{\theta}_{\mathbf{stat.}}) p(\boldsymbol{\theta}_{\mathbf{syst.}}), \tag{5.9}$$

where each factor corresponds to prior knowledge or assumptions about a distinct parameter subset. Together with the likelihood defined in Equation 5.5, the goal of Bayesian inference is to update the probability distribution over $\boldsymbol{\theta}$ in light of the observed data $\dot{\boldsymbol{N}}_{\mathbf{exp}}$. Applying Bayes' theorem [40], the posterior distribution becomes

$$p_{\mathrm{NAP}}(\boldsymbol{\theta} | \dot{\boldsymbol{N}}_{\mathbf{exp}}) = \frac{p_{\mathrm{NAP}}(\dot{\boldsymbol{N}}_{\mathbf{exp}} | \boldsymbol{\theta})\, p(\boldsymbol{\theta})}{p(\dot{\boldsymbol{N}}_{\mathbf{exp}})}, \tag{5.10}$$

where $p(\dot{\boldsymbol{N}}_{\mathbf{exp}})$ is the distribution of the observed data, also known as the evidence. This term is independent of the model and, for the purposes of the analysis, was treated as an unknown constant. The posterior distribution $p_{\mathrm{NAP}}(\boldsymbol{\theta}|\dot{\boldsymbol{N}}_{\mathbf{exp}})$, is written more compactly without the evidence term as

$$p_{\mathrm{NAP}}(\boldsymbol{\theta}|\dot{\boldsymbol{N}}_{\mathbf{exp}}) \propto p_{\mathrm{NAP}}(\dot{\boldsymbol{N}}_{\mathbf{exp}}|\boldsymbol{\theta})p(\boldsymbol{\theta}). \tag{5.11}$$

For the sterile neutrino analysis, the primary quantity of interest is the marginal posterior distribution over the sterile parameters $p(\boldsymbol{\theta}_{\mathbf{sterile}}|\dot{\boldsymbol{N}}_{\mathbf{exp}})$, which can be obtained by integrating over the remaining variables from the full distribution:

$$p_{\mathrm{NAP}}(m_4^2, |U_{e4}|^2|\dot{\boldsymbol{N}}_{\mathbf{exp}}) \propto \int_{\boldsymbol{\theta}_{\mathbf{syst.}}} \int_{\boldsymbol{\theta}_{\mathbf{stat.}}} \int_{m_\nu^2} p(\boldsymbol{\theta}|\dot{\boldsymbol{N}}_{\mathbf{exp}})\, \mathrm{d}m_\nu^2\, \mathrm{d}\boldsymbol{\theta}_{\mathbf{stat.}}\, \mathrm{d}\boldsymbol{\theta}_{\mathbf{syst.}}. \tag{5.12}$$

If this process were applied instead to the likelihood $p(\dot{\boldsymbol{N}}_{\mathbf{exp}}|\boldsymbol{\theta})$ across all parameters $\boldsymbol{\theta}$, the result would be the evidence $p(\dot{\boldsymbol{N}}_{\mathbf{exp}})$. Equivalent expressions for the SAP campaigns can be written by replacing the term $p_{\mathrm{NAP}}(\dot{\boldsymbol{N}}_{\mathbf{exp}}|\boldsymbol{\theta})$ with $P_{\mathrm{SAP}}(\boldsymbol{N}_{\mathbf{exp}}|\boldsymbol{\theta})$.

The posterior distribution Equation 5.12 serves as the Bayesian analog to the results of the Frequentist analysis, where the active neutrino mass was treated as a fit parameter and both statistical and systematic uncertainties were incorporated. The Bayesian equivalent of the "stat-only" analysis with active neutrino mass fixed to zero, is given by the conditional posterior distribution,

$$p_{\mathrm{NAP}}(m_4^2, |U_{e4}|^2|\dot{\boldsymbol{N}}_{\mathbf{exp}}, m_\nu^2 = 0\,\mathrm{eV}^2, \boldsymbol{\theta}_{\mathbf{syst.}} = \boldsymbol{\theta}_{\mathbf{ext}}) \propto \int_{\boldsymbol{\theta}_{\mathbf{stat.}}} p(\boldsymbol{\theta}|\dot{\boldsymbol{N}}_{\mathbf{exp}})\, \mathrm{d}\boldsymbol{\theta}_{\mathbf{stat.}}. \tag{5.13}$$

where only the statistical nuisance parameters $\boldsymbol{\theta}_{\mathbf{stat.}}$ are marginalized, and where the active neutrino mass is fixed to $m_\nu^2 = 0\,\mathrm{eV}^2$ and the systematic parameters $\boldsymbol{\theta}_{\mathbf{syst.}}$ are fixed to their nominal values $\boldsymbol{\theta}_{\mathbf{ext}}$.

5.1.1 Computing Highest Posterior Density Regions

Two-dimensional posterior distributions are commonly summarized using Highest Posterior Density (HPD) regions. An HPD region is defined as the smallest area of the parameter space that contains a specified probability mass of the posterior distribution. Formally, for $p_{\mathrm{NAP}}(m_4^2, |U_{e4}|^2|\dot{\boldsymbol{N}}_{\mathbf{exp}})$ the HPD region C at a credibility level $100(1-\alpha)\%$ is defined such that:

$$C = \{m_4^2, |U_{e4}|^2 : p_{\mathrm{NAP}}(m_4^2, |U_{e4}|^2|\dot{\boldsymbol{N}}_{\mathbf{exp}}) \geq b\}, \tag{5.14}$$

where b is the largest constant satisfying

$$\int_C p_{\mathrm{NAP}}(m_4^2, |U_{e4}|^2|\dot{\boldsymbol{N}}_{\mathbf{exp}})\, \mathrm{d}m_4^2\, \mathrm{d}|U_{e4}|^2 = 1 - \alpha. \tag{5.15}$$

This definition ensures that the HPD region contains the specified probability mass $1 - \alpha$ and that every point inside the region has a higher posterior density than any point outside the region. In the case of unimodal and symmetric distributions, the HPD region coincides with the central credible region. However, for multimodal distributions, the HPD region may consist of disjoint intervals, capturing the modes with the highest densities (see [159, 155, 100] for more details).

To facilitate efficient studies of the implications of different priors distributions $p(m_4^2,\, |U_{e4}|^2)$ on the HPD region, the prior was expanded as in Equation 5.9, and the relation in Equation 5.10 was employed to yield

$$p_{\mathrm{NAP}}(m_4^2, |U_{e4}|^2|\dot{\boldsymbol{N}}_{\mathbf{exp}}) \propto p(m_4^2,\, |U_{e4}|^2)\mathcal{L}_{\mathrm{marg}}(m_4^2,\, |U_{e4}|^2; \dot{\boldsymbol{N}}_{\mathbf{exp}}), \tag{5.16}$$

where $\mathcal{L}_{\mathrm{marg}}(m_4^2,\, |U_{e4}|^2; \dot{\boldsymbol{N}}_{\mathbf{exp}})$ denotes the marginal likelihood, defined as

$$\mathcal{L}_{\mathrm{marg}}(m_4^2,\, |U_{e4}|^2; \dot{\boldsymbol{N}}_{\mathbf{exp}}) = \int_{\boldsymbol{\theta}_{\mathbf{syst.}}} \int_{\boldsymbol{\theta}_{\mathbf{stat.}}} \int_{m_\nu^2} p(\dot{\boldsymbol{N}}_{\mathbf{exp}}|\boldsymbol{\theta}) p(m_\nu^2) p(\boldsymbol{\theta}_{\mathbf{stat.}}) p(\boldsymbol{\theta}_{\mathbf{syst.}})\, \mathrm{d}m_\nu^2\, \mathrm{d}\boldsymbol{\theta}_{\mathbf{stat.}}\, \mathrm{d}\boldsymbol{\theta}_{\mathbf{syst.}}. \tag{5.17}$$

Conditional marginal likelihoods were defined similarly based on Equation 5.13.

For a fixed set of sterile neutrino parameters m_4^2 and $|U_{e4}|^2$, (conditional) marginal likelihoods are independent of the prior on $p(m_4^2,\, |U_{e4}|^2)$. To exploit this property, the following algorithm, similar to the Grid scan approach described in Section 4.2.6.1, was developed:

1. A two-dimensional logarithmic grid of size 25 × 25 was constructed over the parameter space defined by $m_4^2 \in [0.1, 1600]\,\mathrm{eV}^2$ and $|U_{e4}|^2 \in [0.001, 0.5]$. The upper-limit of $1600\,\mathrm{eV}^2$ on m_4^2 was chosen based on the energy range of the analysis, which included electron energies up to $E_0 - 40\,\mathrm{eV}$.

2. For each point on the grid, the sterile neutrino parameters were fixed and the corresponding (conditional) marginal likelihood was computed. In addition, the (conditional) marginal likelihood for the null case ($m_4^2 = 0\,\mathrm{eV}^2, |U_{e4}|^2 = 0$) was also evaluated.

3. For a given sterile neutrino prior distribution $p(m_4^2,\, |U_{e4}|^2)$, the probability mass within each grid square was computed via numerical integration, using cubic spline interpolation of the (conditional) posterior defined in Equation 5.16. The mean probability density of each grid square was then obtained by dividing its probability mass by its area.

4. The grid squares were then sorted in descending order of their mean probability densities. A probability density threshold b was determined such that the total probability mass of all grid squares with mean densities greater than b equaled $1-\alpha$ times the total probability mass. A credibility level of 95% was used, corresponding to $\alpha = 0.5$.

5. Finally, the borders of the grid squares with mean probability densities exceeding b were connected to delineate the resulting highest posterior density (HPD) regions.

5.2 Bayes Factor Surface: Evaluation and Interpretation

Computing the highest posterior density (HPD) region requires specifying a prior distribution $p(m_4^2,\, |U_{e4}|^2)$ for the sterile neutrino parameters. As discussed in Section 5.1, assigning a prior distribution to the squared sterile neutrino mass m_4^2 is particularly challenging, since theoretical models allow for sterile neutrinos over a wide range of mass scales. While one can choose priors informed by the experiment's sensitivity, the resulting HPD regions are inherently experiment-specific and do not carry broad interpretability beyond the given analysis.

An alternative approach is the Bayes factor surface, as introduced in [91], which provides a more interpretable framework for presenting experimental results in searches for new physics. Bayes factor surfaces quantify the strength of evidence for or against extended models relative to a reference (null) model. The Bayes factor, denoted B_{10}, is defined as the ratio of the (conditional) marginal likelihood at a given point in sterile neutrino parameter space $(m_4^2,\, |U_{e4}|^2)$ to the marginal likelihood under the null hypothesis ($m_4^2 = 0\,\mathrm{eV}^2$, $|U_{e4}|^2 = 0$):

$$B_{10}(m_4^2,\, |U_{e4}|^2) = \frac{\mathcal{L}_{\mathrm{marg}}(m_4^2,\, |U_{e4}|^2; \dot{\boldsymbol{N}}_{\mathbf{exp}})}{\mathcal{L}_{\mathrm{marg}}(m_4^2 = 0\,\mathrm{eV}^2,\, |U_{e4}|^2 = 0; \dot{\boldsymbol{N}}_{\mathbf{exp}})}. \tag{5.18}$$

The Bayes factor B_{10} quantifies the posterior odds in favor of a sterile-neutrino hypothesis $(m_4^2,\, |U_{e4}|^2)$ relative to the null hypothesis. A value of $B_{10} > 1$ indicates that the sterile model is more plausible than the null. For example, $B_{10} = 5$ signifies that the sterile hypothesis is five times as likely as the null. By evaluating B_{10} on a grid of $(m_4^2,\, |U_{e4}|^2)$ values, as outlined in the algorithm in Section 5.1.1, one obtains a Bayes factor surface that may be displayed as a heat map or contour plot, thereby revealing regions of varying support for sterile neutrinos. All nuisance parameters are marginalized prior to the computation of B_{10}, so each point on the surface implements a simple hypothesis test directly analogous to a likelihood-ratio comparison and does not depend on any prior for $(m_4^2,\, |U_{e4}|^2)$.

To provide a calibrated interpretation analogous to frequentist confidence levels, evidence thresholds from Jeffreys' scale can be adopted [130]. Contours at $B_{10} = 3$ correspond to moderate evidence in favor of the sterile hypothesis, those at $B_{10} = 10$ to strong evidence, and those at $B_{10} = 30$ to very strong evidence. Conversely, regions in which B_{10} falls below $1/3$ may be regarded as areas of moderate evidence against the sterile hypothesis, analogous to exclusion regions in the frequentist analysis. Alternatively, one may perform Monte Carlo simulations under the null hypothesis to determine a threshold K such that the probability, under the null hypothesis, that the Bayes factor B_{10} exceeds K matches a desired false-alarm rate. If HPD or other credible regions are required, a prior distribution must be specified for $(m_4^2,\, |U_{e4}|^2)$ and the posterior integrated accordingly, but for hypothesis testing the calibrated Bayes factor contours themselves serve as the Bayesian analogue of both confidence levels and sensitivity/exclusion regions. Finally, Bayes factor surfaces obtained from independent experiments that do not share systematic uncertainties may be combined by multiplying their respective B_{10} values at each $(m_4^2, |U_{e4}|^2)$ point, thereby providing a coherent joint measure of evidence across multiple datasets.

5.3 Assessing the Impact of Nuisance Parameter Uncertainties through Importance-Weight Ratios

To assess the impact of a selected subset of nuisance variables $\hat{\boldsymbol{\theta}}_{\mathbf{syst.}}$, the analysis employed the importance-weight ratio $R_{\hat{\boldsymbol{\theta}}_{\mathbf{syst.}}}$, defined as

$$\begin{aligned} &R_{\hat{\boldsymbol{\theta}}_{\mathbf{syst.}}}(m_4^2,\, |U_{e4}|^2 | \dot{\boldsymbol{N}}_{\mathbf{exp}}, m_\nu^2 = 0\,\mathrm{eV}^2,\, \tilde{\boldsymbol{\theta}}_{\mathbf{syst.}} = \tilde{\boldsymbol{\theta}}_{\mathbf{ext}}) \\ &= \frac{\int_{\boldsymbol{\theta}_{\mathbf{stat.}}} p(\dot{\boldsymbol{N}}_{\mathbf{exp}}|\boldsymbol{\theta}) p(\boldsymbol{\theta}_{\mathbf{stat.}})\; \mathrm{d}\boldsymbol{\theta}_{\mathbf{stat.}}}{\int_{\hat{\boldsymbol{\theta}}_{\mathbf{syst.}}} \int_{\boldsymbol{\theta}_{\mathbf{stat.}}} p(\dot{\boldsymbol{N}}_{\mathbf{exp}}|\boldsymbol{\theta}) p(\boldsymbol{\theta}_{\mathbf{stat.}}) p(\boldsymbol{\theta}_{\mathbf{syst.}})\, \mathrm{d}\boldsymbol{\theta}_{\mathbf{stat.}}\, \mathrm{d}\hat{\boldsymbol{\theta}}_{\mathbf{syst.}}}, \end{aligned} \tag{5.19}$$

where the active neutrino mass was fixed to $m_\nu^2 = 0\,\mathrm{eV}^2$ and the remaining nuisance parameters $\tilde{\boldsymbol{\theta}}_{\mathbf{syst.}}$ were fixed to their nominal values $\tilde{\boldsymbol{\theta}}_{\mathbf{ext}}$.

The motivation for introducing this ratio arose from the need to quantify how much the contribution of the nuisance parameters affects the marginal likelihood by comparing the likelihood when these parameters are fixed to their nominal (central) values versus when they are marginalized over their prior distributions. Specifically, the numerator represents the marginal likelihood conditioned on their nominal values $\hat{\boldsymbol{\theta}}_{\mathbf{ext}}$, while the denominator accounted for uncertainty by marginalizing over the subset $\hat{\boldsymbol{\theta}}_{\mathbf{syst.}}$. This method aligns with established Bayesian sensitivity analyses, where the influence of nuisance parameters is assessed by comparing conditional and marginal likelihoods [100]. As a result, the importance-weight ratio provides a principled measure of how much each systematic variable influences the posterior inference on $(m_4^2, |U_{e4}|^2)$.

A value of $R_{\hat{\boldsymbol{\theta}}_{\mathbf{syst.}}} = 1$ indicated that fixing these parameters had no effect, suggesting negligible influence on the marginal likelihood. Values significantly greater or less than one signaled that marginalization over $R_{\hat{\boldsymbol{\theta}}_{\mathbf{syst.}}}$ led to meaningful differences, thus revealing the parameters' impact on the sterile neutrino inference. The greater the deviation of $R_{\hat{\boldsymbol{\theta}}_{\mathbf{syst.}}}$ from unity, the more influential the associated systematic uncertainties were.

In the NAP campaigns, a nuisance variable that significantly impacted the sterile neutrino sensitivity, as observed from the Frequentist analysis (see Figure A.50 for the KNM2 campaign), was the non-Poissonian background component, parameterized by $\mathrm{Bg}_{\mathrm{non-Poi}}$. As indicated in Table A.9, the values of $\mathrm{Bg}_{\mathrm{non-Poi}}$ did not include uncertainties. Instead, these values were fixed and differed from unity. To assess the impact of this variable within the Bayesian framework, the importance-weight ratio was computed as the ratio of conditional likelihoods evaluated with $\mathrm{Bg}_{\mathrm{non-Poi}} = 1$ and with $\mathrm{Bg}_{\mathrm{non-Poi}}$ fixed to the values reported in Table A.9:

$$
\begin{aligned}
&R_{\hat{\boldsymbol{\theta}}_{\mathbf{syst.}}}(m_4^2,\, |U_{e4}|^2 | \dot{\boldsymbol{N}}_{\mathbf{exp}}, m_\nu^2 = 0\,\mathrm{eV}^2,\, \tilde{\boldsymbol{\theta}}_{\mathbf{syst.}} = \tilde{\boldsymbol{\theta}}_{\mathbf{ext}}) \\
&= \frac{\int_{\boldsymbol{\theta}_{\mathbf{stat.}}} p(\dot{\boldsymbol{N}}_{\mathbf{exp}}|\boldsymbol{\theta})\, p(\boldsymbol{\theta}_{\mathbf{stat.}})\; \mathrm{d}\boldsymbol{\theta}_{\mathbf{stat.}}}{\int_{\boldsymbol{\theta}_{\mathbf{stat.}}} p(\dot{\boldsymbol{N}}_{\mathbf{exp}}|\hat{\boldsymbol{\theta}}_{\mathbf{syst.}} = \mathrm{Bg}_{\mathrm{non-Poi}})\, p(\boldsymbol{\theta}_{\mathbf{stat.}})\; \mathrm{d}\boldsymbol{\theta}_{\mathbf{stat.}}}
\end{aligned}
\tag{5.20}
$$

The ratio defined in Equation 5.20 differs from the standard importance-weight ratio in Equation 5.19 because it compares likelihoods conditioned on two fixed values of the non-Poissonian background parameter $\mathrm{Bg}_{\mathrm{non-Poi}}$. This approach is analogous to likelihood profiling, a method commonly employed to assess sensitivity to nuisance parameters [70, 100]. By comparing conditional likelihoods at specific parameter values, the ratio quantifies the local sensitivity of the inference to variations in $\mathrm{Bg}_{\mathrm{non-Poi}}$.

While conditional likelihood ratios and marginalized importance-weight ratios assess nuisance parameters in different ways, the marginalized ratio provides a quantitative measure of the overall impact by integrating over the nuisance prior. Conditional likelihood ratios offer complementary insights into local sensitivity but cannot be quantitatively compared to marginalized ratios. Together, these methods provide a robust framework for identifying and understanding the influence of systematic parameters on the inference of sterile neutrino parameters.

5.4 Computation of Marginal Likelihoods

Computing the marginal likelihoods in Sections 5.1.1, 5.2 and 5.3 involves evaluating multidimensional integrals. From Table 4.6, it can be seen that these integrals can become high-dimensional when all systematic parameters are marginalized, making accurate evaluation difficult, especially when the resulting values are very small.

Grid-based methods and sampling-based methods tested for the analysis are summarized below.

5.4.1 Grid-based Integration Methods

In grid-based methods, integrals are approximated as weighted sums over function values at specified points within the domain of integration [215]. For indefinite integrals, the domain is first truncated to ensure sufficient coverage of the function being integrated. A grid $\boldsymbol{X} \in \mathbb{R}^{N\times D}$ and associated weights $\boldsymbol{w} \in \mathbb{R}^{1\times N}$ for a D dimensional integral are generated based on the chosen quadrature rule. The number of grid points N depends on the quadrature rule and the number of nodes per dimension. The grid points and the weights are determined based on local or global polynomial approximations of the function. The function to be integrated is evaluated at the grid points $\boldsymbol{X}$ to obtain a vector of function values $\boldsymbol{f} \in \mathbb{R}^{N\times 1}$. The approximate integral is then given by the dot product between $\boldsymbol{f}$ and $\boldsymbol{w}$. The function being integrated in the sterile Bayesian analysis is of the form $\exp(g(\boldsymbol{x}))$. Careful handling of the dot product between $\boldsymbol{f}$ and $\boldsymbol{w}$ is necessary to maintain numerical stability, especially when the function exhibits large or small values. To address this issue, computations are carried out in the log domain. The result of the numerical integration method is then an approximation of the logarithm of the integral, which is computed as

$$\log\left(\sum_{i=1}^{N} w_i \cdot \exp(g(\boldsymbol{x_i}))\right) = g^* + \log\left(\sum_{i=1}^{N} w_i \cdot \exp(g(\boldsymbol{x_i}) - g^*\right), \tag{5.21}$$

where $g^* = \max\{g(\boldsymbol{x_1}), g(\boldsymbol{x_2}), \ldots, g(\boldsymbol{x_N})\}$.

The suitability of four grid-based methods was studied for the Bayesian sterile neutrino analysis. The first method employed the trapezoidal rule, using a local linear approximation of the integrand. The second applied Simpson's rule with a local quadratic approximation. The third used Boole's rule, based on a quartic polynomial approximation. The fourth method was Clenshaw-Curtis quadrature [62], which is based on approximating the function as a weighted sum of Chebyshev polynomials over the entire domain of integration. As with most grid-based methods, the number of grid points grows as $\mathcal{O}(n^d)$ for n points per dimension, making such approaches computationally impractical for accurate integration in higher dimensions. However, for the NAP campaigns, some of the conditional marginal likelihood calculations in Equation 5.17 involve only three or four variables. These calculations can be performed with high accuracy using the grid-based methods.

5.4.2 Sampling-based Integration Methods

Sampling-based methods such as Monte Carlo integration are used for integrating high-dimensional functions [217]. A multidimensional definite integral

$$I = \int_\Omega f(\boldsymbol{x})\mathrm{d}\boldsymbol{x}, \tag{5.22}$$

is approximated as

$$I \approx V\frac{1}{N}\sum_{i=1}^{N} f(\boldsymbol{x_i}), \tag{5.23}$$

where $\boldsymbol{x_i}$ are points sampled from the domain $\Omega \subset \mathbb{R}^d$ and V is the volume of the domain

$$V = \int_\Omega \mathrm{d}\boldsymbol{x}. \tag{5.24}$$

While this is the general idea, many methods based on different choices of sampling or weighting of the function values have been developed. Two Python packages that are suited for Bayesian inference of high dimensional models were tested for the Bayesian sterile neutrino analysis. Both methods operate in the logarithmic domain to ensure numerical stability and provide estimates of the uncertainty in the approximate integral value.

`Nautilus` [157] is a Python package implementing Importance Nested Sampling with a neural network to guide sampling. It efficiently estimates posterior distributions and Bayesian evidence by learning from previously evaluated points, enabling accurate integration with fewer likelihood calls. This approach is particularly effective in high-dimensional spaces.

`UltraNest` [55] is a package which implements the nested sampling Monte Carlo algorithm MLFriends ([53, 54]). It adaptively samples within likelihood contours and estimates both posterior distributions and evidence. UltraNest supports parallel computation, scales well with dimensionality, and requires minimal tuning, making it suitable for computationally intensive models.

5.5 First Analysis Results on an Asimov Dataset

This section presents the first results of application of the Bayesian inference framework developed for sterile neutrino search in KATRIN on the KNM2 Asimov dataset. The KNM2 campaign was selected as it provides the highest-statistics dataset among the NAP configurations, while avoiding the complexity of patches in the SAP configuration. As in the primary Frequentist analysis, the active neutrino mass was fixed to $m_\nu^2 = 0\,\mathrm{eV}^2$.

Likelihood evaluations were carried out using the existing Python interface to the KaFit software Appendix A.9. Grid-based integration methods were adapted from standard Python numerical libraries, while sampling-based methods were implemented using functions provided by the `Nautilus` and `UltraNest` packages. Custom code for computing Bayes factors, importance-weight ratios, highest posterior density (HPD) regions, and for result visualization was developed in Jupyter notebooks. All results presented in this chapter were obtained through computations performed on the Kalinka cluster at Institute of Astroparticle Physics, Karlsruhe Institute of Technology.

5.5.1 Evaluation of Numerical Methods for Marginal Likelihood Computation

As no ground truth is available for directly assessing the accuracy of the computed marginal likelihoods, a relative comparison was conducted using values obtained from the Nautilus method as a reference. Specifically, different integration methods were compared in the computation of the conditional marginal likelihood, $\mathcal{L}_{\mathrm{marg}}(m_4^2,\, |U_{e4}|^2; \dot{\boldsymbol{N}}_{\mathbf{exp}},\, m_\nu^2 = 0\,\mathrm{eV}^2,\, \boldsymbol{\theta}_{\mathbf{syst.}} = \boldsymbol{\theta}_{\mathbf{ext}})$. The marginal likelihood was evaluated on a 25 × 25 logarithmic grid spanning the parameter space $m_4^2 \in [0.1, 1600]\,\mathrm{eV}^2$ and $|U_{e4}|^2 \in [0.001, 0.5]$. Additionally, the marginal likelihood for the null case ($m_4^2 = 0\,\mathrm{eV}^2$, $|U_{e4}|^2 = 0$) was computed. The computational effort was kept approximately similar across all methods to ensure a fair comparison.

As uniform distributions were assumed for the statistical parameters $\boldsymbol{\theta}_{\mathbf{stat.}}$, the prior term $p(\boldsymbol{\theta}_{\mathbf{stat.}})$ in the marginal likelihood expression (Equation 5.17) could be treated as a constant and absorbed into the proportionality of the conditional posterior (Equation 5.16). Consequently, the marginal likelihood values divided by the prior term $p(\boldsymbol{\theta}_{\mathbf{stat.}})$, as computed using the Nautilus method, are visualized as a color map in Figure 5.1.

Table 5.1: Summary of the accuracy of different integration methods relative to the Nautilus reference. Reported are the mean, median, and maximum point-wise absolute deviations in the logarithm of the conditional marginal likelihood $\mathcal{L}_{\mathrm{marg}}$, computed over 626 grid points in $(m_4^2,\, |U_{e4}|^2)$ space.

Method	Mean	Median	Maximum
Trapezoidal rule	0.365	5.10×10^{-4}	13.630
Simpson's rule	0.324	5.10×10^{-4}	12.413
Boole's rule	0.315	5.10×10^{-4}	12.206
Clenshaw-Curtis quadrature	0.015	5.10×10^{-4}	0.934
UltraNest	0.054	4.53×10^{-2}	0.445

Table 5.1 summarizes the accuracy of each integration method in terms of the absolute point-wise difference in the logarithm of $\mathcal{L}_{\mathrm{marg}}$ relative to the Nautilus reference, reporting the mean, median, and maximum deviations across 626 grid points. The results indicate that all methods achieve a mean deviation below 0.5, demonstrating generally good agreement with the reference. Notably, UltraNest exhibits a larger median deviation compared to the other methods,

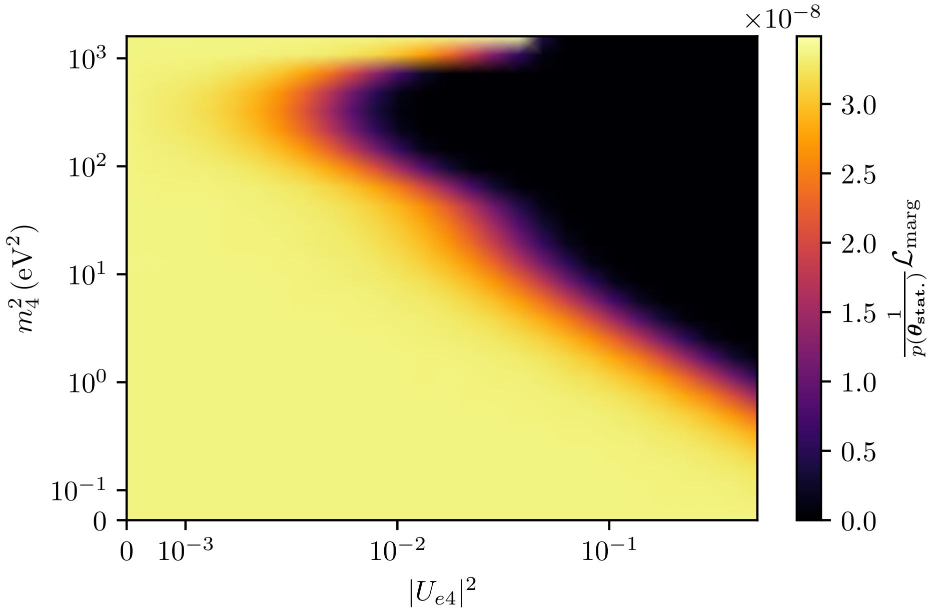

Figure 5.1: Conditional marginal likelihood according to Equation 5.17 scaled by the uniform prior on the statistical nuisance parameters $\frac{1}{p(\boldsymbol{\theta}_{\mathbf{stat.}})}\mathcal{L}_{\mathrm{marg}}\left(m_4^2, |U_{e4}|^2; \dot{\boldsymbol{N}}_{\mathbf{exp}}, m_\nu^2 = 0\,\mathrm{eV}^2, \boldsymbol{\theta}_{\mathbf{syst.}} = \boldsymbol{\theta}_{\mathbf{ext}}\right)$, evaluated over the sterile neutrino parameter space (m_4^2, $|U_{e4}|^2$) for the KNM2 Asimov dataset. The likelihood was marginalized over the statistical nuisance parameters using sampling-based package Nautilus and scaled by their prior distribution as defined in Equation 5.8.

suggesting a consistently higher typical error, which could potentially be reduced by refining the convergence criteria. In contrast, the regular grid-based methods (trapezoidal, Simpson's, and Boole's rules) show larger maximum deviations, reflecting greater variability in accuracy, particularly at grid points corresponding to large negative values of $\mathcal{L}_{\mathrm{marg}}$. This variability could be mitigated by employing finer grids, although such improvements would require significantly higher computational cost. Among the methods considered, Clenshaw-Curtis quadrature achieves the best overall match to the Nautilus result, combining low median and maximum deviations. Given its scalability to higher dimensions, Nautilus was selected for all subsequent analyses.

5.5.2 Bayes Factor Surface and HPD Regions

After marginalizing over all statistical and systematic nuisance parameters and fixing the active neutrino mass at $m_\nu^2 = 0\,\mathrm{eV}^2$, the Bayes factor surface was computed relative to the reference null hypothesis defined by ($m_4^2 = 0\,\mathrm{eV}^2$, $|U_{e4}|^2 = 0$), as shown in Figure 5.2. The resulting surface is displayed as a filled contour plot, with contour levels corresponding to Jeffreys' scale [130]. In some regions of the parameter space, the Bayes factor remains within one order of magnitude of unity, indicating that the marginal likelihood is similar to that under the null hypothesis. In contrast, across a substantial portion of the parameter space, the Bayes factor drops below 0.01, providing strong evidence against the sterile neutrino hypothesis.

For comparison, the 95% confidence level (C.L.) sensitivity contour from the Frequentist analysis is overlaid, incorporating both statistical and systematic uncertainties. Under the assumption of two degrees of freedom for the $\Delta\chi^2$ test statistic, the critical value corresponding to the 95% C.L. is approximately $\mathrm{CDF}^{-1}_{\Delta\chi^2}(0.95) \approx 5.99$. Given that χ^2 is defined as twice the negative logarithm of the likelihood, the sensitivity contour corresponds to the set of sterile neutrino parameters $(m_4^2,\ |U_{e4}|^2)$ satisfying the condition:

$$0.05 \approx \exp(-5.99/2) \approx \frac{\max_{\boldsymbol{\theta}_{\mathbf{stat.}},\ \boldsymbol{\theta}_{\mathbf{syst.}}} p_{\mathrm{NAP}}(\dot{\boldsymbol{N}}_{\mathbf{exp}}|\boldsymbol{\theta}_{\mathbf{stat.}},\ \boldsymbol{\theta}_{\mathbf{syst.}}, m_\nu^2 = 0\,\mathrm{eV}^2,\ m_4^2,\ |U_{e4}|^2) \cdot p(\boldsymbol{\theta}_{\mathbf{syst.}})}{\max_{\boldsymbol{\theta}_{\mathbf{stat.}},\ \boldsymbol{\theta}_{\mathbf{syst.}}} p_{\mathrm{NAP}}(\dot{\boldsymbol{N}}_{\mathbf{exp}}|\boldsymbol{\theta}_{\mathbf{stat.}},\ \boldsymbol{\theta}_{\mathbf{syst.}}, m_\nu^2 = 0\,\mathrm{eV}^2,\ m_4^2 = 0\,\mathrm{eV}^2,\ |U_{e4}|^2 = 0) \cdot p(\boldsymbol{\theta}_{\mathbf{syst.}})} \tag{5.25}$$

where $p_{\mathrm{NAP}}(\dot{\boldsymbol{N}}_{\mathbf{exp}}|\boldsymbol{\theta})$ is the likelihood and $p(\boldsymbol{\theta}_{\mathbf{syst.}})$ is the multivariate Gaussian prior on the systematic parameters.

In Figure 5.2, for squared sterile neutrino masses $m_4^2 \lesssim 100\,\mathrm{eV}^2$, the Frequentist sensitivity contour closely aligns with the Bayes factor contour corresponding to $B_{10} = 0.05$. While the numerical contours coincide, their interpretations differ: the Frequentist contour guarantees 95% coverage under repeated sampling, whereas the $B_{10} = 0.05$ contour indicates approximately 20:1 odds in favor of the null hypothesis over the sterile neutrino hypothesis, under the assumption of a uniform prior on the sterile neutrino parameters.

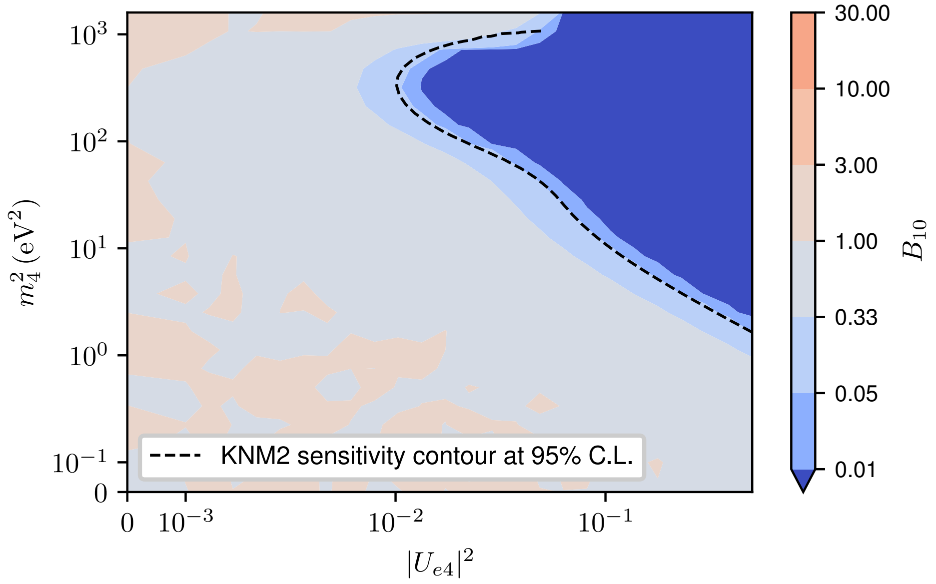

Figure 5.2: Filled contour plots of the Bayes factor defined in Equation 5.18, evaluated across the sterile neutrino parameter space $(m_4^2,\ |U_{e4}|^2)$ using the KNM2 Asimov dataset. For comparison, the 95% confidence level sensitivity contour from the Frequentist analysis, which accounts for both statistical and systematic uncertainties, is overlaid.

The 95% highest posterior density (HPD) region, as described in Section 5.1.1, assuming uniform priors over the ranges $m_4^2 \in [0, 1600]\,\mathrm{eV}^2$ and $|U_{e4}|^2 \in [0, 0.5]$, is illustrated in Figure 5.3a. The posterior probability mass within each grid cell is additionally visualized via a color map. A corresponding HPD region obtained using log-uniform (Jeffreys) priors over the same parameter ranges is shown in Figure 5.3b. The log-uniform prior, also referred to as the Jeffreys prior [129], is considered noninformative and is particularly relevant in this context, as sterile neutrinos could plausibly exist across a wide mass scale. As emphasized in Section 5.2, the HPD regions depend strongly on the choice of prior. This is evident here, with the log-uniform prior producing a more concentrated region at lower values of $(m_4^2,\ |U_{e4}|^2)$.

These findings underscore the value of presenting Bayesian sterile neutrino search results for KATRIN in the form of Bayes factor surfaces, visualized through color maps or filled contour plots.

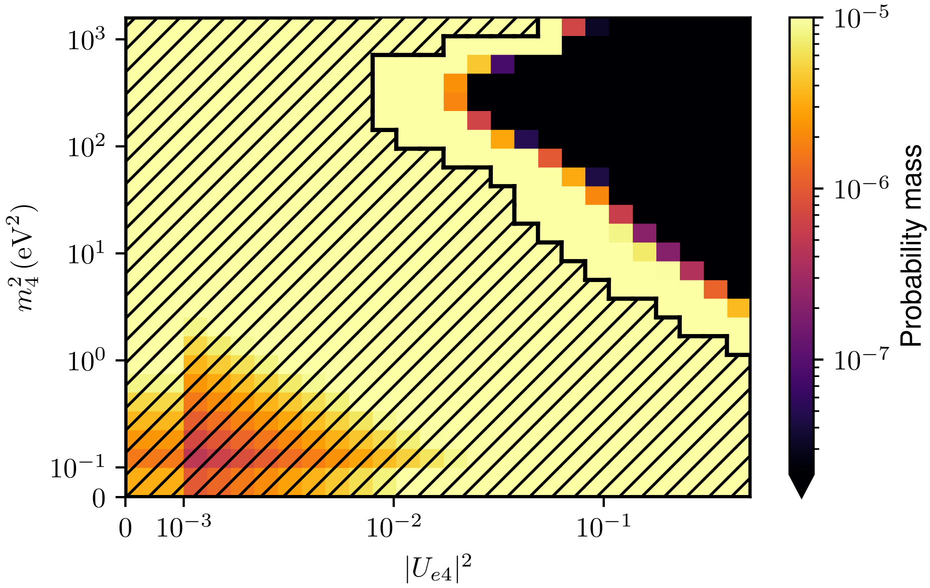

(a)

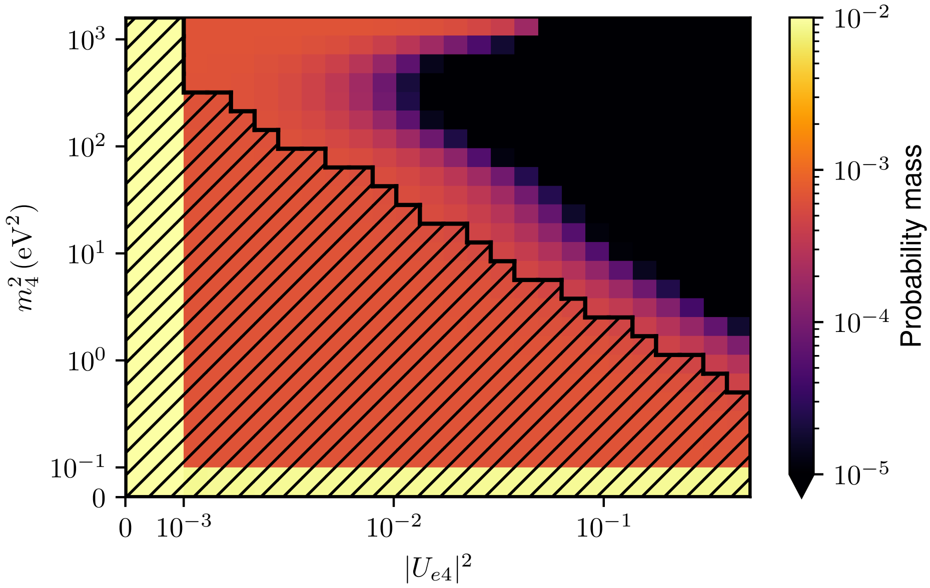

(b)

Figure 5.3: Ninety-five percent highest density probability region in the sterile neutrino parameter space (m_4^2, $|U_{e4}|^2$), evaluated using the KNM2 Asimov dataset (hatched regions). The evaluation assumes (a) uniform priors and (b) log-uniform priors over the ranges $m_4^2 \in [0, 1600], \mathrm{eV}^2$ and $|U_{e4}|^2 \in [0, 0.5]$. The posterior probability mass within each grid cell is additionally visualized using a color map.

5.5.3 Quantifying Impact of Nuisance Parameter Uncertainties

The importance-weight ratios $R_{\hat{\boldsymbol{\theta}}_{\mathbf{syst.}}}$, as defined in Equations (5.19) and (5.20), were computed by marginalizing over all nuisance parameters $\boldsymbol{\theta}_{\mathbf{syst.}}$ as well as for nine designated subsets. These calculations were performed on the same grid of sterile neutrino parameter values used to construct the Bayes factor surface. Deviation from unity, quantified by $R_{\hat{\boldsymbol{\theta}}_{\mathbf{syst.}}} - 1$, was employed as the measure of impact. Table 5.2 reports the minimum, median, and maximum values of this deviation, restricted to grid points where the Bayes factor $B_{10} > 0.05$. This threshold was introduced to exclude regions of parameter space that contribute negligibly to the posterior, where both the marginal and conditional likelihoods are vanishingly small, rendering the computed importance-weight ratios numerically unstable and their contribution to the overall inference insignificant.

Table 5.2: Summary of importance-weight ratios for nuisance parameters. The importance-weight ratios $R_{\hat{\boldsymbol{\theta}}_{\mathbf{syst.}}}$ were computed according to Equations (5.19) and (5.20) over 626 grid points in $(m_4^2, |U_{e4}|^2)$ space. Reported are the minimum, median, and maximum point-wise values $R_{\hat{\boldsymbol{\theta}}_{\mathbf{syst.}}} - 1$ for grid-points where the Bayes factor Equation 5.18 was greater than 0.05.

Nuisance parameter	Minimum	Median	Maximum
Combined systematic uncertainties	-0.506	0.4228	0.448
Column density × inelastic cross section	-0.545	0.3122	0.317
Non-Poissonian background	-0.327	-0.1285	-0.125
Scan-step-duration-dependent background	-0.205	0.0973	0.102
Energy-loss function	-0.295	0.0463	0.115
qU-dependent background slope	0.021	0.0426	0.046
Analyzing-plane magnetic field and potential	0.005	0.0265	0.039
Source-potential variations	-0.039	0.0028	0.012
Maximum magnetic field	-0.378	0.0012	0.004
Source magnetic field	-0.035	0.0001	0.003

The systematic subsets in Table 5.2 are ranked by the absolute value of the median of $R_{\hat{\boldsymbol{\theta}}_{\mathbf{syst.}}} - 1$, providing a comparative view of their relative influence. Importance-weight ratios for the two systematic subsets found to have the greatest impact, namely the product of the column density and inelastic cross section, and the non-Poissonian background, are shown in Figure 5.4a and Figure 5.4b, respectively. For reference, the $B_{10} = 0.05$ contour is also shown in these figures. To help illustrate the range of importance-weight ratios across different systematic uncertainties, Figure 5.5 shows the ratio for the source magnetic field, which was identified as the least influential subset in Table 5.2.

It is observed that the importance-weight ratio maps display certain local irregularities, which arise from minor fluctuations inherent to the sampling-based computation of the integrals. These fluctuations could potentially be reduced by increasing the number of samples used in the estimation. Curiously, in Figure 5.4a, the contours are indented at $m_4^2 \approx 100\ \mathrm{eV}^2$, which is reminiscent of the kink observed in the Raster contours. Similar to the Raster contours, this indentation appears for the product of the column density and inelastic cross section but is absent in the contours for the non-Poissonian background.

While a quantitative comparison with the Raster scans from the Frequentist approach shown in Figure A.50 is not currently feasible, the ranking of the systematic subsets based on their inferred impact shows general agreement. Further methodological work is needed to develop a framework for rigorous quantitative comparison between the Bayesian and Frequentist analyses.

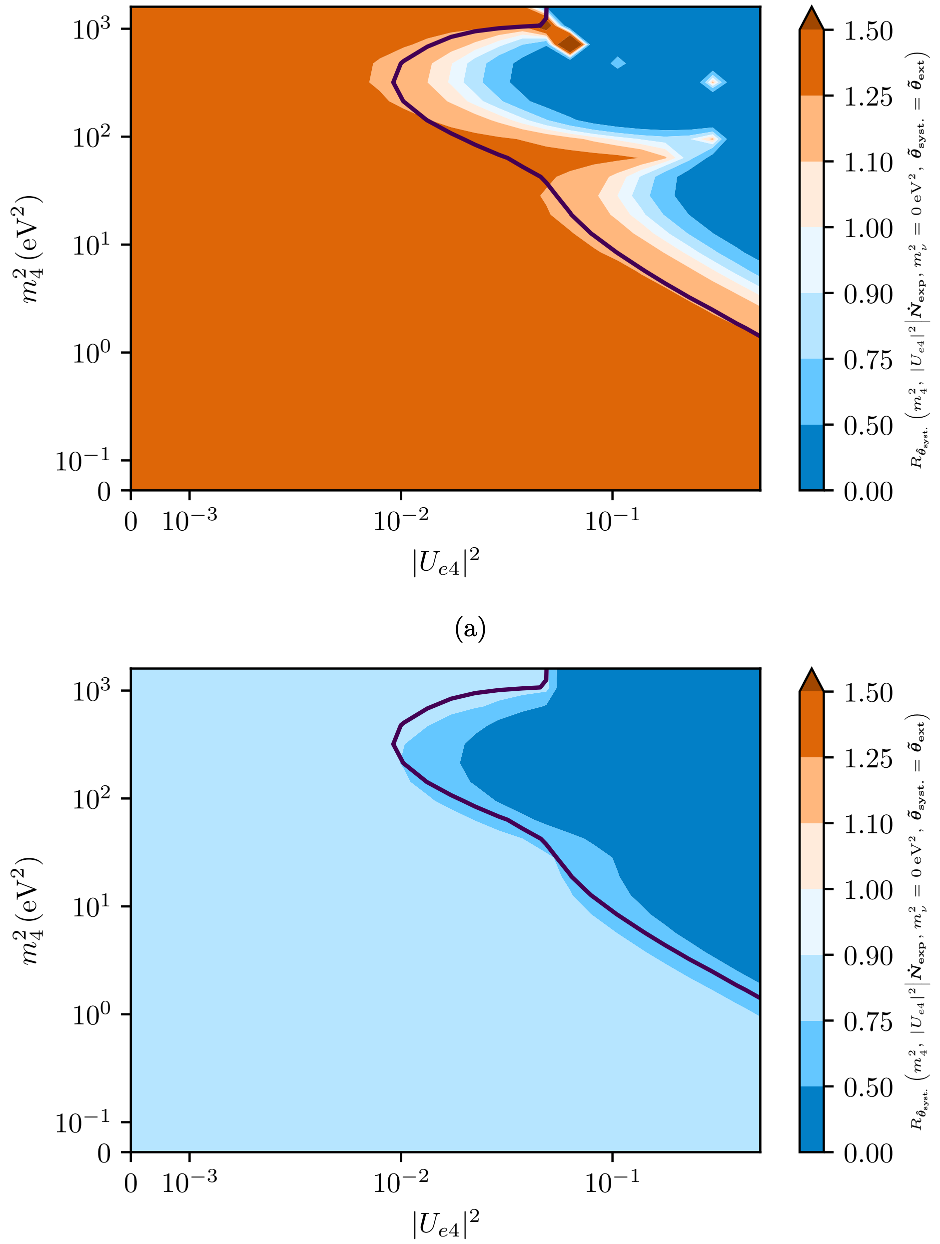

(a)

(b)

Figure 5.4: Filled contour plots of the importance-weight ratios Equations (5.19) and (5.20), corresponding to (a) the product of column density and inelastic cross section and (b) non-Poissonian background, evaluated over the sterile neutrino parameter space (m_4^2, $|U_{e4}|^2$) for the KNM2 Asimov dataset. For reference, the $B_{10} = 0.05$ contour is also shown.

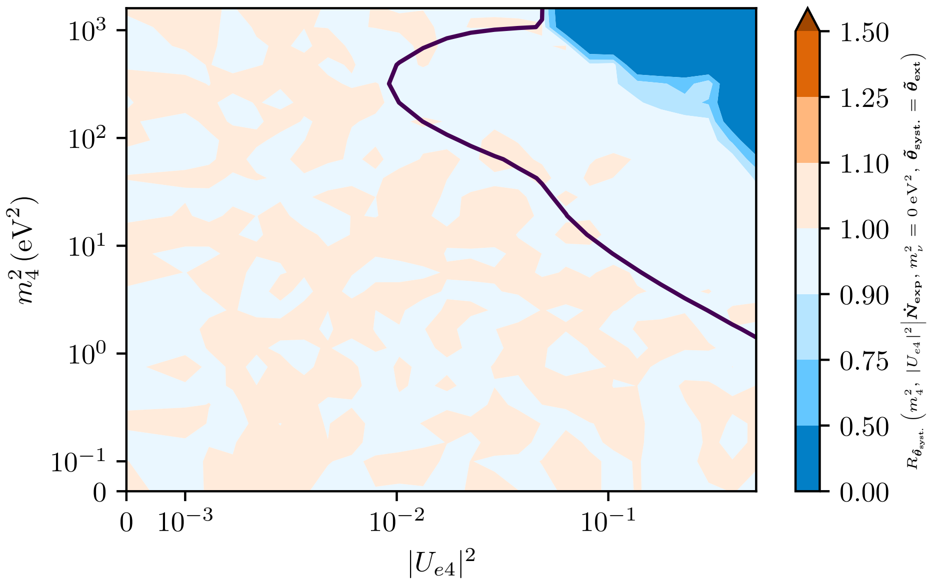

Figure 5.5: Filled contour plots of the importance-weight ratio of Equation 5.19, corresponding to the source magnetic field, evaluated over the sterile neutrino parameter space (m_4^2, $|U_{e4}|^2$) for the KNM2 Asimov dataset. For reference, the $B_{10} = 0.05$ contour is also shown.

5.6 Extending the Bayesian Framework: From Asimov to Full Dataset Analysis

The results presented for the KNM2 Asimov dataset in this chapter are promising and demonstrate the viability of a Bayesian framework for conducting a sterile neutrino search using KATRIN data. These findings complement the primary Frequentist analysis discussed in Chapter 4 by providing an independent statistical approach with distinct interpretational advantages based on Bayes factor.

A thorough comparison of the computational requirements between the Frequentist and Bayesian methods would provide valuable insights into the practical feasibility, scalability, and resource allocation necessary for analyses of all the KATRIN datasets. Owing to the need to compute high-dimensional integrals in the Bayesian framework, as opposed to high-dimensional optimization in the Frequentist framework, the computational cost associated with the Bayesian approach is generally expected to be higher. Although algorithms such as importance nested sampling, employed by Nautilus, are designed for efficient computation of high-dimensional integrals, the number of likelihood evaluations required in the Bayesian analysis is estimated to be approximately two orders of magnitude greater than that of the Frequentist analysis, excluding the additional cost associated with Monte Carlo simulations used to estimate the asymptotic distributions of test statistics in the latter. Consequently, methodological improvements that reduce either the number of likelihood evaluations or the computational time per evaluation would offer substantial benefits.

6

Measurement of the Backscattering at the Rear Wall of KATRIN

"The thing that doesn't fit is the thing that's the most interesting: the part that doesn't go according to what you expected."

— Richard P. Feynman

The rear wall serves as the termination point of the magnetic flux tube in KATRIN's rear section and sets the starting potential of the β-electrons. A detailed description of the rear wall is provided in Section 2.3.1. Tritium molecules can adsorb onto the surface of the rear wall [17], and the resulting radioactive decay contributes to the measured β-decay spectrum of tritium in the source. Electrons originating from the decay of tritium adsorbed on the rear wall are treated as background and are modeled as a separate secondary β-decay spectrum (see Section 3.7.4 for details). This secondary spectrum differs slightly in shape and endpoint from the primary β-decay spectrum of tritium in the source, causing the measured spectrum to be a composite of primary and secondary electrons, which distorts the overall spectral shape. The parameters of the rear wall background model, which characterizes the energy distribution and rate of secondary electrons, are derived from two-fold dedicated calibration measurements. First, the spectral endpoint energy (E_0^{RW}), shape parameter ($w_{\mathrm{GS}}^{\mathrm{RW}}$) and the rear wall signal amplitude A_s^{RW} are extracted from detailed rear wall scans performed with the tritium source evacuated at retarding energies within the analysis range relevant for sterile neutrino search. Since the endpoint and shape parameters remain constant over time while only the signal amplitude increases due to tritium accumulation, the second set of intermittent high-statistics rate measurements conducted at lower retarding energies, typically at 14 keV allow for monitoring the time-dependence of A_s^{RW} (see [17] for details on the parameter estimation procedure). Based on these measurements, the evolution of the rear-wall-induced background rate $R_{\mathrm{RW}}(f)$ as a function of the integral tritium flow f is described using a model that combines exponential saturation and linear growth components, referred to as the growth model. An average value of the rear wall signal amplitude $\overline{A_s^{\mathrm{RW}}}$ is estimated per campaign from $R_{\mathrm{RW}}(f)$. Finally, the three components of the rear wall secondary spectrum, namely E_0^{RW}, $w_{\mathrm{GS}}^{\mathrm{RW}}$ and $\overline{A_s^{\mathrm{RW}}}$ are included in the KATRIN model Section 3.7.4. During the post unblinding investigations for the sterile neutrino analysis Section 4.5, a minor software bug affecting the rear wall signal amplitude A_s^{RW} estimation was identified and subsequently corrected. More details can be found in an KATRIN internal technical report [194].

The background arising from tritium adsorbed on the rear wall and its associated uncertainty had a relatively minor impact on the KNM1–5 sterile neutrino search, as shown in Figure 4.17. However, for the upcoming keV-scale sterile neutrino search with the TRISTAN experiment [68], rear-wall-induced background has been identified as the dominant systematic uncertainty [244, 99]. Consequently, it is critical for TRISTAN to develop a robust understanding and accurate model of the background rate originating from the rear wall.

As noted previously, the current model describes the rear wall background as a β-decay spectrum with a slightly altered shape and endpoint compared to that of tritium molecules in the source. The modification to the spectral shape is heuristic, and its origin or necessity has not been fully understood. One proposed explanation attributes the change to energy loss caused by electron scattering within the rear wall material. More generally, such energy loss due to scattering prior to electrons exiting the rear wall and entering the beamline is of concern for both TRISTAN, as it represents an additional source of systematic uncertainty.

To investigate this effect, dedicated simulation-based models have been developed by collaborators [76]. These models combine simulations of the magnetic and electric fields in KATRIN, using Kassiopeia [97, 138], with Geant4-based simulations of electron scattering within the rear wall material [8, 21]. The measurement and systematic analysis of the rear wall backscattering background presented here were conducted within the scope of this thesis. This chapter presents the first validation of these models using dedicated measurements of the rear-wall-induced additional spectrum.

6.1 Dedicated Rear Wall Measurements

The spectral shape of the rear-wall contribution to the KATRIN spectrum is determined by dedicated scans performed with the source evacuated. These scans are carried out over an energy range that closely matches the analysis window used for neutrino mass and sterile neutrino searches. In each scan, electron counts are recorded for 150 seconds at each retarding potential, using the same magnetic field configuration as in the β-spectrum measurement scans.

In addition to these scans, the rear-wall-induced background rate is measured several times during each campaign in order to monitor how it evolves over time and with cumulative tritium exposure. These dedicated measurements are performed at four fixed retarding energies: 14 keV, 15.2 keV, 15.45 keV, and 16.45 keV. At each setting, data are collected for 300 seconds. During these measurements, the low-field correction system is set to the “MAX” configuration. Details of the “MAX” configuration configuration can be found in [17, Table A.1].

The means and standard deviations of the normalized_rate, which is defined as the measured rates at 15.2 keV, 15.45 keV, and 16.45 keV relative to the rate at 14 keV, across multiple scans are presented in Figure 6.1. These results highlight the need for applying a spectral shape correction for the electron rate originating from tritium decays on the rear wall. In the same figure, the model predictions for these rates, based on the standard β-spectrum and the KATRIN transmission function, are indicated by the square markers. A significant discrepancy was observed between the measured and predicted normalized_rates.

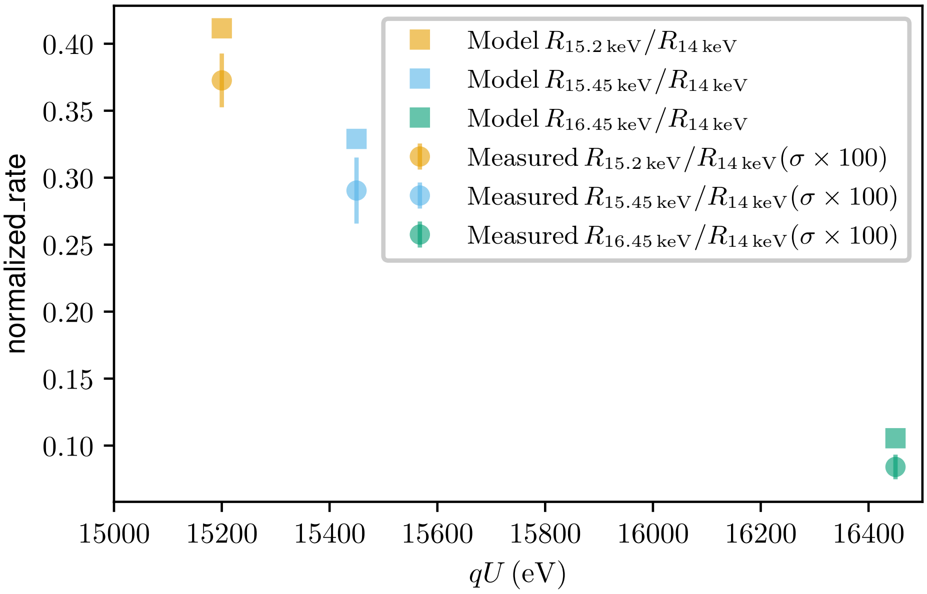

Figure 6.1: Normalized rates for rear-wall-induced background measurements. The rates are normalized to the measured value at 14 keV and compared with the expected normalized rates based on the standard β-spectrum and the KATRIN transmission function, referred to as the "Model".

To investigate whether the observed discrepancy could be attributed to electron scattering in the rear wall, dedicated rear-wall background measurements were carried out in June of 2024 during the KNM13 campaign. Backscattering can also occur within the silicon wafer of the detector. By adjusting the magnetic fields in the rear section and near the detector, it is possible to control the number of electrons that enter the beamline after undergoing backscattering. Three distinct magnetic field configurations were selected for this study. A summary of the settings and corresponding measurements is provided below.

- Nominal setting:
  - The magnetic fields in the rear section and at the detector were set to the standard values used for β-spectrum measurements.
  - Measurements were taken from 12 keV to 18 keV in 500 V increments, with acquisition times ranging between 90 seconds and 1800 seconds.
- Low detector field setting:
  - The detector magnetic field was reduced from 2.5 T to 0.12 T to suppress the detection of electrons scattered in the detector. This change also decreased the area of the rear wall mapped to the detector, thereby reducing the overall event rate and enabling measurements at lower retarding energies without saturating the detector or data acquisition systems.
  - Measurements were conducted from 1 keV to 18 keV in 1 keV steps, with acquisition times ranging between 60 seconds and 1800 seconds.
- Low detector and low rear-section field setting:
  - The magnetic field in the rear section was reduced from 1.23 T to 0.0756 T to change the rear wall backscattering effect.

- Measurements were also taken from 1 keV to 18 keV in 1 keV steps, with acquisition times between 60 seconds and 1800 seconds.

The area of the rear wall mapped to the detector can be estimated using the ratio of the magnetic fields and the known radius of the detector according to the relation:

$$R_{\mathrm{rw}} = \sqrt{\frac{B_{\mathrm{det}}}{B_{\mathrm{rw}}}} R_{\mathrm{det}}, \quad R_{\mathrm{det}} = 0.045\mathrm{m}. \tag{6.1}$$

The calculated radii and corresponding relative areas of the rear wall seen by the detector for each configuration are summarized in Table 6.1.

Table 6.1: Effective radius of the rear wall seen by the detector in each magnetic field configuration.

Configuration	R_{rw} (m)	Relative Area
Nominal field	0.0642	1.00
Low detector field	0.0143	0.04
Low detector and low rear-section field	0.0579	0.81

The mean measured rates and associated uncertainties for the three magnetic field configurations, considering pixels numbered 0 to 99 (see Figure 4.3), are shown in Figure 6.2. These 100 pixels correspond to 9 of the innermost rings out of the 12 concentric rings that make up the arrangement of pixels in the focal-plane detector. The low detector magnetic field setting exhibits a significantly lower rate compared to the nominal setting because the detector observes a much smaller portion of the rear wall. Similarly, the low detector and low rear-section magnetic field setting results in an even lower rate, primarily due to the reduced acceptance angle, which is approximately 7.7° compared to about 32.8° in the nominal configuration. In all three magnetic field configurations, the statistical uncertainties in the measured rates are negligible and therefore do not significantly affect the interpretation of the results.

The normalized_rate, defined as

$$\text{normalized\_rate\_measured}^{qU} = \frac{\sum_{\text{pixel}=0}^{100} \text{rate}_{\text{pixel}}^{qU}}{\sum_{\text{pixel}=0}^{100} \text{rate}_{\text{pixel}}^{12\text{keV}}}, \tag{6.2}$$

for each of the three configurations was compared to the expected normalized_rate based on the standard β-spectrum and the KATRIN transmission function termed “simple model", as shown in Figure 6.3. The normalization with respect to the rate at 12 keV was an arbitrary choice, and similar analyses using alternative normalization points yield consistent results. Therefore, this choice does not significantly influence the outcome of the analysis. Some retarding energies were omitted from the analysis due to errors in setting the retarding voltages during the data acquisition. The normalized_rates for all three configurations were in agreement with each other, yet they deviated from the simple model, as previously noted in Figure 6.1.

The level of agreement between model and measurement can be quantified using the normalized rate ratio, defined as

$$\text{normalized\_rate\_ratio}^{qU} = \frac{\text{normalized\_rate\_simulated}^{qU}}{\text{normalized\_rate\_measured}^{qU}}, \tag{6.3}$$

where normalized_rate_simulated^{qU} is the simulated rate at retarding potential U, normalized to the simulated rate at 12 keV, and normalized_rate_measured^{qU} is the corresponding measured value from Equation 6.2.

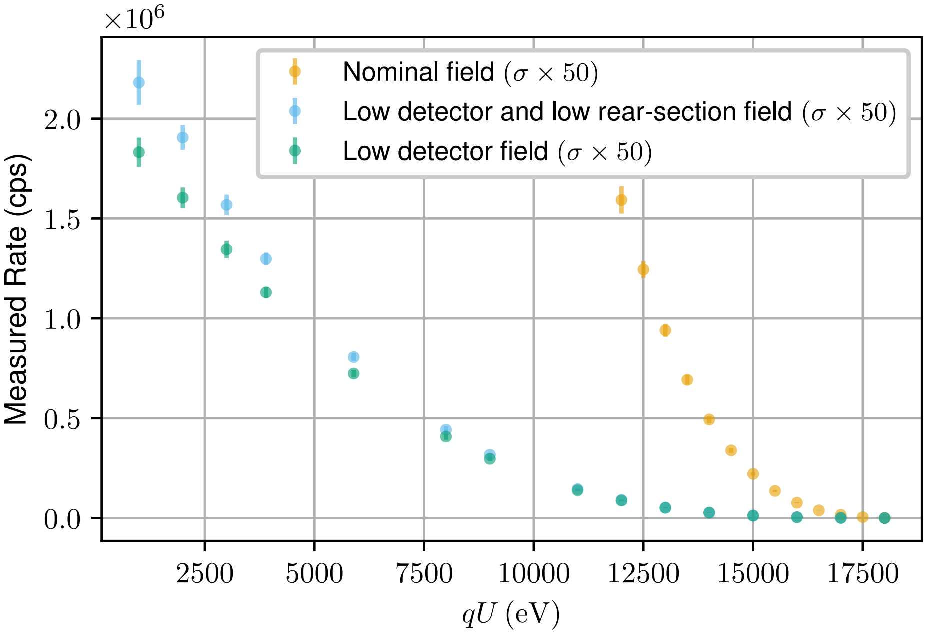

Figure 6.2: Mean measured rates of the rear-wall-induced background and associated uncertainties for three magnetic field configurations, considering pixels numbered 0 to 100.

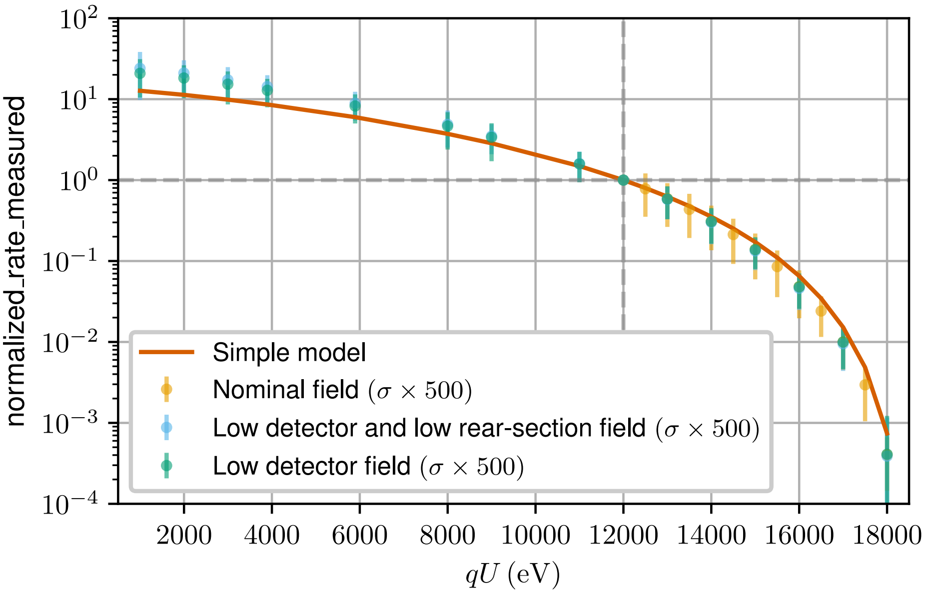

Figure 6.3: Normalized rates for rear-wall-induced background measurements, as defined in Equation 6.2, under three magnetic field configurations. The rates are normalized to the measured value at 12 keV and compared with the expected normalized rates based on the standard β-spectrum and the KATRIN transmission function, referred to as the “simple model”.

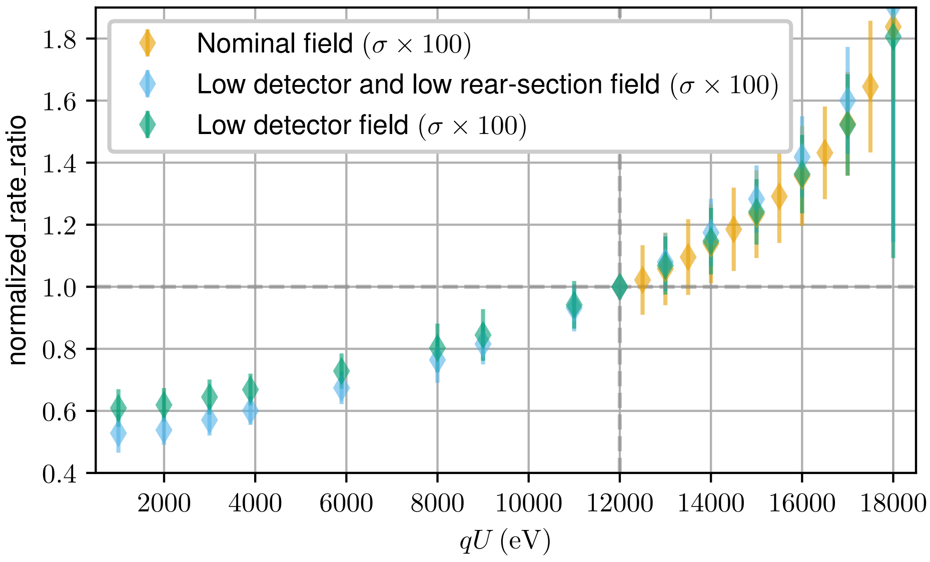

Figure 6.4: Normalized_rate_ratios for rear-wall-induced background, as defined in Equation 6.3, under three magnetic field configurations. Rates are normalized to the value at 12 keV and compared with predictions from a model comprising of the standard β-spectrum and the KATRIN transmission function, referred to as the "simple model".

The normalized_rate_ratio, as defined in Equation 6.3, is shown in Figure 6.4 for the simple model across the three configurations. A value of unity corresponds to perfect agreement between simulation and measurement. Significant deviations are observed, with the measured values differing from the model by more than 75% at 18 keV, highlighting limitations of the simple model in describing the experimental data.

6.2 Full Monte Carlo Simulations

To accurately describe the measured rates, a modified model of the rear-wall spectral shape is required, one that explicitly accounts for the backscattering of electrons at the rear wall. To systematically investigate these backscattering effects, detailed Monte Carlo simulations were performed using the Full MC Geant4 simulation framework developed for the TRISTAN project (version tag v1.1_dev) [1]. The simulations involved detailed tracking of individual electrons through the electromagnetic fields and material components. Simulations were performed across a range of retarding energies and for the three magnetic field configurations that correspond to the measurement settings: the nominal setting, the reduced detector field setting, and the combined reduced detector and rear-section field setting. Magnetic and electric field maps for each configuration and retarding potential were generated using Kassiopeia and subsequently imported into the Full MC framework. A total of 10^8 electrons were simulated, emitted isotropically from the rear-wall surface. Their energies were sampled according to the tritium β-decay spectrum above the given retarding potential. Electron scattering in the rear wall was simulated in Geant4 using both the Penelope [30] and Single Scattering [142] physics models, which differ as follows:

- *Penelope model*:
  Utilizes a mixed transport scheme where hard collisions are simulated discretely and soft

---

[1] I gratefully acknowledge **Cláudio Silva** for his invaluable support in performing the simulations.

interactions are treated via multiple scattering approximations. This approach balances accuracy with computational efficiency, making it well suited for low-energy electron and photon transport in complex materials.

- *Single Scattering model*:
  Treats each electron scattering event individually without condensing multiple interactions into steps. This yields more precise angular distributions and is particularly useful for studying backscattering effects, but requires significantly more computing time.

Energy loss by electrons due to rear-wall scattering was analyzed using histograms generated from the full Monte Carlo simulations. The energy loss distribution for electrons that undergo scattering in the rear wall is shown in Figure 6.5. A clear difference is observed between the energy loss densities predicted by the Penelope and Single Scattering models.

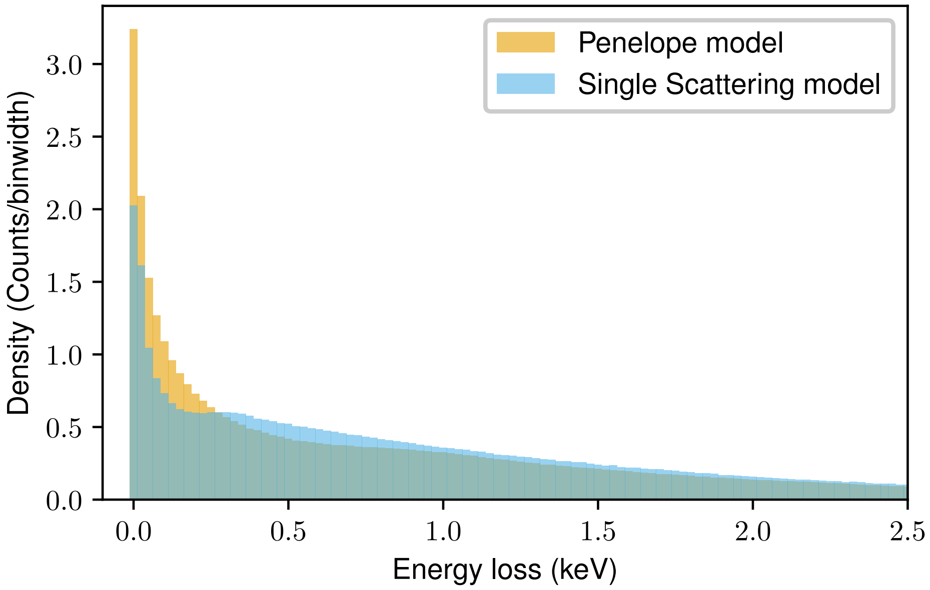

Figure 6.5: Histogram showing the distribution of energy lost by simulated electrons due to scattering processes within the rear wall. Only electrons that undergo scattering are included.

6.3 Validation of Simulations Against Experimental Data

The normalized rates obtained from the Monte Carlo simulations using the Penelope model both with and without accounting for backscattering in the rear wall, are compared to the measurements for the three magnetic field configurations in Figures 6.6 to 6.8. The normalized rates from simulations that include rear-wall backscattering show better agreement with the measured normalized rates for all three experimental configurations. In contrast, simulations that do not include backscattering show significant discrepancies.

The normalized_rate_ratio, as defined in Equation 6.3, is shown in Figure 6.9 for the Penelope model across the three configurations, both with and without backscattering effects. In the absence of backscattering, the normalized_rate_ratio closely reproduces the results of the simple model presented in Figure 6.4. When backscattering was included, the normalized_rate_ratio deviated by less than 15 percent, supporting the hypothesis that the spectral distortion observed in the rear-wall background rate can be attributed to energy loss from electron scattering within the rear wall.

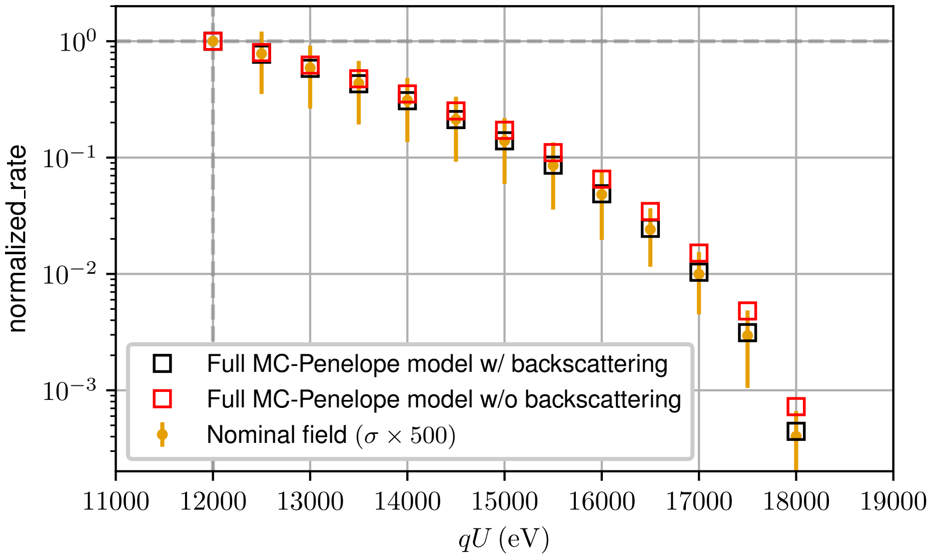

Figure 6.6: Normalized rates for rear-wall-induced background, as defined in Equation 6.2, under the nominal magnetic field setting. Rates are normalized to the value at 12 keV and compared with predictions from TRISTAN Full Monte Carlo simulations using the Penelope model. Simulation results are shown both with and without including backscattering in the rear wall.

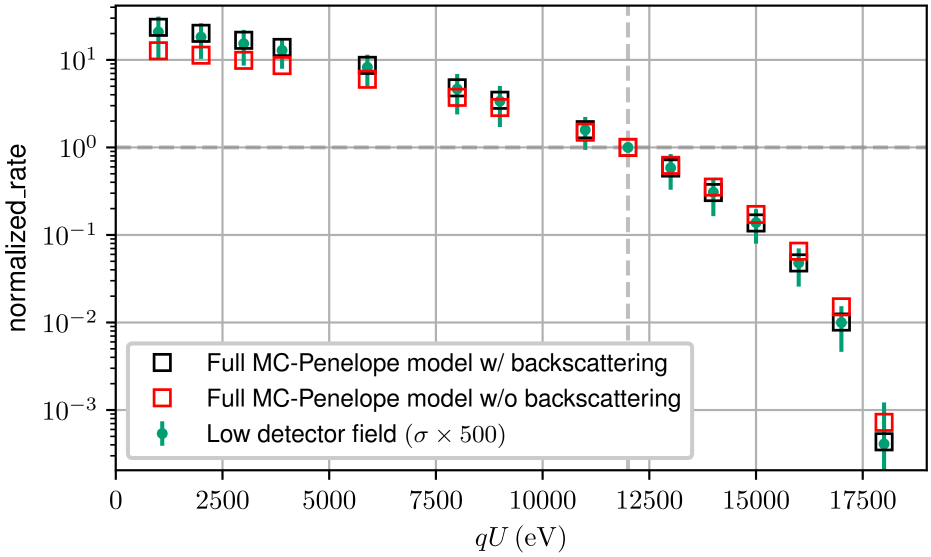

Figure 6.7: Normalized rates for rear-wall-induced background, as defined in Equation 6.2, under the low detector magnetic field setting. Rates are normalized to the value at 12 keV and compared with predictions from TRISTAN Full Monte Carlo simulations using the Penelope model. Simulation results are shown both with and without including backscattering in the rear wall.

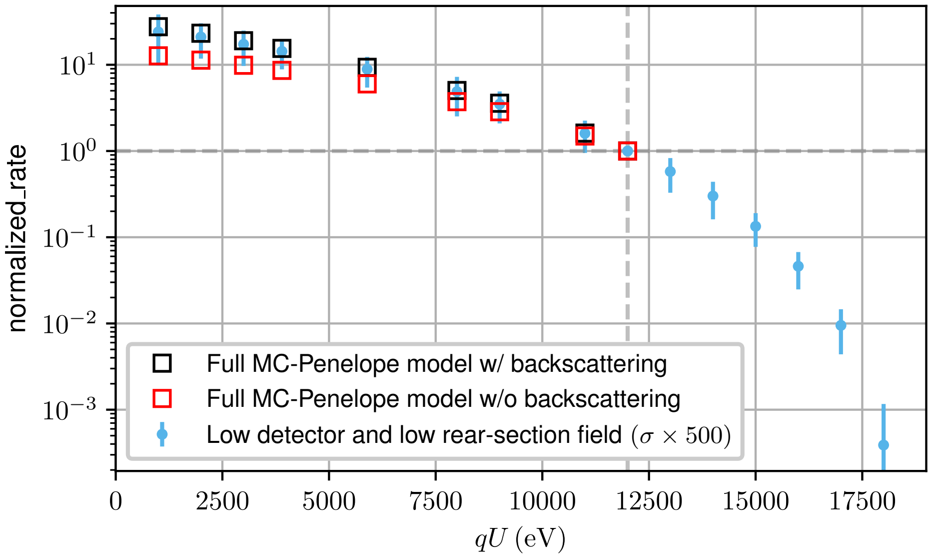

Figure 6.8: Normalized rates for rear-wall-induced background, as defined in Equation 6.2, under the low detector and low rear-section magnetic field setting. Rates are normalized to the value at 12 keV and compared with predictions from TRISTAN Full Monte Carlo simulations using the Penelope model. Simulation results are shown both with and without including backscattering in the rear wall.

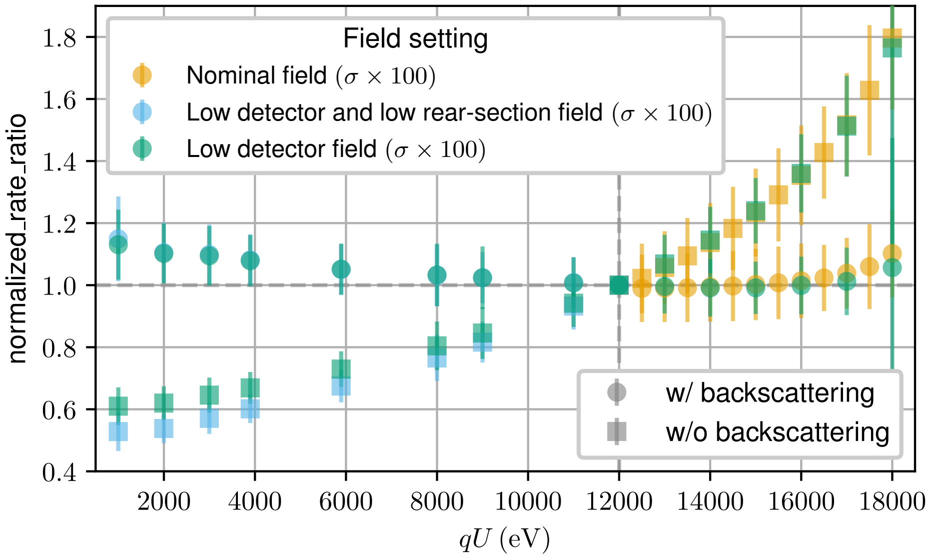

Figure 6.9: Normalized_rate_ratios for rear-wall-induced background, as defined in Equation 6.3, under three magnetic field configurations. Rates are normalized to the value at 12 keV and compared with predictions from TRISTAN Full Monte Carlo simulations using the Penelope model. Simulation results are shown both with and without including backscattering in the rear wall.

The normalized_rate_ratio obtained from the Penelope model was also compared with that from the Single Scattering model under nominal settings, as shown in Figure 6.10. The less than 10% deviation of the normalized_rate_ratio for both models when the backscattering is included demonstrates the robustness of the Monte Carlo simulation framework.

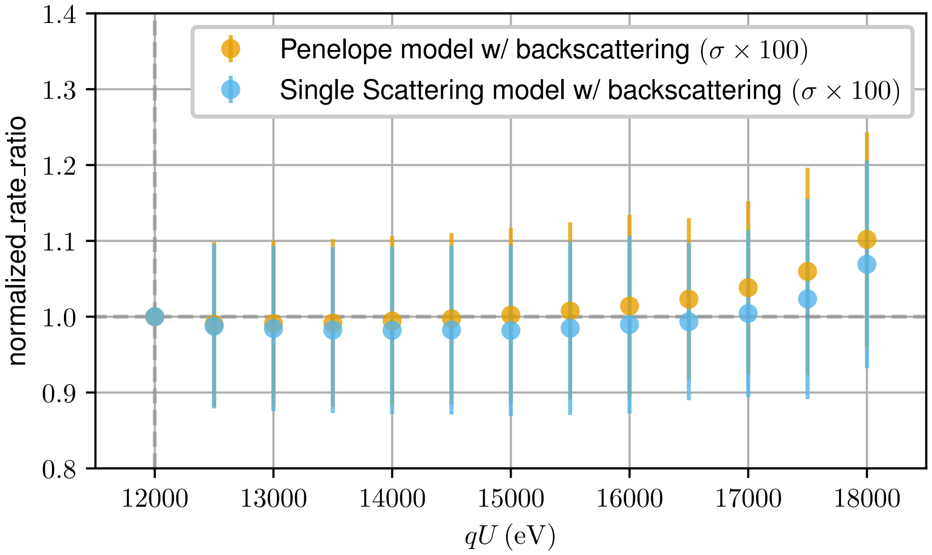

Figure 6.10: Normalized_rate_ratios for rear-wall-induced background, as defined in Equation 6.3, under the nominal field configuration. Rates are normalized to the value at 12 keV and compared with predictions from TRISTAN Full Monte Carlo simulations using the Penelope model and the Single Scattering model. Simulation results are shown both with and without including backscattering in the rear wall.

Remaining minor deviations between simulation and measurement are likely due to the incomplete treatment of backscattering effects from the rear wall. Additionally, radial dependence of the rear-wall-induced background rate may contribute to these deviations. The mean measured rear-wall-induced background rate per pixel for each of the nine rings considered in the preceding analysis under the Nominal field configuration is shown in Figure 6.11. A clear trend is observed, with the background rate increasing from the innermost to the outermost rings. The impact of this radial variation, along with a more refined modeling of the backscattering effects, will be addressed in future studies.

6.4 Next Steps in the Treatment of Rear-Wall Backscattering Systematics

Dedicated measurements of the rear-wall-induced background rate at low retarding energies revealed a clear discrepancy between experimental data and predictions from a simple model. To address this, the Kassiopeia+Geant4 full Monte Carlo simulation, developed as part of the TRISTAN project, was employed to incorporate rear-wall backscattering effects, leading to a significantly improved agreement between simulation and measurement. Given that rear-wall backscattering constitutes a major systematic effect for TRISTAN, this work enhances the understanding of the phenomenon through a combination of detailed simulations and dedicated in situ measurements, contributing to a more accurate characterization and, ultimately, a reduction of the associated systematic uncertainty.

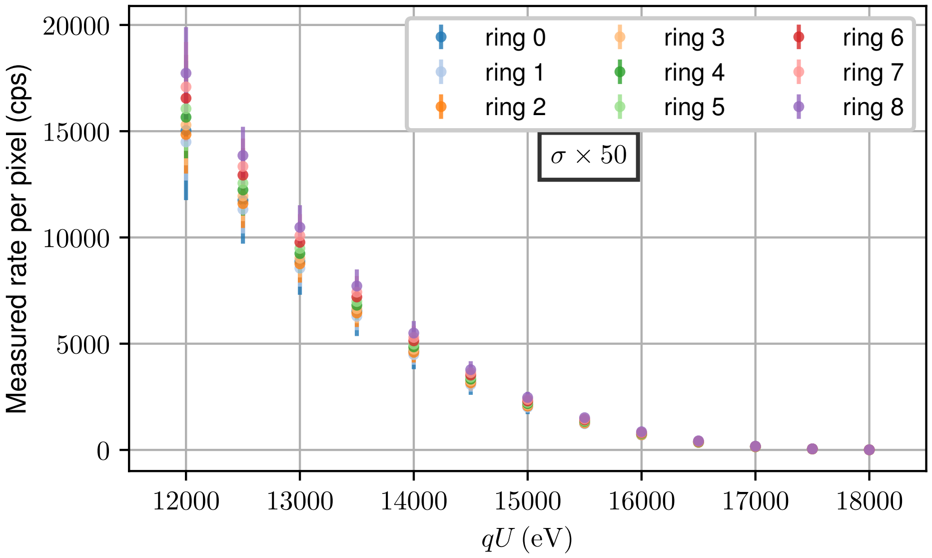

Figure 6.11: Mean measured rear-wall-induced background rate per pixel for each of the nine rings under the Nominal field configuration.

Further validation may be achieved through measurements that have been performed with Krypton in the source or by analyzing rear-wall-induced background measurements near the tritium endpoint. Additionally, cleaning the rear wall and conducting scans at ≈ 1% of the nominal tritium column density would allow for a targeted investigation of the rear-wall backscattering impact on the neutrino mass analysis. Preliminary studies indicate that energy loss due to rear-wall backscattering can meaningfully affect the neutrino mass [166, 167]. This effect becomes increasingly significant if the analysis range is extended.

Although the Kassiopeia+Geant4 model offers a high-fidelity simulation of the backscattering process, it is computationally too expensive for routine use in data analysis. As an alternative, the energy loss (see Figure 6.5) can be approximated using basis functions, such as a Gaussian mixture, following the approach used to model inelastic scattering in the WGTS. This simplified model could be incorporated into the full KATRIN analysis framework, making it feasible to apply to the complete KATRIN dataset.

7

Summary & Outlook

The work presented in this thesis investigates the existence of light sterile neutrinos within the 3+1 neutrino mixing framework, utilizing high-precision tritium β-decay measurements from the first five science runs of the KATRIN experiment. The analysis followed a frequentist approach and was independently conducted by two analysis teams using distinct software frameworks. The combined efforts of both analysis paths led to the release of the latest KATRIN results on sterile neutrino searches based on the first five science runs [137].

Right-handed sterile neutrinos, spanning a wide range of masses, are a well-motivated extension of the Standard Model, which currently contains only left-handed (active) neutrino fields. The observation of neutrino flavor oscillations implied that neutrinos had non-degenerate masses and that flavor eigenstates mixed. This discovery resolved the solar neutrino deficit, although several experimental anomalies remained unexplained. Right-handed sterile neutrinos could facilitate the - as of now unknown - mass generation mechanism of neutrinos. To achieve this, the Standard Model is minimally extended by adding gauge-singlet right-handed neutrino fields. Introduction of these new fields is termed as “Extended Standard Model". These hypothetical neutral leptons, are commonly referred to as sterile neutrinos, mix with the three active neutrinos (ν_e, ν_μ, ν_τ) but do not engage in standard weak interactions. In general, theoretical frameworks impose no constraints on the number of sterile neutrinos, their mass scales, or the magnitude of their mixing with active neutrino states. Since sterile neutrinos lack Standard Model interactions, they can only be probed via active–sterile mixing, leading to an imprint on neutrino oscillation patterns, non-unitarity of the PMNS matrix, kinks in β-decay spectra, and contributions to the effective mass in neutrinoless double-β decay.

Additionally, a possible existence of sterile neutrinos is motivated by two intriguing hints: the anomalous results from short baseline neutrino oscillation experiments requiring eV scale-singlets, and keV-scale candidates suggested by unexplained X-ray lines potentially contributing to dark matter. This thesis focuses exclusively on the eV-scale sterile neutrino, modeled as a single sterile neutrino ν_4 at the eV mass scale in the 3 (active)+ 1(sterile) scheme. Such model can be tested with cosmological data, short baseline neutrino oscillation experiments, direct neutrino mass measurements and neutrinoless double beta decay searches.

Cosmological observations constrain the effective number of relativistic neutrino species N_{eff} and the sum of neutrino masses $\sum m_\nu \lesssim 0.072\,\text{eV}$, consistent with three neutrino species. However, these constraints assume that the sterile neutrino was in thermal equilibrium with active neutrinos during neutrino decoupling, an assumption that may not hold in all models. The sterile state also induces fast oscillations at short baselines and modifies effective neutrino masses relevant to beta decay and neutrinoless double beta decay. Despite some tension between appearance and disappearance data, the 3+1 model remains the simplest and most experimentally accessible framework for sterile neutrino searches.

Chapter 1 reviewed the theoretical foundation for neutrino physics, outlining the Standard Model treatment of neutrinos, the phenomenon of neutrino oscillations, and the motivation for sterile neutrinos arising from both experimental anomalies and theoretical considerations. Direct neutrino mass experiments, such as the Karlsruhe Tritium Neutrino (KATRIN) experiment, probe the absolute neutrino mass scale by analyzing distortions in the β-decay spectrum near its kinematic endpoint. A sterile neutrino at the eV scale, if mixed with the electron flavor, would induce a spectral kink below the endpoint, with an amplitude set by the active-sterile mixing strength. KATRIN is thus well positioned to test the $3+1$ scenario through high precision tritium β-decay spectroscopy.

Chapter 2 presented the design and operation of the KATRIN experiment, outlining the beamline, spectrometer, and detector systems that enable high-precision β-decay measurements.

Chapter 3 focused on the modeling of the experimental response, including the treatment of systematic effects, relevant calibration measurements, and their integration into the predicted electron rate observed by KATRIN.

Building on the theoretical and experimental foundations established in the preceding chapters, the main contributions and results of this thesis were presented in chapter 4, 5 and 6 and are individually summarized below:

Chapter 4 reported the search for eV-scale sterile neutrinos using data from the first five KATRIN science runs (KNM-1–5) conducted between April 2019 and July 2021. This dataset comprised 1,757 high-precision β-decay scans and approximately 36 million electrons measured within the retarding-potential window from $E_0 - 40\,\mathrm{eV}$ to $E_0 + 135\,\mathrm{eV}$, which defined the primary search region for sterile neutrinos. This analysis builds on earlier KATRIN publications [11, 12], which were based on the first two campaigns and analyzed six million electrons within a 40 eV window below the β-decay endpoint. The results presented in this thesis find no significant sterile-neutrino signal, improve the exclusion limits on eV-scale sterile neutrino parameters, and form parts of the results released in [137].

Several experimental upgrades accompanied the dataset expansion. The tritium source calibration incorporated co-circulated $^{83\mathrm{m}}$Kr conversion electrons, and ozone cleaning was employed in KNM5 to reduce β-decay background from tritium accumulation on the rear wall.

The measurement campaigns initially utilized the normal analyzing plane (NAP) configuration with 117 detector pixels, then transitioned from KNM3 onward to a shifted analyzing plane (SAP) configuration. This modification reduced the spectrometer background significantly. To address the spatial variations arising due to the SAP configuration, pixels were grouped into fourteen patches of nine pixels each, enabling patchwise nuisance parameter treatment.

The frequentist analysis framework modeled the integral β-decay rate as a Gaussian likelihood for high-count NAP data and a Poisson likelihood for the more segmented SAP patches. These were combined into a joint $\chi^2_{\mathrm{combined}}$ function incorporating Gaussian pull terms to constrain nuisance parameters.

The best-fit sterile neutrino parameters were determined by minimizing the test statistic $\chi^2 = -2\ln\mathcal{L}$, where $\mathcal{L}$ denotes the likelihood function, over all model parameters with $m_4^2 \in [0, 1600]\,\mathrm{eV}^2$ and $|U_{e4}|^2 \in [0, 0.5]$. The goodness-of-fit was evaluated using the best-fit χ^2_{bf} value and its expected asymptotic distribution under the null hypothesis. The statistical significance was assessed through $\Delta\chi^2_{\mathrm{bf}} = \chi^2_{\mathrm{null}} - \chi^2_{\mathrm{bf}}$ and its corresponding asymptotic distribution. Determining the critical thresholds for hypothesis testing and constructing confidence contours required reliable knowledge of these asymptotic distributions. Although Wilks' theorem is often used to justify chi-squared approximations, a dedicated Monte Carlo study was performed. This study confirmed that, even though some of the conditions required for applicability of Wilks' theorem were not satisfied, the Monte Carlo distributions aligned with the asymptotic expectations. Consequently, the asymptotic distributions were employed in the final analysis. Without such validation, assuming incorrect asymptotic distributions could lead to mis-estimation of p-values or confidence intervals, potentially resulting in overstated or understated significance of the sterile neutrino signal.

Sensitivity analysis was first performed on each of the five KNM campaigns. For each campaign, both statistical-only and full (statistical+systematic) analyses produced 95% C.L. sensitivity contours in the $(m_4^2, |U_{e4}|^2)$ plane. Raster scans then confirmed that the sensitivity was dominated by statistical uncertainties. Applying the analysis to data, all campaigns except KNM4 yielded open exclusion contours; KNM4 alone exhibited a closed contour at $m_4^2 = 37.49\,\mathrm{eV}^2$ and $|U_{e4}|^2 = 0.045$ (99.94% C.L.), motivating the subsequent post-unblinding investigations. Post-unblinding investigations of KNM4 employed data subdivision, background re-modeling, and systematic re-evaluation to identify the origin of the closed contour. Background mis-modeling, particularly related to scan-step-duration-dependent effects, was identified as a primary contributor. Implementation of a quadratic time-dependent background model reduced the significance below the 95% threshold for the KNM4-b data subset. Further studies addressed discrepancies in the energy-loss model, source-potential drifts, and rear-wall background estimates. A shift of approximately 60 meV in the fitted endpoint E_0 across data subsets was attributed to time-dependent variations in the source potential. This shift, together with differences in the measurement time distributions, introduced a spectral distortion in the integrated β-decay spectrum of the combined KNM4 dataset. The resulting feature was misinterpreted as a sterile neutrino signature. To address this, the KNM4 dataset was partitioned into two subsets, KNM4-NOM and KNM4-OPT, based on their measurement time characteristics. In the subsequent re-analysis of the KNM1–5 datasets, all relevant systematic parameters, including those associated with energy loss and source-potential drift, were revised accordingly.

No significant sterile-neutrino signal was observed in the KATRIN search based on the first five measurement campaigns. The resulting 95% C.L. exclusion contour significantly improves upon earlier results and constrains a substantial portion of the parameter space associated with the Reactor Antineutrino Anomaly and the gallium anomaly, including the BEST experiment's best-fit point, which is now excluded at 96.56% C.L. Furthermore, KATRIN fully excludes the Neutrino-4 claim of oscillations at $\Delta m_{41}^2 = 7.3\,\mathrm{eV}^2$, rejecting its best-fit point at 99.99% C.L. KATRIN's results challenge the light sterile-neutrino hypothesis and complement reactor-based oscillation experiments by probing higher Δm_{41}^2 values, with sensitivity overlapping recent PROSPECT and STEREO limits around $\Delta m_{41}^2 \sim 3\,\mathrm{eV}^2$, where reactor experiments like PROSPECT, STEREO, and DANSS provide strong constraints through distinct background suppression techniques and high-statistics datasets.

When the 95% C.L. exclusion contour derived from the KNM1–5 data was overlaid on the sensitivity projection, multiple intersections between the contours were observed. For certain values of m_4^2, the observed exclusion reached smaller mixing angles than predicted by the sensitivity analysis. This behavior was investigated using pseudo-experiments and found to be consistent with statistical fluctuations under the null hypothesis. The impact of different treatments of the active neutrino mass on the exclusion limits was also examined. A technical constraint requiring the active neutrino mass to be positive and smaller than the sterile neutrino mass was found to reproduce the contour obtained when the active neutrino mass was fixed to zero for $m_4^2 \approx 40\,\mathrm{eV}^2$, while gradually shifting toward the contour of an unconstrained active neutrino mass at higher m_4^2 values.

Furthermore, the linear correlation between the active and sterile neutrino masses was quantified by generating Asimov datasets across a grid of true $(m_4^2, |U_{e4}|^2)$ values with $m_\nu^2 = 0$. For each grid point, the χ^2 function was minimized at perturbed m_4^2 values to extract the slope α_{slope} in the linear relation $m_\nu^2 = \alpha_{\mathrm{slope}}\, m_4^2 + \mathrm{const}$. The resulting contour map demonstrated a high negative correlation for low sterile neutrino masses and high mixing, highlighting the degeneracy between the active and sterile neutrino branches. This degeneracy indicates that in certain regions of parameter space, variations in the active neutrino mass can partially mimic or compensate for sterile neutrino effects, complicating the separation of the two signals. As a result, careful treatment of the active neutrino mass is essential to avoid biased inference of sterile parameters, and in some cases.

Chapter 5 presented the development and application of a Bayesian analysis framework for the sterile neutrino search in the KATRIN experiment, providing a complementary approach to the Frequentist methods previously employed. Within this framework, model parameters including sterile neutrino mass and mixing were treated as random variables, and experimental constraints and systematic uncertainties were explicitly incorporated through prior probability distributions. One key advantage of the Bayesian approach is that it does not rely on knowledge of the asymptotic distribution of the test statistic under the null hypothesis, verification of which can be computationally intensive in the Frequentist framework.

The analysis combined KATRIN's likelihood functions with priors on both physics parameters and nuisance parameters, employing marginalization to obtain posterior distributions over the sterile parameters $(m_4^2, |U_{e4}|^2)$. Computationally, the analysis employed both grid-based quadrature methods and advanced sampling techniques, including nested sampling algorithms (`Nautilus`, `UltraNest`), to evaluate high-dimensional marginalization integrals robustly.

Using noninformative priors for the sterile neutrino parameters, the analysis constructed Highest Posterior Density (HPD) regions as the smallest subsets of parameter space containing the specified posterior probability mass, determined through an efficient logarithmic grid scan over m_4^2 and $|U_{e4}|^2$. While HPD regions are a standard way to summarize two-dimensional posterior distributions, they depend strongly on the choice of prior distribution for the sterile neutrino parameters. To support the sterile neutrino search, a Bayes factor surface was constructed by evaluating the ratio $B_{10}(m_4^2,\, |U_{e4}|^2)$ of the marginalized likelihood under the sterile neutrino hypothesis, with fixed values of m_4^2 and $|U_{e4}|^2$, to that under the null hypothesis defined by $m_4^2 = 0$ and $|U_{e4}|^2 = 0$. This surface provided an interpretable measure of relative model support across the parameter space, enabling identification of regions with moderate, strong, or very strong evidence for or against sterile neutrinos. The Bayes factor along with any choice of prior on the sterile neutrino parameters can be used to compute HPD regions at any desired credibility levels.

To assess the impact of systematic uncertainties, an importance weight-ratio was defined, comparing the marginal likelihood computed with nuisance parameters fixed at their nominal values to that obtained when those parameters were integrated over their prior distributions. Values of this ratio significantly different from unity indicated that marginalizing over systematic uncertainties meaningfully altered the inferred evidence for sterile neutrino parameters, thereby quantifying the degree to which systematic effects influenced the sterile-neutrino inference.

The developed Bayesian framework was demonstrated in this thesis using an Asimov dataset. It showed sensitivity comparable to the Frequentist analysis and was also able to effectively assess the impact of systematic uncertainties and is now available to be applied to forthcoming KATRIN data analyses.

Chapter 6 addressed the systematic effect of rear-wall backscattering in the KATRIN experiment. The KATRIN rear wall is a metal plate that terminates the experiment's magnetic flux tube and serves as a surface where residual tritium molecules can adsorb and undergo β-decay. A discrepancy between the measured electron spectrum and the predictions of the simplified model, which combines the β-decay spectrum with the transmission function, was hypothesized to arise from electrons entering the rear-wall material, scattering, and propagating back into the spectrometer with reduced energies. Such backscattering can also occur for electrons starting from the source in the direction of the rear-wall. Since a significant fraction of these backscattered electrons are expected to lose more than 40 eV of energy, placing them outside the current analysis window, the effect is anticipated to have minimal impact on the present eV-scale sterile neutrino search. However, it becomes critically important for the forthcoming experimental program of KATRIN, searching for keV-scale sterile neutrino with the TRISTAN detector upgrade, where precise modeling of energy losses far below the tritium endpoint is required.

To characterize this effect, measurements of the rear-wall-induced background were performed at retarding energies between 1 keV and 18 keV under multiple magnetic-field configurations that varied the acceptance of backscattered electrons and the rear-wall area visible to the detector. These data revealed significant deviations from the predictions of the simplified model, indicating that electron scattering in the rear-wall material plays a key role.

A high-fidelity Monte Carlo simulation combining numerical simulations of electro-magnetic field maps generated using the Kassiopeia software and Geant4's Penelope and Single Scattering physics models was tested to explicitly simulate electron scattering within the rear wall and track backscattering from the rear wall. Simulations that excluded backscattering failed to reproduce the data, yielding a level of discrepancy comparable to that of the simplified model. Including backscattering significantly reduced the discrepancy, but further analysis is needed to fully account for the remaining deviation.

This lays the groundwork for extracting an energy-loss kernel suitable for parametrization, enabling the development of fast and reliable corrections for rear-wall backscattering effects in future high-sensitivity neutrino-mass and keV-scale sterile-neutrino analyses.

Outlook

The following recommendations outline potential avenues for future research that could enhance the sensitivity and robustness of the sterile neutrino search conducted with the KATRIN experiment.

- **Analysis of the Complete KATRIN Dataset:** This thesis presented KATRIN's sterile neutrino exclusion bounds based on the first five science runs (KNM1–KNM5), corresponding to approximately 36 million signal electrons. Upon completion of KATRIN's data collection campaign at the end of 2025, the full dataset is expected to include roughly five times the number of signal electrons analyzed in this work. Based on this increased statistical power, the projected sensitivity to sterile neutrino parameters has been estimated and is compared to the current exclusion limits as well as the 95% C.L. exclusion contours from the STEREO [22] and DANSS [171] experiments, as shown in Figure 7.1. A successful analysis of the complete dataset will enable KATRIN to achieve further improved sensitivity to eV-scale sterile neutrino parameters and provide a decisive test of the anomalies reported by previous short-baseline experiments.
- **Extended Analysis Range: Analysis Range:** The current analysis framework processes the KATRIN dataset down to 40 eV below the tritium β-decay endpoint. However, routine data acquisition extends to 90 eV below the endpoint, in principle enabling a broader search window for sterile neutrinos. To assess the sensitivity across the full energy interval, Asimov datasets were generated based on the KNM1–5 conditions, with event rates fixed to the expected values under the null hypothesis, neglecting statistical fluctuations. Ongoing efforts are focused on accurately modeling energy-dependent systematic effects across this extended range, which is essential to ensure reliable interpretation of the data. Preliminary sensitivity studies presented in this thesis suggest that expanding the analysis window to include the full 90 eV range can significantly enhance sensitivity to sterile neutrino masses in the range $300, \mathrm{eV}^2 \leq m_4^2 \leq 3000, \mathrm{eV}^2$. Future work should focus on refining these systematic models and incorporating them into the analysis framework to fully leverage the additional data.
- **Investigating Kinks in Raster Scans:** Kinks observed in Raster scans by both analysis teams were initially hypothesized to arise from the specific choice of measurement time

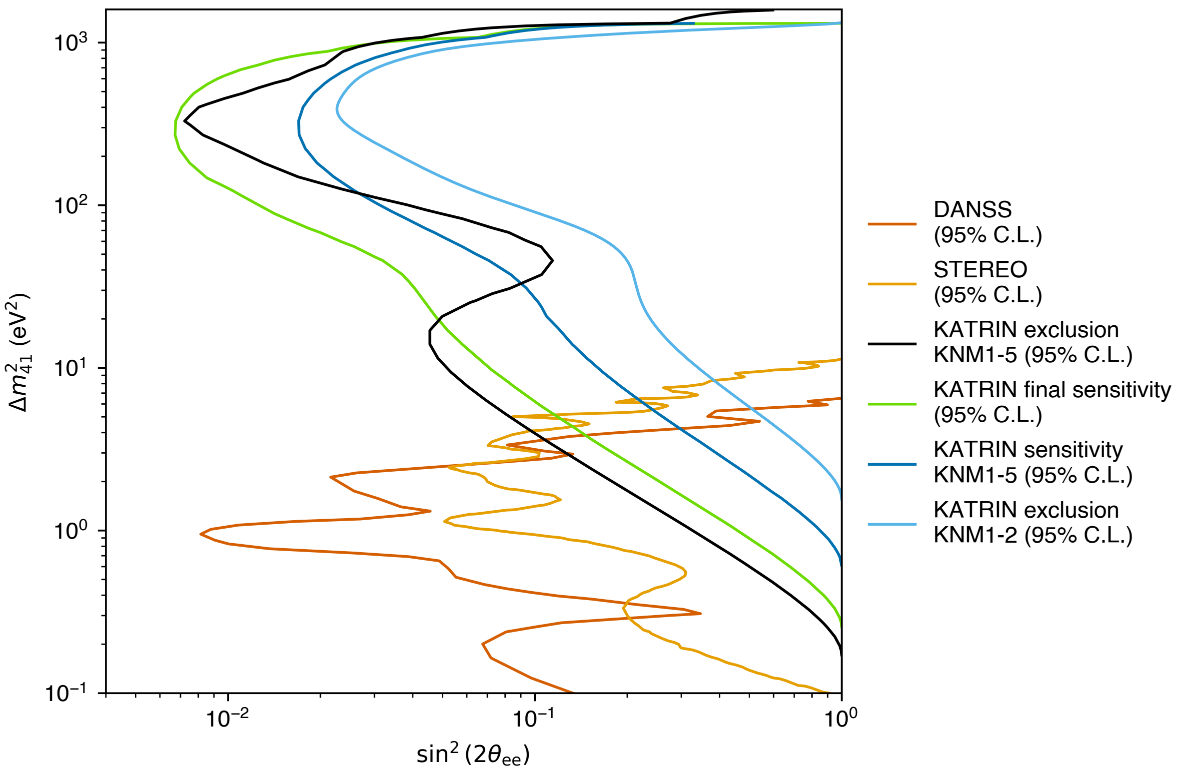

Figure 7.1: 95% C.L. sensitivity curve in the (Δm^2_{41}, $\sin^2(2\theta_{ee})$) parameter space, projected from the analysis of the complete KATRIN dataset, compared with the 95% C.L. exclusion contours from reactor-based experiments [171, 22]. The 95% C.L. exclusion curve derived from the KNM1–5 datasets, as presented in this thesis, is also shown.

distributions (MTDs). To test this, scans were performed using time-uniform MTDs with randomly selected retarding energies. The persistence of kinks in these conditions suggests that the choice of MTD alone does not account for their presence. Further investigation is required to determine the underlying cause of these features, particularly why they appear in some systematic scenarios but not others.

- **Rear-Wall Backscattering Effects:** This thesis successfully addressed the discrepancies between observed and predicted rear-wall-induced background rates by combining dedicated measurements with detailed Monte Carlo simulations using numerical simulations of field maps obtained with Kassiopeia code and Geant4. The improved modeling of rear-wall backscattering is particularly important for the upcoming TRISTAN detector upgrade [58, 68], where it constitutes a key systematic effect. Further validation of the model is planned through dedicated krypton measurements and low-source-density tritium scans. To enable efficient incorporation into the large-scale KATRIN analysis framework, a simplified energy-loss model based on basis functions is proposed, facilitating practical application while retaining the essential physics.

- **Bayesian analysis framework for SAP and combined datasets:** The Bayesian framework for sterile neutrino search with KATRIN developed in this thesis was demonstrated on a Asimov dataset collected under the NAP configuration. The next step is to apply the Bayesian framework to datasets collected under SAP configurations to verify its robustness across different experimental conditions. A subsequent challenge will be to extend the framework for a joint analysis of the combined KNM1–KNM5 and further datasets.

- **Tackling computational challenges:** A direct comparison of the computational demands of the Frequentist and Bayesian methods will clarify their relative feasibility for large-scale KATRIN analyses. Because high-dimensional integration is required, the Bayesian approach is expected to need approximately ten times more likelihood evaluations than the Frequentist approach. Algorithmic improvements that reduce either the number of evaluations or the cost per evaluation would therefore be highly beneficial.

- **Studying 3+1+decay Model:** The (3+1) sterile neutrino model, which posits a single additional mass eigenstate, has been proposed to explain anomalies observed in short-baseline neutrino experiments. However, global fits reveal a significant tension between appearance and disappearance neutrino oscillation data sets, with the (3+1) model unable to simultaneously accommodate all observations. Extended models, such as the (3+2) scenario, cannot resolve this tension, while the (3+1+decay) model, allowing the fourth neutrino state to decay, reduces the tension to approximately 3.2σ [77]. Cosmological constraints, particularly from measurements of the effective number of relativistic species and the sum of neutrino masses, challenge the existence of fully thermalized eV-scale sterile neutrinos, but scenarios involving partial thermalization or decay can alleviate these tensions. Consequently, while the (3+1) model offers a straightforward extension to address certain anomalies, it remains insufficient to reconcile all experimental and cosmological data, necessitating further investigation into more complex models and mechanisms. KATRIN's precise spectral measurements enable direct comparison between the (3+1) and (3+1+decay) sterile neutrino scenarios, allowing it to test whether spectral distortions are more consistent with mixing alone or with additional decay dynamics.

A Appendix

A.1 Protocol for First KNM1-KNM5 Unblinding

The unblinding protocol outlined below was used to ensure a robust and unbiased sterile neutrino search in the KATRIN experiment. The main focus was on maintaining consistency across the different datasets and minimizing potential errors.

A.1.1 Sterile Neutrino Analysis on Asimov Dataset

- The sterile neutrino analysis was initially performed on Asimov datasets with $m_\nu^2 = 0, m_4^2 = 0, |U_{e4}|^2 = 0$.
- The true (unblinded) final state distribution (FSD) was employed to generate the Asimov dataset, as FSD blinding does not affect the baseline sterile neutrino analysis focused on spectral distortions well below the endpoint energy E_0.
- The primary analysis assumed a fixed active neutrino mass of 0 eV, in line with previous KSN1-2 publications [12]. A complementary analysis was conducted with the active neutrino mass as a fit parameter.
- The region of interest used for the primary analysis was $E_0 - 40\text{eV}$.
- The parameter space for finding the best fit was restricted to $\mathrm{m}_4^2 \leq 1000\ \mathrm{eV}^2$ due to limited number of data points available in the range of 31 eV to 40 eV below the end point. Collected statistics is high for the energy range close to the endpoint of the β-decay spectrum.

A.1.2 Cross-Checks for NAP and SAP Campaigns

- Cross-checks were performed for the Nominal Analyzing Plane (NAP) and Shifted Analyzing Plane (SAP) campaigns using two independent analysis approaches, implemented in the KaFit and Netrium frameworks, respectively.
- Checks included comparing best-fit values, significance of best-fit values, sensitivity contours and raster contours for all individual and the combined dataset.

A.1.3 Final Analysis on Experimental Dataset

- If all cross-checks passed, the analysis was performed on the experimental dataset.
- Cross-checks between the two teams are performed again for the results on the experimental datasets.

A.2 Extended Studies of the Empirical Distributions of χ^2 and $\Delta\chi^2$

Assessing the goodness-of-fit of a model with its best-fit parameters requires knowledge of the distribution of the χ^2 test statistic (see Section 4.2.4). Likewise, evaluating the significance of a best-fit sterile neutrino hypothesis and constructing exclusion contours relies on the distribution of $\Delta\chi^2$ (see Section 4.2.5). If the regularity conditions required by Wilks' theorem [252] are satisfied, the asymptotic chi-squared distribution of the test statistic may be applied, thereby eliminating the need for computationally intensive Monte Carlo simulations.

The regularity conditions required for the application of Wilks' theorem are not satisfied for the Grid Scan method (see Section 4.2.6.1), necessitating an empirical determination of the test statistic distribution. Monte Carlo simulations performed for the KNM1 and KNM2 datasets [230, Sec. 11.10] demonstrate that, although the conditions necessary for the validity of Wilks' theorem are not satisfied, the $\Delta\chi^2$ test statistic empirically follows a chi-squared distribution with two degrees of freedom.

In Section 4.3, results from Monte Carlo simulations for the Grid Scan method applied to the KNM5 dataset were presented and found to be consistent with those obtained for KNM1 and KNM2.

This section extends the validation to two additional inference methods, applied to the KNM5 dataset. In addition, results are presented for the Grid Scan method applied to the combined KNM1–5 dataset. Two sets of pseudo-experiments were generated: one based on an Asimov dataset corresponding to the null hypothesis ($m_4^2 = 0, \text{eV}^2$, $|U_{e4}|^2 = 0$), and the other based on a representative alternative hypothesis ($m_4^2 = 55.66, \text{eV}^2$, $|U_{e4}|^2 = 0.013$).

For completeness, the results from the Grid Scan method for the KNM5 dataset are reiterated here, along with definitions of the distribution similarity metrics used for validation.

A.2.1 Monte Carlo Simulation Framework

Starting from the Asimov datasets generated with $m_\nu^2 = 0\,\text{eV}^2$,$m_4^2 = 0\,\text{eV}^2$ and $|U_{e4}|^2 = 0$, $\mathcal{O}(10^3)$ randomized pseudo-experiments were generated to account for statistical fluctuations. Each randomized dataset was constructed by treating the count rate in each detector pixel at each retarding potential set-point as a Poisson-distributed random variable, with the mean given by the corresponding Asimov data.

Grid scans (see Section 4.2.6.1) were performed with each of the randomized datasets using 25×25 logarithmic grid in the sterile neutrino parameter space $m_4^2 \in [0.1, 1600]\,\text{eV}^2$ and $|U_{e4}|^2 \in [0.001, 0.5]$ considering only statistical uncertainties. The best-fit parameters were determined for each pseudo-experiment, and the corresponding χ^2_{bf} values were recorded, along with the test statistic and $\Delta\chi^2 = \chi^2_{\text{null}} - \chi^2_{\text{bf}}$. For the KNM5 dataset, in addition to the Grid Scan approach, a single fit treating the sterile neutrino mass m_4^2 and mixing $|U_{e4}|^2$ as fit parameters was investigated. Furthermore, a hybrid method was explored, wherein the best-fit parameter set obtained from the Grid Scan was used as the initial guess for the single fit with m_4^2 and $|U_{e4}|^2$ as fit parameters. In all cases, the active neutrino mass was fixed to its true value used in the datasets $m_\nu^2 = 0\,\text{eV}^2$.

For the single fits with m_4^2 and mixing $|U_{e4}|^2$ treated as fit parameters, two parameter domains were explored. The first restricted the fit to physically meaningful values: $m_4^2 \in [0, 1600]\,\text{eV}^2$ and $|U_{e4}|^2 \in [0, 0.5]$. The second allowed for non-physical values to test the fit behavior beyond the physical boundaries, with $m_4^2 \in [-1600, 1600]\,\text{eV}^2$ and $|U_{e4}|^2 \in [-0.5, 0.5]$. Within the physically allowed region, two different initial conditions were tested for the fit: one at $m_4^2 = 0\,\mathrm{eV}^2$, $|U_{e4}|^2 = 0$ and the other at $m_4^2 = 800\,\mathrm{eV}^2$, $|U_{e4}|^2 = 0.4$.

A summary of the three fitting methods and their respective configurations is provided below.

1. Method 1: Grid scan with 25×25 grid.
2. Method 2: Single fit with m_4^2 and $|U_{e4}|^2$ as fit parameters.
    (a) Physically allowed domain: $m_4^2 \in [0, 1600]\,\mathrm{eV}^2$ and $|U_{e4}|^2 \in [0, 0.5]$
        i. Initial condition: $m_4^2 = 0\,\mathrm{eV}^2$, $|U_{e4}|^2 = 0$
        ii. Initial condition: $m_4^2 = 800\,\mathrm{eV}^2$, $|U_{e4}|^2 = 0.4$
    (b) Non-physical domain: $m_4^2 \in [-1600, 1600]\,\mathrm{eV}^2$ and $|U_{e4}|^2 \in [-0.5, 0.5]$
        i. Initial condition: $m_4^2 = 0\,\mathrm{eV}^2$, $|U_{e4}|^2 = 0$
3. Method 3: Hybrid method with the best-fit parameter set obtained from the Grid Scan as the initial condition for the single fit.

In some pseudo-experiments, it is possible that $\chi^2_{\mathrm{bf}} > \chi^2_{\mathrm{null}}$ due to issues related to fit convergence or numerical tolerances. In such cases, χ^2_{bf} was set equal to χ^2_{null}, and consequently, $\Delta\chi^2$ was defined to be zero.

For Method 2, where the sterile neutrino parameters are restricted to the physically allowed domain, the true values $m_4^2 = 0\,\mathrm{eV}^2$ and $|U_{e4}|^2 = 0$ lie on the boundary of the parameter space. In such cases, the asymptotic distribution of the $\Delta\chi^2$ test statistic is no longer a standard chi-squared distribution but follows a so-called $\bar{\chi}^2$ distribution [51], given by

$$\bar{\chi}^2 = 0.25\delta(0) + 0.5\chi_1^2 + 0.25\chi_2^2, \tag{A.1}$$

where $\delta(0)$ denotes the Dirac delta function centered at zero.

A.2.2 Quantifying Distribution Similarity

The similarity between the empirical distributions of χ^2_{bf} and $\Delta\chi^2$ and reference distributions, such as chi-squared distributions, can be quantified using the following statistical metrics.

Kolmogorov-Smirnov (KS) Statistic

It is the maximum vertical distance between the empirical CDF (ECDF) and the theoretical CDF [59]. With n samples of a variable x and reference CDF $F(\cdot)$, the statistic can be calculated using the following steps.

1. Sort the samples: $x_{(1)} \le x_{(2)} \le \cdots \le x_{(n)}$
2. Compute $D^+ = \max_i \left(\frac{i}{n} - F(x_{(i)})\right)$ and $D^- = \max_i \left(F(x_{(i)}) - \frac{i-1}{n}\right)$.
3. KS statistic: $D = \max(D^+, D^-)$.

Smaller D indicates higher similarity.

Cramér-von Mises Criterion

It is the integrated squared difference between ECDF and CDF [59], given formally as

$$\omega^2 = \frac{1}{12n} + \sum_{i=1}^{n} \left(F(x_{(i)}) - \frac{2i-1}{2n} \right)^2 \tag{A.2}$$

Smaller ω^2 implies closer match.

The Kolmogorov-Smirnov statistic indicates the maximum discrepancy while Cramér-von Mises criterion compares the overall shape of the CDF. To estimate the expected values of the two similarity metrics, 10000 samples were drawn from the χ^2_{348} and χ^2_2 distributions. The empirical cumulative distribution function (ECDF) and the two metrics, along with their associated uncertainties, were calculated using bootstrapping. Bootstrapping involves generating new sample sets by resampling with replacement from the original dataset. From the ECDF of the χ^2_2 samples, the 95th percentile value, $\mathrm{ECDF}^{-1}(0.95)$, was also estimated. This corresponds to the 95% confidence level used in the sterile neutrino analysis (see Section 4.2.5). The reference and empirical probability density functions (PDFs) and cumulative distribution functions (CDFs) for the χ^2_{348} distribution, along with the values of the two similarity metrics, are presented in Figure A.1; the corresponding results for the χ^2_2 distribution are shown in Figure A.2. For both distributions, the empirical PDFs and CDFs exhibit good visual agreement with the corresponding reference distribution functions.

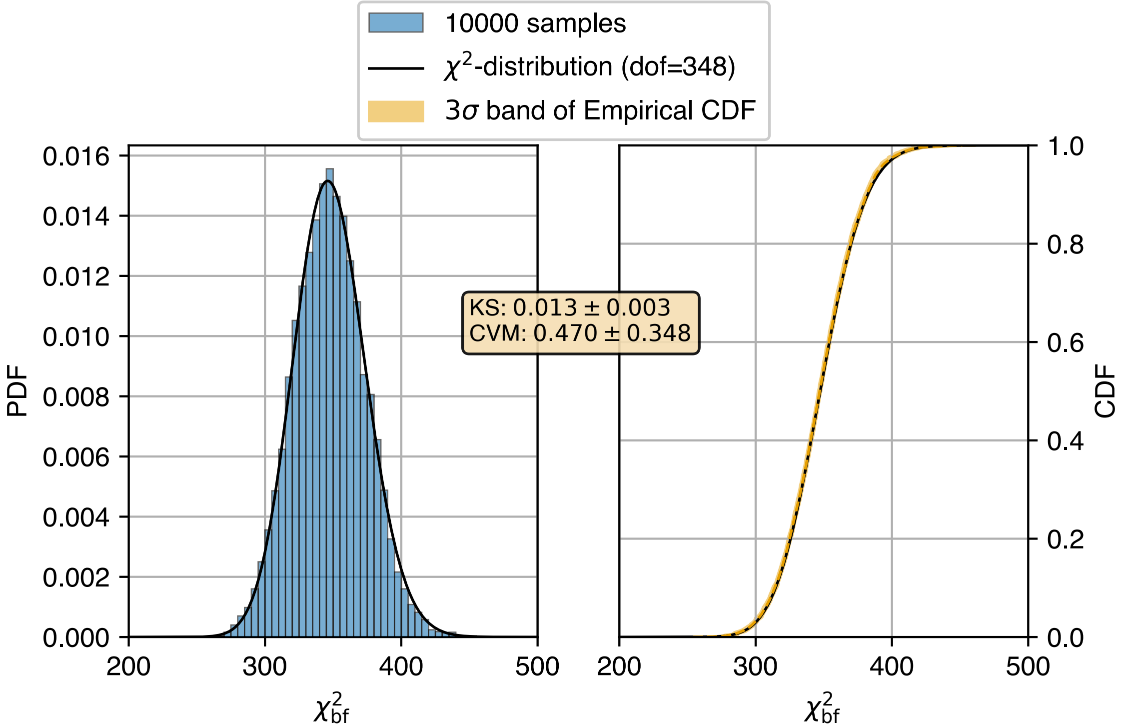

Figure A.1: Illustration of the Kolmogorov–Smirnov (KS) and Cramér–von Mises (CVM) metrics. Empirical probability density function (PDF, left) and cumulative distribution function (CDF, right) of 10000 samples drawn from the chi-squared distribution with 348 degrees of freedom. The black line represents the reference distribution. The empirical CDF's 3σ confidence band is shown in orange. The KS and CVM metrics indicate a low overall discrepancy.

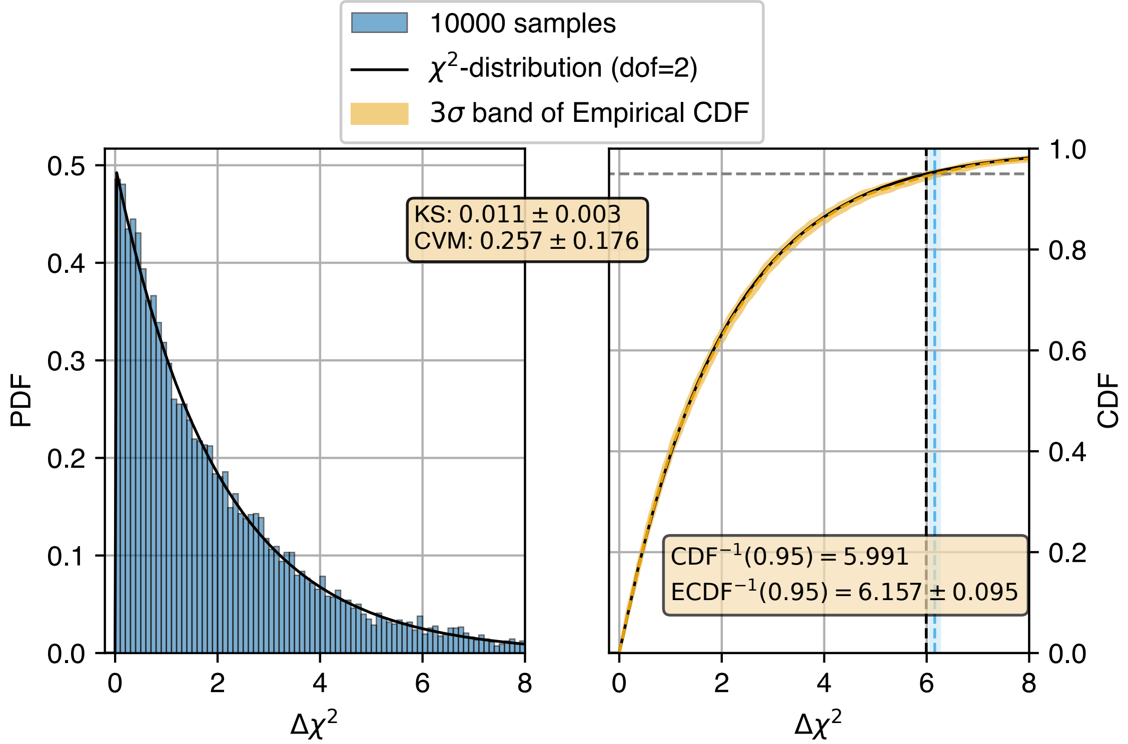

Figure A.2: Illustration of the Kolmogorov–Smirnov (KS) and Cramér–von Mises (CVM) metrics. Empirical probability density function (PDF, left) and cumulative distribution function (CDF, right) of 10000 samples drawn from the chi-squared distribution with 2 degrees of freedom. The black line represents the reference distribution. The empirical CDF's 3σ confidence band is shown in orange. The Kolmogorov–Smirnov (KS) and Cramér–von Mises (CVM) metrics indicate a low overall discrepancy. The 95th percentile value for the reference distribution is shown with the black dashed line alongside the estimated 95th percentile value with 1σ confidence band in light blue.

A.2.3 Results Using Method 1

Results for the Grid scan method are shown in Figure A.3 for χ^2_{bf} and in Figure A.4 for $\Delta\chi^2$. The empirical PDFs and CDFs exhibit good visual agreement with the corresponding reference chi-squared distributions, indicating low overall discrepancy. This observation is quantitatively supported by the Kolmogorov–Smirnov (KS) and Cramér–von Mises (CVM) similarity metrics. These results are consistent with the findings reported in [230, Sec. 11.10] for the KNM1 and KNM2 datasets, which demonstrate that despite the violation of Wilks' regularity conditions, the $\Delta\chi^2$ test statistic empirically follows a chi-squared distribution with two degrees of freedom.

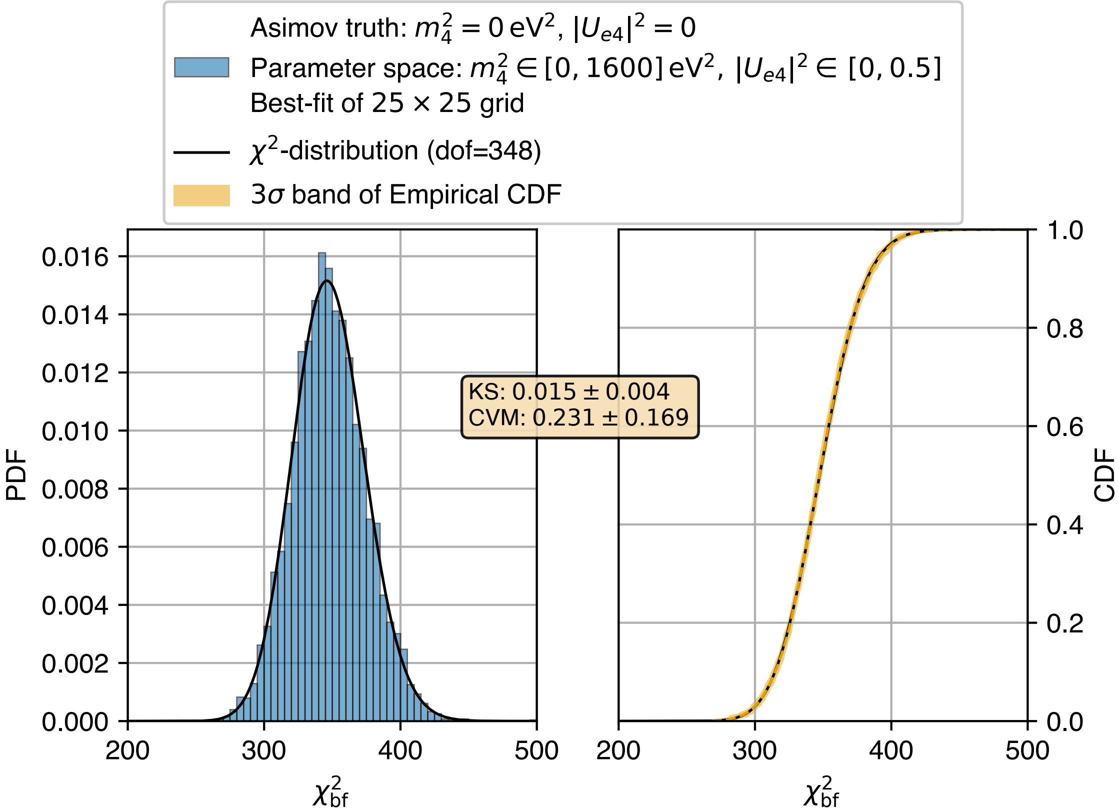

Figure A.3: Application of the Kolmogorov–Smirnov (KS) and Cramér–von Mises (CVM) metrics. Empirical probability density function (PDF, left) and cumulative distribution function (CDF, right) of the best-fit χ^2_{bf} values obtained from 10000 KNM5 pseudo-experiments using Method 1, where the sterile neutrino parameters were restricted to the physical domain. The Asimov dataset corresponds to the null hypothesis. The black line represents the reference distribution. The empirical CDF's 3σ confidence band is shown in orange. The KS and CVM metrics indicate a low overall discrepancy.

A.2.4 Results Using Method 2

Results for the configuration 2.a.i are shown in Figure A.5 for χ^2_{bf} and in Figure A.6 for $\Delta\chi^2$. While good agreement is observed for the χ^2_{bf}, a slight deviation is evident in the case of $\Delta\chi^2$. This discrepancy may stem from convergence of fits to local minima, potentially caused by the non-convex nature of the underlying optimization problem. As a remedy, an alternative initial guess was employed in configuration 2.a.ii to improve the fit convergence and mitigate the effects of the non-convex optimization landscape.

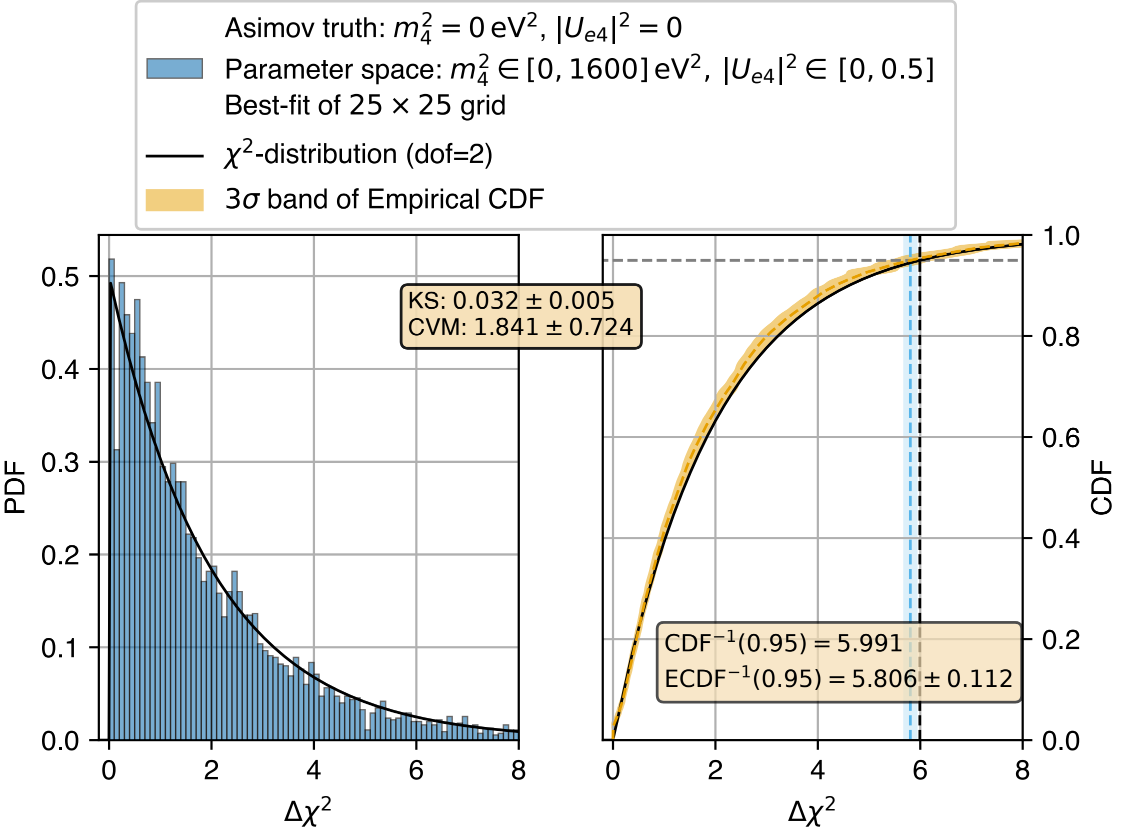

Figure A.4: Application of the Kolmogorov–Smirnov (KS) and Cramér–von Mises (CVM) metrics. Empirical probability density function (PDF, left) and cumulative distribution function (CDF, right) of the $\Delta\chi^2$ test statistic obtained from 10000 KNM5 pseudo-experiments using Method 1, where the sterile neutrino parameters were restricted to the physical domain. The Asimov dataset corresponds to the null hypothesis. The black line represents the reference distribution. The KS and CVM metrics indicate a low overall discrepancy. The empirical CDF's 3σ confidence band is shown in orange. The 95th percentile value for the reference distribution is shown with the black dashed line alongside the estimated 95th percentile value with 1σ confidence band in light blue.

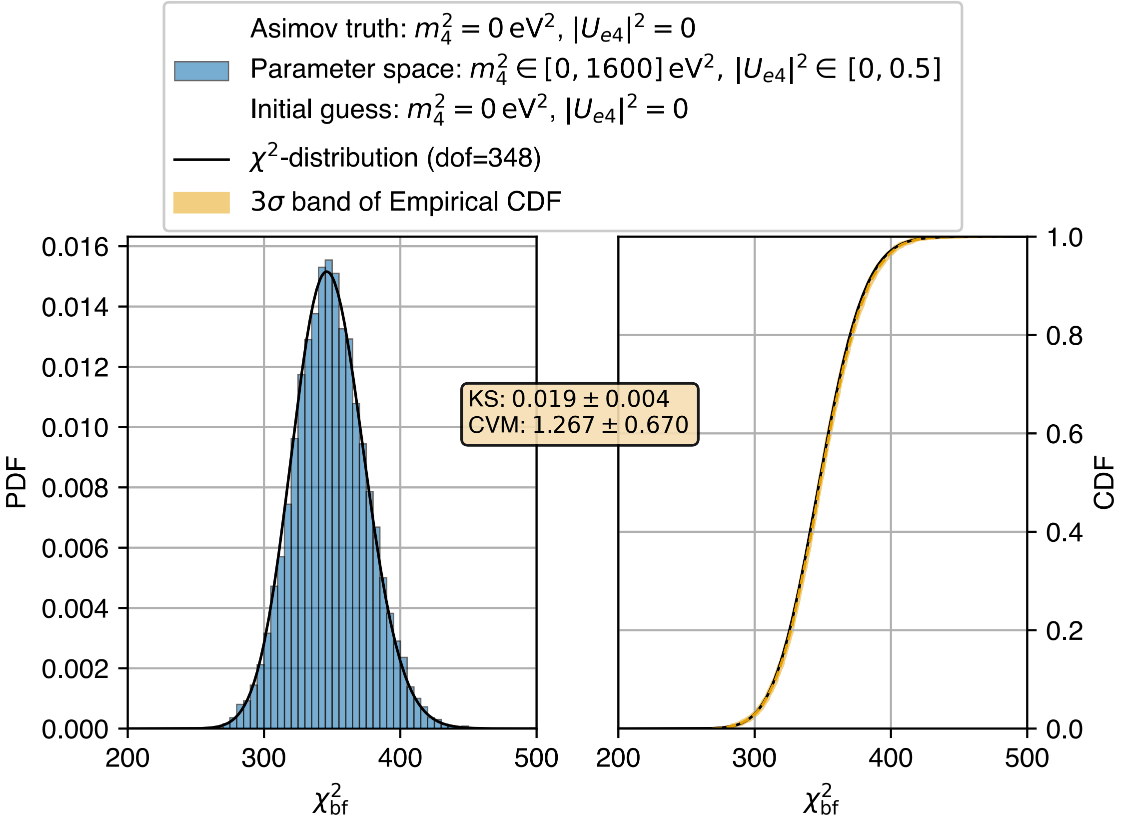

Figure A.5: Application of the Kolmogorov–Smirnov (KS) and Cramér–von Mises (CVM) metrics. Empirical probability density function (PDF, left) and cumulative distribution function (CDF, right) of the best-fit χ^2_{bf} values obtained from 10000 KNM5 pseudo-experiments using Method 2.a.i, where the sterile neutrino parameters were restricted to the physical domain. The Asimov dataset corresponds to the null hypothesis. The black line represents the reference distribution. The empirical CDF's 3σ confidence band is shown in orange. The KS and CVM metrics indicate a low overall discrepancy.

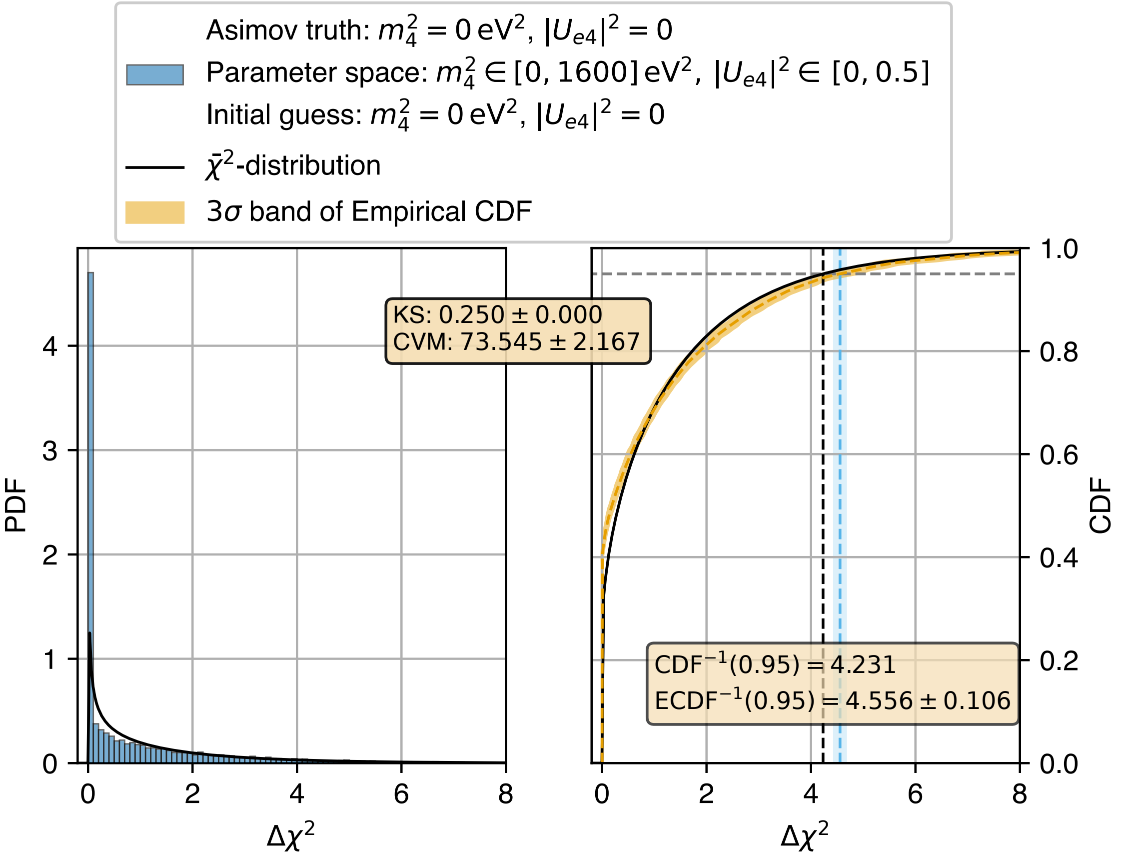

Figure A.6: Application of the Kolmogorov–Smirnov (KS) and Cramér–von Mises (CVM) metrics. Empirical probability density function (PDF, left) and cumulative distribution function (CDF, right) of the $\Delta\chi^2$ test statistic obtained from 10000 KNM5 pseudo-experiments using Method 2.a.i, where the sterile neutrino parameters were restricted to the physical domain. The Asimov dataset corresponds to the null hypothesis. The black line represents the reference distribution. The KS and CVM metrics indicate a slight discrepancy. The empirical CDF's 3σ confidence band is shown in orange. The 95th percentile value for the reference distribution is shown with the black dashed line alongside the estimated 95th percentile value with 1σ confidence band in light blue.

Results for the configuration 2.a.ii are shown in Figure A.7 for χ^2_{bf} and in Figure A.8 for $\Delta\chi^2$. Again a good agreement is observed for the χ^2_{bf} while a slight deviation is evident in the case of $\Delta\chi^2$. Since the observed deviation is comparable to that seen in configuration 2.a.i, it is not possible to attribute the discrepancy solely to issues with fit convergence.

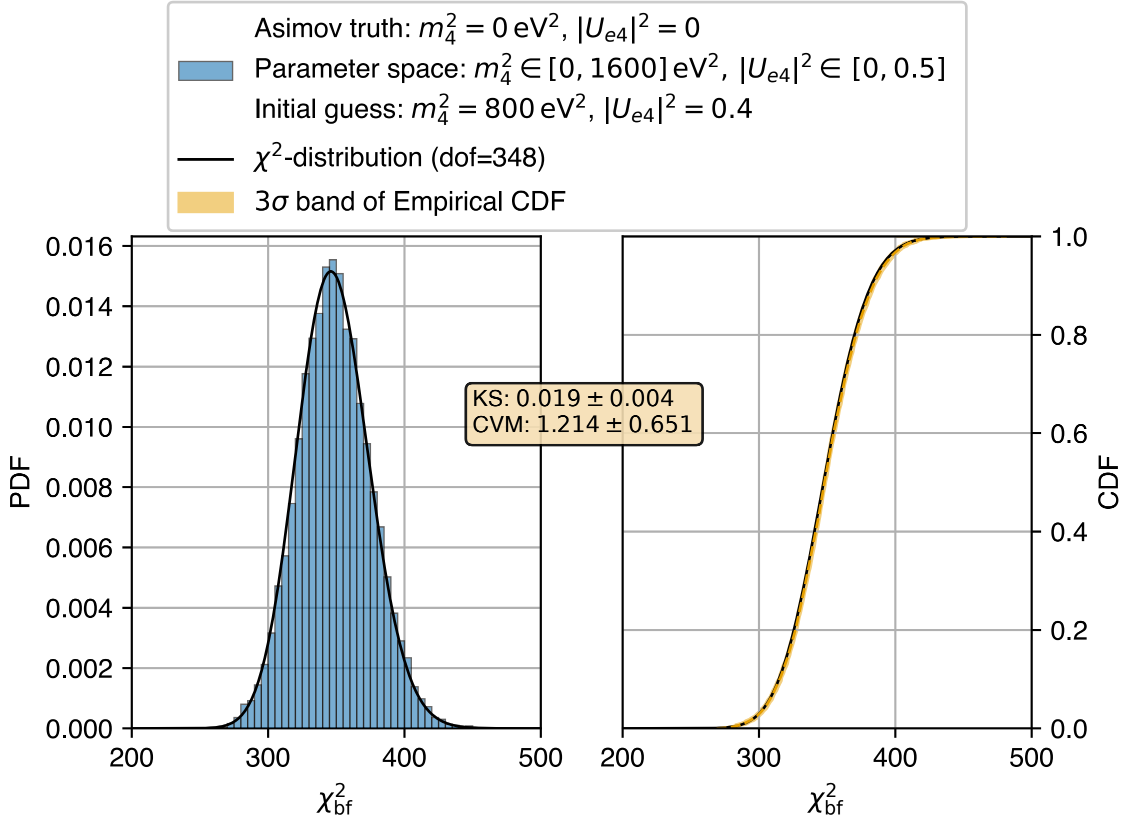

Figure A.7: Application of the Kolmogorov–Smirnov (KS) and Cramér–von Mises (CVM) metrics. Empirical probability density function (PDF, left) and cumulative distribution function (CDF, right) of the best-fit χ^2_{bf} values obtained from 10000 KNM5 pseudo-experiments using Method 2.a.ii, where the sterile neutrino parameters were restricted to the physical domain. The Asimov dataset corresponds to the null hypothesis. The black line represents the reference distribution. The empirical CDF's 3σ confidence band is shown in orange. The KS and CVM metrics indicate a low overall discrepancy.

Since the true parameter values lie within the interior of the search space for configuration 2.b.i, the resulting test statistic distribution is expected to align well with the predictions of Wilks' theorem. Results for the configuration 2.b.i are shown in Figure A.9 for χ^2_{bf} and in Figure A.10 for $\Delta\chi^2$. While good agreement is observed for the χ^2_{bf}, a significant deviation is observed in the case of $\Delta\chi^2$. Although the true parameters lie within the interior of the search space, the model becomes degenerate when $m_4^2 = 0\,\text{eV}^2$ or $|U_{e4}|^2 = 0$, effectively reducing the degrees of freedom. Reduction in the effective degrees of freedom may also explain the slight deviations seen in Figure A.6 and Figure A.8.

A.2.5 Results Using Method 3

Results for the Grid scan method are shown in Figure A.11 for χ^2_{bf} and in Figure A.12 for $\Delta\chi^2$. The results are expected to align with those of configuration 2.a. While there is good agreement

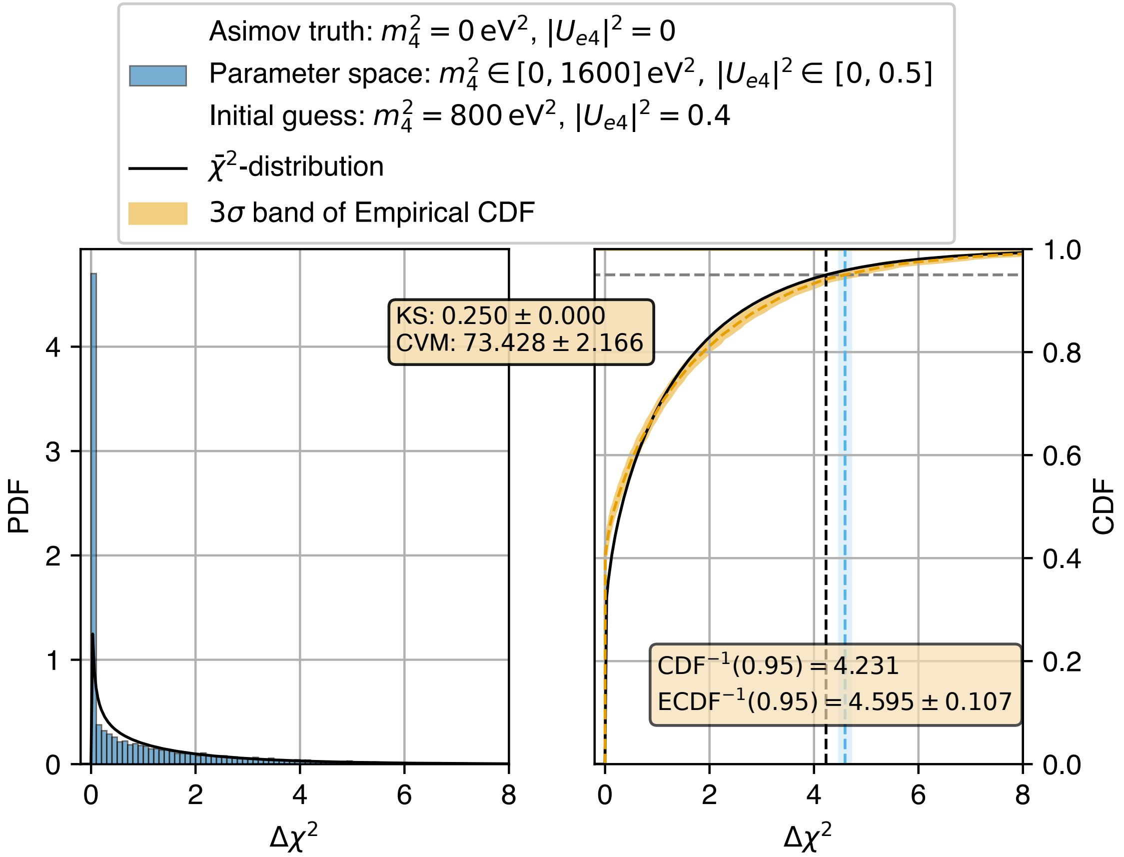

Figure A.8: Application of the Kolmogorov–Smirnov (KS) and Cramér–von Mises (CVM) metrics. Empirical probability density function (PDF, left) and cumulative distribution function (CDF, right) of the $\Delta\chi^2$ test statistic obtained from 10000 KNM5 pseudo-experiments using Method 2.a.ii, where the sterile neutrino parameters were restricted to the physical domain. The Asimov dataset corresponds to the null hypothesis. The black line represents the reference distribution. The KS and CVM metrics indicate a slight discrepancy. The empirical CDF's 3σ confidence band is shown in orange. The 95th percentile value for the reference distribution is shown with the black dashed line alongside the estimated 95th percentile value with 1σ confidence band in light blue.

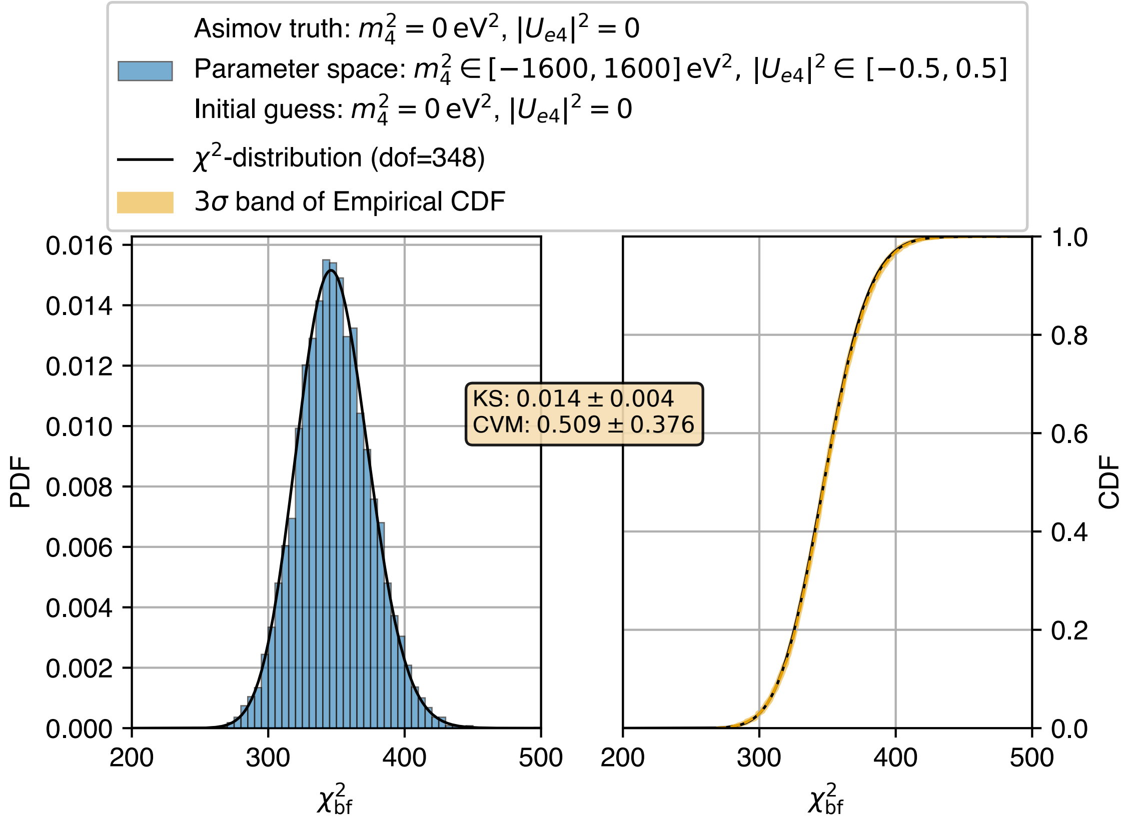

Figure A.9: Application of the Kolmogorov–Smirnov (KS) and Cramér–von Mises (CVM) metrics. Empirical probability density function (PDF, left) and cumulative distribution function (CDF, right) of the best-fit χ^2_{bf} values obtained from 10000 KNM5 pseudo-experiments using Method 2.b.i, where the sterile neutrino parameters were allowed to have non-physical values. The Asimov dataset corresponds to the null hypothesis. The black line represents the reference distribution. The empirical CDF's 3σ confidence band is shown in orange. The KS and CVM metrics indicate a low overall discrepancy.

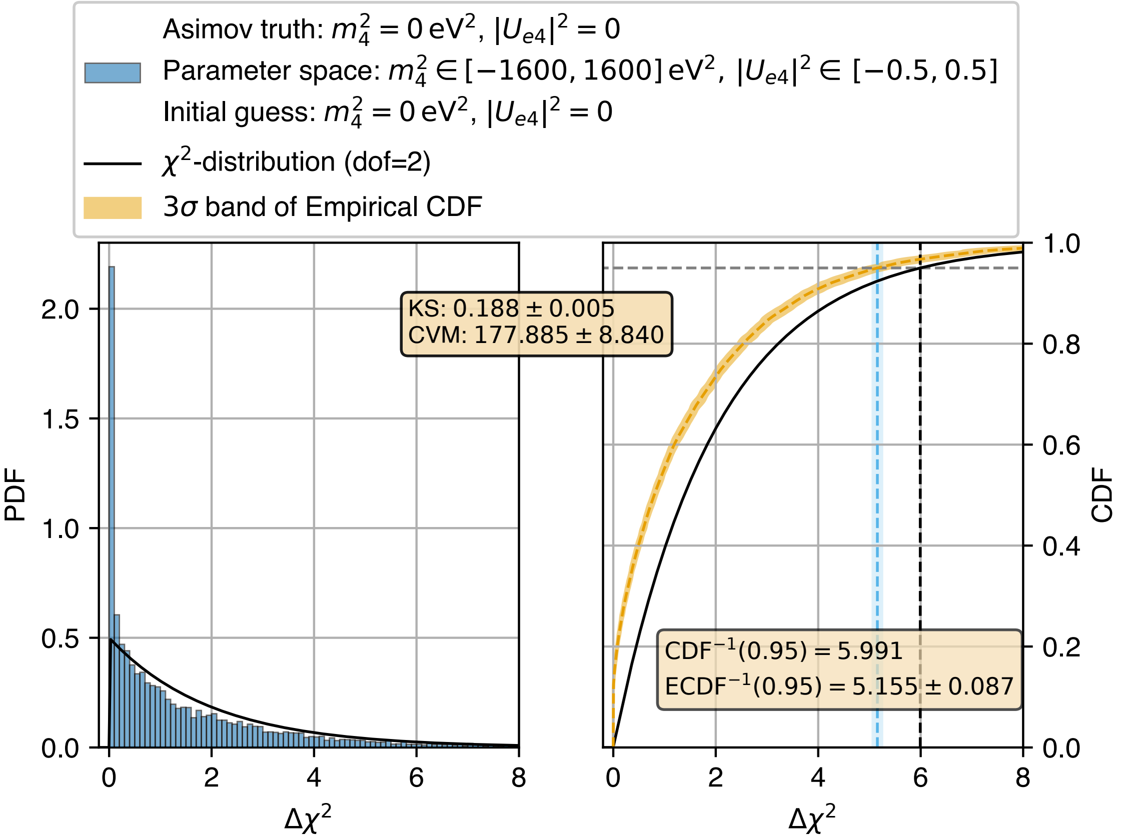

Figure A.10: Application of the Kolmogorov–Smirnov (KS) and Cramér–von Mises (CVM) metrics. Empirical probability density function (PDF, left) and cumulative distribution function (CDF, right) of the $\Delta\chi^2$ test statistic obtained from 10000 KNM5 pseudo-experiments using Method 2.b.i, where the sterile neutrino parameters were were allowed to have non-physical values. The Asimov dataset corresponds to the null hypothesis. The black line represents the reference distribution. The KS and CVM metrics indicate a significant discrepancy. The empirical CDF's 3σ confidence band is shown in orange. The 95th percentile value for the reference distribution is shown with the black dashed line alongside the estimated 95th percentile value with 1σ confidence band in light blue.

for χ^2_{bf}, a significant deviation is observed in the case of $\Delta\chi^2$. The origin of this deviation remains an open question and requires further investigation.

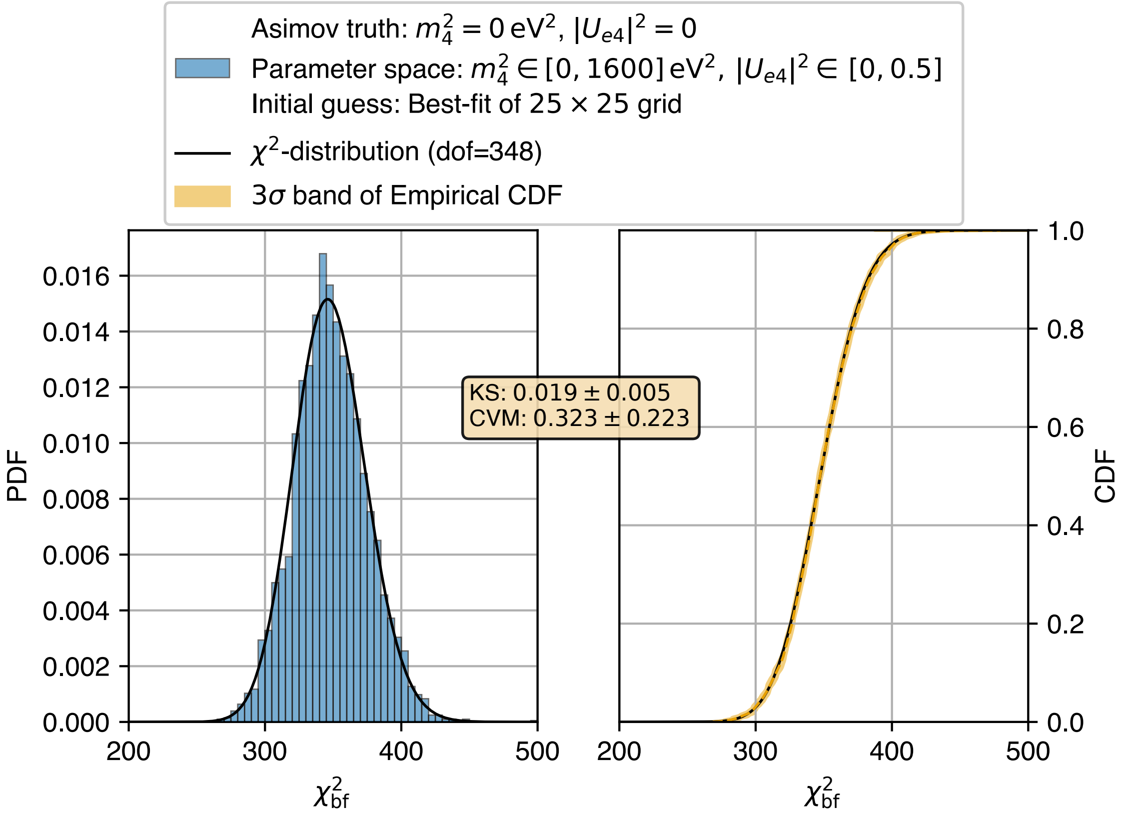

Figure A.11: Application of the Kolmogorov–Smirnov (KS) and Cramér–von Mises (CVM) metrics. Empirical probability density function (PDF, left) and cumulative distribution function (CDF, right) of the best-fit χ^2_{bf} values obtained from 10000 KNM5 pseudo-experiments using Method 3, where the sterile neutrino parameters were restricted to the physical domain. The Asimov dataset corresponds to the null hypothesis. The black line represents the reference distribution. The empirical CDF's 3σ confidence band is shown in orange. The KS and CVM metrics indicate a low overall discrepancy.

A.2.6 Results for KNM1-5 dataset

Due to computational limitations only 2000 pseudo-experiments were conducted for KNM1-5. To estimate the expected values of the two similarity metrics, 2000 samples were drawn from the χ^2_{1429} and χ^2_2 distributions. The reference and empirical probability density functions (PDFs) and cumulative distribution functions (CDFs) for the χ^2_{1429} distribution, along with the values of the two similarity metrics, are presented in Figure A.13; the corresponding results for the χ^2_2 distribution are shown in Figure A.14. For both distributions, the empirical PDFs and CDFs exhibit good visual agreement with the corresponding reference distribution functions. However, the uncertainties in the ECDF and 95th percentile are higher than those seen in Figure A.14 due to the lower number of samples.

Results for the Grid scan method are shown in Figure A.15 for χ^2_{bf} and in Figure A.16 for $\Delta\chi^2$. In case of χ^2_{bf}, the empirical PDFs and CDFs exhibit good visual agreement with the corresponding reference chi-squared distributions, indicating low overall discrepancy. This observation is quantitatively supported by the Kolmogorov–Smirnov (KS) and Cramér–von Mises (CVM) similarity metrics. For $\Delta\chi^2$, a small deficit is observed in the empirical PDF near $\Delta\chi^2 = 0$. This

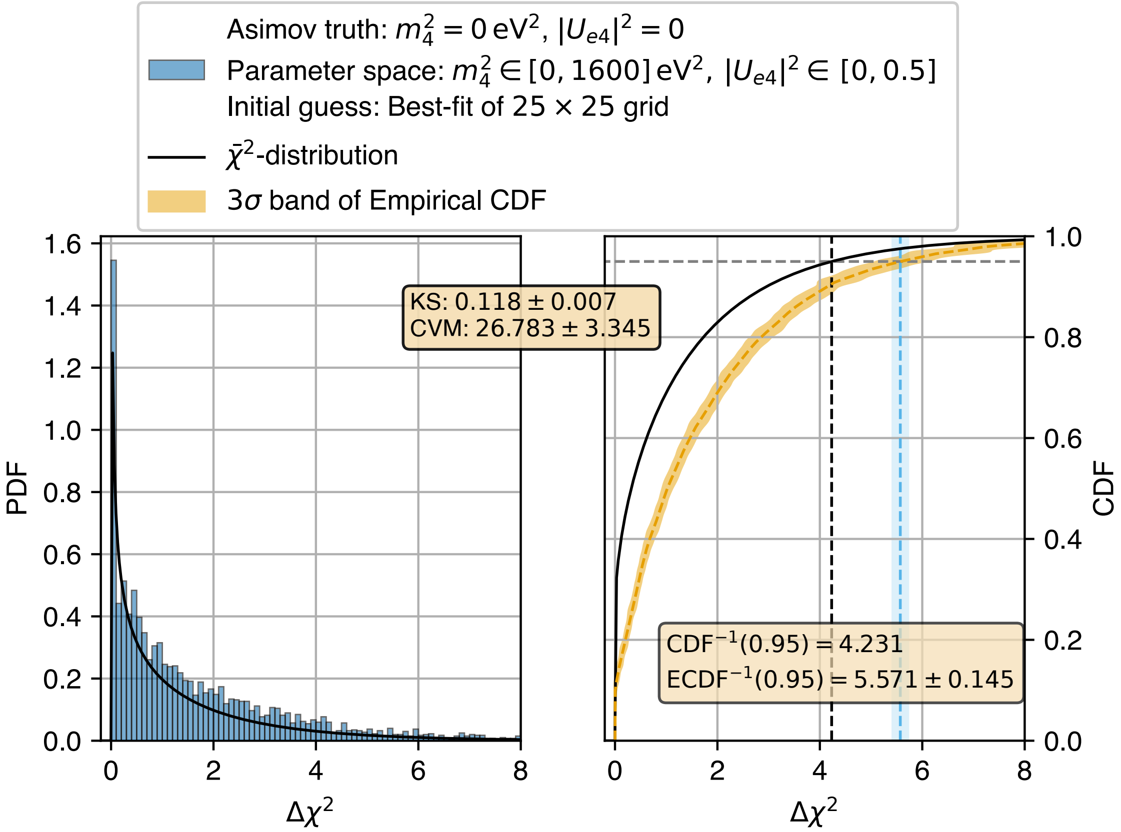

Figure A.12: Application of the Kolmogorov–Smirnov (KS) and Cramér–von Mises (CVM) metrics. Empirical probability density function (PDF, left) and cumulative distribution function (CDF, right) of the $\Delta\chi^2$ test statistic obtained from 10000 KNM5 pseudo-experiments using Method 3, where the sterile neutrino parameters were restricted to the physical domain. The Asimov dataset corresponds to the null hypothesis. The black line represents the reference distribution. The KS and CVM metrics indicate a significant discrepancy. The empirical CDF's 3σ confidence band is shown in orange. The 95th percentile value for the reference distribution is shown with the black dashed line alongside the estimated 95th percentile value with 1σ confidence band in light blue.

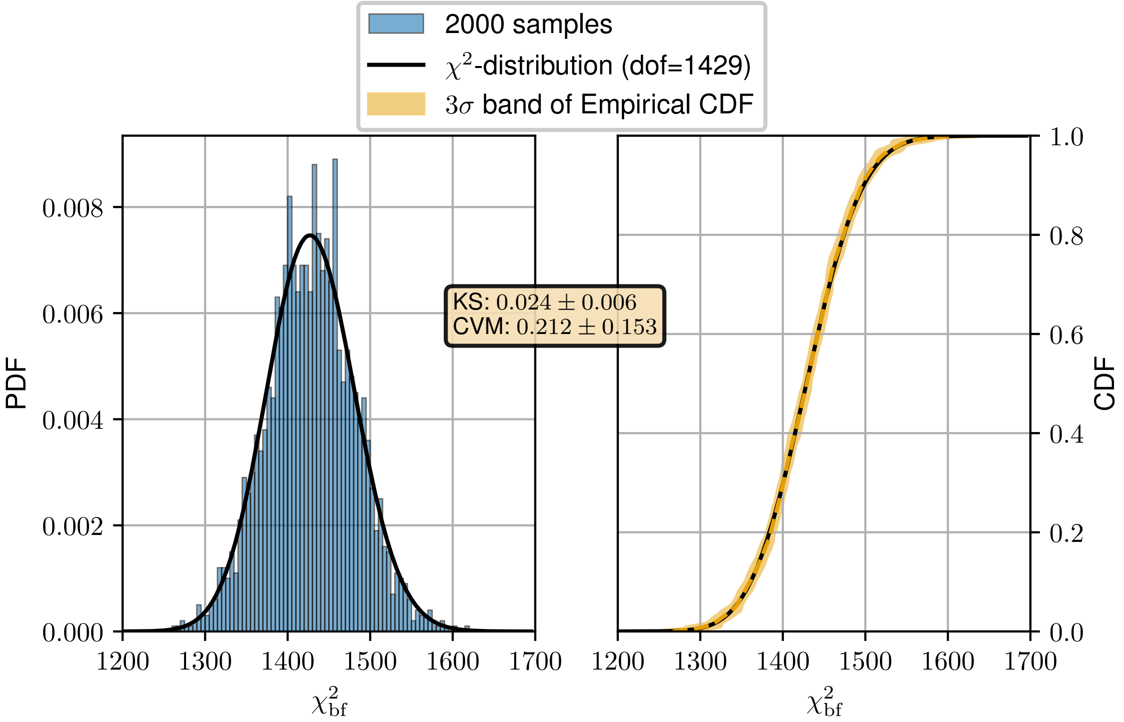

Figure A.13: Illustration of the Kolmogorov–Smirnov (KS) and Cramér–von Mises (CVM) metrics. Empirical probability density function (PDF, left) and cumulative distribution function (CDF, right) of 2000 samples drawn from the chi-squared distribution with 1429 degrees of freedom. The black line represents the reference distribution. The empirical CDF's 3σ confidence band is shown in orange. The KS and CVM metrics indicate a low overall discrepancy. The 95th percentile value for the reference distribution is shown with the black dashed line alongside the estimated 95th percentile value with 1σ confidence band in light blue.

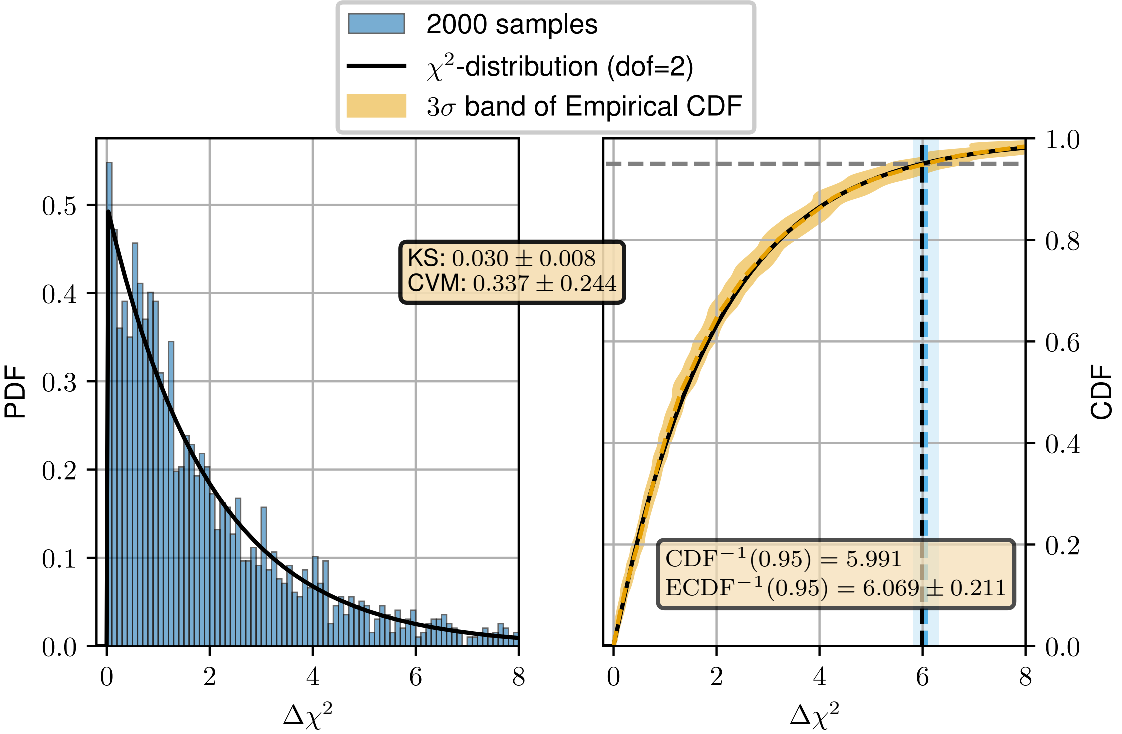

Figure A.14: Illustration of the Kolmogorov–Smirnov (KS) and Cramér–von Mises (CVM) metrics. Empirical probability density function (PDF, left) and cumulative distribution function (CDF, right) of 2000 samples drawn from the chi-squared distribution with 2 degrees of freedom. The black line represents the reference distribution. The empirical CDF's 3σ confidence band is shown in orange. The KS and CVM metrics indicate a low overall discrepancy. The estimated 95th percentile value matches well with that of the reference distribution.

can be attributed to the best-fit values of m_4^2 and $|U_{e4}|^2$ being constrained to values on a 25×25 grid. Despite these deviations, the reference 95th percentile value of 5.991 remains within the 2σ interval of the empirical estimate, 5.749 ± 0.215.

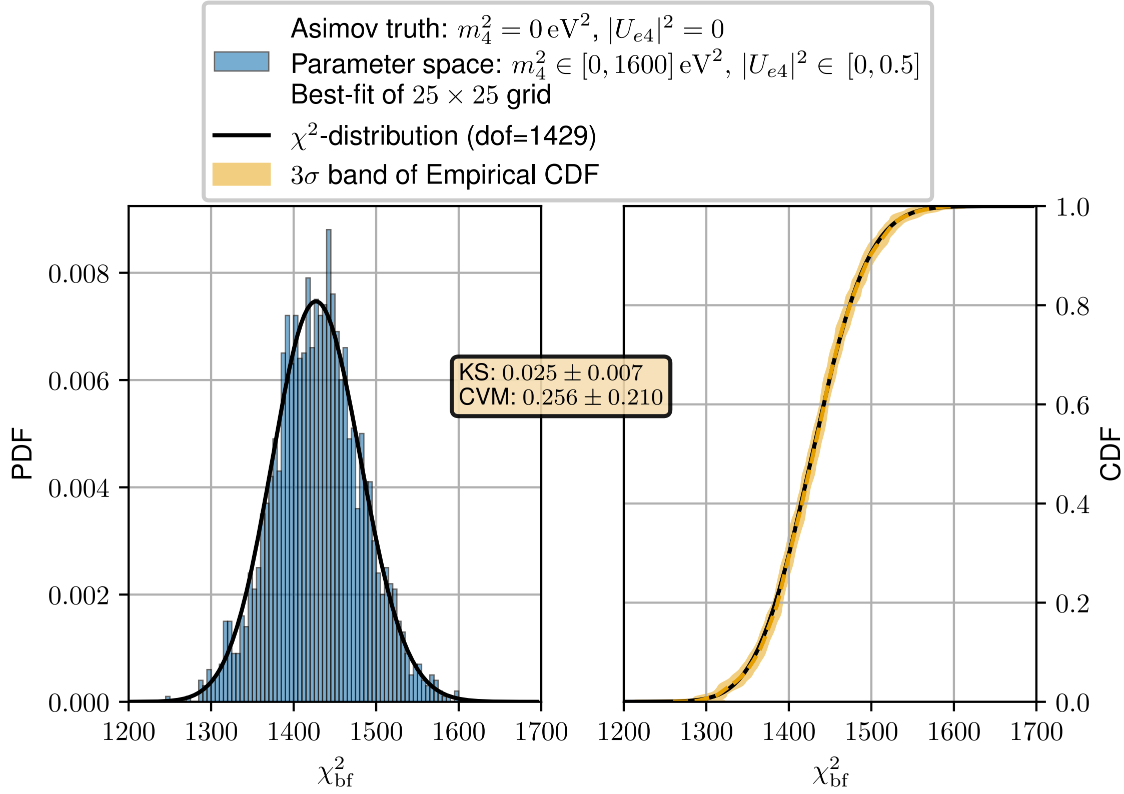

Figure A.15: Application of the Kolmogorov–Smirnov (KS) and Cramér–von Mises (CVM) metrics. Empirical probability density function (PDF, left) and cumulative distribution function (CDF, right) of the best-fit χ^2_{bf} values obtained from 2000 KNM1-5 pseudo-experiments using Method 1, where the sterile neutrino parameters were restricted to the physical domain. The Asimov dataset corresponds to the null hypothesis. The black line represents the reference distribution. The empirical CDF's 3σ confidence band is shown in orange. The KS and CVM metrics indicate a low overall discrepancy. The 95th percentile value for the reference distribution is shown with the black dashed line alongside the estimated 95th percentile value with 1σ confidence band in light blue.

The exclusion contours presented in Chapter 4 correspond to pairs of (m_4^2, $|U_{e4}|^2$) values that satisfy the condition specified in Equation 4.10. The cumulative distribution function $F(\Delta\chi^2)$ in Equation 4.10 represents the distribution of $\Delta\chi^2 = \chi^2(m_4^2, |U_{e4}|^2) - \chi^2_{\mathrm{bf}}$. To investigate the behavior of this distribution when the best-fit sterile neutrino parameters differ significantly from the null hypothesis, an Asimov dataset resembling the KNM1–5 configuration was generated with $m_\nu^2 = 0\,\mathrm{eV}^2$,$m_4^2 = 55.66\,\mathrm{eV}^2$ and $|U_{e4}|^2 = 0.013$. The Monte Carlo procedure described in Appendix A.2.1 was employed, using Method 1.

Results for the Grid scan method are shown in Figure A.17 for χ^2_{bf} and in Figure A.18 for $\Delta\chi^2$. In case of χ^2_{bf}, the empirical PDFs and CDFs exhibit good visual agreement with the corresponding reference chi-squared distributions, indicating low overall discrepancy. In the case of $\Delta\chi^2$, a pronounced excess is observed in the empirical PDF at $\Delta\chi^2 = 0$, followed by a deficit in the interval $0 < \Delta\chi^2 \lesssim 1$. These observations can also be attributed to the best-fit values of m_4^2 and $|U_{e4}|^2$ being constrained to values on a 25×25 grid. A lower level of discrepancy was reported in [137, Section 10], where a finer 50×50 grid was used. Despite these

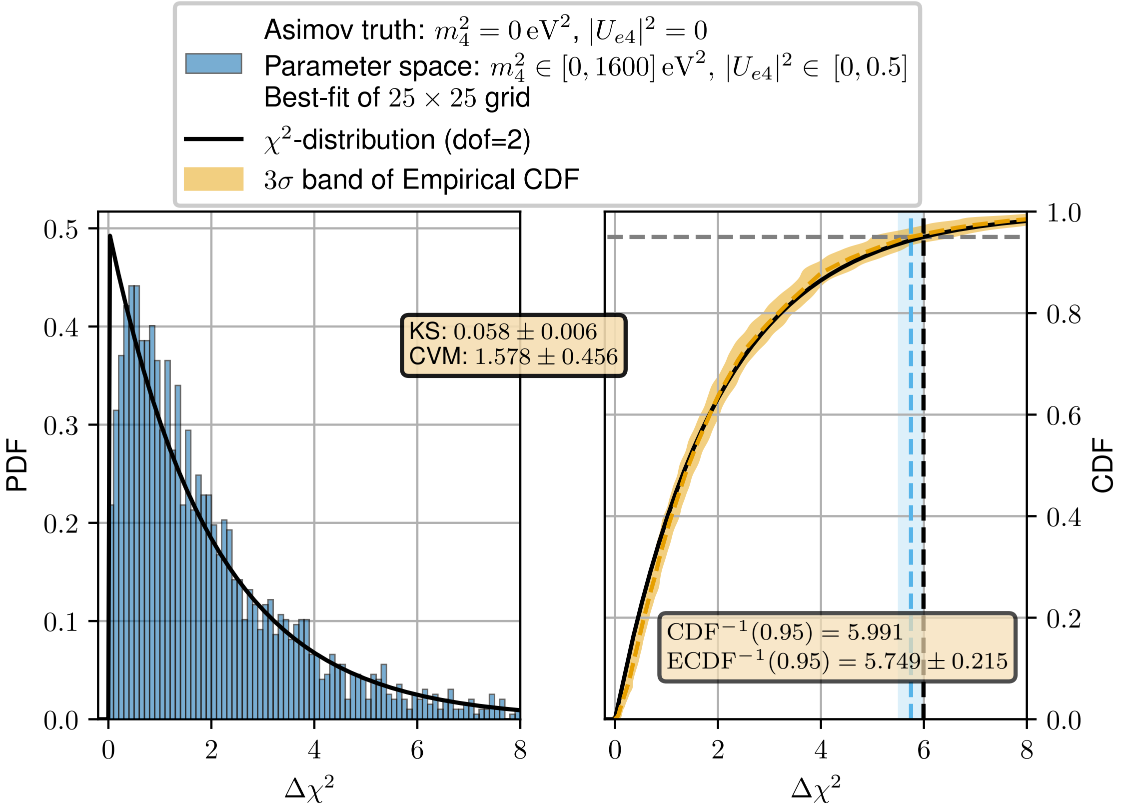

Figure A.16: Application of the Kolmogorov–Smirnov (KS) and Cramér–von Mises (CVM) metrics. Empirical probability density function (PDF, left) and cumulative distribution function (CDF, right) of the $\Delta\chi^2$ test statistic obtained from 2000 KNM1-5 pseudo-experiments using Method 1, where the sterile neutrino parameters were restricted to the physical domain. The Asimov dataset corresponds to the null hypothesis. The black line represents the reference distribution. The KS and CVM metrics indicate a low overall discrepancy. The empirical CDF's 3σ confidence band is shown in orange. The 95th percentile value for the reference distribution is shown with the black dashed line alongside the estimated 95th percentile value with 1σ confidence band in light blue.

deviations, the reference 95th percentile value of 5.991 remains within the 1σ interval of the empirical estimate, 5.860 ± 0.172.

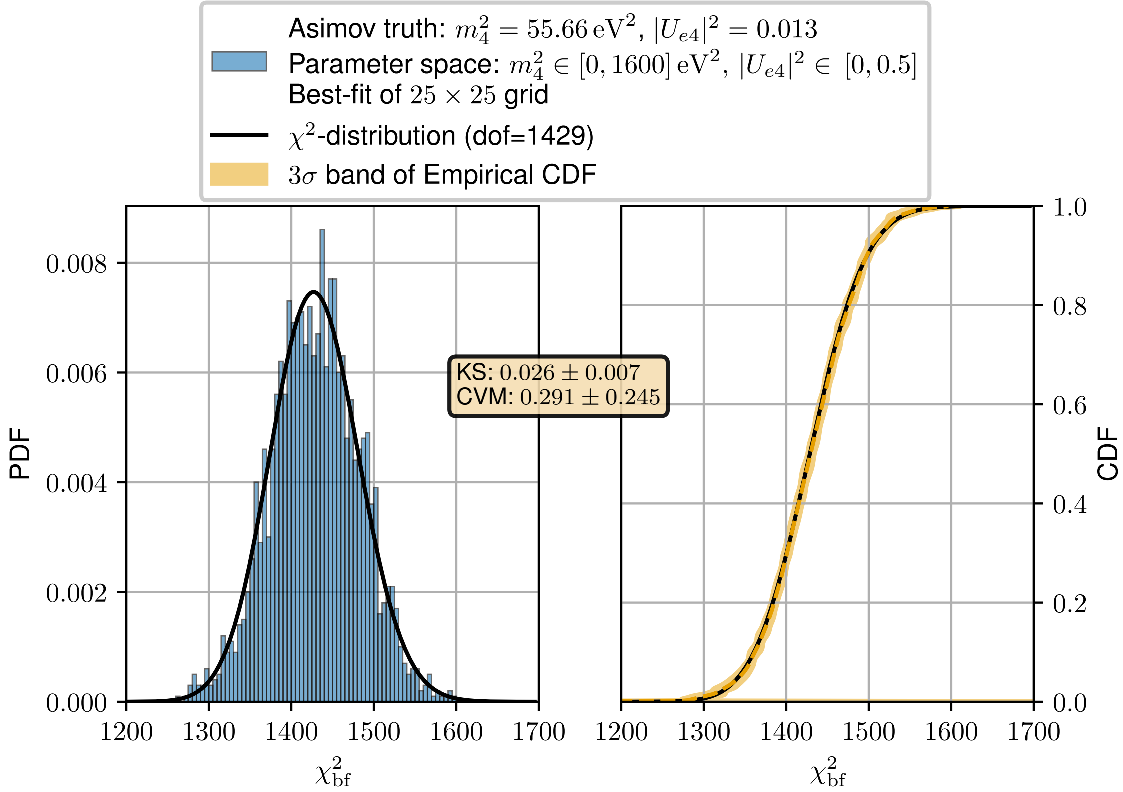

Figure A.17: Application of the Kolmogorov–Smirnov (KS) and Cramér–von Mises (CVM) metrics. Empirical probability density function (PDF, left) and cumulative distribution function (CDF, right) of the best-fit χ^2_{bf} values obtained from 2000 KNM1-5 pseudo-experiments using Method 1, where the sterile neutrino parameters were restricted to the physical domain. The Asimov dataset corresponds to $m_\nu^2 = 0\,\mathrm{eV}^2$,$m_4^2 = 55.66\,\mathrm{eV}^2$ and $|U_{e4}|^2 = 0.013$. The black line represents the reference distribution. The empirical CDF's 3σ confidence band is shown in orange. The KS and CVM metrics indicate a low overall discrepancy.

From the results obtained with Method 1 for the KNM5 and KNM1-5 pseudo-experiments, it was observed that, although the regularity conditions for Wilks' theorem were not strictly met, the empirical distributions were found to match well with the chi-squared distributions.

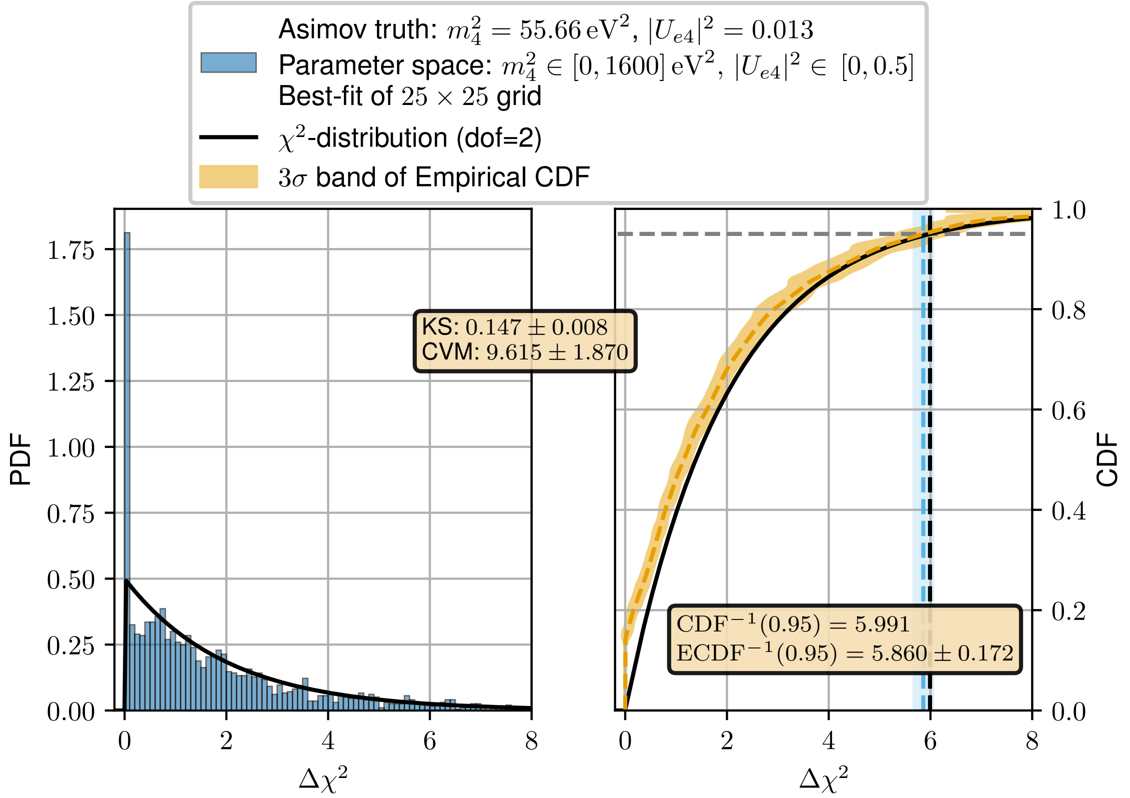

Figure A.18: Application of the Kolmogorov–Smirnov (KS) and Cramér–von Mises (CVM) metrics. Empirical probability density function (PDF, left) and cumulative distribution function (CDF, right) of the $\Delta\chi^2$ test statistic obtained from 2000 KNM1-5 pseudo-experiments using Method 1, where the sterile neutrino parameters were restricted to the physical domain. The Asimov dataset corresponds to $m_\nu^2 = 0\,\mathrm{eV}^2$,$m_4^2 = 55.66\,\mathrm{eV}^2$ and $|U_{e4}|^2 = 0.013$. The black line represents the reference distribution. The KS and CVM metrics indicate a low overall discrepancy. The empirical CDF's 3σ confidence band is shown in orange. The 95th percentile value for the reference distribution is shown with the black dashed line alongside the estimated 95th percentile value with 1σ confidence band in light blue.

A.3 Impact of Grid Resolution on Sterile Neutrino Contours

The choice of a 50×50 grid for the Grid Scan method (see Section 4.2.6.1) was based on tests conducted during the KNM1-2 sterile neutrino analysis. Grid sizes up to 100 × 100 were tested to ensure the contours converged [230, Sec. 11.2.3]. While no evidence suggested that the 50×50 grid would be inadequate for the KNM1-5 analysis, it was necessary to demonstrate that the 25×25 grid is sufficient for estimating the empirical distributions in Section 4.3 and for studying the intersection of sensitivity and exclusion contours in Section 4.8.

Grid sizes of 10×10, 25×25 (used in Section 4.3), 50×50 (used in KNM1-5 sterile neutrino analysis) and 100×100 were chosen for the study. For the Grid Scan method, logarithmically spaced points were selected for the sterile neutrino parameters in the ranges $\mathrm{m}_4^2 \in [0.1, 1600]\,\mathrm{eV}^2$ and $|U_{e4}|^2 \in [0.001, 0.5]$. To reduce the computational cost, the impact of the grid size was studied only on the KNM5 Asimov and experimental datasets, considering only statistical uncertainties.

Using the contour computation described in Section 4.2.6.1, the 95% C.L. sensitivity contours (shown in Figure A.19) and exclusion contours (shown in Figure A.20) were obtained for the various grid sizes. When the contour from the 100 × 100 grid was taken as the reference, significant deviations were observed for the contour from the 10×10 grid for some sterile neutrino masses. However, the contours from the 25 × 25 and 50 × 50 grids were found to match closely with the contour from the 100 × 100 grid for $m_4^2 < 1000\,\mathrm{eV}^2$. Even for higher sterile neutrino masses, small differences were noted between the contours of the 25 × 25 and 100 × 100 grids. Quantification of these differences was not straightforward, as the contour computation function returned a different number of contour points for the various grid sizes. An interpolation would have been required to obtain contour points for the same set of sterile masses before performing a quantitative comparison. Since the choice of interpolation would introduce an additional factor, only a qualitative comparison was shown through the contour plots.

Based on the close agreement observed between the sensitivity and exclusion contours for the 25 × 25 and 50 × 50 grids with the 100 × 100 grids, it was concluded that the 50 × 50 grid was sufficiently justified for the sterile neutrino search. Additionally, the 25 × 25 grid was found to provide sufficiently accurate results at one-fourth the computational cost of the 50 × 50 grid.

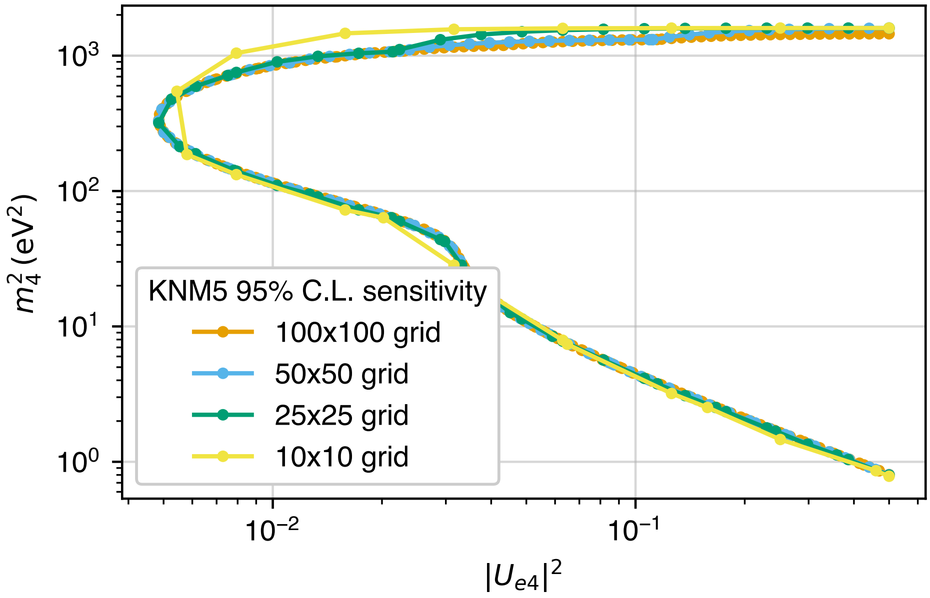

Figure A.19: Sensitivity contours for the KNM5, considering only statistical uncertainties. The contours were computed were computed the Grid scan method with various sized grids. on grids of various sizes. Minor differences were observed between the contours from the 25 × 25 and 50 × 50 grid compared to the 100 × 100 grid.

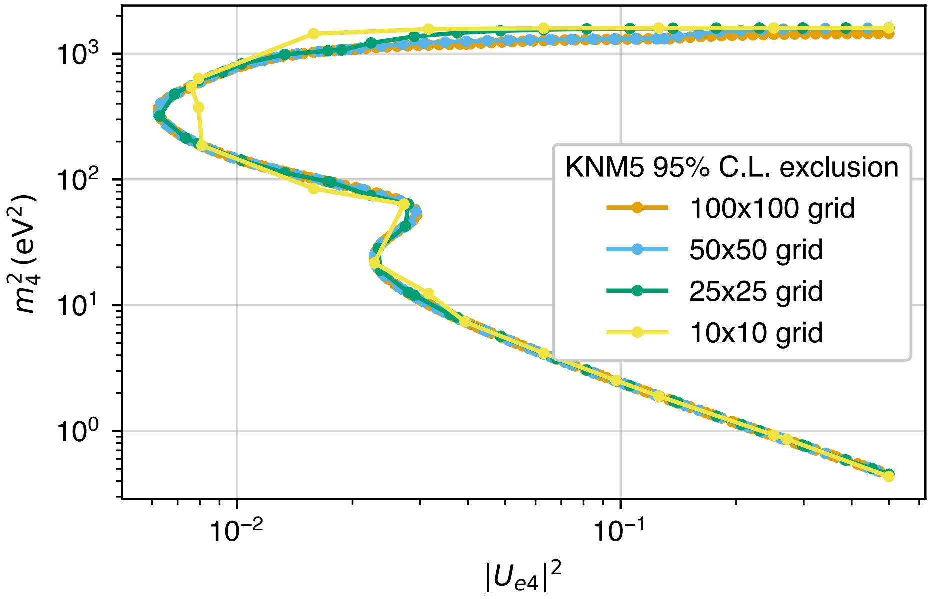

Figure A.20: Exclusion contours for the KNM5, considering only statistical uncertainties. The contours were computed were computed the Grid scan method with various sized grids. on grids of various sizes. Minor differences were observed between the contours from the 25 × 25 and 50 × 50 grid compared to the 100 × 100 grid.

A.4 Quantifying the Accuracy of Quadratic Interpolation for the χ^2 Profile

In the Raster Scan method Section 4.2.6.2, quadratic interpolation was used to interpolate the $\Delta\chi^2$ values from a set of data points $(|U_{e4}|^2, \Delta\chi^2)$ at a fixed sterile neutrino mass. This choice of quadratic interpolation was motivated by the expected quadratic nature of χ^2 under the Gaussian approximation to the likelihood Equation 4.3. While local quadratic interpolation using quadratic splines can be sensitive to noise, in the Raster Scan method, the values being interpolated-$\Delta\chi^2$-typically vary smoothly with respect to $|U_{e4}|^2$. A brief study was conducted to assess the interpolation accuracy and stability of various interpolation methods.

As in the case of the grid-size study Appendix A.3, four grids of sterile neutrino parameters were defined. These grids consisted of a single set of 50 logarithmically spaced points for $\mathrm{m}_4^2 \in [0.1, 1600]\,\mathrm{eV}^2$, combined with four sets of $|U_{e4}|^2 \in [0.001, 0.5]$, each containing 10, 25, 50 and 100 points respectively. To minimize computational cost, the interpolation accuracy was assessed only on the KNM5 Asimov dataset, considering only statistical uncertainties. For each set of fixed sterile neutrino parameters, χ^2 function Equation 4.4 was minimized to obtain results as minimized χ^2 matrices of dimensions 50×10, 50×25, 50×50 and 50×100. Let ${}^{g}\chi^2_{i,j}$ denote the minimized χ^2 for m_4^2 index i and $|U_{e4}|^2$ index j from the grid size g of $|U_{e4}|^2$ values. Hence we can have $i \in \{1, 2, \ldots, 50\}$ and $j \in \{1, 2, \ldots, g\}$.

Standard univariate interpolation methods from the `scipy.interpolate` module-*slinear*, *quadratic*, *CubicSpline*, *Pchip* and *Akima1D*-were considered. For each m_4^2 index i, interpolation functions ${}^{g}_{\text{interpolation-type}}\widetilde{\chi^2}_i(|U_{e4}|^2)$ were generated. For example, ${}^{50}_{quadratic}\widetilde{\chi^2}_i(|U_{e4}|^2)$ would represent a quadratic spline-based function of $|U_{e4}|^2$ created from the values ${}^{50}\chi^2_{i,j}\ \forall\, j \in \{1, 2, \ldots, 50\}$. For each interpolation method and each m_4^2 index i, a normalized root mean square error (NRMSE) was computed as:

$$
{}^{g}_{interpolation-type}\mathrm{NRMSE}_i = \sqrt{\frac{1}{100}\sum_{j=1}^{100}\left(\frac{{}^{100}\chi^2_{i,j} - {}^{g}_{interpolation-type}\widetilde{\chi^2}_i(|U_{e4}|^2_j)}{{}^{100}\chi^2_{i,j}}\right)^2}\,, \tag{A.3}
$$

where $|U_{e4}|^2_j$ are sterile neutrino mixing values from the 50×100 grid. NRMSE was used to quantify how well a particular interpolation method performs when interpolating from a $50{\times}g$ grid to a 50×100 grid.

The NRMSE results for the various interpolation methods and four grid sizes are presented in Figure A.21. For all interpolation methods, the NRMSE for the 50 × 100 grid is of the order of machine precision, as expected. This behavior arises because, for most interpolation methods, the error is minimal when query points match the points from which the interpolation is performed. It is important to note that the tests were carried out using χ^2 values, rather than $\Delta\chi^2$, as $\Delta\chi^2 = \chi^2 - \chi^2_{\min}$ for some constant χ^2_{min}. Therefore, the interpolation accuracy for $\Delta\chi^2$ will be of the same order as that for χ^2. Additionally, some yellow points are missing in Figure A.21 because the NRMSE is zero for these points, which cannot be plotted on a log scale.

To better visualize the NRMSE, the results for the 50 × 100 grid were excluded, as shown in Figure A.22. For all methods, except *slinear*, the NRMSE values are less than 10^{-3} for the 50×50 grid, which was used for studying the impact of the systematic uncertainties on the sterile neutrino analysis Section 4.2.6.2. The only exception is for $m_4^2 = 1600$, where all methods exhibit similar performance with NRMSE values around $\sim 10^{-2}$. Among the interpolation methods, *CubicSpline* shows the lowest average NRMSE across the m_4^2 values, followed closely by *quadratic* interpolation. Based on these results, the choice of *quadratic* interpolation for interpolating $\Delta\chi^2$ values in the Raster Scan method is therefore justified.

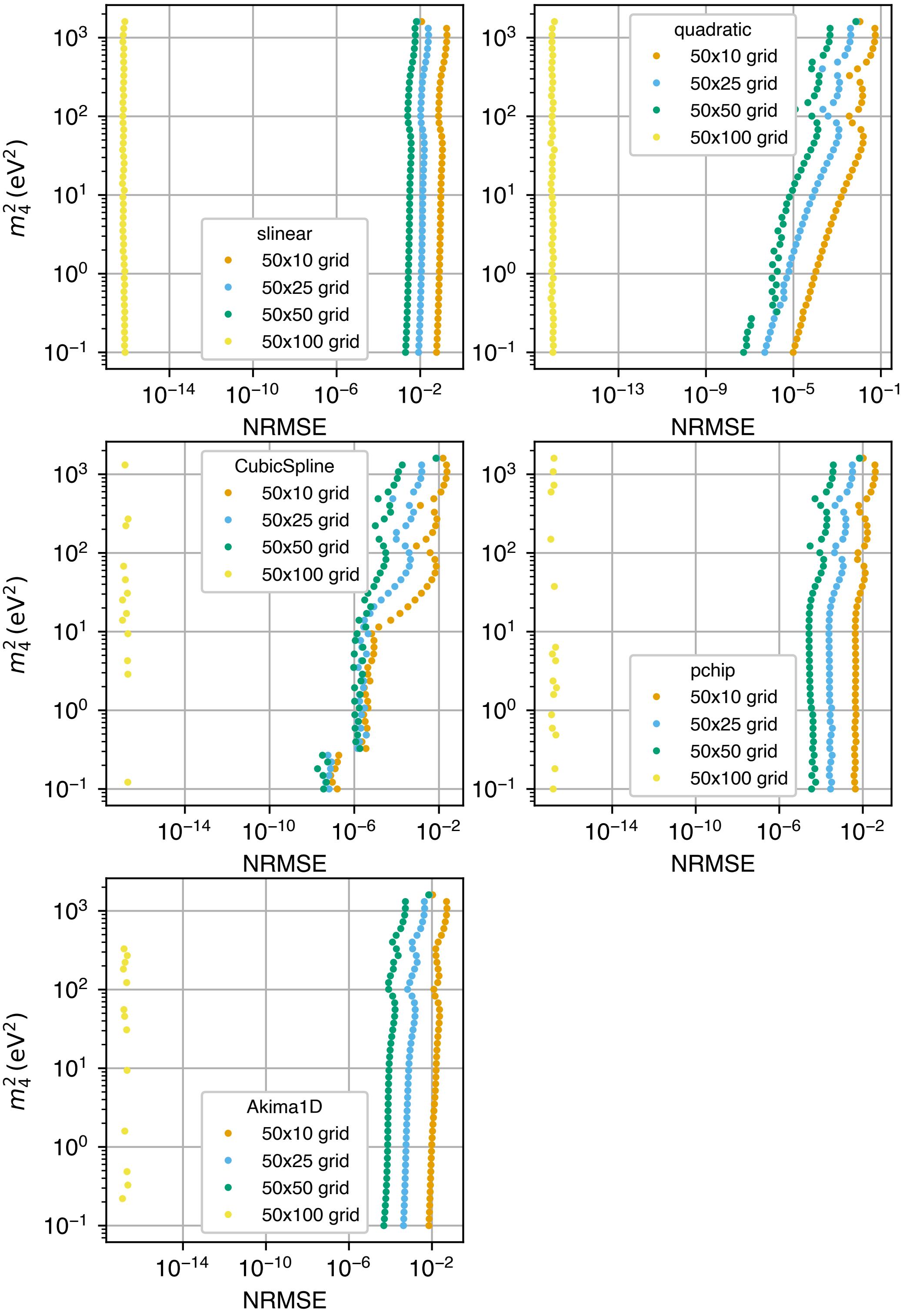

Figure A.21: Normalized root mean squared error (NRMSE), as defined by Equation A.3, for various interpolation methods applied to χ^2 values obtained from fits considering only statistical uncertainties on the KNM5 Asimov dataset. Results are shown for 50 sterile neutrino mass values across four different grid resolutions in sterile neutrino mixing. All interpolation methods achieve near machine precision NRMSE for the 50×100 grid as the error is minimal when query points match the points from which the interpolation is performed.

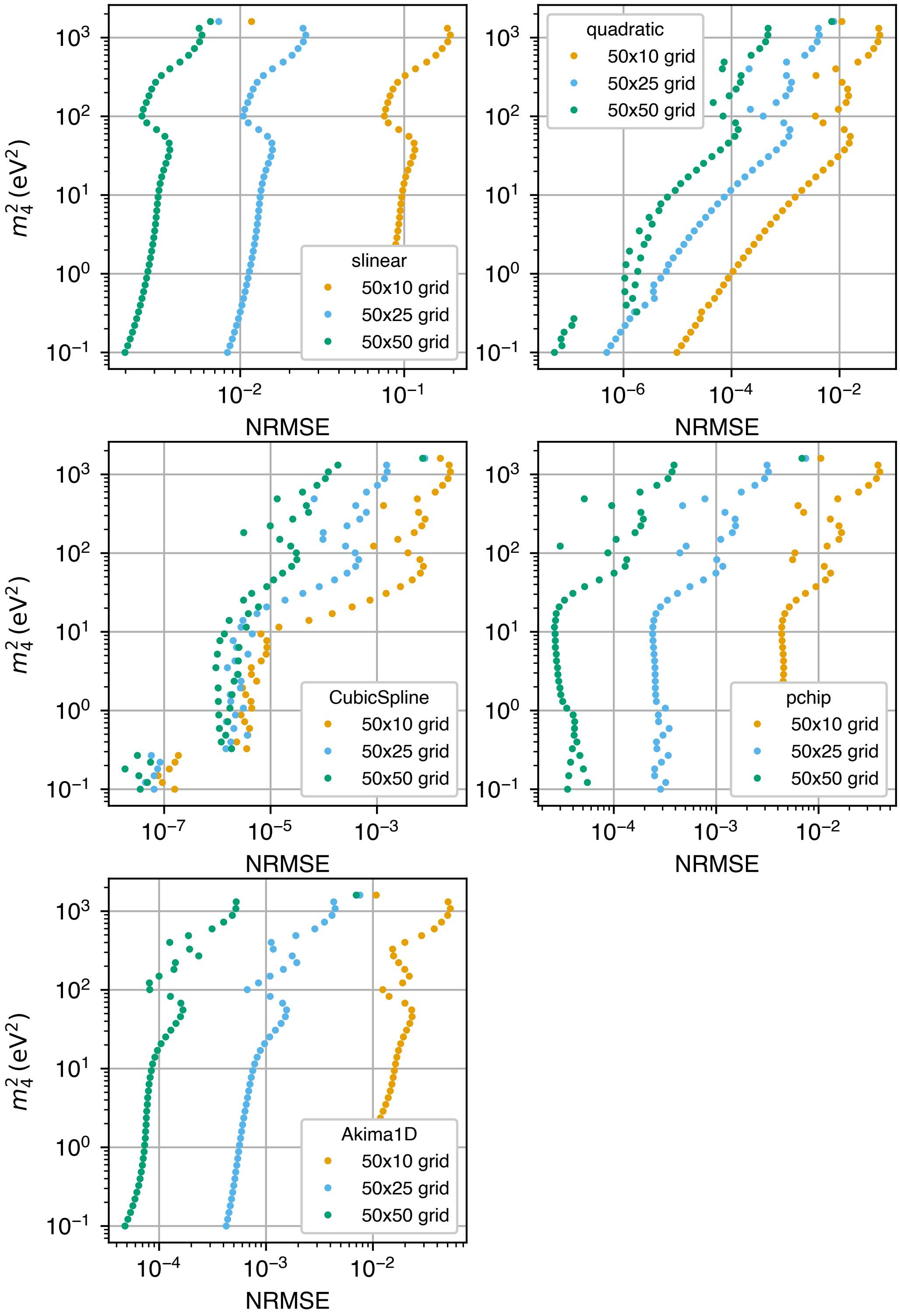

Figure A.22: Normalized root mean squared error (NRMSE), as defined by Equation A.3, for various interpolation methods applied to χ^2 values obtained from fits considering only statistical uncertainties on the KNM5 Asimov dataset. Results are shown for 50 sterile neutrino mass values across three different grid resolutions in sterile neutrino mixing. The *CubicSpline* interpolation shows the lowest average NRMSE across the m_4^2 values, followed closely by *quadratic* interpolation.

A.5 Impact of Analysis Energy Window on Sensitivity to Sterile Neutrino

The analyses presented in Chapter 4 and Chapter 5 are based on datasets where the lowest retarding potential set-point is 40, eV below the endpoint E_0 of the β-decay spectrum. This choice is motivated by the fact that systematic uncertainties are well-characterized within this energy range, ensuring a reliable interpretation of the data.

In particular, the systematic uncertainties associated with the energy-loss function and inelastic scattering cross section are better understood closer to the endpoint. By limiting the analysis to energies no more than 40 eV below the endpoint, the impact of these uncertainties is minimized, leading to more robust results. The KATRIN experiment however collects data up to 90 eV below the endpoint. Extending the analysis window to $E_0 - 90\,\mathrm{eV}$ could improve sensitivity to the light sterile neutrino.

To study this, a KNM1-5 like Asimov dataset was generated using the measurement time distributions shown in Figure A.23. Frequentist analysis as in Chapter 4 was performed considering only statistical uncertainties with datasets containing retarding potential set-points up to 40 eV, 60 eV and 90 eV below the end-point. The obtained sensitivity contours are shown in Figure A.24. As expected, the sensitivity improves significantly for $m_4^2 > 1600\,\mathrm{eV}^2$. Sensitivity also improves for $m_4^2 < 100\,\mathrm{eV}^2$, which can be attributed to increased statistics. The sterile neutrino mass range $100\,\mathrm{eV}^2 \lesssim m_4^2 \lesssim 200\,\mathrm{eV}^2$ is interesting as no visible difference in sensitivity is observed. Further analysis of this sterile mass range, including a more complete understanding of systematic uncertainties in the extended window, remains an open subject of investigation.

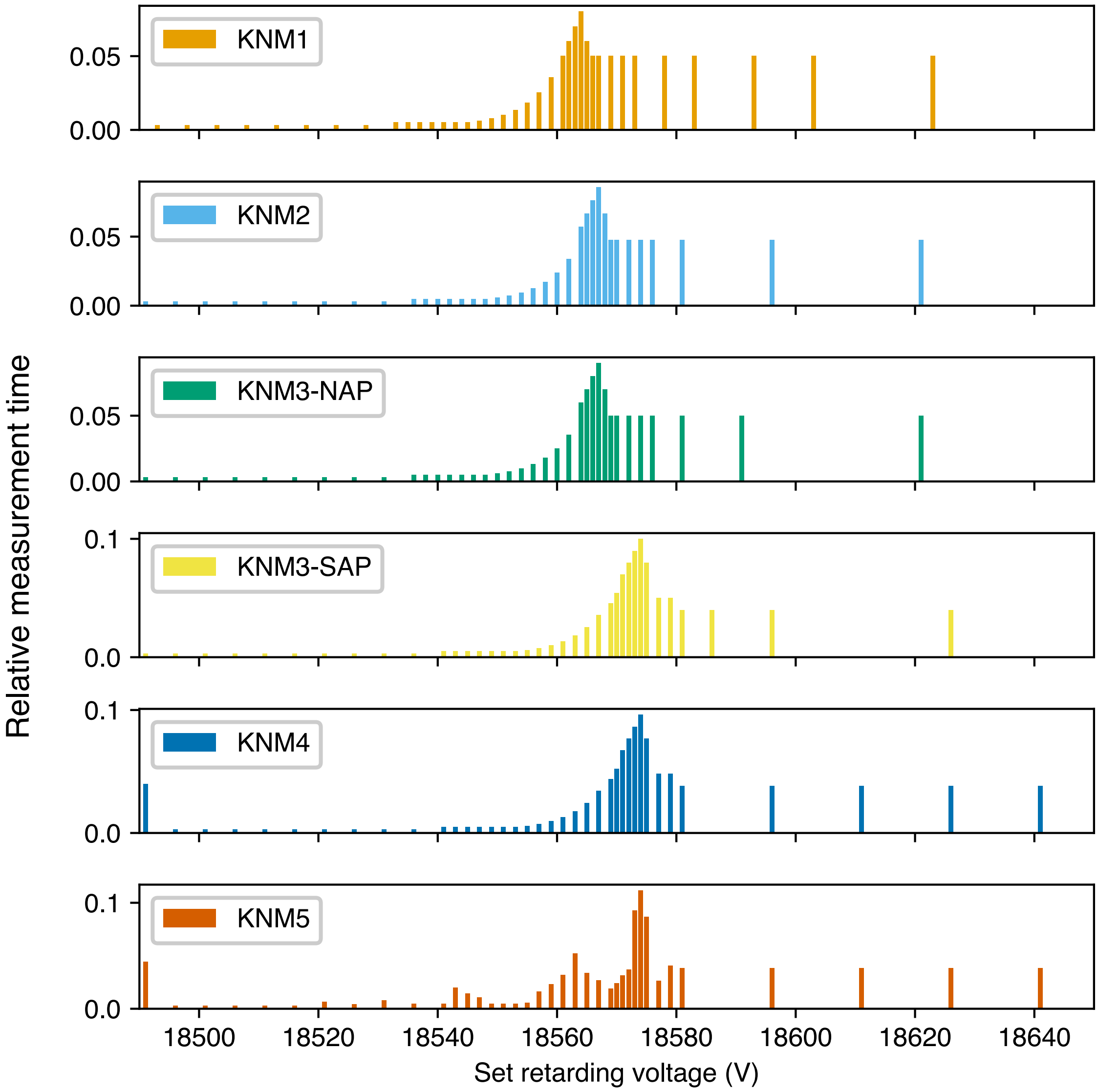

Figure A.23: KNMx measurement time distributions used in the first five science runs of KATRIN. The distributions are shown until 90 eV below the endpoint. The KNM4 distribution shown here is a representative one as four different MTDs were used during the KNM4 period.

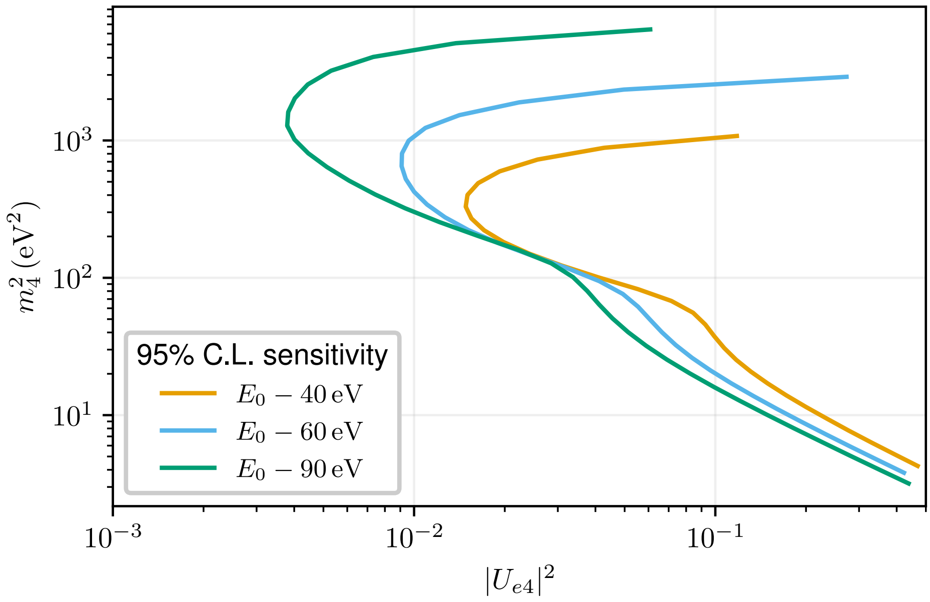

Figure A.24: Sensitivity contours at 95% C.L. in the sterile neutrino parameters space considering only statistical uncertainties. The contours were obtained by analyzing KNM1-5 like Asimov datasets containing retarding potential set-points up to 40 eV, 60 eV and 90 eV below the endpoint. Significant improvement in sensitivity is obtained for $m_4^2 > 1600\,\mathrm{eV}^2$ and $m_4^2 < 100\,\mathrm{eV}^2$.

A.6 Studying Kinks in Raster Contours

For many of the raster contours in Figure 4.10, a distinct kink is observed in the range $30 \lesssim m_4^2 \lesssim 80$, indicating a very low impact of the systematic uncertainty for those particular values of m_4^2. From a physical standpoint, this behavior does not have an immediate explanation. Similar features are also present in the contours for the individual datasets shown in Figures A.49 to A.55, albeit appearing over different ranges of m_4^2. It was hypothesized that these kinks may be artifacts arising from the measurement time distribution (MTD), which was optimized for neutrino mass determination rather than sterile neutrino searches.

To investigate this hypothesis, the KNM2 configuration was selected for generating Asimov datasets with varying MTDs due to the computational efficiency of analyzing datasets measured with NAP configuration. By normalizing the total measurement time to unity, the MTDs can be interpreted as probability mass functions defined by the retarding voltage set-points and the relative measurement time allocated to each. For the study, the relative measurement time was fixed uniformly across all set-points. An initial Asimov dataset was generated using uniform relative measurement time at the set-points from the KNM2 measurement campaign (see Figure 4.2) except the background measurement point at 18621 V; this MTD was labeled MTD-1. The total measurement time was kept consistent with the actual KNM2 campaign. Although only 28 scan-steps up to $E_0 - 40$ eV are displayed in Figure 4.2, the full KNM2 dataset comprises 39 scan-steps ranging from 18276 V to 18711 V. Both the generated and the original normalized MTDs are shown in Figure A.25. Additionally, 198 further Asimov datasets were created with uniform relative measurement time. In these, the lowest scan-step was fixed at 18276 V, the highest at 18711 V, and 37 intermediate set-points were randomly selected at integer voltages between 18468 V and 18621 V with uniform probability. These MTDs were labeled MTD-2 through MTD-199. All datasets were generated with $m_\nu^2 = 0, \mathrm{eV}^2$ and $m_4^2 = 0, \mathrm{eV}^2$. Three randomly selected MTDs are also illustrated in Figure A.25. The MTD used for the KNM2 Asimov dataset in the sensitivity analysis of Section 4.7 was labeled MTD-0.

The analysis was performed using data up to $E_0 - 40\,\mathrm{eV}$. Due to the randomly selected retarding voltage set-points, the number of data points varied across the datasets. The number of scan-steps used in the analysis is listed for the example MTDs shown in Figure A.25. Raster scans (see Section 4.2.6.2) were conducted on all datasets using a threshold of $\Delta\chi^2 = 1$, considering the systematic uncertainty arising from the product of column density and inelastic cross section. This particular systematic was chosen due to its dominant impact among source-related uncertainties (see Figure A.50).

The presence of a kink in the $\sigma_{|U_{e4}|^2,\mathrm{syst.}}$ contour was identified algorithmically: a kink was declared if the minimum value of $\sigma_{|U_{e4}|^2,\mathrm{syst.}}$ occurred at a sterile neutrino mass smaller than that corresponding to the minimum of $\sigma_{|U_{e4}|^2,\mathrm{stat.}}$. Using this criterion, a kink was detected in approximately 77% of the datasets. No consistent pattern was found in the MTDs of datasets where no kink was detected. In several such cases, a visible kink was present but was not pronounced to be detected according to the algorithmic criteria. To assess whether the kink was an artifact of the chosen threshold, raster scans were also performed using $\Delta\chi^2 = 4.00$. Kinks were again detected in approximately 77% of the datasets. The median raster contours for both thresholds, along with bands covering 68.3% of all contours, are shown in Figure A.26. The contribution of the systematic uncertainty to the $|U_{e4}|^2$ sensitivity exhibited the same qualitative behavior across sterile neutrino masses for both thresholds. The primary distinction from the contour presented in Figure A.50 was the shift in the sterile-neutrino mass at which the kink occurred in the median sensitivity curve, moving from approximately $\approx 70\,\mathrm{eV}^2$ to $\approx 100\,\mathrm{eV}^2$. This shift may be attributed to differences in the number of scan-steps within the analysis energy range, potentially affecting the signal-to-noise ratio (SNR). Given that a kink was observed in a significant majority of datasets, regardless of the measurement-time distribution (MTD), it was

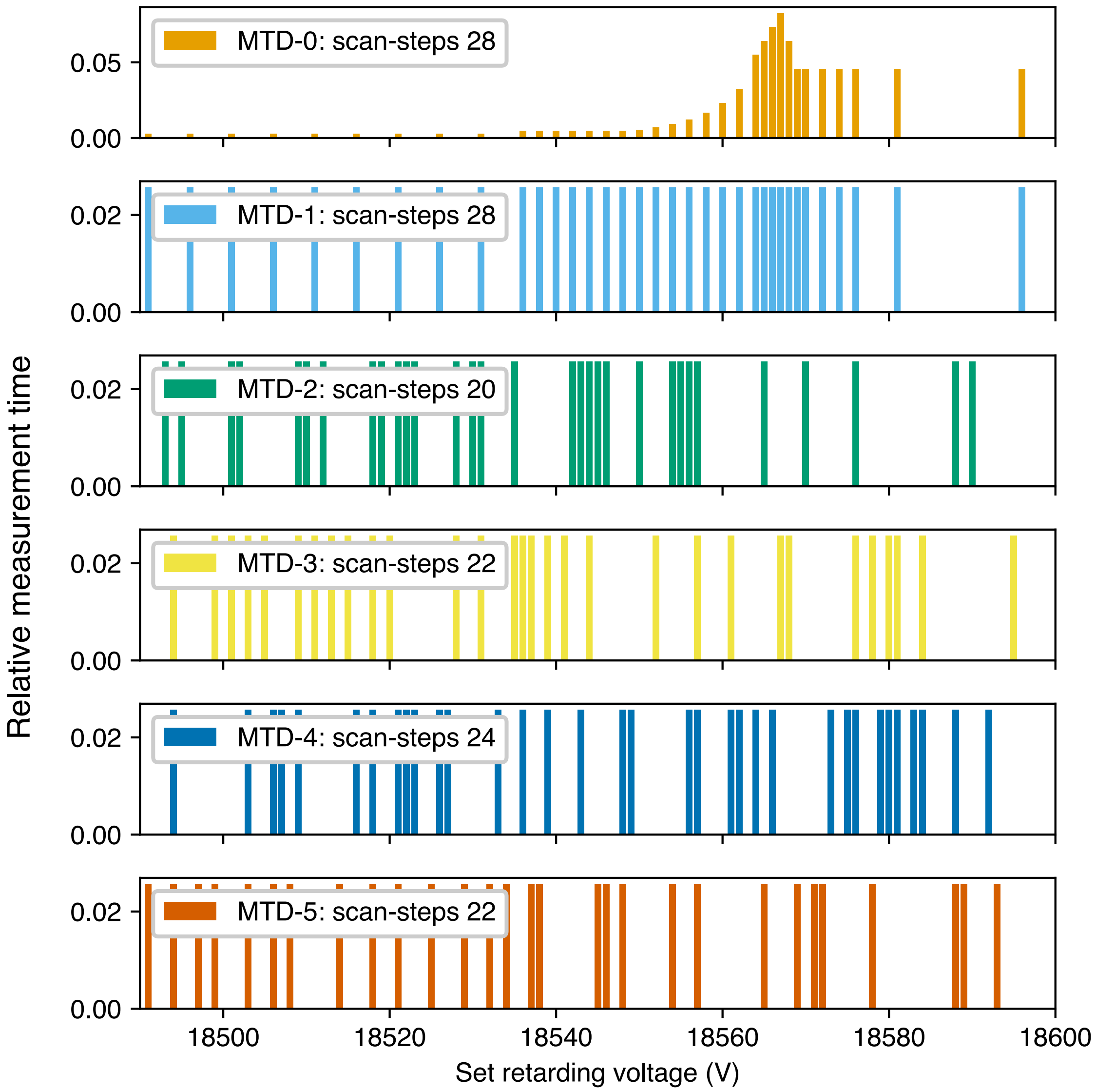

Figure A.25: Measurement time distributions used for the generation of datasets with the KNM2 configuration, shown in the range 18490 V to 18600 V. MTD-0 corresponds to the distribution used in the actual KNM2 measurement campaign. MTD-1 features uniform measurement time across the same retarding voltage set-points as MTD-0. MTD-2 to MTD-5 use set-points randomly selected at integer voltages between 18468 V and 18621 V. The number of scan-steps up to $E_0 - 40\,\mathrm{eV}$ for each MTD is also indicated.

concluded that the occurrence of the kink could not be solely attributed to the choice of MTD. A dedicated study to investigate the influence of SNR on the presence and position of the kink is deferred to future work.

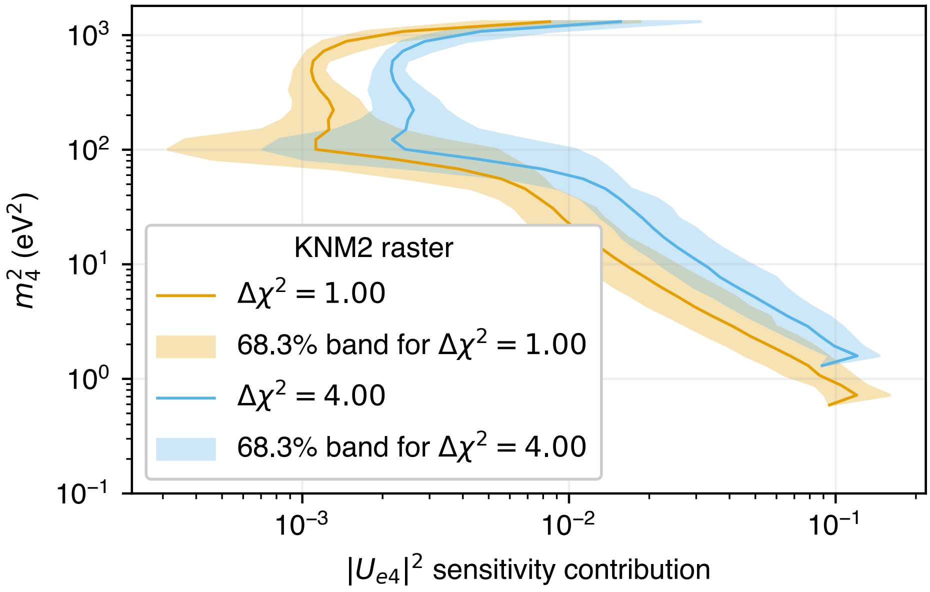

Figure A.26: Contribution of the uncertainty in product of column density and inelastic cross section to the $|U_{e4}|^2$ sensitivity presented in the form of raster contours. Median raster contours and bands covering 68.3% of all contours from 200 datasets for thresholds of $\Delta\chi^2 = 1.0$ and $\Delta\chi^2 = 4.0$. same qualitative behavior across sterile neutrino masses for both thresholds with a kink in the range $100 \lesssim m_4^2 \lesssim 200$.

A.7 Post-Unblinding Investigation

Multiple investigative approaches were employed to identify the source of the closed contour in KNM4 after the first unblinding. One of the first ideas was to divide the data from KNM4 campaign into datasets based on the direction in which scan-sets were performed. The grouping resulted in the KNM4-up dataset, KNM4-down dataset and KNM4-random dataset. The KNM4-up dataset was formed by merging counts from all the scans in which the retarding voltage set-points per scan-step were increased from the lowest to the highest voltage. The KNM4-down dataset was formed by merging counts from all the scans in which the retarding voltage set-points per scan-step were decreased from the highest to the lowest voltage. The KNM4-random dataset was formed by merging counts from all the scans in which the retarding voltage set-points were changed in randomly among the scan-steps. Grid scans were performed on the three datasets considering only the statistical uncertainties. A summary of the number of scans in each dataset along with the best-fit sterile neutrino parameters are given in Table A.1 and the corresponding exclusion contours are shown in Figure A.27. A significant sterile neutrino signal was seen for the KNM4-down dataset and KNM4-random dataset. The three datasets were combined in pairs and the analysis was repeated. A summary of the number of scans in each dataset along with the best-fit sterile neutrino parameters are given in Table A.2 and the corresponding exclusion contours are shown in Figure A.28. A significant sterile neutrino was seen for all three combinations.

Table A.1: Summary of the best-fit sterile neutrino parameters by grouping of scans in KNM4 based on the direction of the scan.

Data set (No. of scans)	Considered Uncertainties	m_4^2 (eV^2)	$\lvert U_{e4}\rvert^2$	χ^2_{bf}/dof	p	$\Delta\chi^2$	Significance
KNM4-up (156)	stat.-only	37.49	0.035	314.9/348	0.90	2.51	71.49%
KNM4-down (156)	stat.-only	37.49	0.058	321.1/348	0.85	7.35	97.47%
KNM4-random (158)	stat.-only	55.66	0.058	381.77/348	0.10	12.81	99.83%

A similar re-combination was performed for data from the KNM5 campaign. A summary of the number of scans in each dataset along with the best-fit sterile neutrino parameters are given in Table A.3. While the best-fit sterile neutrino parameters for the KNM5-down dataset differs significantly from that of the other two datasets, no significant sterile neutrino was found in any of the datasets. Hence the hypothesis of the anomaly being linked to the order in which the retarding voltages were set in each scan remained unproven.

Data from the KNM4 campaign can be divided into KNM4-a, KNM4-b, KNM4-c, KNM4-d and KNM4-e datasets based on differences in measurement configuration. The KNM4-a, KNM4-b and KNM4-c datasets were measured with the so-called KNM4-NOM measurement time distribution shown in Figure 4.14. Compared to KNM4-a, for KNM4-b the measurement time at each retarding voltage set-point was multiplied by factor 1.5 and $E_0 - 310$ eV monitoring point was shifted to $E_0 - 90$ eV. Compared to KNM4-b, for KNM4-c the scan-steps with retarding voltage set-points between 18571 V and 18575 V split into two scan-steps with operation of the Penning trap wiper in between. The KNM4-d and KNM4-e datasets were measured with the so-called KNM4-OPT measurement time distribution shown in Figure 4.14. For KNM4-d the Penning trap wiper was operated after each 100 s of operation while for KNM4-e the pre-spectrometer voltage was reduced to mitigate the Penning trap induced background. Table A.4

Table A.2: Summary of the best-fit sterile neutrino parameters by pairing groups of scans in KNM4 based on the direction of the scan.

Data set (No. of scans)	Considered Uncertainties	m_4^2 (eV^2)	$\lvert U_{e4}\rvert^2$	$\chi^2_{\mathrm{bf}}/\mathrm{dof}$	p	$\Delta\chi^2$	Significance
KNM4-up + KNM4-down (312)	stat.-only	37.49	0.045	329.68/348	0.75	9.30	99.04%
KNM4-down + KNM4-random (314)	stat.-only	45.68	0.051	364.33/348	0.26	16.46	99.97%
KNM4-random + KNM4-up (315)	stat.-only	45.68	0.045	366.42/348	0.26	10.86	99.56%

Table A.3: Summary of the best-fit sterile neutrino parameters by grouping of scans in KNM5 based on the direction of the scan.

Data set (No. of scans)	Considered Uncertainties	m_4^2 (eV^2)	$\lvert U_{e4}\rvert^2$	$\chi^2_{\mathrm{bf}}/\mathrm{dof}$	p	$\Delta\chi^2$	Significance
KNM5-up (144)	stat.-only	55.66	0.021	303.3/348	0.96	1.61	55.29%
KNM5-down (137)	stat.-only	884.55	0.014	364.94/348	0.26	3.10	78.78%
KNM5-random (141)	stat.-only	55.66	0.018	335.88/348	0.67	1.06	41.14%

Table A.4: Summary of scans in sub-campaigns of KNM4

Dataset	KNM4-a	KNM4-b	KNM4-c	KNM4-d	KNM4-e
No. of scans	97	173	50	111	39
Scan duration	~ 2 h	~ 3 h	~ 3 h (scan-step < 10 min)	100 s blocks	100 s blocks
Pre-spectrometer voltage	10.413 kV	10.413 kV	10.413 kV	10.413 kV	100 V

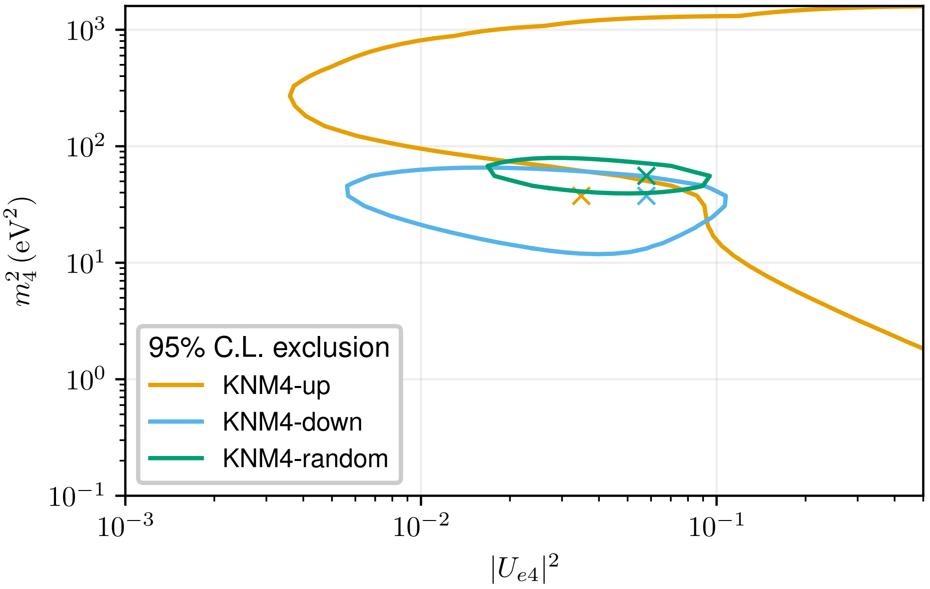

Figure A.27: Exclusion contours at 95% C.L. considering only statistical uncertainties for KNM4 datasets based on the direction in which scan-sets were performed. The best-fit sterile neutrino parameters are marked with ×.

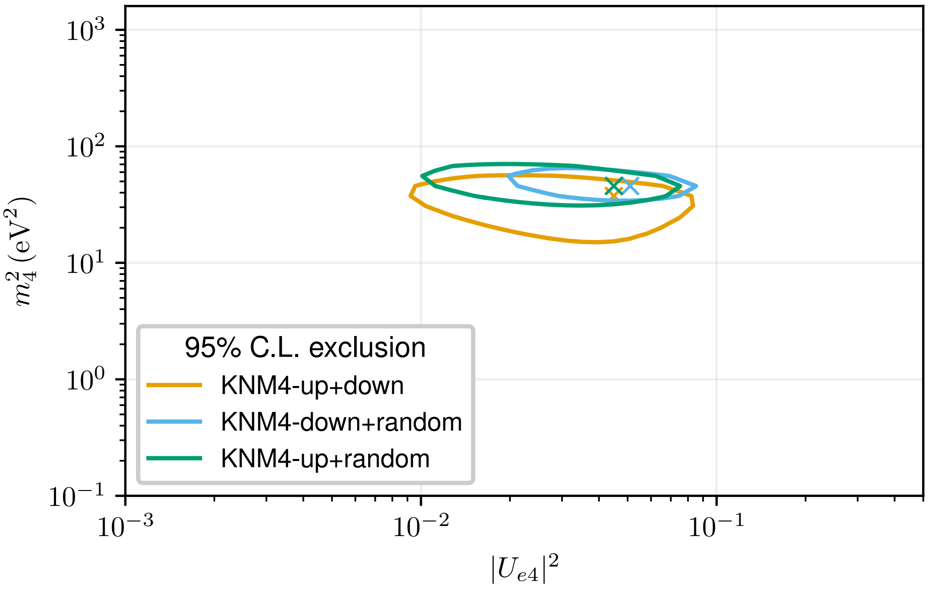

Figure A.28: Exclusion contours at 95% C.L. considering only statistical uncertainties for KNM4 datasets based on combinations of the directions in which scan-sets were performed. The best-fit sterile neutrino parameters are marked with ×.

shows a summary of the number of scans in each dataset. Grid scans were performed on the five datasets considering only the statistical uncertainties and a common scan-step-duration-dependent background rate parameter $\mathrm{Bg}_{\mathrm{Penning}} = 10.102 \pm 1.879\ \mu\mathrm{cps/s}$. The obtained exclusion contours are shown in Figure A.29. A significant sterile neutrino signal is detected in the KNM4-b and KNM4-e datasets. It was hypothesized that incorrect systematic parameters could be the reason for the closed contours. From Figure A.31, it can be seen that the scan-step-duration-dependent background has the highest impact on the sensitivity followed closely by source-potential variations. Hence using a common value of scan-step-duration-dependent background

Table A.5: Summary of the best-fit sterile neutrino parameters for KNM4 sub-campaigns. Significant sterile neutrino signals detected in KNM4-b and KNM4-e datasets.

Data set	Considered Uncertainties	m_4^2 (eV^2)	$\lvert U_{e4}\rvert^2$	χ^2_{bf}/dof	p	$\Delta\chi^2$	Significance
KNM4-a	stat.-only	30.77	0.045	353.88/348	0.40	1.63	55.82%
KNM4-b	stat.-only	55.66	0.040	360.16/348	0.32	8.61	98.65%
KNM4-c	stat.-only	884.56	0.016	366.06/348	0.24	1.18	44.54%
KNM4-d	stat.-only	0.88	0.440	290.74/306	0.73	1.65	56.14%
KNM4-e	stat.-only	82.63	0.058	302.24/306	0.55	8.22	98.36%

rate parameter $\mathrm{Bg}_{\mathrm{Penning}} = 10.102 \pm 1.879$ (μcps/s) for all the five datasets could lead to the observed sterile neutrino signal. The $\mathrm{Bg}_{\mathrm{Penning}}$ was re-estimated for each of the KNM4-a, -b, -c and -d datasets and the values are listed in Table A.6. The value of $\sigma^2_{\mathrm{shift,drift}}$ was also re-estimated and is listed in Table A.6. The exclusion contours obtained considering only the statistical uncertainties and dataset specific parameters are shown in Figure A.30. The exclusion contours considering $\mathrm{Bg}_{\mathrm{Penning}}$ as a fit parameter along with statistical uncertainties are shown in Figure A.32. A summary of the best-fit sterile neutrino parameters are given in Table A.5. A significant sterile neutrino signal was still detected in the KNM4-b and KNM4-e datasets even with $\mathrm{Bg}_{\mathrm{Penning}}$ being a fit parameter.

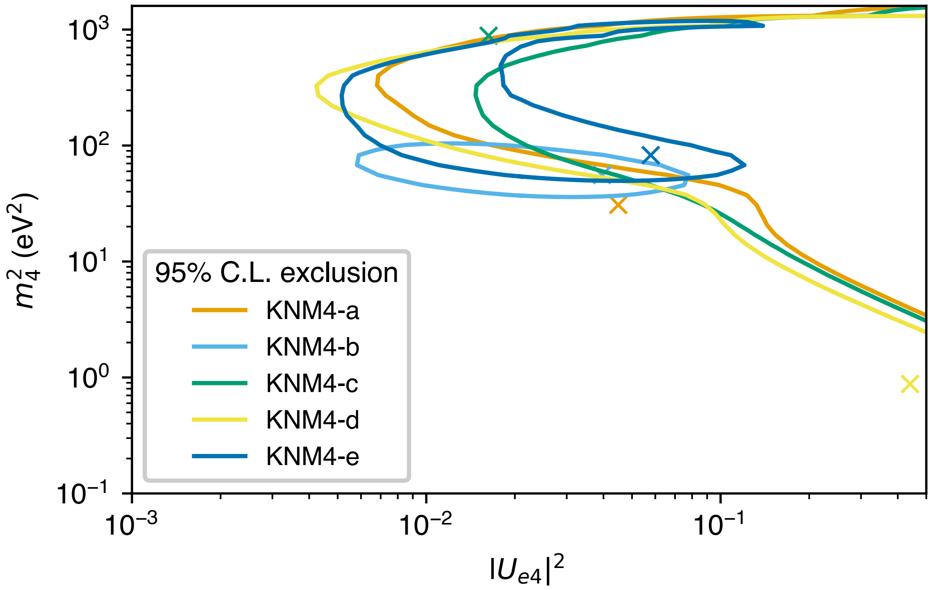

Figure A.29: Exclusion contours at 95% C.L. considering only statistical uncertainties. The common value of scan-step-duration-dependent background rate parameter $\mathrm{Bg}_{\mathrm{Penning}} = 10.102 \pm 1.879$ (μcps/s) for all the five datasets was used. The best-fit sterile neutrino parameters are marked with ×.

Multiple studies were undertaken to further understand the anomaly. Two studies were performed to test the hypothesis that an incorrect estimate of the scan-step-duration-dependent background was the reason for the anomaly seen in KNM4-b. As the scan-step-duration-dependent background was completely mitigated in KNM4-e, only a study on source-potential variations was performed.

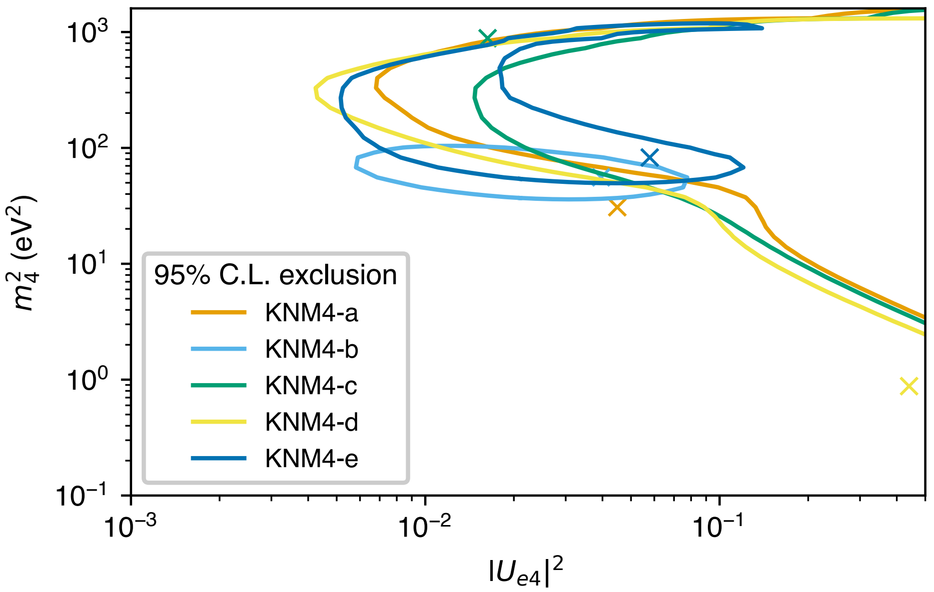

Figure A.30: Exclusion contours at 95% C.L. considering only statistical uncertainties. Specific values of $\mathrm{Bg}_{\mathrm{Penning}}$ parameter used for each dataset. The best-fit sterile neutrino parameters are marked with ×.

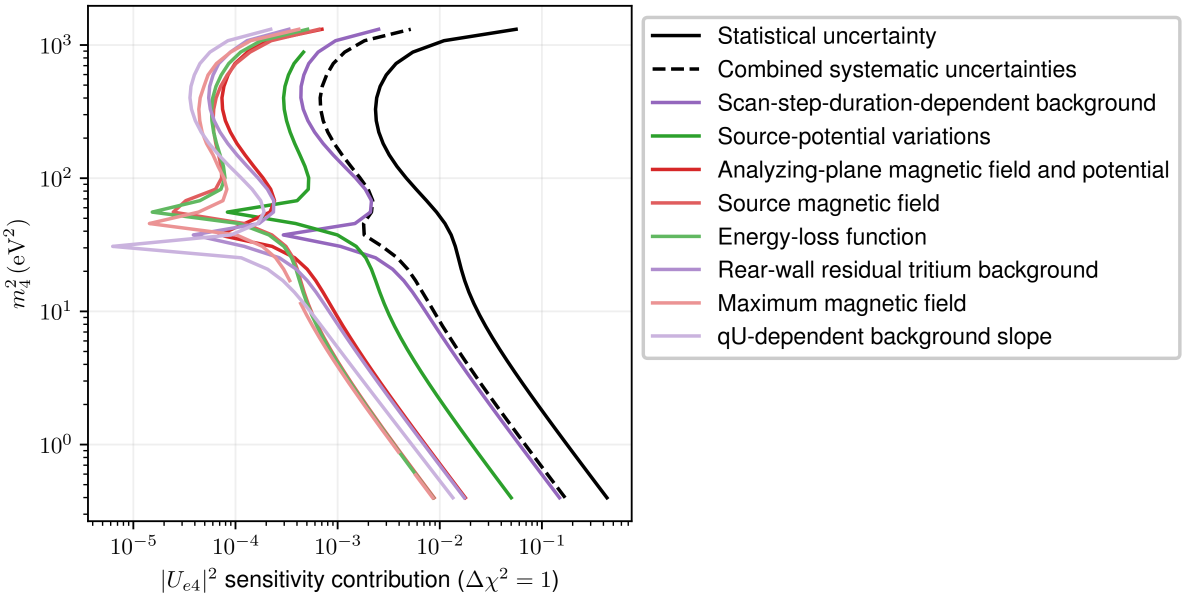

Figure A.31: Contributions of statistical and systematic uncertainties on sterile neutrino mixing $|U_{e4}|^2$ sensitivity for the KNM4 dataset. The presented raster contours are based on the systematic parameters of the first unblinding. Source related systematics are shown in green, background related in purple and transmission related in red. Lightness of the line color indicates the level of impact with higher impact denoted by a darker color. The scan-step-duration-dependent background has the highest impact.

A.7.1 Reduced Scan-Step Durations for KNM4-b

As mentioned in Table A.4, the duration of each scan in KNM4-b dataset was 3 hours. To reduce the impact of the scan-step-duration-dependent background, data from each scan-step

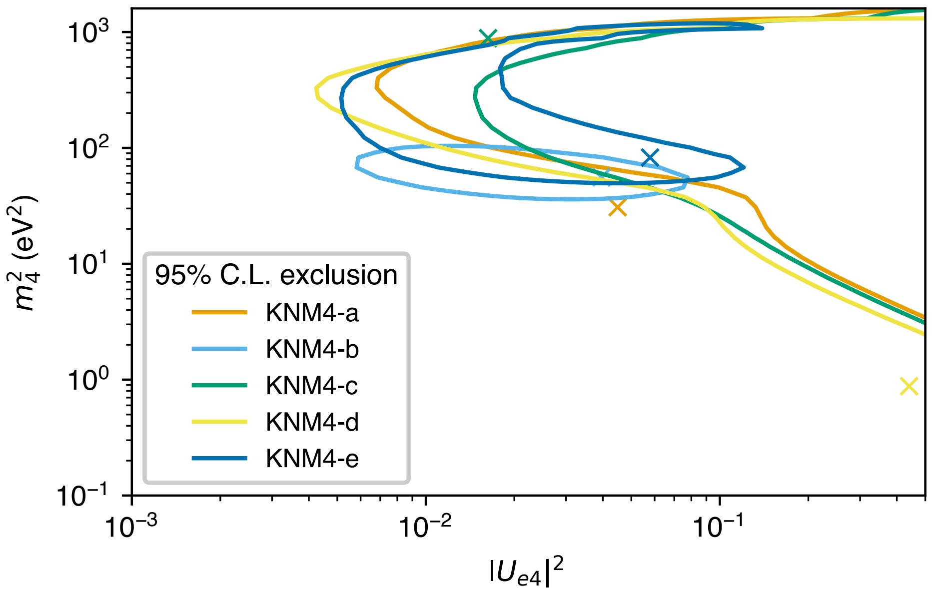

Figure A.32: Exclusion contours at 95% C.L. considering statistical uncertainties and the uncertainty in $\mathrm{Bg}_{\mathrm{Penning}}$. Dataset specific values of $\mathrm{Bg}_{\mathrm{Penning}}$ and $\sigma^2_{\mathrm{shift,drift}}$ listed in Table A.6 were used. The best-fit sterile neutrino parameters are marked with ×.

Table A.6: Summary of scan-step-duration-dependent background parameter values. For the KNM4 dataset the common estimated values was $\mathrm{Bg}_{\mathrm{Penning}} = 10.102 \pm 1.879$ μcps/s

Data set	$\mathrm{Bg}_{\mathrm{Penning}}$ μcps/s	$\sigma^2_{\mathrm{shift,drift}}$ eV^2
KNM4-a	4.781 ± 5.215	0.761 ± 0.248
KNM4-b	11.429 ± 2.114	0.761 ± 0.248
KNM4-c	6.272 ± 5.286	0.761 ± 0.248
KNM4-d	25.137 ± 19.592	0.119 ± 0.181
KNM4-e	0 ± 0	0.119 ± 0.181

was trimmed to have an effective scan duration of 2 hours. The scan-step-duration-dependent background parameter $\mathrm{Bg}_{\mathrm{Penning}}$ was re-estimated for the reduced duration to be 8.105 ± 3.876 μcps/s. The exclusion contour considering only statistical uncertainties for the trimmed KNM4-b dataset is shown in Figure A.33. A sterile neutrino signal was still found with best-fit $m_4^2 = 55.66$ eV^2 and $|U_{e4}|^2 = 0.051$ with a significance of 95.22%. While reducing the scan duration reduced the significance of the best-fit, it was still significant and could not explain the anomaly.

A.7.2 Increased Uncertainty on Scan-Step-Duration-Dependent Background in KNM4-b

Uncertainty on the scan-step-duration-dependent background rate parameter $\mathrm{Bg}_{\mathrm{Penning}} = 11.429 \pm 2.114$ μcps/s was increased 10-fold to $\mathrm{Bg}_{\mathrm{Penning}} = 11.429 \pm 21.14$ μcps/s. The KNM4-b dataset was analyzed considering $\mathrm{Bg}_{\mathrm{Penning}}$ as a fit parameter to obtain the exclusion contour shown in Figure A.34. An open contour was obtained, indicating that no significant sterile neutrino signal was found. The best-fit sterile neutrino parameters were $m_4^2 = 67.82$ eV^2 and $|U_{e4}|^2 = 0.045$

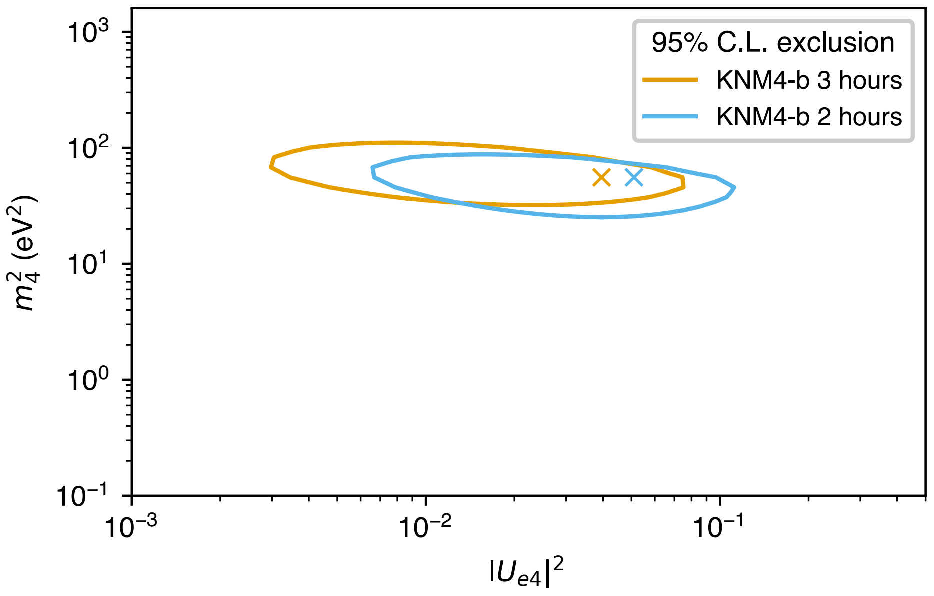

Figure A.33: Exclusion contours of KNM4-b dataset at 95% C.L. considering only statistical uncertainties. The KNM4-b 2 hours dataset was obtained by trimming each scan-step of KNM4-b 3 hours dataset to have an effective scan duration of 2 hours. The best-fit sterile neutrino parameters are marked with ×.

with a significance of 90.39%. This lead to a re-analysis of the model and estimation methods for the $\mathrm{Bg}_{\mathrm{Penning}}$ parameter.

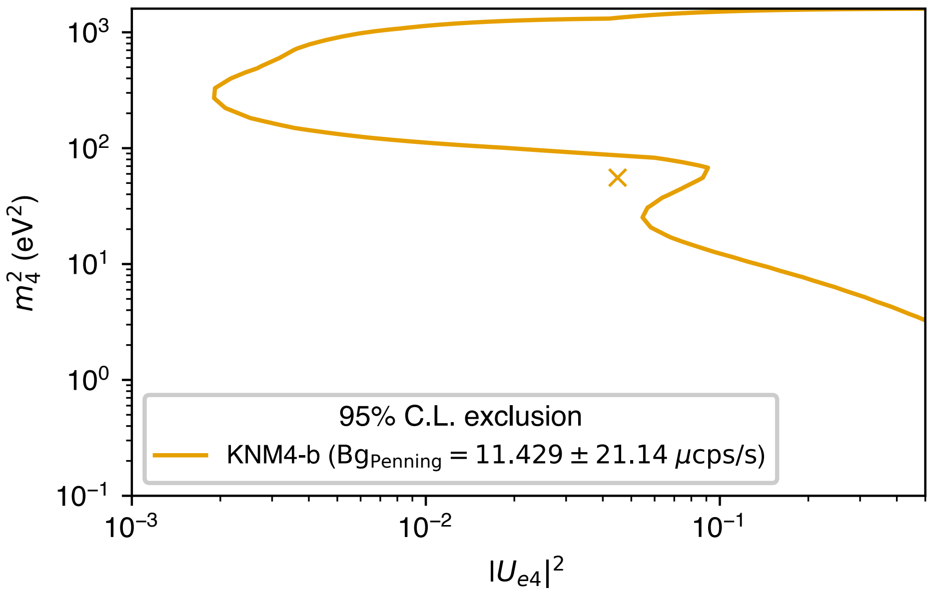

Figure A.34: Exclusion contours of KNM4-b dataset at 95% C.L. considering statistical uncertainties and the uncertainty in $\mathrm{Bg}_{\mathrm{Penning}}$. The best-fit sterile neutrino parameters are marked with ×. Increasing the uncertainty in $\mathrm{Bg}_{\mathrm{Penning}}$ results in an open contour indicating that an incorrect scan-step-duration-dependent background rate could be the reason for the observation of a sterile neutrino like signal in the KNM4-b dataset.

A.7.3 Quadratic Model for Scan-Step-Duration-Dependent Background Rate

Initially, the scan-step-duration-dependent background rate was modeled as a linear function of time. However, through simulations and dedicated measurements [135, Section 3.5], the rate was found to have a sigmoid-like shape with the rate plateauing after 1500 s. As the longest scan-step in the KNM1-5 dataset was 1080 s, it was decided to model the scan-step-duration-dependent background rate, which is primarily due to the electrons trapped by the Penning trap, as a quadratic function of time Section 3.7. As the frequent wiping of the Penning trap and reduced pre-spectrometer voltage significantly reduces the scan-step-duration-dependent background in KNM4-d and KNM4-e, it was assumed to be zero for the KNM4-d and KNM4-e datasets.

The Asimov dataset of KNM4 generated using a linear model with $\mathrm{Bg}_{\mathrm{Penning}} = 10.102 \pm 1.879$ μcps/s, was analyzed using a quadratic model for the scan-step-duration-dependent background rate for KNM4-a, KNM4-b and KNM4-c with $\mathrm{Bg}_{\mathrm{Penning}} = 0.014 \pm 0.002$ $\mu\mathrm{cps/s}^2$. The contours of this cross-fitting are shown in Figure A.35. The contours are labeled “linear-quadratic" to indicate that the Asimov data was generated with a linear model while a quadratic model was used for analysis. Asimov data was also generated using the quadratic model and analyzed using a quadratic model. This results in the sensitivity contours labeled “quadratic-quadratic" in Figure A.35. The “linear-linear" sensitivity contours are also shown. The “quadratic-quadratic" contours indicate a better sensitivity for $m_4^2 \gtrsim 70\,\mathrm{eV}^2$ in comparison to the “linear-linear" sensitivity contours. However, the sensitivity with a quadratic model is worse compared to the linear model for $m_4^2 \lesssim 70\,\mathrm{eV}^2$.

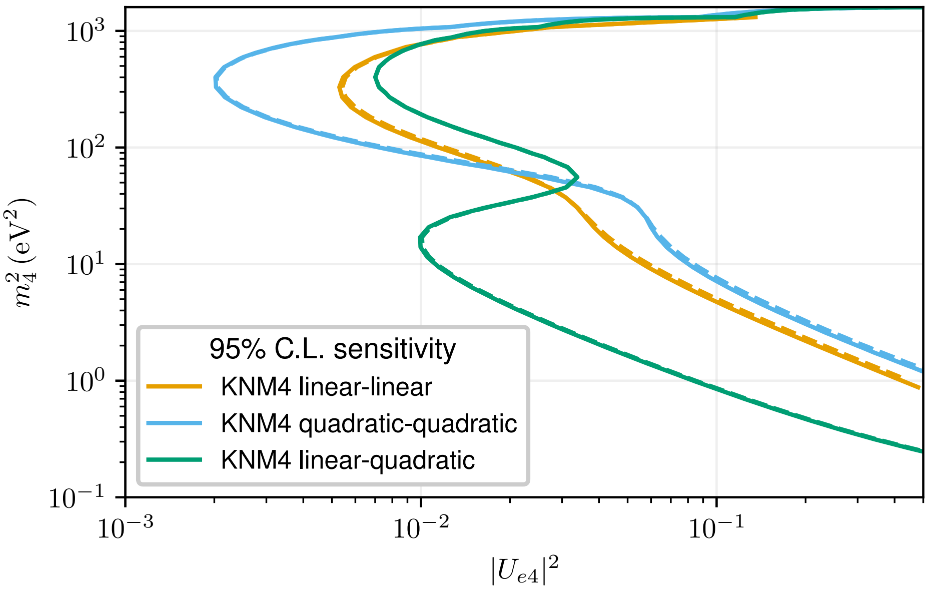

Figure A.35: Sensitivity contours of KNM4 dataset at 95% C.L. considering statistical uncertainties (solid lines) and the uncertainty in $\mathrm{Bg}_{\mathrm{Penning}}$ (dashed lines). The contours labeled “linear-quadratic" indicate that the Asimov data was generated with a linear model while a quadratic model was used for analysis. Similarly “quadratic-quadratic" are based on Asimov data generated using the quadratic model and analyzed using a quadratic model.

The KNM4-b experimental dataset was re-analyzed with the quadratic model for the Penning trap related background. The exclusion contours considering only statistical uncertainties and including $\mathrm{Bg}_{\mathrm{Penning}}$ as a fit parameter are shown in Figure A.36. The use of a quadratic model results in open contours with best-fit $m_4^2 = 37.49$ eV^2 and $|U_{e4}|^2 = 0.051$ with a significance of 92.98% considering only statistical uncertainties and best-fit $m_4^2 = 37.49$ eV^2 and $|U_{e4}|^2 = 0.051$

with a significance of 93.94% when $\mathrm{Bg}_{\mathrm{Penning}}$ is a fit parameter. Significance of the best-fit parameters remained very high considering the detection threshold of 95%. Hence, mismatch in the scan-step-duration-dependent background rate model was considered a major factor in the emergence of the closed contour in KNM4, though not the only contributing factor.

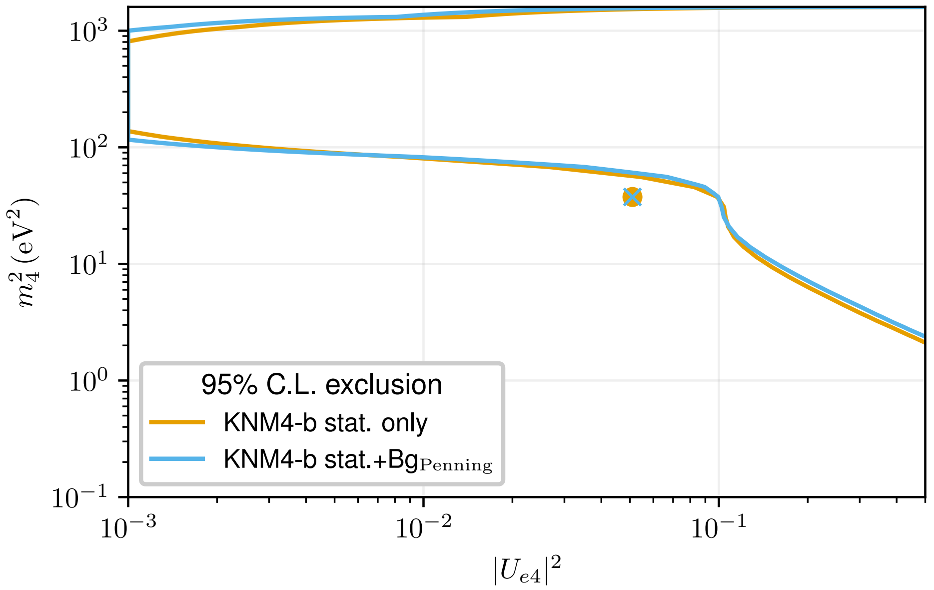

Figure A.36: Exclusion contours of KNM4-b dataset at 95% C.L. considering statistical uncertainties and the uncertainty in $\mathrm{Bg}_{\mathrm{Penning}}$. The best-fit sterile neutrino parameters are marked with × and •. A quadratic model for the scan-step-dependent-background rate was used. The open contours support the hypothesis that the closed obtained in the KNM4-b dataset was due to an incorrect scan-step-duration-dependent background rate.

A.7.4 Impact of Source-Potential Variations on KNM4-e Dataset

A closed contour was obtained for the KNM4-e dataset even with dataset specific values $\mathrm{Bg}_{\mathrm{Penning}} = 0\ \mu\mathrm{cps/s}^2$ and $\sigma^2_{\mathrm{shift,drift}} = 0.119 \pm 0.181\ \mathrm{eV}^2$ in Figure A.30. The source-potential related parameters are considered fit parameters and grid scan was performed to obtain the exclusion contour Figure A.37. The exclusion contour obtained by increasing the uncertainty on $\sigma^2_{\mathrm{shift,drift}}$ and σ_0^2 ten-fold is also shown in Figure A.37. Closed contours were still obtained in spite of the increased uncertainty, thereby negating the hypothesis that source-potential related systematics were responsible. As the KNM4-e dataset was the smallest (39/470 scans) in KNM4 it was considered to be an outlier for the KSN1-5 re-analysis.

A.7.5 Increase in Uncertainty of Energy Loss Parameters

The parameters of the energy loss model Section 3.5.2.2 were initially estimated by fitting the model with a single set of parameters to data obtained from both differential (time-of-flight) mode and integral mode measurements Section 2.3.3. The values so obtained were listed in Table A.10. However, re-visiting the estimation led to the realization that fitting the three Gaussian model to the individual time-of-flight measurements or integral mode measurements leads to significantly different set of estimates as shown in Table A.7. For the re-analysis of the KNM1-5 dataset, it was decided to keep the same central values as in Table A.10 but increase

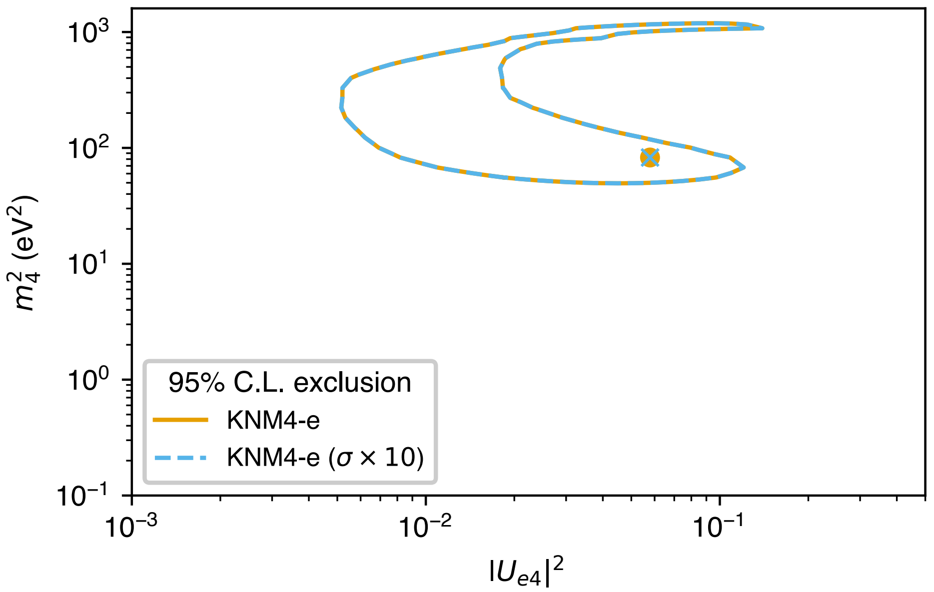

Figure A.37: Exclusion contours of KNM4-e dataset at 95% C.L. considering statistical uncertainties and the uncertainty in source-potential related systematic parameters. The best-fit sterile neutrino parameters are marked with × and •. Increasing the uncertainty does not have any impact on the contour.

the uncertainty ten-fold. The updated values are listed in Table A.8. The resulting uncertainty in the energy loss can be visualized through a Monte Carlo envelope of the density mixture. Figure A.38 shows the median densities and the shaded region corresponds to the 95% interval.

Table A.7: Parameters of three Gaussian energy loss model Section 3.5.2.2 used for KNM1-5 analysis estimated using data from integral mode measurements and differential mode (time-of-flight) measurements. The correlation matrices are shown in Figure A.46 and Figure A.47

Energy-loss parameter name	Integral measurement	Differential measurement
$a_1(\mathrm{eV}^{-1})$	0.023 ± 0.006	0.033 ± 0.001
$m_1(\mathrm{eV})$	11.820 ± 0.060	11.921 ± 0.008
$\sigma_1(\mathrm{eV})$	0.093 ± 0.019	0.184 ± 0.006
$a_2(\mathrm{eV}^{-1})$	0.288 ± 0.002	0.298 ± 0.001
$m_2(\mathrm{eV})$	12.792 ± 0.006	12.805 ± 0.002
$\sigma_2(\mathrm{eV})$	0.494 ± 0.006	0.468 ± 0.002
$a_3(\mathrm{eV}^{-1})$	0.073 ± 0.001	0.076 ± 0.000
$m_3(\mathrm{eV})$	15.008 ± 0.012	14.958 ± 0.004
$\sigma_3(\mathrm{eV})$	0.955 ± 0.019	0.888 ± 0.012

The energy-loss parameters from Table A.8 were used to generate an KNM1-5 Asimov dataset. Sensitivity-like contours were determined for the three sets of parameters shown in Figure A.38, considering statistical and energy-loss related uncertainties Figure A.39. For higher $m_4^2 \gtrsim 200\,\mathrm{eV}^2$, sensitivity for the parameters from the combined dataset is worst among the three due to higher uncertainty in the energy-loss parameters. Interestingly, for lower sterile neu-

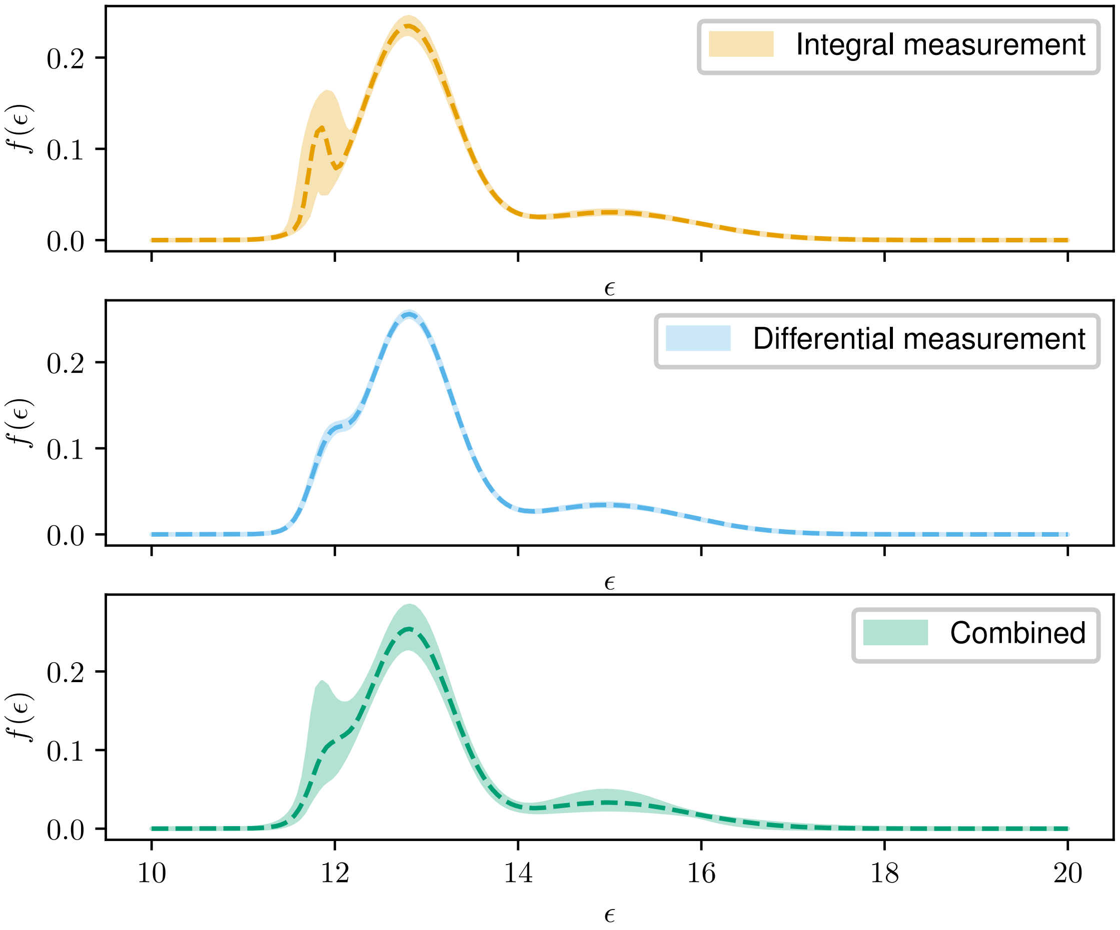

Figure A.38: Uncertainty in the energy loss visualized through Monte Carlo envelopes of the density mixtures. The median densities are shown by the dashed lines and and the shaded region corresponds to the 95% interval.

trino masses $m_4^2 \lesssim 50\,\text{eV}^2$, the sensitivity contour lies between the contours of the integral and differential measurements.

A.7.6 Re-combination of KNM4 Data

Prior to revising the background models and systematic parameter re-estimations, the patch-wise best-fit values of endpoint E_0, flat background rate Bg and signal parameter Sig, from fits on the KNM4-x datasets with $m_\nu^2 = 0\,\text{eV}^2$, $m_4^2 = 0\,\text{eV}^2$ and $|U_{e4}|^2 = 0$ considering only statistical uncertainties were studied Figures A.40 to A.42. No clear distinction between the datasets can be seen for any of the three parameters. However, looking at the means over the patches of the converged values Figures 4.13, A.43 and A.44, a pattern emerges. The endpoint of KNM4-a and KNM4-b datasets is $\sim 60\,\text{meV}$ lower than that of KNM4-d and KNM4-e. The endpoints of KNM4-c and the combined KNM4 dataset lie in between. The shift in the endpoint was attributed to the drift of the source-potential with time [135, Section 5.3]. The $\sim 60\,\text{mV}$ shift can be captured by the $\sigma^2_{\text{shift,drift}}$ parameter Table A.6. As a result, the KNM4 dataset was split into KNM4-NOM and KNM4-OPT datasets based on the MTDs Figure 4.14. Table 4.5 gives a summary of the statistics in the two datasets. The means over the patches of the converged E_0 values for the new datasets are shown in Figure 4.15. The KNM1-5 re-analysis was therefore

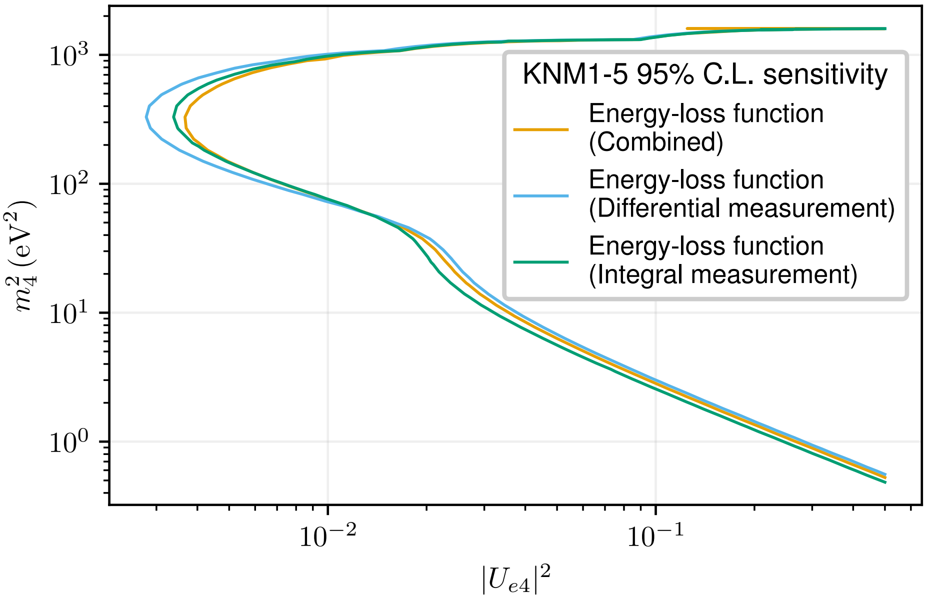

Figure A.39: Sensitivity-like contours of KNM1-5 dataset at 95% C.L. considering statistical uncertainties and the uncertainties in energy-loss parameters. The energy-loss parameters Figure A.38 are estimated from the individual differential and integral datasets or the combined dataset.

performed using the split KNM4 dataset and updated systematic parameters, which are provided in Table A.9 and Table A.8.

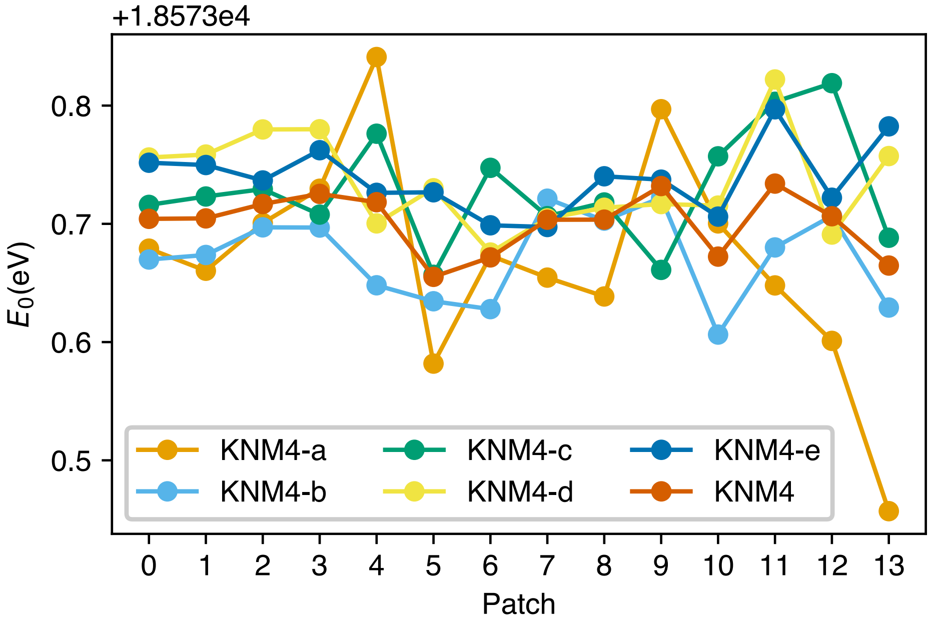

Figure A.40: Patch-wise best-fit values of endpoint E_0 for the KNM4-x datasets with $m_\nu^2 = 0\,\mathrm{eV}^2$, $m_4^2 = 0\,\mathrm{eV}^2$ considering only statistical uncertainties.

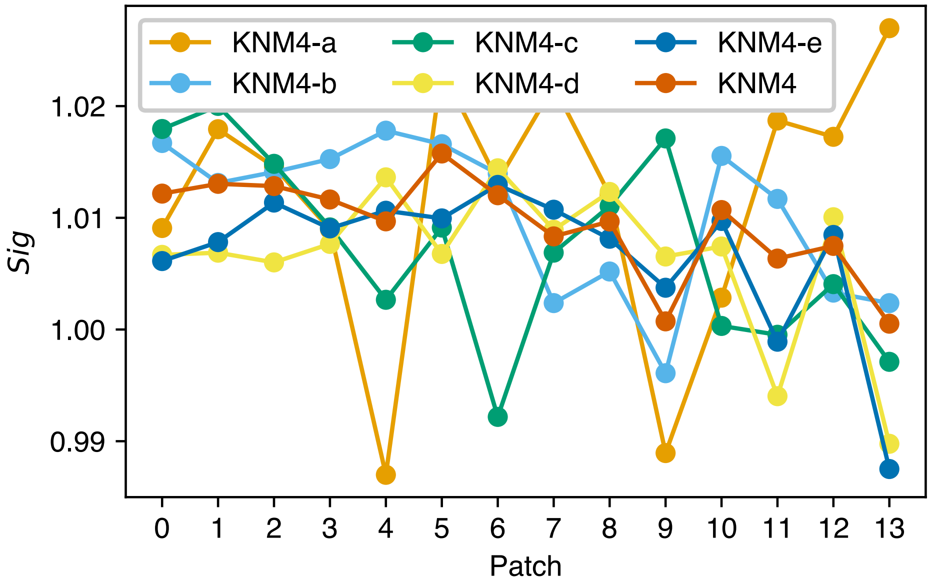

Figure A.41: Patch-wise best-fit values of signal parameter Sig for the KNM4-x datasets with $m_\nu^2 = 0\,\mathrm{eV}^2$, $m_4^2 = 0\,\mathrm{eV}^2$ considering only statistical uncertainties.

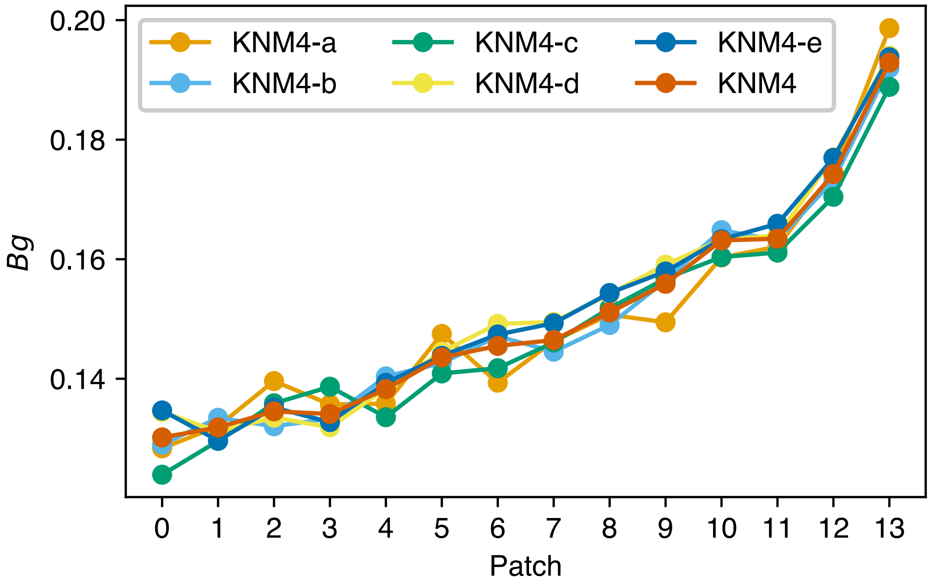

Figure A.42: Patch-wise best-fit values of flat background rate Bg for the KNM4-x datasets with $m_\nu^2 = 0\,\mathrm{eV}^2$, $m_4^2 = 0\,\mathrm{eV}^2$ considering only statistical uncertainties.

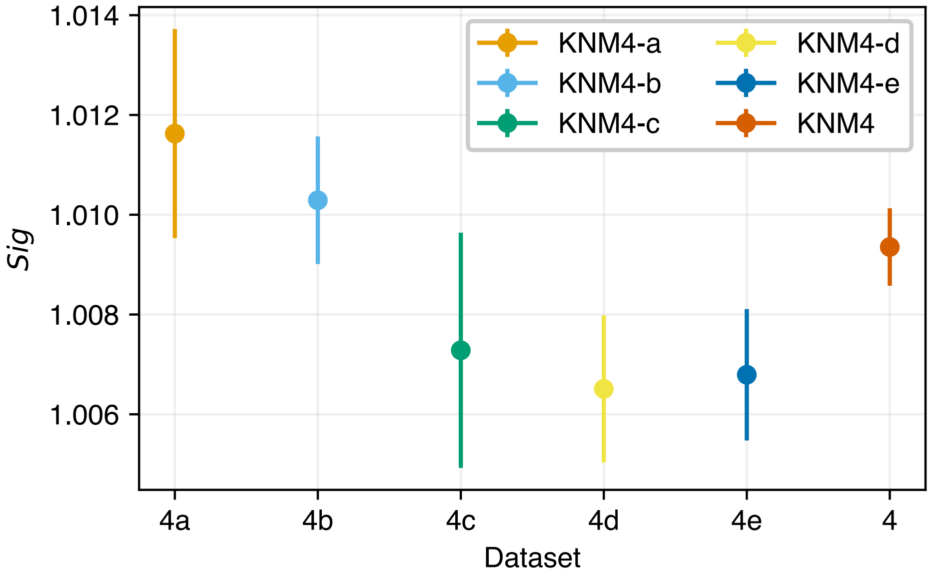

Figure A.43: Best-fit values and uncertainties of signal parameter Sig for the KNM4-x datasets with $m_\nu^2 = 0\,\mathrm{eV}^2$, $m_4^2 = 0\,\mathrm{eV}^2$ considering only statistical uncertainties.

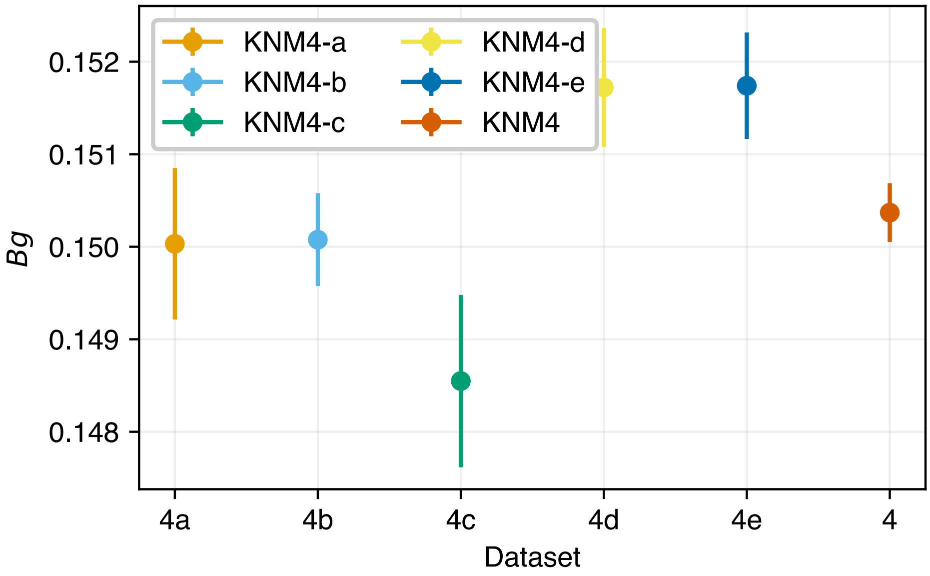

Figure A.44: Best-fit values and uncertainties of flat background rate Bg for the KNM4-x datasets with $m_\nu^2 = 0\,\mathrm{eV}^2$, $m_4^2 = 0\,\mathrm{eV}^2$ considering only statistical uncertainties.

Table A.8: Updated parameters of three Gaussian energy loss model Section 3.5.2.2 used for KNM1-5 re-analysis. The correlation matrix is shown in Figure A.48.

Eloss parameter name	
$a_1(\mathrm{eV}^{-1})$	0.033 ± 0.011
$m_1(\mathrm{eV})$	11.919 ± 0.075
$\sigma_1(\mathrm{eV})$	0.184 ± 0.062
$a_2(\mathrm{eV}^{-1})$	0.296 ± 0.006
$m_2(\mathrm{eV})$	12.805 ± 0.019
$\sigma_2(\mathrm{eV})$	0.468 ± 0.019
$a_3(\mathrm{eV}^{-1})$	0.076 ± 0.003
$m_3(\mathrm{eV})$	14.968 ± 0.036
$\sigma_3(\mathrm{eV})$	0.907 ± 0.114

Table A.9: Updated summary of parameter inputs used in the sterile neutrino search after the first unblinding and investigations. Each column contains central values and uncertainties for a single campaign. If a systematic is not present, negligible, or eliminated in a campaign, it is marked with *n.a.* Some of the inputs are taken into account as patch-wise values in the analysis; in this case, the mean value and mean uncertainty are listed.

Parameter	KNM1	KNM2	KNM-SAP	KNM-NAP	KNM4-NOM	KNM4-OPT	KNM5
$\sigma_0^2\,(10^{-3}\,\mathrm{eV}^2)$	0.900 ± 0.900	0.880 ± 0.880	0.890 ± 0.150	$^{a)}0.890 \pm 0.190$	$^{a)}0.890 \pm 0.190$	$^{a)}0.890 \pm 0.190$	$^{a)}0.890 \pm 0.190$
$\Delta^{\dagger}_{10,\mathrm{eff}}$ (mV)	0.000 ± 18.730	0.000 ± 22.950	0.000 ± 18.930	$^{a)}0.000 \pm 21.040$	$^{a)}0.000 \pm 21.040$	$^{a)}0.000 \pm 21.040$	$^{a)}0.000 \pm 21.040$
$\sigma^2_{\mathrm{shift,drift}}\,(10^{-3}\,\mathrm{eV}^2)$	-1.990 ± 1.695	3.782 ± 0.758	0.111 ± 1.286	-1.317 ± 0.650	0.731 ± 0.248	0.119 ± 0.181	8.594 ± 0.876
$\mathrm{Bg}^{\dagger}_{\mathrm{Penning}^{\dagger}}$ (μcps/s^2)	0.00 ± 0.010	0.003 ± 0.006	0.015 ± 0.006	0.030 ± 0.010	0.012 ± 0.002	n.a.	n.a.
$\rho d\sigma$	0.393 ± 0.005	1.527 ± 0.016	0.746 ± 0.008	1.347 ± 0.014	1.367 ± 0.014	1.367 ± 0.014	1.369 ± 0.013
$\mathrm{Bg}^{\dagger}_{\mathrm{slope}^{\dagger}}$ (μcps/eV)	$^{a)}1.057 \pm 3.759$	$^{a)}1.057 \pm 3.759$	$^{b)}1.292 \pm 0.822$	$^{a)}1.057 \pm 3.759$	$^{b)}1.292 \pm 0.822$	$^{b)}1.292 \pm 0.822$	$^{b)}1.292 \pm 0.822$
B_{ana} $(10^{-4}\,T)$	6.306 ± 0.063	6.308 ± 0.063	$^{a)*)}5.355 \pm 0.263$	6.289 ± 0.063	$^{a)*)}5.355 \pm 0.263$	$^{a)*)}5.355 \pm 0.263$	$^{*)}5.525 \pm 0.011$
$\sigma^2_{\mathrm{ana}}\,(10^{-3}\,\mathrm{eV}^2)$	1.202	1.306	$^{a)*)}54.715 \pm 51.162$	1.130	$^{a)*)}54.715 \pm 51.162$	$^{a)*)}54.715 \pm 51.162$	$^{*)}13.346 \pm 1.190$
$B_{\mathrm{src}}\,(T)$	$^{a)}2.506 \pm 0.006$	$^{a)}2.506 \pm 0.006$	$^{a)}2.506 \pm 0.006$	$^{a)}2.506 \pm 0.006$	$^{a)}2.506 \pm 0.006$	$^{a)}2.506 \pm 0.006$	$^{a)}2.506 \pm 0.006$
E-loss	Parameters and uncertainties provided in Table A.8						
$B_{pch}\,(T)$	4.240 ± 0.004	4.239 ± 0.004	$^{a)*)}4.242 \pm 0.004$	4.241 ± 0.004	$^{a)*)}4.242 \pm 0.004$	$^{a)*)}4.242 \pm 0.004$	$^{a)*)}4.242 \pm 0.004$
$\mathrm{Sig}_{\mathrm{rw}}\,(10^{-3})$	n.a.	n.a.	$^{a)*}4.564 \pm 0.065$	2.880 ± 0.040	$^{a)*)}3.812 \pm 0.055$	$^{a)*)}5.108 \pm 0.074$	$^{*)}1.999 \pm 0.036$
$E_{0,\mathrm{rw}} - 18575$ (eV)	n.a.	n.a.	$^{a)}1.140 \pm 0.360$	$^{a)}1.140 \pm 0.360$	$^{b)}1.230 \pm 0.360$	$^{b)}1.230 \pm 0.360$	0.980 ± 0.500
$w_{\mathrm{GS,rw}}$	n.a.	n.a.	$^{a)}-0.110 \pm 0.033$	$^{a)}-0.110 \pm 0.033$	$^{a)}-0.110 \pm 0.033$	$^{a)}-0.110 \pm 0.033$	-0.134 ± 0.046
$\mathrm{Bg}_{\mathrm{non-Poi}}$	1.064	1.112	n.a.	1.106	n.a.	n.a.	n.a.

$^{a)b)}$ Values or uncertainties of this parameter are correlated between campaigns.

$^{*)}$ Values are patch-wise, here the mean is given.

† $\Delta_{10,\mathrm{eff}}$ is given as an effective value, representative for the individual Δi_0 which would lead to an equivalent systematic error in the 40 eV fit range.

†† The input values for the Penning trap induced background and the high voltage dependent background slope are scaled to the area of 148 pixels.

A.8 Code Archival

Access to the relevant analysis code can be granted upon request to the KATRIN collaboration. The following repositories have been archived to ensure reproducibility and transparency of the results presented in this thesis:

- The code used to perform the final sterile neutrino search, based on the combined KNM1 through KNM5 datasets, is archived at https://nuserv.uni-muenster.de:8443/pb7970/ksn-1-5_reunb2
- The code used for conducting pseudo-experiments, including studies of the χ^2 and $\Delta\chi^2$ distributions to evaluate the applicability of Wilks' theorem, as well as investigations into the crossing of sensitivity and exclusion contours, is archived at https://nuserv.uni-muenster.de:8443/pb7970/kafit_sterile_wilks_test

A.9 The KATRIN Software Framework: KASPER and KaFit

KASPER is a software package, a versatile collection of C++ libraries and tools designed for simulation, data processing, and comprehensive analysis. Actively maintained and continuously developed, KASPER plays a pivotal role in supporting the diverse computational needs of the KATRIN collaboration. The suite is organized into three primary categories: utilities, analysis, and simulation, each of which is integral to the experiment's success.

A.9.1 Source and Spectrum Calculation (SSC) Package

At the core of the KASPER suite is the **Source and Spectrum Calculation (SSC)** package. This package is crucial for modeling the experimental setup and accurately calculating the integrated tritium β-decay spectrum. Unlike trajectory simulation tools like `Kassiopeia`, which simulate individual electron paths, SSC is designed to compute the entire kinematic β-spectrum. It achieves this by convolving the theoretical spectrum with the response function of the experimental apparatus, thereby providing a comprehensive description of the source, transmission, and detection processes.

The SSC package is designed with a modular architecture, allowing researchers to easily configure and adapt different models for the source, energy loss functions, and transmission functions through XML configuration files. This modularity not only enhances flexibility but also allows for detailed customization to match specific experimental conditions. Furthermore, SSC has been optimized for performance; it incorporates caching mechanisms and parallel processing capabilities to significantly reduce computational time while maintaining high precision in the calculations.

A.9.2 KaFit: Fitting Framework

Complementing SSC, the **KaFit** framework is an advanced fitting toolset specifically developed for sensitivity studies and the analysis of KATRIN data. KaFit is built on the ROOT framework, offering robust support for both frequentist and Bayesian statistical methods. The framework's primary application, `kafit-fitter`, is designed to manage and execute the fitting process, which involves configuring the model (often using SSC), handling input data, and optimizing the fit parameters.

KaFit uses the `MIGRAD` minimization algorithm from the `MINUIT` optimization package to perform the fitting, which works by minimizing the negative log-likelihood to find the best-fit parameters. The fitting process is highly streamlined, with the results being automatically recorded once the convergence criteria are satisfied. The entire setup, including data handling, model configuration, and parameter management, is defined through XML files, making the fitting process transparent and reproducible.

In addition to its core functionalities, KaFit includes several auxiliary tools that enhance its utility. For instance, the `kafit-runsummarygenerator` can generate Monte Carlo pseudo-experiments, enabling systematic studies and testing of fitting routines prior to applying them to real data. The `kafit-runsummarymerger` tool allows for the pre-merging of datasets, which simplifies data handling and accelerates the fitting process by reducing the need to process multiple run summaries during each fit.

Together, KASPER and KaFit form a powerful and flexible software ecosystem that underpins the KATRIN experiment's data analysis efforts. By enabling precise spectrum calculations and robust statistical analysis, these tools are instrumental in advancing our understanding of neutrino properties and the search for new physics beyond the Standard Model.

A.9.2.1 Installation and Configuration

KaFit is installed as part of KASPER by enabling specific build flags:

- To build KaFit: `BUILD_KAFIT=ON`
- To build the Source and Spectrum Calculation package: `BUILD_SSC=ON`

KaFit also includes a Python-based visualization module, **KaFigure**. To install KaFigure, the following flag must be set:

- `BUILD_KAFIGURE=ON`

KaFigure depends on several Python libraries, including `matplotlib`, `numpy`, `pandas`, `scipy`, `termcolor`, and `tabulate`, which can be installed using pip.

A.9.2.2 Data Formats and Conversion Tools

KaFit supports multiple tree-structured data formats used for various stages of data processing:

- **Supported Formats:** `XML`, `KTF`, `JSON`, `YAML`.
- **Conversion Tool:** The `ktf-treedump` utility allows conversion between these formats. For instance, to convert a `.ktf` file to `.json`:

```
ktf-treedump --precision=15 yourFile.ktf --format=json > yourFile.json
```

This flexibility ensures that users can select the format best suited to their specific needs while maintaining compatibility across different tools in KASPER.

A.9.2.3 Data Handling and Preparation

KaFit handles various data types, ensuring both experimental and simulated data are processed effectively:

- **Experimental Data:** Downloaded run summaries from IDLE.
- **Asimov Data:** Generated using the `RunSummaryGenerator`, based on experimental data or user-defined "dummy" summaries.

Run Registers are crucial for organizing run summaries and ensuring correct data structuring for the fitting process.

A.9.2.4 Monte Carlo Simulation and Summary Merging

KaFit offers tools for generating and managing Monte Carlo (MC) summaries, essential for sensitivity studies:

- **Generating MC Summaries:** The `RunSummaryGenerator` is used to create MC summaries tailored to specific analyses.
- **Merging Summaries:** The `RunSummaryMerger` merges run summaries, optimizing the fitting process by reducing computational load. The command for merging:

```
kafit-runsummarymerger --config=kafit.xml --runlist=RunRegister_filename.ktf \
                       --firstrun=x --runs=y --prefix=output_name
```

A.9.2.5 Parameter Management and ExtendedParameterDocs

KaFit uses **ExtendedParameterDocs** to manage parameters during fitting:

- **ExtendedParameterDocs:** Define parameters, constraints, and correlations. These documents can be automatically generated, reducing setup errors and streamlining the fitting process.

A.9.2.6 Executing the Fit

KaFit executes fits to determine central values and uncertainties:

- **Components of a Fit:**
  - **Log-Likelihood Function:** Minimizes during the fit.
  - **Minimization Method:** Uses Minuit2 for frequentist analyses.
  - **Ensemble Test:** Validates the fit using pseudo-experiments.

Frequentist Analysis typically uses the Minuit2 algorithm, with configurations defined in files like `kafit.xml`.

A.10 Additional plots

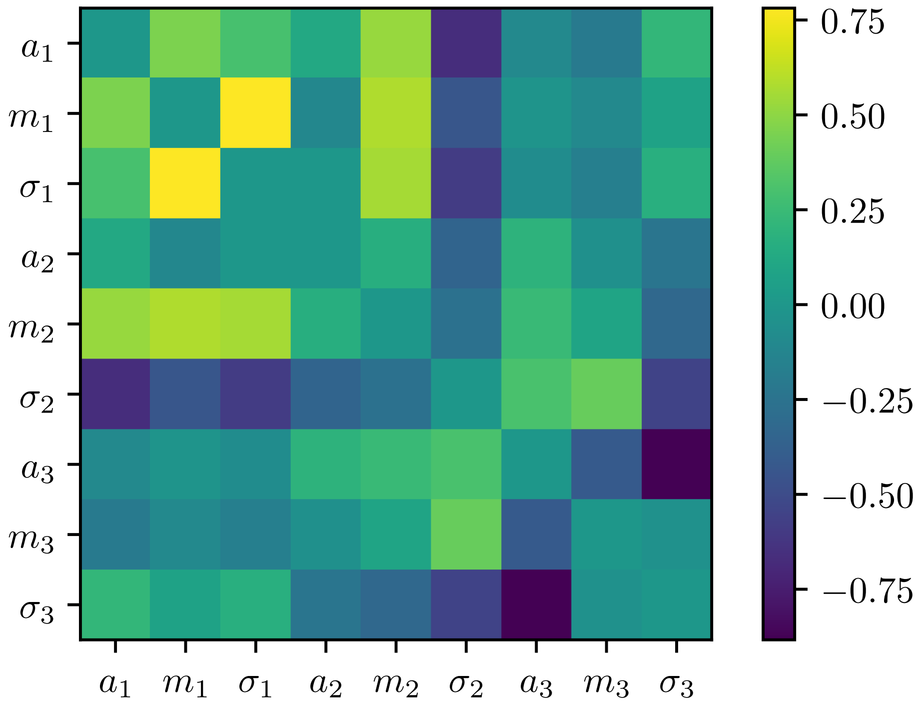

Figure A.45: Correlations between energy loss parameters used for the first unblinding.

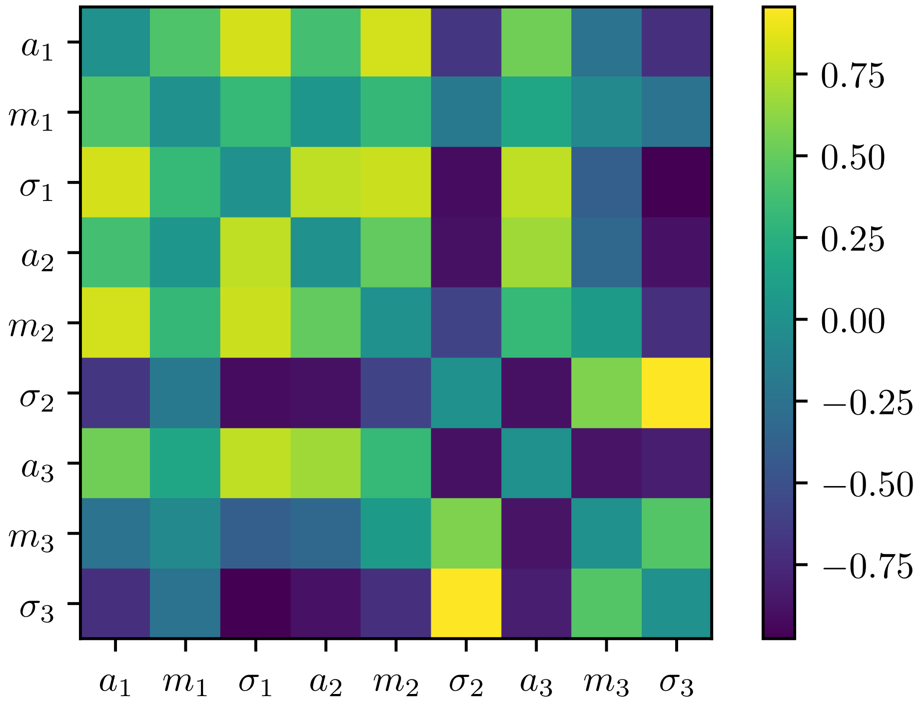

Figure A.46: Correlations between energy loss parameters estimated from integral measurements.

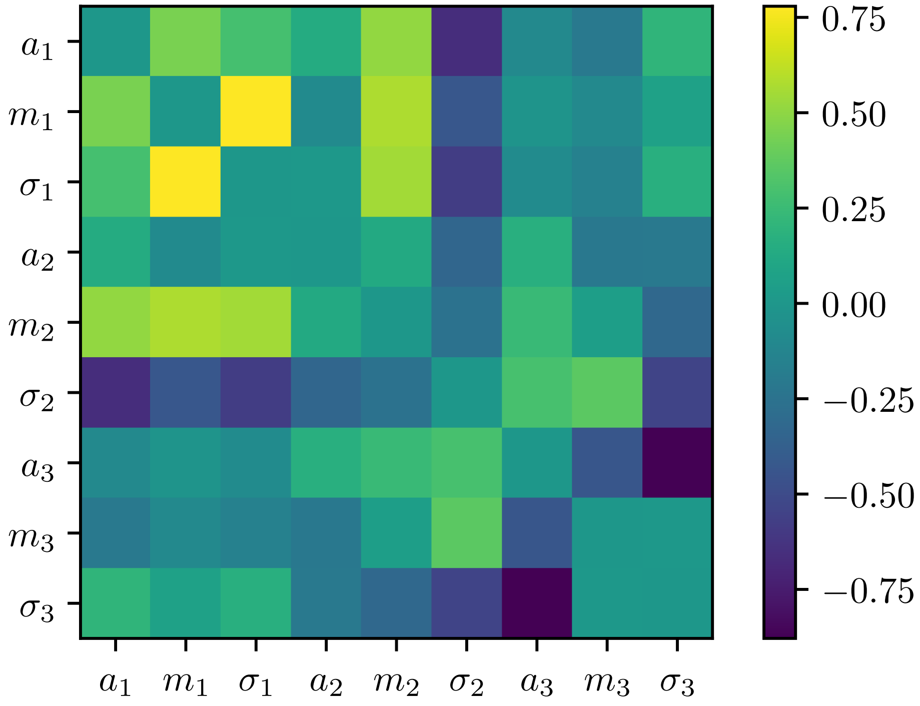

Figure A.47: Correlations between energy loss parameters estimated from differential (time-of-flight) measurements.

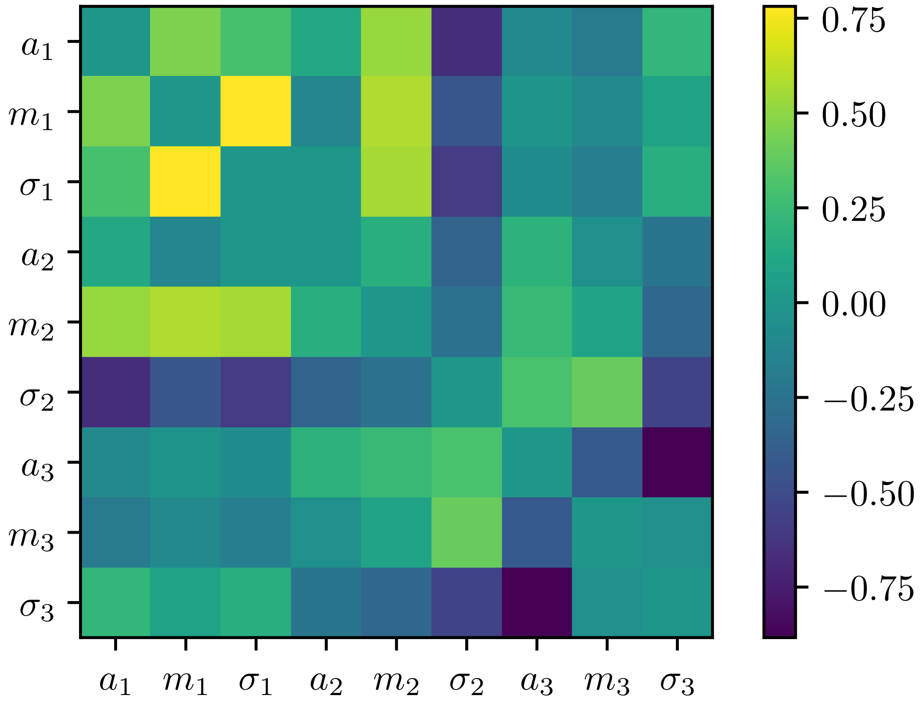

Figure A.48: Correlations between energy loss parameters used for the final unblinding.

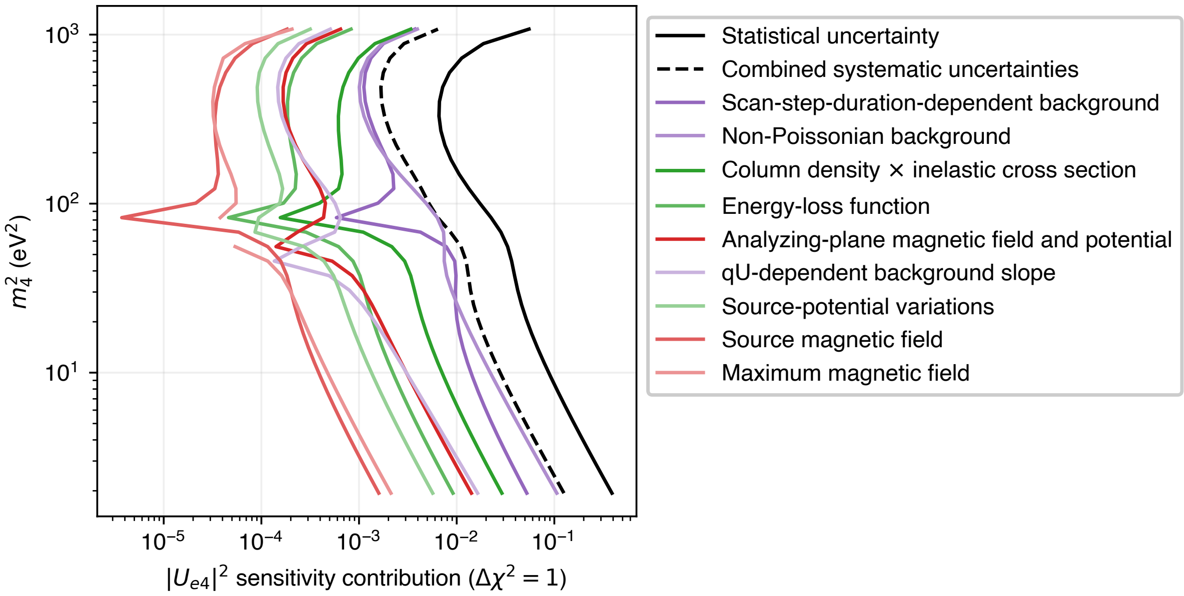

Figure A.49: Contributions of statistical and systematic uncertainties on sterile neutrino mixing $|U_{e4}|^2$ sensitivity for the KNM1 dataset considering various systematic uncertainties individually and combined. The presented raster contours are based on the systematic parameters of the second unblinding. Source related systematics are shown in green, background related in purple and transmission related in red. Lightness of the line color indicates the level of impact with higher impact denoted by a darker color.

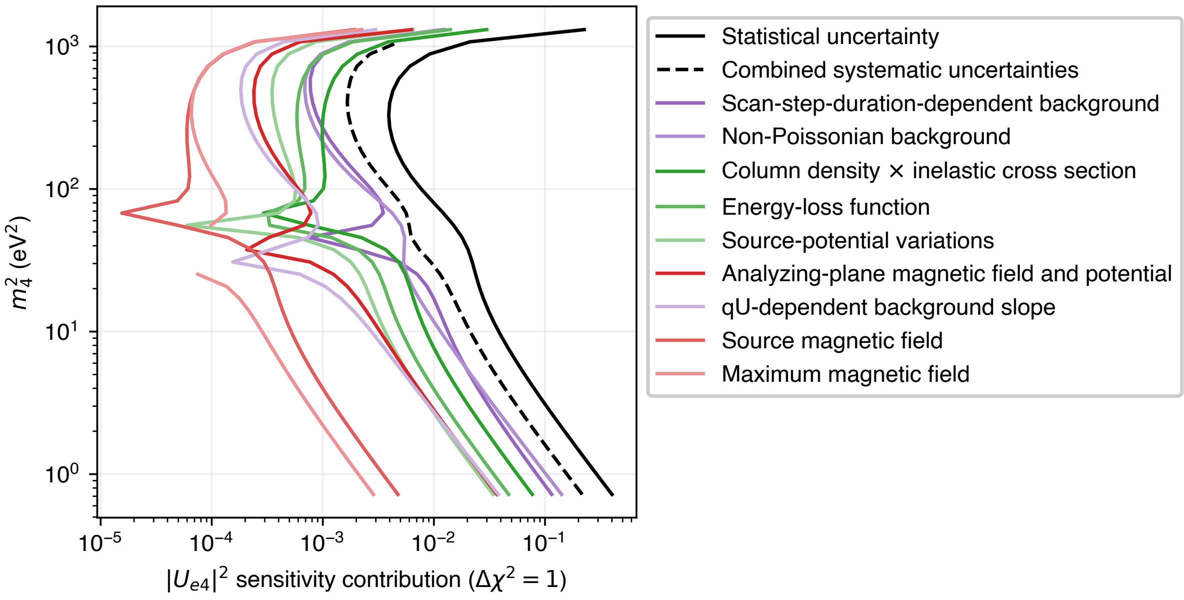

Figure A.50: Contributions of statistical and systematic uncertainties on sterile neutrino mixing $|U_{e4}|^2$ sensitivity for the KNM2 dataset considering various systematic uncertainties individually and combined. The presented raster contours are based on the systematic parameters of the second unblinding. Source related systematics are shown in green, background related in purple and transmission related in red. Lightness of the line color indicates the level of impact with higher impact denoted by a darker color.

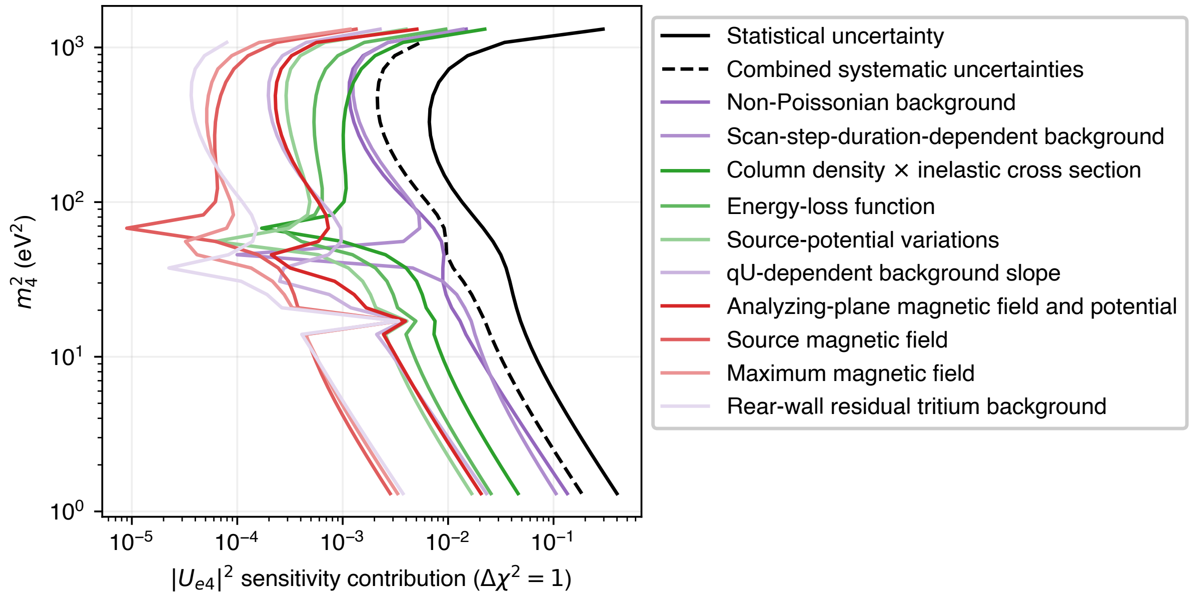

Figure A.51: Contributions of statistical and systematic uncertainties on sterile neutrino mixing $|U_{e4}|^2$ sensitivity for the KNM3-NAP dataset considering various systematic uncertainties individually and combined. The presented raster contours are based on the systematic parameters of the second unblinding. Source related systematics are shown in green, background related in purple and transmission related in red. Lightness of the line color indicates the level of impact with higher impact denoted by a darker color.

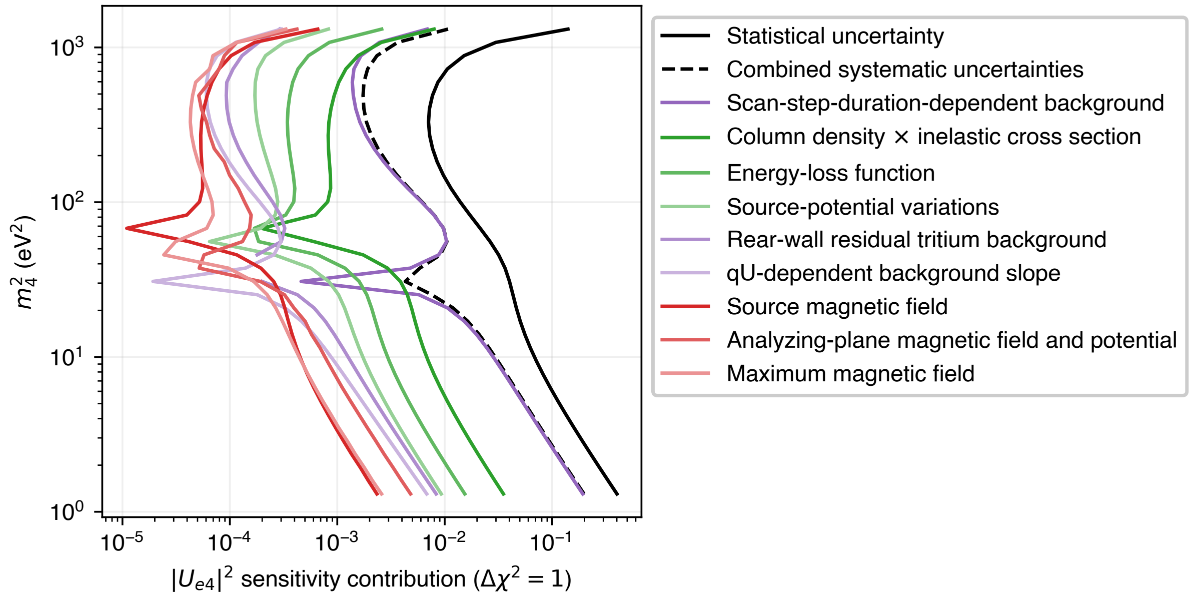

Figure A.52: Contributions of statistical and systematic uncertainties on sterile neutrino mixing $|U_{e4}|^2$ sensitivity for the KNM3-SAP dataset considering various systematic uncertainties individually and combined. The presented raster contours are based on the systematic parameters of the second unblinding. Source related systematics are shown in green, background related in purple and transmission related in red. Lightness of the line color indicates the level of impact with higher impact denoted by a darker color.

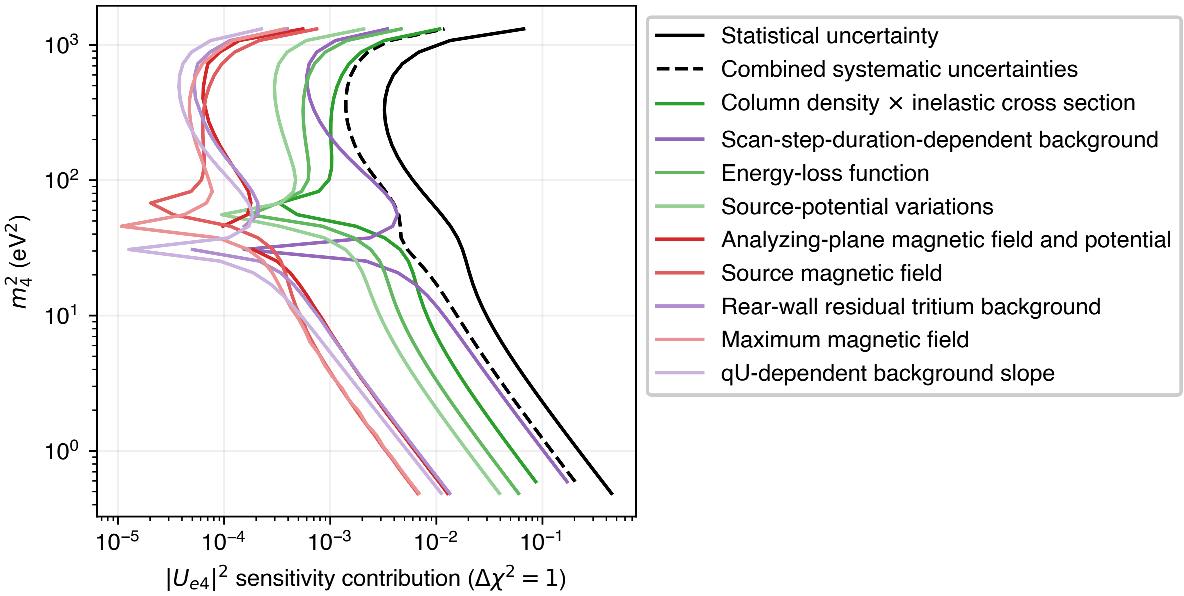

Figure A.53: Contributions of statistical and systematic uncertainties on sterile neutrino mixing $|U_{e4}|^2$ sensitivity for the KNM4-NOM dataset considering various systematic uncertainties individually and combined. The presented raster contours are based on the systematic parameters of the second unblinding. Source related systematics are shown in green, background related in purple and transmission related in red. Lightness of the line color indicates the level of impact with higher impact denoted by a darker color.

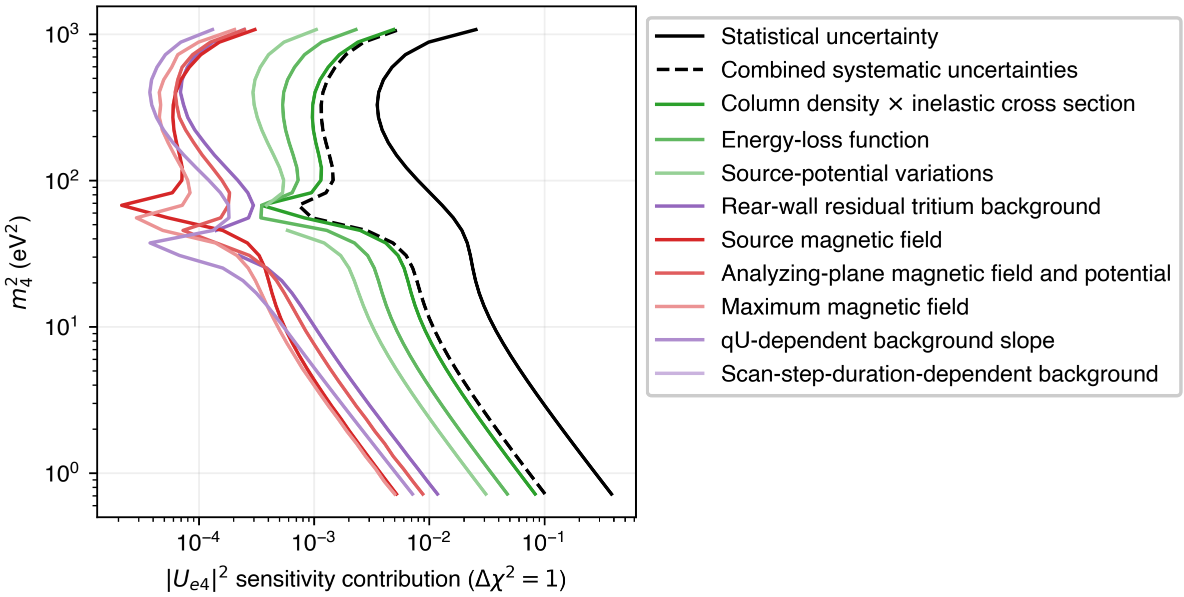

Figure A.54: Contributions of statistical and systematic uncertainties on sterile neutrino mixing $|U_{e4}|^2$ sensitivity for the KNM4-OPT dataset considering various systematic uncertainties individually and combined. The presented raster contours are based on the systematic parameters of the second unblinding. Source related systematics are shown in green, background related in purple and transmission related in red. Lightness of the line color indicates the level of impact with higher impact denoted by a darker color.

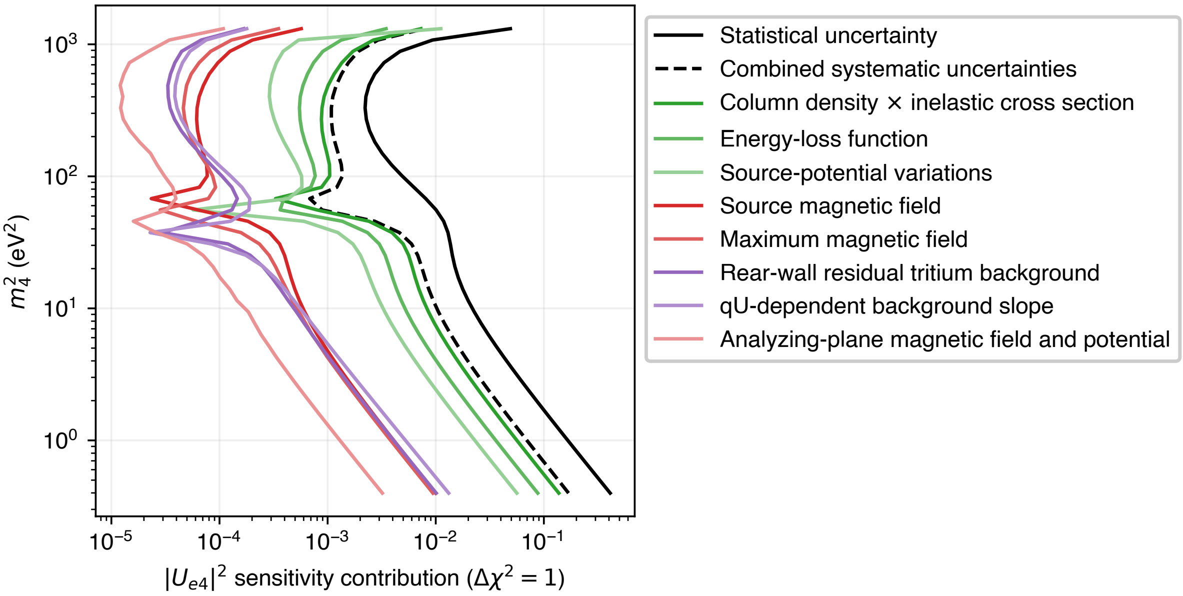

Figure A.55: Contributions of statistical and systematic uncertainties on sterile neutrino mixing $|U_{e4}|^2$ sensitivity for the KNM5 dataset considering various systematic uncertainties individually and combined. The presented raster contours are based on the systematic parameters of the second unblinding. Source related systematics are shown in green, background related in purple and transmission related in red. Lightness of the line color indicates the level of impact with higher impact denoted by a darker color.

Table A.10: Parameters of three Gaussian energy loss model Section 3.5.2.2: Parameter values used for KNM1-5 analysis. For correlations between the parameters see [214, Tables 4 and 6] or Figure A.45.

Eloss parameter name	
$a_1(\mathrm{eV}^{-1})$	0.033 ± 0.001
$m_1(\mathrm{eV})$	11.919 ± 0.008
$\sigma_1(\mathrm{eV})$	0.184 ± 0.007
$a_2(\mathrm{eV}^{-1})$	0.296 ± 0.001
$m_2(\mathrm{eV})$	12.805 ± 0.002
$\sigma_2(\mathrm{eV})$	0.468 ± 0.002
$a_3(\mathrm{eV}^{-1})$	0.076 ± 0.000
$m_3(\mathrm{eV})$	14.968 ± 0.004
$\sigma_3(\mathrm{eV})$	0.907 ± 0.013

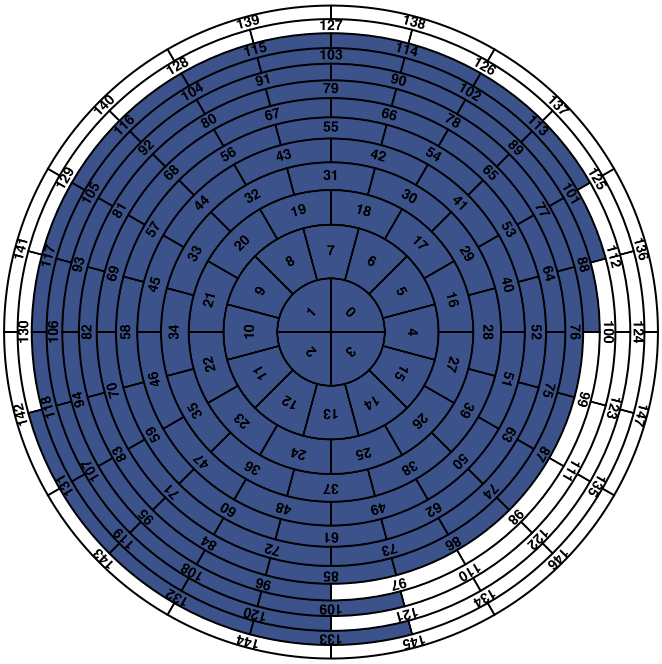

Figure A.56: Segmented pixel map of the focal-plane detector with the patch layout of the KNM1 campaign. White pixels are excluded from the analysis.

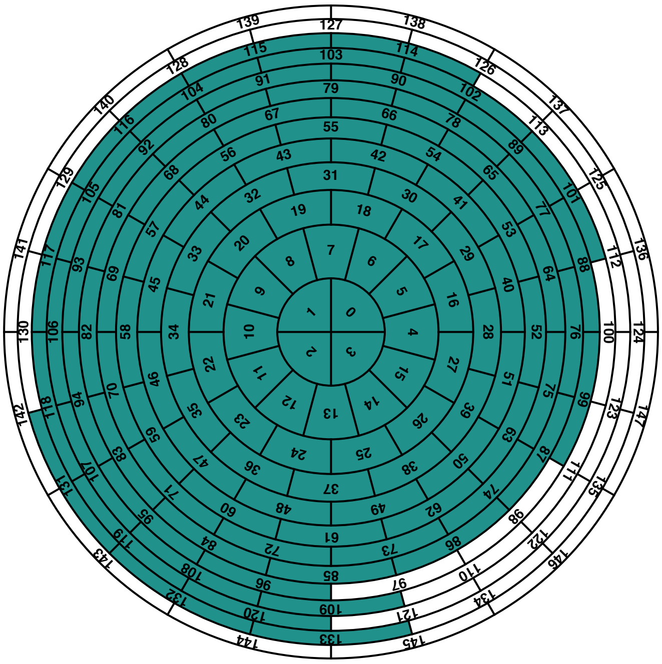

Figure A.57: Segmented pixel map of the focal-plane detector with the patch layout of the KNM2 campaign. White pixels are excluded from the analysis.

List of Figures

List of Tables

Bibliography

[1] G. Aad et al. “Observation of a new particle in the search for the Standard Model Higgs boson with the ATLAS detector at the LHC”. *Physics Letters B* 716(1) (Sept. 2012), pp. 1–29. DOI: 10.1016/j.physletb.2012.08.020.

[2] J. Abdurashitov et al. “Results from SAGE”. *Phys. Lett. B* 328 (1994), pp. 234–248. DOI: 10.1016/0370-2693(94)90454-5.

[3] J. Abdurashitov et al. “Measurement of the solar neutrino capture rate with gallium metal. III. Results for the 2002–2007 data-taking period”. *Physical Review C* 80(1) (July 2009), p. 015807. DOI: 10.1103/PhysRevC.80.015807.

[4] T. Abrahão et al. “Search for signatures of sterile neutrinos with Double Chooz”. *The European Physical Journal C* 81(8) (Aug. 2021), p. 775. DOI: 10.1140/epjc/s10052-021-09459-0.

[5] R. Acciarri et al. “A Proposal for a Three Detector Short-Baseline Neutrino Oscillation Program in the Fermilab Booster Neutrino Beam”. (Mar. 2015). DOI: 10.48550/arXiv.1503.01520.

[6] M. Acero et al. “White paper on light sterile neutrino searches and related phenomenology”. *Journal of Physics G: Nuclear and Particle Physics* 51(12) (Oct. 2024), p. 120501. DOI: 10.1088/1361-6471/ad307f.

[7] H. Acharya, M. Aker, D. Batzler, et al. “Measurement of the inhomogeneity of the KATRIN tritium source electric potential by high-resolution spectroscopy of conversion electrons from 83m-Kr”. (Mar. 2025). DOI: 10.48550/arXiv.2503.13221.

[8] S. Agostinelli, J. Allison, K. Amako, et al. “Geant4—a simulation toolkit”. *Nuclear Instruments and Methods in Physics Research Section A: Accelerators, Spectrometers, Detectors and Associated Equipment* 506(3) (2003), pp. 250–303. DOI: https://doi.org/10.1016/S0168-9002(03)01368-8.

[9] M. Agostini et al. “Toward the discovery of matter creation with neutrinoless $\beta\beta$ decay”. *Rev. Mod. Phys.* 95 (May 2023), p. 025002. DOI: 10.1103/RevModPhys.95.025002.

[10] A. Aguilar-Arevalo et al. “The MiniBooNE detector”. *Nuclear Instruments and Methods in Physics Research Section A: Accelerators, Spectrometers, Detectors and Associated Equipment* 599(1) (Feb. 2009), pp. 28–46. DOI: 10.1016/j.nima.2008.10.028.

[11] M. Aker, K. Altenmüller, A. Beglarian, et al. “Bound on $3+1$ Active-Sterile Neutrino Mixing from the First Four-Week Science Run of KATRIN”. *Phys. Rev. Lett.* 126 (Mar. 2021), p. 091803. DOI: 10.1103/PhysRevLett.126.091803.

[12] M. Aker, D. Batzler, A. Beglarian, et al. “Improved eV-scale sterile-neutrino constraints from the second KATRIN measurement campaign”. *Phys. Rev. D* 105 (Apr. 2022), p. 072004. DOI: 10.1103/PhysRevD.105.072004.

[13] M. Aker, A. Beglarian, J. Behrens, et al. “Direct neutrino-mass measurement with sub-electronvolt sensitivity”. *Nature Physics* 18(2) (Feb. 2022), pp. 160–166. DOI: 10.1038/s41567-021-01463-1.

[14] M. Aker et al. “Analysis methods for the first KATRIN neutrino-mass measurement”. *Phys. Rev. D* 104 (July 2021), p. 012005. DOI: 10.1103/PhysRevD.104.012005.

[15] M. Aker et al. “Measurement of the electric potential and the magnetic field in the shifted analysing plane of the KATRIN experiment”. *The European Physical Journal C* 84(12) (Dec. 2024). DOI: 10.1140/epjc/s10052-024-13596-7.

[16] M. Aker et al. “Suppression of Penning discharges between the KATRIN spectrometers”. *The European Physical Journal C* 80(9) (Sept. 2020). DOI: 10.1140/epjc/s10052-020-8278-y.

[17] M. Aker. “Tritium Sorption on the KATRIN Rear Wall: Effects, Dynamics and Mitigation”. PhD thesis. Karlsruher Institut für Technologie (KIT), Jan. 2025. DOI: 10.5445/IR/1000178375.

[18] M. Aker, K. Altenmüller, A. Beglarian, et al. “Quantitative Long-Term Monitoring of the Circulating Gases in the KATRIN Experiment Using Raman Spectroscopy”. *Sensors* 20(17) (Jan. 2020), p. 4827. DOI: 10.3390/s20174827.

[19] M. Aker, M. Sturm, F. Priester, et al. “In Situ Tritium Decontamination of the KATRIN Rear Wall Using an Ultraviolet/Ozone Treatment”. *Fusion Science and Technology* 80(3) (2024), p. 303. DOI: 10.1080/15361055.2023.2214695.

[20] ALEPH Collaboration et al. *Physics Reports* 427(5–6) (May 2006), pp. 257–454. DOI: 10.1016/j.physrep.2005.12.006.

[21] J. Allison, K. Amako, J. Apostolakis, et al. "Recent developments in Geant4". *Nuclear Instruments and Methods in Physics Research Section A: Accelerators, Spectrometers, Detectors and Associated Equipment* 835 (2016), pp. 186–225. DOI: https://doi.org/10.1016/j.nima.2016.06.125.

[22] H. Almazán et al. "STEREO neutrino spectrum of ^{235}U fission rejects sterile neutrino hypothesis". *Nature* 613(7943) (2023), pp. 257–261. DOI: 10.1038/s41586-022-05568-2.

[23] J. Amsbaugh, J. Barrett, A. Beglarian, et al. "Focal-plane detector system for the KATRIN experiment". *Nuclear Instruments and Methods in Physics Research Section A: Accelerators, Spectrometers, Detectors and Associated Equipment* 778 (2015), pp. 40–60. DOI: 10.1016/j.nima.2014.12.116.

[24] F. P. An et al. "Improved Search for a Light Sterile Neutrino with the Full Configuration of the Daya Bay Experiment". *Phys. Rev. Lett.* 117 (Oct. 2016), p. 151802. DOI: 10.1103/PhysRevLett.117.151802.

[25] R. Andrae, T. Schulze-Hartung, and P. Melchior. "Dos and don'ts of reduced chi-squared". (Dec. 2010). DOI: 10.48550/arXiv.1012.3754.

[26] M. Andriamirado et al. "Final Search for Short-Baseline Neutrino Oscillations with the PROSPECT-I Detector at HFIR". *Phys. Rev. Lett.* 134 (Apr. 2025), p. 151802. DOI: 10.1103/PhysRevLett.134.151802.

[27] M. Arenz et al. "Reduction of stored-particle background by a magnetic pulse method at the KATRIN experiment". *The European Physical Journal C* 78(9) (Sept. 2018). DOI: 10.1140/epjc/s10052-018-6244-8.

[28] M. Arenz et al. "The KATRIN Superconducting Magnets: Overview and First Performance Results". *Journal of Instrumentation* 13(08) (Aug. 2018), T08005–T08005. DOI: 10.1088/1748-0221/13/08/T08005.

[29] C. Argüelles et al. "Snowmass white paper: beyond the standard model effects on neutrino flavor". *The European Physical Journal C* 83(1) (Jan. 2023), p. 15. DOI: 10.1140/epjc/s10052-022-11049-7.

[30] M. Asai, M. Cortés-Giraldo, V. Giménez-Alventosa, et al. "The PENELOPE Physics Models and Transport Mechanics. Implementation into Geant4". *Frontiers in Physics* 9 (2021), p. 738735. DOI: 10.3389/fphy.2021.738735.

[31] V. Aseev, A. Belesev, A. Berlev, et al. "Upper limit on the electron antineutrino mass from the Troitsk experiment". *Phys. Rev. D* 84 (Dec. 2011), p. 112003. DOI: 10.1103/PhysRevD.84.112003.

[32] A. Ashtari Esfahani, M. Betancourt, Z. Bogorad, et al. "Bayesian analysis of a future β decay experiment's sensitivity to neutrino mass scale and ordering". *Phys. Rev. C* 103 (June 2021), p. 065501. DOI: 10.1103/PhysRevC.103.065501.

[33] C. Athanassopoulos et al. "The liquid scintillator neutrino detector and LAMPF neutrino source". *Nuclear Instruments and Methods in Physics Research Section A: Accelerators, Spectrometers, Detectors and Associated Equipment* 388(1) (Mar. 1997), pp. 149–172. DOI: 10.1016/S0168-9002(96)01155-2.

[34] J. Aubert et al. "Experimental Observation of a Heavy Particle J". *Physical Review Letters* 33(23) (Dec. 1974), pp. 1404–1406. DOI: 10.1103/PhysRevLett.33.1404.

[35] M. Babutzka. "Design and development for the Rearsection of the KATRIN experiment". PhD thesis. Karlsruher Institut für Technologie (KIT), 2014. DOI: 10.5445/IR/1000045598.

[36] J. Bahcall. "Solar Neutrinos. I. Theoretical". *Physical Review Letters* 12(11) (Mar. 1964), pp. 300–302. DOI: 10.1103/PhysRevLett.12.300.

[37] J. Bahcall et al. "Standard solar models and the uncertainties in predicted capture rates of solar neutrinos". *Reviews of Modern Physics* 54(3) (July 1982), pp. 767–799. DOI: 10.1103/RevModPhys.54.767.

[38] V. Barinov et al. "Results from the Baksan Experiment on Sterile Transitions (BEST)". *Phys. Rev. Lett.* 128(23) (2022), p. 232501. DOI: 10.1103/PhysRevLett.128.232501.

[39] V. Barinov et al. "Search for electron-neutrino transitions to sterile states in the BEST experiment". *Phys. Rev. C* 105(6) (2022), p. 065502. DOI: 10.1103/PhysRevC.105.065502.

[40] T. Bayes and n. Price. "LII. An essay towards solving a problem in the doctrine of chances. By the late Rev. Mr. Bayes, F. R. S. communicated by Mr. Price, in a letter to John Canton, A. M. F. R. S". *Philosophical Transactions of the Royal Society of London* 53 (Jan. 1997), pp. 370–418. DOI: 10.1098/rstl.1763.0053.

[41] G. Beamson, H. Porter, and D. Turner. "The collimating and magnifying properties of a superconducting field photoelectron spectrometer". *Journal of Physics E: Scientific Instruments* 13(1) (Jan. 1980), p. 64. DOI: 10.1088/0022-3735/13/1/018.

[42] A. Beglarian et al. "Forward Beam Monitor for the KATRIN experiment". *Journal of Instrumentation* 17(03) (2022), T03002. DOI: 10.1088/1748-0221/17/03/T03002.

[43] J. Behrens et al. "A pulsed, mono-energetic and angular-selective UV photo-electron source for the commissioning of the KATRIN experiment". *The European Physical Journal C* 77(6) (June 2017). DOI: 10.1140/epjc/s10052-017-4972-9.

[44] J. Behrens. “Design and commissioning of a monoenergetic photoelectron source and active background reduction by magnetic pulse at the KATRIN experiment”. Ph.D. thesis. Westfälische Wilhelms-Universität Münster, 2016. URL: https://www.katrin.kit.edu/publikationen/phd%5C_behrens.pdf (visited on 06/08/2025).

[45] S. Bilenky and B. Pontecorvo. “Lepton mixing and neutrino oscillations”. *Physics Reports* 41(4) (1978), pp. 225–261. DOI: https://doi.org/10.1016/0370-1573(78)90095-9.

[46] S. M. Bilenky, C. Giunti, and W. Grimus. “Neutrino mass spectrum from the results of neutrino oscillation experiments”. *The European Physical Journal C* 1(1–2) (Mar. 1998), pp. 247–253. DOI: 10.1007/bf01245814.

[47] S. Bilenky and S. Petcov. “Massive Neutrinos and Neutrino Oscillations”. *Rev. Mod. Phys.* 59 (1987), p. 671. DOI: 10.1103/RevModPhys.59.671.

[48] F. Block. “Determination of Electromagnetic Fields and Tritium Column Density for Neutrino Mass Analysis with KATRIN”. PhD thesis. Karlsruher Institut für Technologie (KIT), 2022. DOI: 10.5445/IR/1000145073.

[49] L. Bodine, D. Parno, and R. Robertson. “Assessment of molecular effects on neutrino mass measurements from tritium β decay”. *Physical Review C* 91(3) (Mar. 2015), p. 035505. DOI: 10.1103/PhysRevC.91.035505.

[50] S. Böser, C. Buck, C. Giunti, et al. “Status of light sterile neutrino searches”. *Progress in Particle and Nuclear Physics* 111 (2020), p. 103736. DOI: https://doi.org/10.1016/j.ppnp.2019.103736.

[51] A. Brazzale and V. Mameli. “Likelihood Asymptotics in Nonregular Settings: A Review with Emphasis on the Likelihood Ratio”. *Statistical Science* 39(2) (May 2024), pp. 322–345. DOI: 10.1214/23-STS910.

[52] R. Brun and F. Rademakers. “ROOT: An object oriented data analysis framework”. *Nucl. Instrum. Meth. A* 389 (1997). Ed. by M. Werlen and D. Perret-Gallix, pp. 81–86. DOI: 10.1016/S0168-9002(97)00048-X.

[53] J. Buchner. “A statistical test for Nested Sampling algorithms”. *Statistics and Computing* 26(1) (Jan. 2016), pp. 383–392. DOI: 10.1007/s11222-014-9512-y.

[54] J. Buchner. “Collaborative Nested Sampling: Big Data versus Complex Physical Models”. *Publications of the Astronomical Society of the Pacific* 131(1004) (Aug. 2019), p. 108005. DOI: 10.1088/1538-3873/aae7fc.

[55] J. Buchner. *JohannesBuchner/UltraNest*. Apr. 2025. URL: https://github.com/JohannesBuchner/UltraNest (visited on 05/16/2025).

[56] A. Caldwell, M. Ettengruber, A. Merle, et al. “Global Bayesian analysis of neutrino mass data”. *Phys. Rev. D* 96(7) (2017), p. 073001. DOI: 10.1103/PhysRevD.96.073001.

[57] T. Caldwell et al. *ORCA: Control and DAQ Software*. 2024. URL: https://github.com/unc-enap/Orca (visited on 06/08/2025).

[58] M. Carminati et al. “The TRISTAN 166-pixel detector: Preliminary results with a planar setup”. *Nuclear Instruments and Methods in Physics Research Section A: Accelerators, Spectrometers, Detectors and Associated Equipment* 1049 (Apr. 2023), p. 168046. DOI: 10.1016/j.nima.2023.168046.

[59] G. Casella and R. Berger. *Statistical Inference*. 2nd. Pacific Grove, CA: Duxbury Press, 2002.

[60] S. Chatrchyan et al. “Observation of a new boson at a mass of 125 GeV with the CMS experiment at the LHC”. *Physics Letters B* 716(1) (Sept. 2012), pp. 30–61. DOI: 10.1016/j.physletb.2012.08.021.

[61] D. Cianci et al. “Prospects of light sterile neutrino oscillation and CP violation searches at the Fermilab Short Baseline Neutrino Facility”. *Physical Review D* 96(5) (Sept. 2017), p. 055001. DOI: 10.1103/PhysRevD.96.055001.

[62] C. Clenshaw and A. Curtis. “A method for numerical integration on an automatic computer”. *Numerische Mathematik* 2(1) (Dec. 1960), pp. 197–205. DOI: 10.1007/BF01386223.

[63] B. Cleveland et al. “Measurement of the Solar Electron Neutrino Flux with the Homestake Chlorine Detector”. *The Astrophysical Journal* 496(1) (Mar. 1998), p. 505. DOI: 10.1086/305343.

[64] C. Collaboration. “With or without ν? Hunting for the seed of the matter-antimatter asymmetry”. (Apr. 2024). DOI: 10.48550/arXiv.2404.04453.

[65] K. Collaboration. *KATRIN Design Report 2004*. Tech. rep. Karlsruhe Institute of Technology (KIT), Jan. 2005. URL: https://www.katrin.kit.edu/publikationen/DesignReport2004-12Jan2005.pdf (visited on 06/08/2025).

[66] M. collaboration et al. “First constraints on light sterile neutrino oscillations from combined appearance and disappearance searches with the MicroBooNE detector”. *Physical Review Letters* 130(1) (Jan. 2023), p. 011801. DOI: 10.1103/PhysRevLett.130.011801.

[67] T. collaboration, M. Aker, K. Altenmüller, et al. “The design, construction, and commissioning of the KATRIN experiment”. *Journal of Instrumentation* 16(08) (Aug. 2021), T08015. DOI: 10.1088/1748-0221/16/08/T08015.

[68] T. Collaboration. *TRISTAN Technical Design Report*. Tech. rep. Karlsruhe Institute of Technology (KIT), 2020. URL: https://www.katrin.kit.edu/downloads/TRISTAN%5C_%5C_Technical%5C_Design%5C_Report%5C%20(10).pdf (visited on 06/08/2025).

[69] C. Cowan et al. "Detection of the Free Neutrino: a Confirmation". *Science* 124(3212) (July 1956), pp. 103–104. DOI: 10.1126/science.124.3212.103.

[70] G. Cowan. *Statistical Data Analysis*. Oxford University Press, 1998.

[71] G. Danby et al. "Observation of High-Energy Neutrino Reactions and the Existence of Two Kinds of Neutrinos". *Physical Review Letters* 9(1) (July 1962), pp. 36–44. DOI: 10.1103/PhysRevLett.9.36.

[72] B. Dasgupta and J. Kopp. "Sterile neutrinos". *Physics Reports* 928 (Sept. 2021), pp. 1–63. DOI: 10.1016/j.physrep.2021.06.002.

[73] R. Davis, D. Harmer, and K. Hoffman. "Search for Neutrinos from the Sun". *Physical Review Letters* 20(21) (May 1968), pp. 1205–1209. DOI: 10.1103/PhysRevLett.20.1205.

[74] J.-P. Dedieu. "Newton-Raphson Method". *Encyclopedia of Applied and Computational Mathematics*. Ed. by B. Engquist. Berlin, Heidelberg: Springer Berlin Heidelberg, 2015, pp. 1023–1028. DOI: 10.1007/978-3-540-70529-1_374.

[75] M. Dentler et al. "Updated global analysis of neutrino oscillations in the presence of eV-scale sterile neutrinos". *Journal of High Energy Physics* 2018(8) (Aug. 2018), p. 10. DOI: 10.1007/JHEP08(2018)010.

[76] M. Descher. "Differential spectrum modeling and sensitivity for keV sterile neutrino search at KATRIN". phd. Karlsruhe Institute of Technology, 2024. DOI: 10.5445/IR/1000166956.

[77] A. Diaz et al. "Where are we with light sterile neutrinos?" *Physics Reports* 884 (Nov. 2020), pp. 1–59. DOI: 10.1016/j.physrep.2020.08.005.

[78] N. Doss and J. Tennyson. "Excitations to the electronic continuum of 3HeT+ in investigations of T2 β-decay experiments". *Journal of Physics B: Atomic, Molecular and Optical Physics* 41(12) (June 2008), p. 125701. DOI: 10.1088/0953-4075/41/12/125701.

[79] N. Doss, J. Tennyson, A. Saenz, et al. "Molecular effects in investigations of tritium molecule $\beta-$ decay endpoint experiments". *Physical Review C* 73 (Feb. 2006), p. 025502. DOI: 10.1103/PhysRevC.73.025502.

[80] O. Dragoun et al. "Feasibility of photoelectron sources with sharp lines of stable energy between 20 and 80keV". *Applied Radiation and Isotopes* 69(4) (2011), pp. 672–677. DOI: https://doi.org/10.1016/j.apradiso.2010.12.015.

[81] DUNE Collaboration. "Deep Underground Neutrino Experiment (DUNE) Near Detector Conceptual Design Report". *Instruments* 5(4) (2021). DOI: 10.3390/instruments5040031.

[82] S. Dyba. "Background reduction by the inner wire electrode and set-up of the condensed krypton source at the neutrino mass experiment KATRIN". PhD thesis. Westfälische Wilhelms-Universität Münster, 2019. URL: https://www.deutsche-digitale-bibliothek.de/item/BR44O3QIXVBDMKTLYN3K4HM22QWBINKA (visited on 06/06/2025).

[83] E. Ellinger. "Development and investigation of the forward beam monitor for the KATRIN experiment". PhD thesis. Wuppertal, Germany: Bergische Universität Wuppertal, 2019. DOI: 10.25926/r160-7a40.

[84] S. Elliott, V. Gavrin, and W. Haxton. "The gallium anomaly". *Progress in Particle and Nuclear Physics* 134 (2024), p. 104082. DOI: 10.1016/j.ppnp.2023.104082.

[85] S. Enomoto. *FPD analysis". In: 40th KATRIN Collaboration Meeting (2021)*. 2021. URL: https://iap-katrin-wiki.iap.kit.edu/katrin/images/7/77/FPD-210308v3.pdf (visited on 06/08/2025).

[86] M. Erhard, J. Behrens, S. Bauer, et al. "Technical design and commissioning of the KATRIN large-volume air coil system". *Journal of Instrumentation* 13(02) (Feb. 2018), P02003. DOI: 10.1088/1748-0221/13/02/P02003.

[87] E. Fermi. "Versuch einer Theorie der β-Strahlen. I". *Zeitschrift für Physik* 88(3–4) (Mar. 1934), pp. 161–177. DOI: 10.1007/bf01351864.

[88] E. Fermi. "Tentativo di una Teoria Dei Raggi". *Il Nuovo Cimento (1924-1942)* 11(1) (Jan. 1934), pp. 1–19. DOI: 10.1007/BF02959820.

[89] R. Feynman and M. Gell-Mann. "Theory of the Fermi Interaction". *Physical Review* 109(1) (Jan. 1958), pp. 193–198. DOI: 10.1103/PhysRev.109.193.

[90] S. Fischer, M. Sturm, M. Schlösser, et al. "Laser Raman Spectroscopy for KATRIN". *Nuclear Physics B - Proceedings Supplements* 229-232 (Aug. 2012), p. 492. DOI: 10.1016/j.nuclphysbps.2012.09.129.

[91] A. Fowlie. "The Bayes factor surface for searches for new physics". *The European Physical Journal C* 84(4) (Apr. 2024), p. 426. DOI: 10.1140/epjc/s10052-024-12792-9.

[92] F. Fraenkle. "Background processes in the KATRIN main spectrometer". *Journal of Physics: Conference Series* 888 (Sept. 2017), p. 012070. DOI: 10.1088/1742-6596/888/1/012070.

[93] F. Fränkle, A. Lokhov, and X. Stribl. *An updated model for the Penning background in KNM1-5 neutrino mass analysis*. 2024. URL: https://iap-katrin-wiki.iap.kit.edu/katrin/images/6/64/Penning%5C_tech%5C_report.pdf (visited on 06/08/2025).

[94] F. Fränkle et al. "Radon induced background processes in the KATRIN pre-spectrometer". *Astroparticle Physics* 35(3) (2011), pp. 128–134. DOI: https://doi.org/10.1016/j.astropartphys.2011.06.009.

[95] F. Friedel. "Ion and plasma systematics during the first KATRIN neutrino mass measurements". PhD thesis. Karlsruher Institut für Technologie (KIT), 2020. DOI: 10.5445/IR/1000126837.

[96] H. Fritsch and P. Minkowski. "Vectorlike weak currents, massive neutrinos, and neutrino beam oscillations". *Physics Letters B* 62(1) (May 1976), pp. 72–76. DOI: 10.1016/0370-2693(76)90051-4.

[97] D. Furse, S. Groh, N. Trost, et al. "Kassiopeia: a modern, extensible C++ particle tracking package". *New Journal of Physics* 19(5) (May 2017), p. 053012. DOI: 10.1088/1367-2630/aa6950.

[98] J. Geiger. "Streuung von 25 keV-Elektronen an Gasen". *Zeitschrift für Physik* 181(4) (Aug. 1964), pp. 413–425. DOI: 10.1007/BF01380873.

[99] T. Geigle. "First Simulations of a Micro-structured Rear Wall for the KATRIN experiment". MA thesis. Karlsruhe, Germany: Karlsruhe Institute of Technology, 2024. URL: https://www.katrin.kit.edu/publikationen/mth%5C_geigle.pdf (visited on 06/08/2025).

[100] A. Gelman et al. *Bayesian Data Analysis*. Third. CRC Press, 2013.

[101] GERDA Collaboration. "Final Results of GERDA on the Search for Neutrinoless Double-β Decay". *Physical Review Letters* 125(25) (Dec. 2020), p. 252502. DOI: 10.1103/PhysRevLett.125.252502.

[102] C. Giunti, Y. Li, and Y. Zhang. "KATRIN bound on 3+1 active-sterile neutrino mixing and the reactor antineutrino anomaly". *JHEP* 05 (2020), p. 061. DOI: 10.1007/JHEP05(2020)061.

[103] C. Giunti and E. M. Zavanin. "Predictions for neutrinoless double-beta decay in the 3+1 sterile neutrino scenario". *Journal of High Energy Physics* 2015(7) (Aug. 2015), p. 171. DOI: 10.1007/JHEP07(2015)171.

[104] C. Giunti et al. "Reactor antineutrino anomaly in light of recent flux model refinements". *Physics Letters B* 829 (June 2022), p. 137054. DOI: 10.1016/j.physletb.2022.137054.

[105] C. Giunti and C. Kim. *Fundamentals of Neutrino Physics and Astrophysics*. Oxford University Press, 2007. DOI: 10.1093/acprof:oso/9780198508717.001.0001.

[106] C. Giunti and T. Lasserre. "eV-Scale Sterile Neutrinos". *Annual Review of Nuclear and Particle Science* 69(Volume 69, 2019) (Oct. 2019), pp. 163–190. DOI: 10.1146/annurev-nucl-101918-023755.

[107] C. Giunti and M. Laveder. "Status of 3+1 Neutrino Mixing". *Physical Review D* 84(9) (Nov. 2011), p. 093006. DOI: 10.1103/PhysRevD.84.093006.

[108] F. Glück, G. Drexlin, B. Leiber, et al. "Electromagnetic design of the large-volume air coil system of the KATRIN experiment". *New Journal of Physics* 15(8) (Aug. 2013), p. 083025. DOI: 10.1088/1367-2630/15/8/083025.

[109] M. Goldhaber, L. Grodzins, and A. Sunyar. "Helicity of Neutrinos". *Physical Review* 109(3) (Feb. 1958), pp. 1015–1017. DOI: 10.1103/PhysRev.109.1015.

[110] J. Goldstone, A. Salam, and S. Weinberg. "Broken Symmetries". *Physical Review* 127(3) (Aug. 1962), pp. 965–970. DOI: 10.1103/PhysRev.127.965.

[111] V. Gribov and B. Pontecorvo. "Neutrino astronomy and lepton charge". *Physics Letters B* 28(7) (Jan. 1969), pp. 493–496. DOI: 10.1016/0370-2693(69)90525-5.

[112] S. Groh. "Modeling of the response function and measurement of transmission properties of the KATRIN experiment". PhD thesis. Karlsruher Institut für Technologie (KIT), 2015. DOI: 10.5445/IR/1000046546.

[113] P. D. Group et al. "Review of Particle Physics". *Progress of Theoretical and Experimental Physics* 2022(8) (Aug. 2022), p. 083C01. DOI: 10.1093/ptep/ptac097.

[114] W. Hampel et al. "Final results of the 51Cr neutrino source experiments in GALLEX". *Physics Letters B* 420(1) (Feb. 1998), pp. 114–126. DOI: 10.1016/S0370-2693(97)01562-1.

[115] W. Hampel et al. "GALLEX solar neutrino observations: results for GALLEX IV". *Physics Letters B* 447(1) (Feb. 1999), pp. 127–133. DOI: 10.1016/S0370-2693(98)01579-2.

[116] F. Hasert et al. "Observation of neutrino-like interactions without muon or electron in the gargamelle neutrino experiment". *Physics Letters B* 46(1) (Sept. 1973), pp. 138–140. DOI: 10.1016/0370-2693(73)90499-1.

[117] F. Heizmann. "Analysis tools and methods for tritium data taking with the KATRIN experiment". PhD thesis. Karlsruher Institut für Technologie (KIT), 2019. 248 pp. DOI: 10.5445/IR/1000093536.

[118] S. Hickford, L. Köllenberger, and W. Xu. "Optimization-based Bayesian sensitivity on neutrino mass and constraints on cosmology with the KATRIN experiment". 2023. URL: https://publikationen.bibliothek.kit.edu/1000156024 (visited on 05/09/2025).

[119] P. Higgs. “Broken Symmetries and the Masses of Gauge Bosons”. *Physical Review Letters* 13(16) (Oct. 1964), pp. 508–509. DOI: 10.1103/PhysRevLett.13.508.

[120] K. Hirata et al. “Observation of ^{8}B Solar Neutrinos in the Kamiokande-II Detector”. *Physical Review Letters* 63(1) (July 1989), pp. 16–19. DOI: 10.1103/PhysRevLett.63.16.

[121] M. Howe et al. *ORCA: Object-oriented Real-time Control and Acquisition*. 2024. URL: http://orca.physics.unc.edu (visited on 06/08/2025).

[122] Z. Hu et al. “Global oscillation data analysis on the 3ν mixing without unitarity”. *Journal of High Energy Physics* 2021(1) (Jan. 2021), p. 124. DOI: 10.1007/JHEP01(2021)124.

[123] P. Huber. “Determination of antineutrino spectra from nuclear reactors”. *Physical Review C* 84(2) (Aug. 2011), p. 024617. DOI: 10.1103/PhysRevC.84.024617.

[124] P. Huber and E. Ronchetti. *Robust Statistics*. 2nd ed. John Wiley & Sons, 2009.

[125] K. Hugenberg. “An angular resolved pulsed UV LED photoelectron source for KATRIN”. *Progress in Particle and Nuclear Physics* 64(2) (2010), pp. 288–290. DOI: https://doi.org/10.1016/j.ppnp.2009.12.031.

[126] J. Hunter. “Matplotlib: A 2D graphics environment”. *Computing in Science & Engineering* 9(3) (2007), pp. 90–95. DOI: 10.1109/MCSE.2007.55.

[127] M. INOKUTI. “Inelastic Collisions of Fast Charged Particles with Atoms and Molecules—The Bethe Theory Revisited”. *Reviews of Modern Physics* 43(3) (July 1971), pp. 297–347. DOI: 10.1103/RevModPhys.43.297.

[128] E. Jaynes. *Probability theory: The logic of science*. Cambridge: Cambridge University Press, 2003.

[129] H. Jeffreys. “An invariant form for the prior probability in estimation problems”. *Proceedings of the Royal Society of London. Series A. Mathematical and Physical Sciences* 186(1007) (1946), pp. 453–461. DOI: 10.1098/rspa.1946.0056.

[130] H. Jeffreys. *The Theory of Probability*. 3rd ed. Oxford University Press, 1961.

[131] S. Jonsell, A. Saenz, and P. Froelich. “Neutrino-mass determination from tritium β decay: Corrections to and prospects of experimental verification of the final-state spectrum”. *Physical Review C* 60(3) (July 1999), p. 034601. DOI: 10.1103/PhysRevC.60.034601.

[132] KamLAND-Zen Collaboration. “Search for the Majorana Nature of Neutrinos in the Inverted Mass Ordering Region with KamLAND-Zen”. *Physical Review Letters* 130(5) (Jan. 2023), p. 051801. DOI: 10.1103/PhysRevLett.130.051801.

[133] C. Karl, P. Eller, and S. Mertens. “Fast and precise model calculation for KATRIN using a neural network”. *The European Physical Journal C* 82(5) (May 2022), p. 439. DOI: 10.1140/epjc/s10052-022-10384-z.

[134] KARMEN Collaboration et al. “Upper Limits for Neutrino Oscillations $\overline{\nu}\_\mu \to \overline{\nu}\_e$ from Muon Decay at Rest”. *Physical Review D* 65(11) (June 2002), p. 112001. DOI: 10.1103/PhysRevD.65.112001.

[135] KATRIN Collaboration. “Direct neutrino-mass measurement based on 259 days of KATRIN data”. *Science* 388(6743) (Apr. 2025), pp. 180–185. DOI: 10.1126/science.adq9592.

[136] KATRIN Collaboration. “Improved Upper Limit on the Neutrino Mass from a Direct Kinematic Method by KATRIN”. *Physical Review Letters* 123(22) (Nov. 2019), p. 221802. DOI: 10.1103/PhysRevLett.123.221802.

[137] KATRIN Collaboration. “Sterile-neutrino search based on 259 days of KATRIN data”. (Mar. 2025). DOI: 10.48550/arXiv.2503.18667.

[138] KATRIN Experiment. *Kassiopeia: The KATRIN Simulation Tool*. 2025. URL: https://katrin-experiment.github.io/Kassiopeia/index.html (visited on 06/08/2025).

[139] J. Kellerer. “Simulation of the KATRIN Source Plasma using Monte Carlo and Particle in Cell Methods”. PhD thesis. Karlsruher Institut für Technologie (KIT), Mar. 2022. DOI: 10.5445/IR/1000143868.

[140] K. Kelly and J. Kopp. “More Ingredients for an Altarelli Cocktail at MiniBooNE”. *Journal of High Energy Physics* 2023(5) (May 2023), p. 113. DOI: 10.1007/JHEP05(2023)113.

[141] T. Kibble. “Symmetry Breaking in Non-Abelian Gauge Theories”. *Physical Review* 155(5) (Mar. 1967), pp. 1554–1561. DOI: 10.1103/PhysRev.155.1554.

[142] S. Kim, M. Pia, T. Basaglia, et al. “Validation Test of Geant4 Simulation of Electron Backscattering”. *arXiv preprint arXiv:1502.01507* (2015). URL: https://arxiv.org/abs/1502.01507 (visited on 06/08/2025).

[143] Y.-K. Kim and M. Rudd. “Binary-encounter-dipole model for electron-impact ionization”. *Physical Review A* 50(5) (Nov. 1994), pp. 3954–3967. DOI: 10.1103/PhysRevA.50.3954.

[144] M. Kleesiek, J. Behrens, G. Drexlin, et al. “β-Decay spectrum, response function and statistical model for neutrino mass measurements with the KATRIN experiment”. *The European Physical Journal C* 79(3) (Mar. 2019), p. 204. DOI: 10.1140/epjc/s10052-019-6686-7.

[145] M. Kleesiek. “A Data-Analysis and Sensitivity-Optimization Framework for the KATRIN Experiment”. PhD thesis. Karlsruher Institut für Technologie (KIT), 2014. DOI: 10.5445/IR/1000043301.

[146] M. Klein. “Tritium ions in KATRIN: blocking, removal and detection”. PhD thesis. Karlsruher Institut für Technologie (KIT), 2019. DOI: 10.5445/IR/1000093526.

[147] K. Kodama et al. “Observation of tau neutrino interactions”. *Physics Letters B* 504(3) (Apr. 2001), pp. 218–224. DOI: 10.1016/S0370-2693(01)00307-0.

[148] O. Kofoed-Hansen. “Maximum β-Energies and the Mass of the Neutrino”. *Physical Review* 71(7) (Apr. 1947), pp. 451–452. DOI: 10.1103/PhysRev.71.451.

[149] C. Köhler. “Determination of the Column Density in the KATRIN Beamline with a Monoenergetic Electron Source”. Master’s thesis. Technical University of Munich, 2019. URL: https://www.ph.nat.tum.de/fileadmin/w00bya/neutrinos/Thesis/Master/KATRIN%5C_Koehler%5C_Christoph%5C_19.pdf (visited on 06/08/2025).

[150] W. Kol/os, H. Monkhorst, and K. Szalewicz. “Energy unresolved differential cross section for electron scattering by H2”. *The Journal of Chemical Physics* 77(3) (Aug. 1982), pp. 1323–1334. DOI: 10.1063/1.443955.

[151] L. Köllenberger. “Combined neutrino-mass analysis of the first five KATRIN science runs”. PhD thesis. Karlsruher Institut für Technologie (KIT), 2024. 223 pp. DOI: 10.5445/IR/1000170238.

[152] H. Kramers. “XCIII. On the theory of X-ray absorption and of the continuous X-ray spectrum”. *The London, Edinburgh, and Dublin Philosophical Magazine and Journal of Science* 46(275) (1923), pp. 836–871. DOI: 10.1080/14786442308565244.

[153] C. Kraus, B. Bornschein, L. Bornschein, et al. “Final results from phase II of the Mainz neutrino mass search in tritium β decay”. *The European Physical Journal C - Particles and Fields* 40(4) (Apr. 2005), pp. 447–468. DOI: 10.1140/epjc/s2005-02139-7.

[154] L. Kuckert. “The Windowless Gaseous Tritium Source of the KATRIN Experiment - Characterisation of Gas Dynamical and Plasma Properties”. PhD thesis. Karlsruher Institut für Technologie (KIT), 2016. 296 pp. DOI: 10.5445/IR/1000065077.

[155] B. Lambert. *A Student’s Guide to Bayesian Statistics*. SAGE Publications Ltd, 2018.

[156] L. Landau. “On the conservation laws for weak interactions”. *Nuclear Physics* 3(1) (Mar. 1957), pp. 127–131. DOI: 10.1016/0029-5582(57)90061-5.

[157] J. Lange. “nautilus: boosting Bayesian importance nested sampling with deep learning”. *Monthly Notices of the Royal Astronomical Society* 525(2) (Aug. 2023), pp. 3181–3194. DOI: 10.1093/mnras/stad2441.

[158] L. Langer and R. Moffat. “The Beta-Spectrum of Tritium and the Mass of the Neutrino”. *Physical Review* 88(4) (Nov. 1952), pp. 689–694. DOI: 10.1103/PhysRev.88.689.

[159] P. Lee. *Bayesian Statistics: An Introduction*. 4th. Wiley, 2012.

[160] T. Lee and C. Yang. “Parity Nonconservation and a Two-Component Theory of the Neutrino”. *Physical Review* 105(5) (Mar. 1957), pp. 1671–1675. DOI: 10.1103/PhysRev.105.1671.

[161] T. Lee and C. Yang. “Question of Parity Conservation in Weak Interactions”. *Physical Review* 104(1) (Oct. 1956), pp. 254–258. DOI: 10.1103/PhysRev.104.254.

[162] J. Liu. “Total Cross Sections for High-Energy Electron Scattering by H_2 ($^1\Sigma^+\_g$), N_2 ($^1\Sigma^+\_g$), and O_2 ($^3\Sigma^-\_g$)”. *Physical Review A* 35(2) (Jan. 1987), pp. 591–597. DOI: 10.1103/PhysRevA.35.591.

[163] J. Liu. “Total Inelastic Cross Section for Collisions of H_2 with Fast Charged Particles”. *Physical Review A* 7(1) (Jan. 1973), pp. 103–109. DOI: 10.1103/PhysRevA.7.103.

[164] V. Lobashev and P. Spivak. “A method for measuring the electron antineutrino rest mass”. *Nuclear Instruments and Methods in Physics Research Section A: Accelerators, Spectrometers, Detectors and Associated Equipment* 240(2) (Oct. 1985), pp. 305–310. DOI: 10.1016/0168-9002(85)90640-0.

[165] A. Lokhov, B. Bieringer, G. Drexlin, et al. “Background reduction at the KATRIN experiment by the shifted analysing plane configuration”. *The European Physical Journal C* 82(3) (Mar. 2022), p. 258. DOI: 10.1140/epjc/s10052-022-10220-4.

[166] A. Lokhov and C. Silva. *RW backscattering for m^2*. 2024. URL: https://iap-katrin-wiki.iap.kit.edu/katrin/images/0/05/2024-12-18-RW%5C_backscattering%5C_for%5C_m2.pdf (visited on 06/08/2025).

[167] A. Lokhov and C. Wiesinger. *Neutrino mass analysis*. 2025. URL: https://indico.kit.edu/event/4844/contributions/19353/attachments/8876/14872/2025-03-18-Mnu-Analysis-overview-CM48.pdf (visited on 06/08/2025).

[168] LSND Collaboration et al. “Evidence for Neutrino Oscillations from the Observation of $\overline{\nu}\_e$ Appearance in a $\overline{\nu}\_\mu$ Beam”. *Physical Review D* 64(11) (Nov. 2001), p. 112007. DOI: 10.1103/PhysRevD.64.112007.

[169] L. Lucas and M. Unterweger. "Comprehensive Review and Critical Evaluation of the Half-Life of Tritium". *Journal of Research of the National Institute of Standards and Technology* 105(4) (2000), pp. 541–549. DOI: 10.6028/jres.105.043.

[170] M. Machatschek. "A Phenomenological Theory of KATRIN Source Potential Systematics and its Application in Krypton-83m Calibration Measurements". PhD thesis. Karlsruher Institut für Technologie (KIT), May 2021. DOI: 10.5445/IR/1000132391.

[171] I. Machikhiliyan. "The DANSS Neutrino Spectrometer: the Results of Reactor Antineutrino Studies". *Phys. Part. Nucl.* 53(2) (2022), pp. 546–551. DOI: 10.1134/S1063779622020502.

[172] Z. Maki, M. Nakagawa, and S. Sakata. "Remarks on the Unified Model of Elementary Particles". *Progress of Theoretical Physics* 28(5) (Nov. 1962), pp. 870–880. DOI: 10.1143/PTP.28.870.

[173] A. Marsteller, M. Battcher, B. Bornschein, et al. "Operation modes of the KATRIN experiment Tritium Loop System using $^{83\mathrm{m}}$Kr". *Journal of Instrumentation* 17(12) (Dec. 2022), P12010. DOI: 10.1088/1748-0221/17/12/P12010.

[174] E. Martin. "Electron Detection Systems for KATRIN Detector and Spectrometer Section". (Aug. 2017). URL: http://hdl.handle.net/1773/40285 (visited on 06/08/2025).

[175] M. Matsuyama, Y. Torikai, M. Hara, et al. "New technique for non-destructive measurements of tritium in future fusion reactors". *Nuclear Fusion* 47(7) (2007), S464. DOI: 10.1088/0029-5515/47/7/S09.

[176] M. Matsuyama, T. Murai, and K. Watanabe. "Quantitative measurement of surface tritium by β-ray-induced X-ray spectrometry (BIXS)". *Fusion Science and Technology* 41(3 II) (2002), pp. 505–509. DOI: 10.13182/fst02-a22640.

[177] T. Matsuyama. "Beta-ray-induced X-ray spectrometry for tritium analysis in materials". *Radiation Measurements* 23(4) (1994), pp. 473–480. DOI: 10.1016/0168-9002(94)91213-0.

[178] T. Matsuyama and other authors. "Application of Beta-ray-induced X-ray Spectrometry (BIXS) for tritium analysis". *Fusion Engineering and Design* 49–50 (2000), pp. 885–891. DOI: 10.1016/S0920-3796(00)00326-4.

[179] T. Matsuyama and other authors. "Application of Beta-ray-induced X-ray Spectrometry (BIXS) for tritium analysis in materials". *Journal of Nuclear Materials* 290–293 (2001), pp. 437–442. DOI: 10.1016/S0022-3115(00)00581-X.

[180] T. Matsuyama and other authors. "Beta-ray-induced X-ray spectrometry for tritium analysis in materials". *Journal of Radioanalytical and Nuclear Chemistry* 234(1) (1998), pp. 929–936. DOI: 10.1023/A:1013521019314.

[181] M. Medina Restrepo and E. Myers. "Mass Difference of Tritium and Helium-3". *Phys. Rev. Lett.* 131 (Dec. 2023), p. 243002. DOI: 10.1103/PhysRevLett.131.243002.

[182] G. Mention, M. Fechner, T. Lasserre, et al. "The Reactor Antineutrino Anomaly". *Phys. Rev. D* 83 (2011), p. 073006. DOI: 10.1103/PhysRevD.83.073006.

[183] S. Mertens. "Study of Background Processes in the Electrostatic Spectrometers of the KATRIN Experiment". PhD thesis. Karlsruher Institut für Technologie (KIT), 2012. DOI: 10.5445/IR/1000027058.

[184] MicroBooNE Collaboration et al. "First Constraints on Light Sterile Neutrino Oscillations from Combined Appearance and Disappearance Searches with the MicroBooNE Detector". *Physical Review Letters* 130(1) (Jan. 2023), p. 011801. DOI: 10.1103/PhysRevLett.130.011801.

[185] MicroBooNE Collaboration et al. "Search for an Excess of Electron Neutrino Interactions in MicroBooNE Using Multiple Final-State Topologies". *Physical Review Letters* 128(24) (June 2022), p. 241801. DOI: 10.1103/PhysRevLett.128.241801.

[186] MicroBooNE Collaboration et al. "Search for Neutrino-Induced Neutral-Current Δ Radiative Decay in MicroBooNE and a First Test of the MiniBooNE Low Energy Excess under a Single-Photon Hypothesis". *Physical Review Letters* 128(11) (Mar. 2022), p. 111801. DOI: 10.1103/PhysRevLett.128.111801.

[187] MicroBooNE Collaboration1 et al. "Search for an Anomalous Excess of Inclusive Charged-Current ν_e Interactions in the MicroBooNE Experiment Using Wire-Cell Reconstruction". *Physical Review D* 105(11) (June 2022), p. 112005. DOI: 10.1103/PhysRevD.105.112005.

[188] M. Minh. "Bayesian Analysis of the First Data of the KATRIN Experiment". MA thesis. Munich, Germany: Technical University of Munich, 2018. URL: https://www.katrin.kit.edu/publikationen/MSc%5C_Ha%5C_Minh.pdf (visited on 06/08/2025).

[189] MiniBooNE Collaboration et al. "Search for Electron Neutrino Appearance at the $\Delta m^2 \sim 1\,\mathrm{eV}^2$ Scale". *Physical Review Letters* 98(23) (June 2007), p. 231801. DOI: 10.1103/PhysRevLett.98.231801.

[190] MiniBooNE Collaboration et al. "Search for Muon Neutrino and Antineutrino Disappearance in MiniBooNE". *Physical Review Letters* 103(6) (Aug. 2009), p. 061802. DOI: 10.1103/PhysRevLett.103.061802.

[191] MiniBooNE Collaboration et al. "Significant Excess of Electronlike Events in the MiniBooNE Short-Baseline Neutrino Experiment". *Physical Review Letters* 121(22) (Nov. 2018), p. 221801. DOI: 10.1103/PhysRevLett.121.221801.

[192] MiniBooNE Collaboration et al. "Updated MiniBooNE neutrino oscillation results with increased data and new background studies". *Physical Review D* 103(5) (Mar. 2021), p. 052002. DOI: 10.1103/PhysRevD.103.052002.

[193] MINOS+ Collaboration et al. "Search for Sterile Neutrinos in MINOS and MINOS+ Using a Two-Detector Fit". *Physical Review Letters* 122(9) (Mar. 2019). Publisher: American Physical Society, p. 091803. DOI: 10.1103/PhysRevLett.122.091803.

[194] **S. Mohanty**. *KNM5 systematic inputs update and other improvements*. 2024. URL: https://iap-katrin-wiki.iap.kit.edu/katrin/images/9/9d/RW%5C_report%5C_reupdated.pdf (visited on 06/08/2025).

[195] T. A. Mueller et al. "Improved predictions of reactor antineutrino spectra". *Physical Review C* 83(5) (May 2011), p. 054615. DOI: 10.1103/PhysRevC.83.054615.

[196] P. Musset and J.-P. Vialle. "Neutrino physics with gargamelle". *Physics Reports* 39(1) (Mar. 1978), pp. 1–130. DOI: 10.1016/0370-1573(78)90051-0.

[197] E. Myers et al. "Atomic Masses of Tritium and Helium-3". *Physical Review Letters* 114(1) (Jan. 2015), p. 013003. DOI: 10.1103/PhysRevLett.114.013003.

[198] S. Navas et al. "Review of Particle Physics". *Physical Review D* 110(3) (Aug. 2024), p. 030001. DOI: 10.1103/PhysRevD.110.030001.

[199] E. Otten and C. Weinheimer. "Neutrino mass limit from tritium β decay". *Reports on Progress in Physics* 71(8) (July 2008), p. 086201. DOI: 10.1088/0034-4885/71/8/086201.

[200] S. Parke and M. Ross-Lonergan. "Unitarity and the three flavor neutrino mixing matrix". *Physical Review D* 93(11) (June 2016), p. 113009. DOI: 10.1103/PhysRevD.93.113009.

[201] Particle Data Group, M. Tanabashi, et al. "Review of Particle Physics". *Physical Review D* 98(3) (Aug. 2018), p. 030001. DOI: 10.1103/PhysRevD.98.030001.

[202] W. Pauli. "On the conservation of the Lepton charge". *Il Nuovo Cimento (1955-1965)* 6(1) (July 1957), pp. 204–215. DOI: 10.1007/BF02827771.

[203] W. Pauli. *Pauli letter collection: letter to Lise Meitner*. URL: https://cds.cern.ch/record/83282 (visited on 06/08/2025).

[204] M. Perl et al. "Evidence for Anomalous Lepton Production in e^+e^- Annihilation". *Physical Review Letters* 35(22) (Dec. 1975), pp. 1489–1492. DOI: 10.1103/PhysRevLett.35.1489.

[205] F. Perrin. "Possibilité d'émission de particules neutres de masse intrinsèque nulle dans les radioactivités β". *Comptes-Rendus* 197 (1933), p. 1625. URL: https://neutrino-history.in2p3.fr/wp-content/uploads/2020/02/Perrin-d%5C%C3%5C%A9c-1933-NB.pdf (visited on 06/08/2025).

[206] M. Peskin. *An Introduction To Quantum Field Theory*. Boca Raton: CRC Press, May 2018. DOI: 10.1201/9780429503559.

[207] A. Picard, H. Backe, H. Barth, et al. "A solenoid retarding spectrometer with high resolution and transmission for keV electrons". *Nuclear Instruments and Methods in Physics Research Section B: Beam Interactions with Materials and Atoms* 63(3) (Feb. 1992), pp. 345–358. DOI: 10.1016/0168-583X(92)95119-C.

[208] H. Pollock. "The discovery of synchrotron radiation". *American Journal of Physics* 51(3) (Mar. 1983), pp. 278–280. DOI: 10.1119/1.13289.

[209] B. Pontecorvo. "Electron and Muon Neutrinos". *Zh. Eksp. Teor. Fiz.* 37 (1959), pp. 1751–1757. URL: https://centropontecorvo.df.unipi.it/Articles/Electron%5C_and%5C_muon%5C_neutrinos%5C_Zh%5C_Eksp%5C_Teor%5C_Fiz-1959.pdf (visited on 06/08/2025).

[210] B. Pontecorvo. "Inverse beta processes and nonconservation of lepton charge". *Zh. Eksp. Teor. Fiz.* 34 (1957), p. 247. URL: http://jetp.ras.ru/cgi-bin/dn/e%5C_007%5C_01%5C_0172.pdf (visited on 06/08/2025).

[211] B. Pontecorvo. "Mesonium and Antimesonium". *Soviet Journal of Experimental and Theoretical Physics* 6 (Jan. 1958), p. 429. URL: https://ui.adsabs.harvard.edu/abs/1958JETP....6..429P (visited on 06/08/2025).

[212] B. Pontecorvo. "Neutrino Experiments and the Problem of Conservation of Leptonic Charge". *Zh. Eksp. Teor. Fiz.* 53 (1967), pp. 1717–1725. URL: http://www.jetp.ras.ru/cgi-bin/dn/e%5C_026%5C_05%5C_0984.pdf (visited on 06/08/2025).

[213] M. Prall, P. Renschler, F. Glück, et al. "The KATRIN pre-spectrometer at reduced filter energy". *New Journal of Physics* 14(7) (July 2012), p. 073054. DOI: 10.1088/1367-2630/14/7/073054.

[214] "Precision measurement of the electron energy-loss function in tritium and deuterium gas for the KATRIN experiment". 81 (July 2021), p. 579. DOI: 10.1140/epjc/s10052-021-09325-z.

[215] W. Press, S. Teukolsky, W. Vetterling, et al. *Numerical Recipes: The Art of Scientific Computing*. 3rd. New York, NY, USA: Cambridge University Press, 2007.

[216] O. Rest. "Precision high voltage at the KATRIN experiment and new methods for an absolute calibration at ppm-level for high-voltage dividers". PhD thesis. Westfälische Wilhelms-Universität Münster, Dec. 2024. URL: https://www.uni-muenster.de/imperia/md/content/physik%5C_kp/agweinheimer/theses/diss-oliver%5C_rest.pdf (visited on 06/06/2025).

[217] C. Robert and G. Casella. *Monte Carlo Statistical Methods*. 2nd. New York: Springer, 2004.

[218] C. Rodenbeck, S. Wüstling, S. Enomoto, et al. "Wideband precision stabilization of the -18.6kV retarding voltage for the KATRIN spectrometer". *Journal of Instrumentation* 17(06) (June 2022), P06003. DOI: 10.1088/1748-0221/17/06/P06003.

[219] C. Rodenbeck. "Inelastic electron scattering in tritium gas and ppm-precise energy scale at the KATRIN experiment". PhD thesis. Westfälische Wilhelms-Universität Münster, 2023. URL: https://repositorium.uni-muenster.de/document/miami/374e661f-f5d8-416d-b305-85f192884730/diss%5C_rodenbeck.pdf (visited on 06/08/2025).

[220] M. Röllig, F. Priester, M. Babutzka, et al. "Activity monitoring of a gaseous tritium source by beta induced X-ray spectrometry". *Fusion Engineering and Design* 88(6–8) (2013), pp. 1263–1266. DOI: 10.1016/j.fusengdes.2012.11.001.

[221] M. Röllig. "Tritium analytics by beta induced X-ray spectrometry". Dissertation. Institut für Technische Physik (ITEP), 2015, pp. XI, 202. DOI: 10.5445/IR/1000054050.

[222] C. Röttele. "Tritium suppression factor of the KATRIN transport section". PhD thesis. Karlsruher Institut für Technologie (KIT), 2019. DOI: 10.5445/IR/1000096733.

[223] R. Sack. "Measurement of the energy loss of 18.6 keV electrons on deuterium gas and determination of the tritium Q-value at the KATRIN experiment". PhD thesis. Westfälische Wilhelms-Universität Münster, 2020. URL: https://repositorium.uni-muenster.de/document/miami/9b681416-192f-42d9-a9dc-3d4b59a50624/diss%5C_sack.pdf (visited on 06/08/2025).

[224] A. Saenz and P. Froelich. "Effect of final-state interactions in allowed $\beta-$ decays. II. Reliability of the β-decay spectrum for T_2". *Physical Review C* 56(4) (Oct. 1997), pp. 2162–2184. DOI: 10.1103/PhysRevC.56.2162.

[225] A. Saenz, S. Jonsell, and P. Froelich. "Improved Molecular Final-State Distribution of HeT$^+$ for the β-Decay Process of T_2". *Physical Review Letters* 84(2) (Jan. 2000), pp. 242–245. DOI: 10.1103/PhysRevLett.84.242.

[226] A. Salam. "On parity conservation and neutrino mass". *Il Nuovo Cimento (1955-1965)* 5(1) (Jan. 1957), pp. 299–301. DOI: 10.1007/BF02812841.

[227] S. Schael et al. "Precision electroweak measurements on the Z resonance". *Physics Reports* 427(5–6) (2006), pp. 257–454. DOI: 10.1016/j.physrep.2005.12.006.

[228] A. Schaller. "Characterization and mitigation of the background in KATRIN". PhD thesis. Technical University of Munich, 2020.

[229] L. Schimpf. "Characterisation of energy loss processes of 18.6 keV electrons inside the windowless tritium source of KATRIN". PhD thesis. Karlsruher Institut für Technologie (KIT), 2021. 232 pp. DOI: 10.5445/IR/1000131810.

[230] L. Schlüter. "Neutrino-Mass Analysis with sub-eV Sensitivity and Search for Light Sterile Neutrinos with the KATRIN Experiment". PhD thesis. Technische Universität München, 2022, p. 211. URL: https://mediatum.ub.tum.de/1661391 (visited on 06/08/2025).

[231] S. Schneidewind, J. Schürmann, A. Lokhov, et al. "Improved treatment of the T molecular final-states uncertainties for the KATRIN neutrino-mass measurement". *The European Physical Journal C* 84(5) (May 2024), p. 494. DOI: 10.1140/epjc/s10052-024-12802-w.

[232] S. Schneidewind. "Improvement of the neutrino mass sensitivity and background reduction of the KATRIN experiment". PhD thesis. Westfälische Wilhelms-Universität Münster, 2025.

[233] A. Sejersen Riis, S. Hannestad, and C. Weinheimer. "Analysis of simulated data for the KArlsruhe TRItium Neutrino experiment using Bayesian inference". *Phys. Rev. C* 84 (Oct. 2011), p. 045503. DOI: 10.1103/PhysRevC.84.045503.

[234] A. Serebrov, A. Fomin, and R. Samoilov. "The Experiment Neutrino-4 on the Search for Sterile Neutrino at SM-3 Reactor". *Moscow Univ. Phys. Bull.* 77(2) (2022), pp. 401–406. DOI: 10.3103/S0027134922020904.

[235] D. Sivia. *Data Analysis: A Bayesian Tutorial*. Oxford University Press, June 2006. DOI: 10.1093/oso/9780198568315.001.0001.

[236] SNO Collaboration. "Measurement of the Rate of $\nu\_e + d \to p + p + e^-$ Interactions Produced by ^{8}B Solar Neutrinos at the Sudbury Neutrino Observatory". *Physical Review Letters* 87(7) (July 2001), p. 071301. DOI: 10.1103/PhysRevLett.87.071301.

[237] SNO Collaboration et al. “Combined analysis of all three phases of solar neutrino data from the Sudbury Neutrino Observatory”. *Physical Review C* 88(2) (Aug. 2013), p. 025501. DOI: 10.1103/PhysRevC.88.025501.

[238] M. Sturm et al. “Kilogram scale throughput performance of the KATRIN tritium handling system”. *Fusion Engineering and Design* 170 (Sept. 2021), p. 112507. DOI: 10.1016/j.fusengdes.2021.112507.

[239] Super-Kamiokande Collaboration et al. “Evidence for Oscillation of Atmospheric Neutrinos”. *Physical Review Letters* 81(8) (Aug. 1998), pp. 1562–1567. DOI: 10.1103/PhysRevLett.81.1562.

[240] Super-Kamiokande Collaboration et al. “Solar ^{8}B and hep Neutrino Measurements from 1258 Days of Super-Kamiokande Data”. *Physical Review Letters* 86(25) (June 2001), pp. 5651–5655. DOI: 10.1103/PhysRevLett.86.5651.

[241] Super-Kamiokande Collaboration et al. “Solar neutrino measurements in Super-Kamiokande-IV”. *Physical Review D* 94(5) (Sept. 2016), p. 052010. DOI: 10.1103/PhysRevD.94.052010.

[242] The MicroBooNE Collaboration et al. “Search for an Anomalous Excess of Charged-Current ν_e Interactions without Pions in the Final State with the MicroBooNE Experiment”. *Physical Review D* 105(11) (June 2022), p. 112004. DOI: 10.1103/PhysRevD.105.112004.

[243] The Royal Swedish Academy of Sciences. *The 2015 Nobel Prize in Physics - Press release*. URL: https://www.nobelprize.org/prizes/physics/2015/press-release/ (visited on 05/23/2025).

[244] K. Trost. “Mitigation of Rear Wall Backscattering in keV Sterile Neutrino Search at the KATRIN Experiment”. MA thesis. Karlsruhe, Germany: Karlsruhe Institute of Technology, 2024. URL: https://www.katrin.kit.edu/publikationen/mth%5C_trost.pdf (visited on 06/08/2025).

[245] K. Valerius, H. Hein, H. Baumeister, et al. “Prototype of an angular-selective photoelectron calibration source for the KATRIN experiment”. *Journal of Instrumentation* 6(01) (Jan. 2011), P01002. DOI: 10.1088/1748-0221/6/01/P01002.

[246] K. Valerius et al. “A UV LED-based fast-pulsed photoelectron source for time-of-flight studies”. *New Journal of Physics* 11(6) (June 2009), p. 063018. DOI: 10.1088/1367-2630/11/6/063018.

[247] K. Valerius. “Electromagnetic design and inner electrode for the KATRIN main spectrometer”. *Progress in Particle and Nuclear Physics* 57(1) (July 2006), pp. 58–60. DOI: 10.1016/j.ppnp.2005.11.011.

[248] B. Wall et al. “Dead layer on silicon p–i–n diode charged-particle detectors”. *Nuclear Instruments and Methods in Physics Research Section A: Accelerators, Spectrometers, Detectors and Associated Equipment* 744 (Apr. 2014), pp. 73–79. DOI: 10.1016/j.nima.2013.12.048.

[249] E. Wang, L. Alvarez-Ruso, and J. Nieves. “Single photon events from neutral current interactions at MiniBooNE”. *Physics Letters B* 740 (Jan. 2015), pp. 16–22. DOI: 10.1016/j.physletb.2014.11.025.

[250] C. Wiesinger and A. Lokhov. *KNM1-5 summary*. 2024. URL: https://indico.ph.tum.de/event/7566/contributions/8866/attachments/5932/7897/2024-03-21-KNM1-5%5C%20Summary.pdf (visited on 06/08/2025).

[251] D. Wilkinson. “Small terms in the beta-decay spectrum of tritium”. *Nuclear Physics A* 526(1) (Apr. 1991), pp. 131–140. DOI: 10.1016/0375-9474(91)90301-L.

[252] S. Wilks. “The Large-Sample Distribution of the Likelihood Ratio for Testing Composite Hypotheses”. *The Annals of Mathematical Statistics* 9(1) (1938), pp. 60–62. URL: https://www.jstor.org/stable/2957648 (visited on 06/08/2025).

[253] C. Wu et al. “Experimental Test of Parity Conservation in Beta Decay”. *Physical Review* 105(4) (Feb. 1957), pp. 1413–1415. DOI: 10.1103/PhysRev.105.1413.

[254] T.-H. Yeh et al. “Probing physics beyond the standard model: limits from BBN and the CMB independently and combined”. *Journal of Cosmology and Astroparticle Physics* 2022(10) (Oct. 2022), p. 046. DOI: 10.1088/1475-7516/2022/10/046.

[255] C. Zhang, X. Qian, and M. Fallot. “Reactor antineutrino flux and anomaly”. *Progress in Particle and Nuclear Physics* 136 (2024), p. 104106. DOI: 10.1016/j.ppnp.2024.104106.

[256] K. Zuber. *Neutrino physics*. Taylor & Francis, 2020. DOI: 10.1201/9781315195612.